



Universidad de Oviedo

**Department of Electrical, Computer and Systems  
Engineering**

Programa de Doctorado en Energía y Control de Procesos

Doctorate Program in Energy and Process Control

**Control And Supervision of  
Permanent Magnet Synchronous  
Machines using High Frequency  
Signal Injection**

by

Daniel Fernandez Alonso

**Dissertation submitted in partial fulfillment of the requirements  
for the degree of Doctor of Philosophy in Electrical Engineering  
with International Mention**

**Advisor:** David Díaz Reigosa. Associate Professor. Dept. of Elec.,  
Computer, & Systems Engineering, University of Oviedo

Gijón, 2016





*A mi familia  
y en especial, a Silvia*



# Acknowledgements

During the development of this thesis I had the chance to travel, meet people and realize the importance of research, sometimes hard, many others rewarding. First of all, I would like to thank my advisor Prof. David Díaz for his time, who leads by example with hard work and dedication. Among other things, I finally learned that *"creer es ignorar"*. In addition, I would like to thank Prof. Fernando Briz, in spite of his busy schedule he always finds time for a discussion. I take this opportunity to thank also the Electrical Engineering Department (University of Oviedo) for providing me all the necessary facilities for the development of this thesis. At the same time, this work cannot be possible without the fellowship awarded by the Principality of Asturias, under the grant BP-13067. As a gesture of appreciation, I would like to remember the people I met during my internship in Japan, at Nissan Advanced Technology Center in 2013, my advisor and the head of EV system Laboratory Katou San, and the rest of the workgroup Yoshida San, Tanaka San and Suzuki San, for allowing me to be part of their team, thank you. I would like to thank also Prof. Zhu, for giving me the chance to be a visiting student at the University of Sheffield and the people I met there: Hanlin, Ali, Mohammed, Ahlam and Fatih. I strongly thank my lab-mates Cristian and Jose Miguel for the selfless aid and coffee discussions. Finally I would like to thank my family: my grandparents Secuendino and Elena, my parents Hipólito y Emma who are the definition of hard work, my brother Andrés, and my sisters Diana and Elena. These last words are the dedication to the most special person, Silvia. You are always there, supporting me and making my life easier. Thank you.



# Resumen

El uso de máquinas síncronas de imanes permanentes (PMSM) se ha visto incrementado durante las últimas décadas debido a su instalación en vehículos eléctricos(EVs) e híbridos(HEVs) o turbinas eólicas. Los límites de operación de las PMSMs viene dado por las pérdidas producidas durante el proceso de conversión de energía, lo que produce incrementos de temperatura en la máquina. De entre todos los elementos que componen las PMSM, los imanes permanentes son la parte que sufre un mayor estrés, desde el punto de vista térmico, ya que sus propiedades dependen de la temperatura y su temperatura máxima de funcionamiento es normalmente la más baja entre todas las partes que componen la máquina. Por ello, es muy importante poder estimar o medir la temperatura de los imanes durante el funcionamiento de la máquina. La medida la temperatura de los imanes en máquinas comerciales plantea problemas de coste, pérdida de robustez o mantenimiento, por lo que no es común disponer de esta variable. Como alternativa a la medida de temperatura, se pueden encontrar métodos de estimación, que se dividen modelos térmicos, métodos basados en la fuerza contraelectromotriz y métodos basados en la inyección de diferentes tipos de señales desde el estator. Los modelos térmicos son específicos para cada diseño y necesitan amplios conocimiento de la máquina para su ajuste, en términos de geometría, de los materiales que la componen o del sistema de refrigeración. El requerimiento de parámetros de la máquina para la implementación de métodos basados en la fuerza contraelectromotriz no es tan riguroso, pero estos métodos no son aplicables cuando la máquina se encuentra parada. Los basados en la inyección de algún tipo de señal, se dividen en métodos los que aplican la inyección de un pulso o métodos que inyectan una señal de alta frecuencia. Ambos, pueden implementarse para todo el rango de velocidades de la máquina y no requieren un conocimiento previo de la misma. La presente tesis propone dos métodos de estimación de temperatura: el primero para estimar la temperatura media del iman y el segundo para estimar la temperatura diferencial producida en el imán. Dos sistemas de medida de

temperatura han sido desarrollados con el objetivo de verificar los métodos propuestos. Además del creciente interés en la estimación de temperatura de los imanes, el interés en la estimación del estado de magnetización ha crecido debido al interés progresivo que empiezan a tener las máquinas síncronas de imanes permanentes de flujo variable (VF-PMSMs) en aplicaciones como EVs o HEVs. Estos tipos de máquinas requieren una estimación precisa del estado de magnetización para su correcto funcionamiento, ya que éste puede cambiar durante el funcionamiento normal de la máquina para permitir trabajar a altas velocidades con menos requerimientos de corriente de debilitamiento. Los métodos existentes se basan en la fuerza contraelectromotriz de la máquina, presentando así los mismos inconvenientes que el uso de esta variable presenta cuando se usa en técnicas de estimación de temperatura. Es por eso que esta tesis también analiza la aplicación de el uso de métodos basados la inyección de señales de alta frecuencia para la estimación del estado de magnetización de la máquina. Basándose en el efecto magnetoresistivo que tiene lugar en los imanes, se presenta un método de estimación del estado de magnetización que utiliza la inyección de señales de alta frecuencia, no interfiere con el funcionamiento normal de la máquina, es aplicable en todo el rango de velocidades y presenta una sensibilidad muy baja a cambios en los parámetros de la máquina.

# Abstract

The use of permanent magnet synchronous machines (PMSMs) has been increasing during the last decades due to their use in e.g. electric vehicles (EVs), hybrid electric vehicles (HEV) or wind turbines. Operating limits of PMSMs are determined by the induced power losses during the energy conversion process, which makes the machine temperature to increase. Among all PMSM constructive parts, permanent magnets (PMs) are the weakness part from the temperature point of view, i.e. their properties strongly depends on the temperature and its maximum operating temperature is typically the lowest among all PMSM constructive parts. For these reasons PM temperature estimation/measurement during normal operation of the machine is a very interesting feature. PM temperature measurement is problematic from installation, cost, robustness and maintenance perspectives, meaning that PM temperature is not usually available in standard machines. An alternative to PM temperature measurement is temperature estimation. PM temperature estimation methods can be divided into thermal models, BEMF based methods and methods based on the injection of some form of test signal into the stator terminal of the machine. Thermal models require previous knowledge of the machine geometry, materials and cooling system, making the model specific for each machine design. BEMF based methods cannot work at standstill or very low speeds and also require previous knowledge of some machine parameters. Methods based on the injection of a test signal can be further divided into pulse injection based methods and high frequency signal injection based methods; Both methods can be used in the whole speed range on the machine and do not require previous knowledge of machine parameters. This thesis proposes two temperature estimation methods: the first one for mean magnet temperature estimation, the second one for differential magnet temperature estimation; two wireless temperature measurement systems have been developed for the verification of the proposed methods. In addition to significant research efforts in PM temperature estimation methods, PM magnetization state (MS) estimation methods have been also the

focus of growing interest due to the increased use of variable flux permanent magnet synchronous machines (VF-PMSMs) in many traction applications, e.g. EVs and HEVs. These type of machines require accurate MS estimation since its MS can be changed during normal operation of the machine to allow high speed operation without the need of flux weakening current injection. Existing MS estimation methods are based on the BEMF, their weaknesses being the same as the BEMF temperature estimation based methods. For this reason, this thesis also analyzes the extension of high frequency signal injection based method for MS estimation purposes. A high frequency signal injection MS estimation method based on the magnetoresistive effect of PMs is proposed in this thesis. The proposed method does not interfere with the normal operation of the drive, can work in the whole speed range of the machine and its sensitivity to machine parameter variation is very low.



# Nomenclature

$\alpha_B$	$B_r$ Reversible temperature coefficient
$\alpha_{cu}$	Copper thermal resistive coefficient
$\alpha_{mag}$	Permanent magnet thermal resistive coefficient
$\beta_B$	Magnet flux thermal coefficient
$\delta$	Skin depth
$\delta_H$	Giant magnetoresistance
$\Delta_x$	Magnet displacement in x direction
$\Delta_y$	Magnet displacement in y direction
$\Theta_{B-I}$	Angle of the magnet surface respect to the external magnetic field
$\Theta_r$	Rotor angular position
$\lambda_{PM}$	Permanent magnet flux
$\mu_0$	Relative permeability of air
$\mu_{CO}$	Absolute permeability of the core
$\mu_r$	Relative permeability
$\rho$	Resistivity
$\Phi_{Z_d}$	Phase of $d$ -axis impedance
$\omega_{hf}$	High frequency signal angular speed
$\omega_r$	Rotor angular speed.
$B_{gap}$	Average airgap flux density
$B_m$	Maximum flux density
$B_r$	Permanent magnet remanence
$B_{r-ini}$	Permanent magnet initial remanence
$F_c$	Centrifugal force
$i_a$	A-phase current
$i_b$	B-phase current
$i_d$	$d$ -axis component of current complex vector
$i_{DCp}^*$	Coil DC current
$i_{dhf}$	$d$ -axis high frequency component component of current complex vector
$i_{dq}$	Current complex vector

$i_{dq}^x$	Current complex vector in rotor $x$ synchronous reference frame
$i_{dqhf}^x$	High frequency current complex vector of $y$ in $x$ reference frame
$i_{dqhfpc}$	Positive component of high frequency current complex vector
$i_{dqhfnc}$	Negative component of high frequency current complex vector
$i_{hfp}^p$	Coil high frequency current referred to primary side
$i_{hfs}^s$	Magnet high frequency current referred to secondary side
$i_q$	$q$ –axis component of current complex vector
$i_{qrhf}$	Rotor $q$ –axis high frequency component of current complex vector
$i_{qhf}$	$q$ –axis high frequency component of current complex vector
$k_{\Delta d}$	Static eccentricity constant
$k_{\Delta m}$	Dynamic eccentricity constant
$k_{\Delta s}$	Mixed eccentricity constant
$K_e$	Eddy current loss constant
$K_p$	Proportional constant
$K_t$	Torque constant
$K_{th}$	Thermocouple constant
$K_v$	Voltage constant
$L_d$	$d$ –axis inductance
$L_{dhf}$	$d$ –axis high frequency inductance
$L_{hfp}$	Coil high frequency inductance
$L_q$	$q$ –axis inductance
$L_{qhf}$	$q$ –axis high frequency inductance
$m$	mass
$M_{ps}$	Mutual coupling between primary and secondary
$N$	Number of turns
$p$	Differential operator
$p.u.$	Per unit
$r$	Rotor radius
$R_d$	$d$ –axis resistance
$R_{dhf}$	$d$ –axis high frequency resistance
$R_{drhf}$	Rotor $d$ –axis high frequency resistance
$R_{dshf}$	Stator $d$ –axis high frequency resistance
$R_{hf}$	Total $d$ –axis high frequency resistance
$R_{hfr}^p$	Coil high frequency resistance referred to primary side
$R_{hfFEr}^p$	Core high frequency resistance referred to primary side
$R_{hfs}^x$	Magnet high frequency resistance referred to "x" side
$R_{pcDC}$	DC components of the estimated high frequency resistance
$R_{pc1\omega_r}$	Component at $\omega_r$ of the estimated high frequency resistance
$R_q$	$q$ –axis resistance
$R_{qhf}$	$q$ –axis high frequency resistance

$R_{qhf}$	$q$ -axis high frequency resistance
$R_{rhf}$	Rotor $d$ -axis high frequency resistance
$R_{shf}$	Stator $d$ -axis high frequency resistance
$R_T$	Total resistance
$s$	Laplace complex variable
$t$	Time
$T_0$	Room temperature
$T_{conn}$	Temperature in the connection point
$T_{em}$	Electromagnetic torque
$T_{max}$	Maximum temperature
$T_{min}$	Minimum temperature
$T_{re}$	Reluctance torque
$T_r$	Rotor temperature
$T_s$	Stator Temperature
$T_{sens}$	Temperature in the sensing point
$v_{dq}$	Voltage complex vector
$v_d$	$d$ -axis component of voltage complex vector
$v_{dhf}$	$d$ -axis component of high frequency voltage complex vector
$v_{drhf}$	Rotor $d$ -axis component of high frequency voltage complex vector
$v_{dq}^x$	Voltage complex vector in $x$ synchronous reference frame
$v_{dqhf}^x$	High frequency voltage complex vector of $y$ in $x$ reference frame
$v_{dqhfpc}$	Positive component of high frequency voltage complex vector
$v_{dqhfnc}$	Negative component of high frequency voltage complex vector
$v_{hfp}^p$	Coil high frequency voltage referred to primary side
$v_q$	$q$ -axis component of voltage complex vector
$v_{qhf}$	$q$ -axis component of high frequency voltage complex vector
$v_{qrhf}$	Rotor $q$ -axis component of high frequency voltage complex vector
$v_{th}$	Output voltage of a thermocouple



# Abbreviations and acronyms

<b>AC</b>	Altern Current
<b>AlNiCo</b>	Aluminum-Niquel-Cobalt
<b>ARPA – E</b>	Advance Research Projects Agency-Energy
<b>BEMF</b>	Back-Electromotive Force
<b>BPF</b>	Band-Pass Filter
<b>BSF</b>	Band-Stop Filter
<b>DC</b>	Direct Current
<b>DSP</b>	Digital Signal Processor
<b>FEA</b>	Finite Element Analysis
<b>FFT</b>	Fast Fourier Transform
<b>FOC</b>	Field Oriented Control
<b>GaAs</b>	Gallium-Arsenide
<b>GMR</b>	Giant Magnetoresistance
<b>I2C</b>	Inter-Integrated Circuit
<b>IEEE</b>	Institute of Electrical and Electronics Engineers
<b>IGBT</b>	Insulated Gate Bipolar Transistor
<b>IM</b>	Induction Machine
<b>IPMSM</b>	Interior Permanent Magnet Synchronous Machine
<b>IR</b>	Infra Red
<b>LAN</b>	Local Area Network
<b>MOSFET</b>	Metal–Oxide–Semiconductor Field-Effect Transistor
<b>MR</b>	Magnetoresistance
<b>MTPA</b>	Maximum Torque Per Ampere
<b>NdFeB</b>	Neodymium-Iron-Boron
<b>NiCuNi</b>	Nickel-Copper-Nickel
<b>PCB</b>	Printed Circuit Board
<b>PI</b>	Proportional-Integral
<b>PM</b>	Permanent Magnet
<b>PMSM</b>	Permanent Magnet Synchronous Machine
<b>PTC</b>	Positive Temperature Coefficient

<b>RMB</b>	Renminbi (Chinese currency)
<b>SmCo</b>	Samarium-Cobalt
<b>SCI</b>	Serial Communications Interface
<b>SCR</b>	Silicon Controlled Rectifier
<b>SPI</b>	Serial Peripheral Interface
<b>SPMSM</b>	Surface Permanent Magnet Synchronous Machine
<b>SPTFMM</b>	Spoke-Type Ferrite Magnet Machine
<b>SRAM</b>	Static Random-Access Memory
<b>VF – PMSM</b>	Variable Flux Permanent Magnet Synchronous Machine

# List of Figures

1.1	Evolution of the energy product value of different families of permanent magnets . . . . .	2
1.2	Comparison of efficiency of IPMSM and IM . . . . .	3
1.3	Magnet grade suffix as function of Dy content . . . . .	5
1.4	Rare earth metal price compared with gold . . . . .	7
2.1	Implementation of the $d$ -axis pulsating current injection . . .	24
2.2	Signal processing for the $d$ -axis pulsating current injection . .	25
2.3	Implementation of the $d$ -axis pulsating voltage injection with $q$ -axis current cancellation . . . . .	27
2.4	Signal processing for the $d$ -axis pulsating current injection with $q$ -axis current cancellation . . . . .	27
2.5	SPM and IPM test machines . . . . .	30
2.6	Magnet temperature measured by each thermocouple as a function of $I_q$ . . . . .	31
2.7	Experimentally measured temperature variation along the magnet. . . . .	32
2.8	SPMSM: Experimentally measured stator and rotor temperatures and magnet temperature estimation error . . . . .	34
2.9	SMPSM: Estimated high-frequency inductance $L_{dhf}$ . . . . .	35
2.10	SMPSM: Magnet temperature estimation error after decoupling the magnetoresistive effect . . . . .	35
2.11	IPMSM: Experimentally measured stator and rotor temperatures and magnet temperature estimation error . . . . .	37
2.12	IPMSM: Estimated high-frequency inductance $L_{dhf}$ . . . . .	38

2.13	IPMSM: Magnet temperature estimation error after decoupling the magnetoresistive effect . . . . .	38
2.14	One third of the cross Section of the IPMSM used for simulations and experimental results . . . . .	40
2.15	Magnet temperature distribution . . . . .	41
2.16	BEMF frequency spectrum . . . . .	42
2.17	Fundamental component of the BEMF vs. mean magnet temperature. . . . .	43
2.18	Estimated $d$ -axis high frequency resistance . . . . .	43
2.19	BEMF 13 <sup>th</sup> harmonic magnitude vs. mean magnet temperature and vs. the 1 <sup>th</sup> harmonic magnitude of the BEMF . . . . .	44
2.20	Back-EMF 13 <sup>th</sup> harmonic magnitude vs. differential magnet temperature . . . . .	45
2.21	Experimentally measured magnet temperatures for different $I_q$ current levels . . . . .	46
2.22	Experimentally measured magnet differential temperature . . . . .	47
2.23	Experimentally measured magnet differential temperature. . . . .	48
2.24	Bemf of the IPMSM . . . . .	49
2.25	BEMF frequency spectrum of the IPMSM . . . . .	50
2.26	Fundamental component of the BEMF vs. mean magnet temperature . . . . .	51
2.27	Estimated $d$ -axis high frequency resistance for the case of uniform and non-uniform temperature distributions . . . . .	51
2.28	BEMF 13th harmonic magnitude for the case of uniform and nonuniform temperature distributions . . . . .	52
2.29	Back-EMF 13 <sup>th</sup> harmonic magnitude vs. differential magnet temperature . . . . .	53
2.30	Temperature estimation error . . . . .	54
3.1	Schematic representation of different types of eccentricities. . . . .	57
3.2	Estimated $d$ -axis high frequency resistance for different eccentricities . . . . .	59
3.3	FFT of the estimated $d$ -axis high frequency resistance for eccentricity 0.75pu . . . . .	59



3.4	DC and $\omega_r$ components for static eccentricity . . . . .	59
3.5	DC and $\omega_r$ components for dynamic eccentricity . . . . .	60
3.6	Mixed eccentricity simulation. . . . .	61
3.7	DC and $\omega_r$ components for mixed eccentricity . . . . .	63
3.8	Machine rotor design and rotor temperature distribution due to lamination grain orientation . . . . .	64
3.9	Estimated $d$ -axis high frequency resistance vs. average tem- perature of the six PMs . . . . .	64
3.10	Schematic representation of the PM placement. . . . .	65
3.11	Estimated $d$ -axis high frequency resistance for different mag- net posistion . . . . .	66
3.12	Experimental test bench, PMSM and load machine (IM). . . . .	66
3.13	Attached mass for dynamic eccentricity. . . . .	67
3.14	Thermal image of the rotor and its schematic representation . . . . .	68
3.15	Attached mass for dynamic eccentricity. . . . .	69
3.16	Experimental results for DC and $\omega_r$ components for mixed eccentricity . . . . .	70
3.17	Cross section of the studied rotors . . . . .	71
3.18	Estimated high frequency resistance vs. magnet temperature of a 36/6 machine . . . . .	73
3.19	Cross section of differnt IPM machines . . . . .	77
3.20	Contour plot of the magnetic flux density for differnt IPM machines . . . . .	79
3.21	Representation of the coil flux and the magnet position for the d-axis injection for different coil pitches of a 36 slot 6 pole machine. . . . .	80
4.1	External magnetic field, $B_{ext}$ , and induced eddy current vectors	87
4.2	Simplified 2D representation of the flux lines in a PMSM . . . . .	87
4.3	Ferrite, SmCo and NdFeB magnet disks . . . . .	89
4.4	Segmented magnet arrangements (SmCo and NdFeB). . . . .	90
4.5	Experimental setup for the PM magnetoresistance evaluation . . . . .	90
4.6	Simplified representation of flux lines in the experimental setup	91

4.7	Equivalent high frequency model of the simplified geometry . .	91
4.8	Signal processing used for magnet high frequency estimation using high frequency/voltage injection . . . . .	95
4.9	H-Bridge power converter . . . . .	95
4.10	Control block diagram of the DC and high frequency signal injection . . . . .	96
4.11	Injected voltage $v_{Lp}^p$ and its corresponding frequency spectrum	97
4.12	Injected current $i_{Lp}^p$ and its corresponding frequency spectrum	98
4.13	Simplified representation of the experimental setup . . . . .	99
4.14	Estimated high frequency resistance $R_{hfs}^p$ of the iron powder core . . . . .	100
4.15	FEA results showing the magnetic flux density of the experi- mental setup . . . . .	101
4.16	Coil reflected magnet high frequency resistance, $R_{hfs}^p$ of a fer- rite, NdFeB and SmCo disks . . . . .	102
4.17	Coil reflected magnet high frequency resistance for different values of the remanent field . . . . .	103
4.18	Schematic representation of the circuit used for PM magneti- zation and demagnetization. . . . .	104
4.19	Coil reflected magnet high frequency resistance for NdFeB magnets vs. the flux density . . . . .	105
4.20	Coil reflected magnet high frequency resistance for a ferrite magnets vs. the flux density . . . . .	105
4.21	Coil reflected magnet high frequency resistance for a SmCo magnets vs. the flux density . . . . .	106
4.22	Coil reflected magnet high frequency resistance in 5 mm and 2.5 mm NdFeB segmented magnets . . . . .	106
4.23	Coil reflected magnet high frequency resistance $R_{hfs}^p$ of non- isolated segmented (5 mm) NdFeB magnets . . . . .	107
4.24	Coil reflected magnet high frequency resistance in 5 mm SmCo non-isolated segmented magnets . . . . .	107
4.25	Coil reflected magnet high frequency resistance $R_{hfs}^p$ of non- isolated segmented SmCo magnets . . . . .	108
4.26	Magnetoresistance variations in multilayer structures. . . . .	110

4.27	Magnetization direction of the coating layers when an external magnetic field is applied on a demagnetized magnet . . . . .	110
4.28	Magnetization direction of the coating layers for a magnetized magnet . . . . .	111
4.29	Enhanced experimental setup for magnetoresistance evaluation, (a) and section of the experimental setup, (b). . . . .	113
4.30	Block diagram of the DC and high frequency signal . . . . .	114
4.31	Equivalent high frequency circuit of the experimental setup without core and magnet . . . . .	115
4.32	Experimental setup configured for core high frequency resistance estimation . . . . .	116
4.33	Experimental setup configured for magnet high frequency resistance estimation . . . . .	117
4.34	Block diagram of the DC and high frequency signal . . . . .	118
4.35	Magnetic flux density distribution on magnet surface for a demagnetized NdFeB magnet . . . . .	119
4.36	Magnetic flux density distribution on magnet surface for a magnetized NdFeB magnet . . . . .	119
4.37	Flux density sensor ans position . . . . .	120
4.38	Reflected high frequency resistance $R_{hfs}^p$ of a NdFeB magnet for two different tickness and coating types . . . . .	121
4.39	Reflected high frequency resistance $R_{hfs}^p$ of a NdFeB magnet for two different tickness and coating types . . . . .	122
4.40	Reflected high frequency resistance $R_{hfs}^p$ of a NdFeB magnet for two different tickness and coating types . . . . .	123
4.41	Reflected high frequency resistance $R_{hfs}^p$ of NdFeB, AlNiCo and SmCo magnets, for 5mm tickness and for two different coatings . . . . .	124
4.42	Reflected high frequency resistance $R_{hfs}^p$ of NdFeB, AlNiCo and SmCo magnets, for 10mm tickness and for two different coatings . . . . .	125
4.43	SPMSM FEA model. . . . .	126
4.44	Rotor position relative to the stator for all the simulations and coordinated system . . . . .	126

4.45	Eddy-current distribution in a PM . . . . .	127
4.46	Eddy-current density distribution in the PM when $I_d$ current changes from -15 to 0 A . . . . .	127
4.47	Signal processing for rotor high-frequency-resistance estima- tion using pulsating voltage injection. . . . .	130
4.48	Experimental test bench (IPMSM). . . . .	130
4.49	Estimated $d$ -axis stator-reflected magnet high-frequency re- sistance obtained both by FEA and experimental . . . . .	131
4.50	Estimated $d$ -axis stator-reflected magnet resistance vs. mag- netization state & speed, for the case of SPMSM and IPMSM . . . . .	133
4.51	Equivalent $d$ -axis high frequency model of a PMSM. . . . .	134
A.1	Schematic representation of the temperature and field mea- surement system. . . . .	158
A.2	Temperature measurement and transmission device . . . . .	159
A.3	Thermocouples' location in the IPMSM . . . . .	160
A.4	Desktop application for temperature measurement system. . . . .	161
B.1	Schematic representation of the temperature and field mea- surement system. . . . .	164
B.2	Field and temperature IC sensors location in the IPMSM . . . . .	165
B.3	Assembling of the electronic system . . . . .	166
B.4	Assembling of field and temperature measurement system in the IPMSM . . . . .	168
B.5	Desktop application for temperature measurement system. . . . .	169
B.6	Experimentally measured magnet temperatures for different $I_q$ currents . . . . .	170
B.7	Experimentally measured magnet temperatures for differnt $I_d$ currents . . . . .	170
B.8	Experimentally measured $d$ -axis current and transient re- sponse of the magnetic field . . . . .	171
B.9	Experimentally measured magnet field for differnt $I_q$ currents . . . . .	172
B.10	Experimentally measured magnet field for differnt $I_d$ currents . . . . .	172

# List of Tables

1.1	Operating temperatures of NdFeB magnets . . . . .	6
2.1	China's domestic price of materials contained in a majority of magnets . . . . .	15
2.2	Typical values of the PM thermal remanent flux coefficient. . .	15
2.3	Machine parameters . . . . .	30
2.4	Case of study for different temperature distribution conditions	42
3.1	Degree of eccentricity . . . . .	62
3.2	Resulting PM temperature . . . . .	63
3.3	Case of study for different magnet position . . . . .	65
3.4	Machine dimensions and possible configurations . . . . .	71
3.5	Rated machine parameters . . . . .	72
3.6	$R_{dhf}$ calculated using pulsating $d$ -axis high frequency current .	74
3.7	$R_{dhf}$ calculated using rotating high frequency current . . . . .	75
3.8	$\alpha_{mag}$ calculated using pulsating $d$ -axis high frequency current .	75
3.9	$\alpha_{mag}$ calculated using rotating high frequency current . . . . .	76
4.1	Cost and temperature sensitivity of different magnet materials	84
4.2	Magnet parameters . . . . .	94
4.3	Experimental Setup parameters . . . . .	96
4.4	Magnetization Circuit Parameters . . . . .	100
4.5	Enhanced experimental setup parameters . . . . .	112
4.6	Magnetic materials and coating thickness . . . . .	118
4.7	Equivalences Between Experimental Setup and a PMSM . . .	135

B.1	System characteristics . . . . .	164
-----	----------------------------------	-----

# Contents

<b>1</b>	<b>Introduction</b>	<b>1</b>
1.1	Background . . . . .	1
1.2	Motivation . . . . .	8
1.3	Reserch contributions . . . . .	9
1.3.1	Conference papers . . . . .	9
1.3.2	Journal Papers . . . . .	10
1.4	Outline of the document . . . . .	11
<b>2</b>	<b>PM temperature estimation</b>	<b>13</b>
2.1	Introduction . . . . .	13
2.1.1	Temperature dependence of PMSM torque . . . . .	13
2.1.2	Review of Magnet temperature measurement methods . . . . .	15
2.1.3	Review of magnet temperature estimation methods . . . . .	17
2.1.3.1	PM temperature estimation using thermal mod- els . . . . .	17
2.1.3.2	PM temperature estimation using BEMF based methods . . . . .	17
2.1.3.3	PM temperature estimation based on a signal injection . . . . .	19
2.2	Magnet temperature estimation using pulsating injection . . .	22
2.2.1	Magnet temperature estimation using $d$ -axis pulsating current injection . . . . .	23

2.2.2	Magnet temperature estimation using $d$ -axis voltage injection and $q$ -axis current cancellation . . .	25
2.2.3	Comparison among high frequency signal injection methods . . . . .	28
2.2.4	High frequency signal selection . . . . .	29
2.2.5	Implementation of the proposed methods . . . . .	30
2.2.6	Experimental results . . . . .	32
2.2.6.1	Experimental results for a SPMSM . . . . .	32
2.2.6.2	Experimental results for an IPMSM . . . . .	36
2.3	PM temperature distribution estimation . . . . .	39
2.3.1	Temperature Estimation using BEMF . . . . .	39
2.3.2	Estimation of the magnet temperature distribution . . . . .	40
2.3.3	Estimation of the mean magnet temperature . . . . .	41
2.3.4	Differential magnet temperature estimation . . . . .	44
2.3.5	Experimental results . . . . .	46
2.4	Conclusions . . . . .	51
<b>3</b>	<b>Machine Design</b>	<b>55</b>
3.1	Introduction . . . . .	55
3.2	Sensitivity to machine assembling tolerances . . . . .	56
3.2.1	Effects of the eccentricity in the estimated PM temperature . . . . .	56
3.2.1.1	Static Eccentricity . . . . .	57
3.2.1.2	Dynamic Eccentricity . . . . .	60
3.2.1.3	Mixed Eccentricity . . . . .	61
3.2.2	Lamination grain orientation effects on the estimated PM temperature . . . . .	62
3.2.3	Effects of the PM assembling tolerances on the estimated PM temperature . . . . .	65
3.2.4	Experimental results . . . . .	66
3.2.4.1	Dynamic eccentricity . . . . .	66



3.3	Influence of stator configuration on temperature estimation . .	68
3.3.1	FEA Results . . . . .	70
3.4	Conclusions . . . . .	81
<b>4</b>	<b>Permanent Magnet Magnetization State Estimation</b>	<b>83</b>
4.1	Introduction . . . . .	83
4.2	Magnetoresistance effect in Permanent Magnets . . . . .	86
4.2.1	Magnetoresistance Measurement System . . . . .	88
4.2.2	High frequency signal injection for magnetization state estimation . . . . .	93
4.2.3	Experimental results . . . . .	94
4.2.3.1	Signal injection . . . . .	94
4.2.3.2	Magnetoresistance of the coil and core . . . .	95
4.2.3.3	Magnetoresistance effect in demagnetized samples . . . . .	98
4.2.3.4	Magnetoresistance effect in magnetized samples	99
4.2.3.5	Magnetoresistance effect in magnetized samples combined with flux-weakening and flux intensifying . . . . .	101
4.2.3.6	Magnetoresistance effect in segmented magnets	103
4.3	Influence of the PM coating in the magnetoresistance effect . . . . .	108
4.3.1	Magnetoresistance effect in thin film layers . . . . .	108
4.3.2	Improved magnetoresistance measurement system . . . . .	109
4.3.3	Experimental results . . . . .	112
4.3.3.1	Characterization of the experimental setup . .	112
4.3.3.2	Experimental results for demagnetized samples	114
4.3.3.3	Experimental results for demagnetized samples	120
4.3.3.4	Experimental results for magnetized samples .	121

4.3.3.5	Experimental results for magnetized samples with flux-weakening and flux intensifying . . . . .	122
4.4	Magnetoresistance effect in PMSMs . . . . .	123
4.4.1	PM High frequency resistance estimation . . . . .	128
4.4.2	Experimental verification of the magnetoresistive effect in PMSMs . . . . .	130
4.4.3	Simulation and experimental results . . . . .	130
4.4.4	Equivalence between the experimental setup and a PMSM	132
4.5	Conclusions . . . . .	134
<b>5</b>	<b>Conclusions and future work</b>	<b>137</b>
5.1	Conclusions . . . . .	137
5.2	Conclusions (Spanish) . . . . .	139
5.3	Future work . . . . .	141
<b>A</b>	<b>Temperature measurement system based on thermocouples</b>	<b>157</b>
A.1	Introduction . . . . .	157
A.2	PM temperature measurement system . . . . .	157
A.3	Desktop application for temperature and field measurement .	159
<b>B</b>	<b>Temperature and flux measurement system</b>	<b>163</b>
B.1	Introduction . . . . .	163
B.2	High resolution PM temperature and field measurement system	164
B.3	Desktop application for temperature and field measurement . .	167
B.4	Temperature and field measurements . . . . .	167
B.4.1	Temperature measurements . . . . .	170
B.4.2	Field measurements . . . . .	171
B.4.2.1	Single sensor test . . . . .	171
B.4.2.2	Full array measurements . . . . .	171

# Chapter 1

## Introduction

### 1.1 Background

Induction motors (IM) are the most extended machines in the industry, due to its simple construction, robustness and low maintenance. But this has not always been the case. Prior to the development and commercialization of silicon controlled rectifiers (SCR) in 1957, IM were not capable of achieving variable speed. At that time, applications that required variable speed used DC machines.

DC machines offer wide speed control range, high starting torque and good dynamics, however they have relatively high maintenance requirements due to the brushes and commutator. The use of DC motors were gradually reduced in the industry since the commercialization of high voltage semiconductor devices in 1970s that allowed variable speed of IM by means of DC/AC converters. IMs were not the only favored with the development of these devices. In the same decade, high performance permanent magnets, PMs (i.e. SmCo and NdFeB) were developed, multiplying the energy product of previous magnet technologies (see Fig. 1.1), highlighting the possibilities of PMSMs. The improvements achieved in PMs led to a major step forward in PMSMs performance (see Fig. 1.2, making these machines essential nowadays in electric traction, power generation or aerospace applications.

PMs can be classified into four types based on their composition: ferrite, AlNiCo, SmCo and NdFeB. Each magnet type has different magnetic properties, the most relevant magnet magnetic properties to be consider in a PMSM design are:

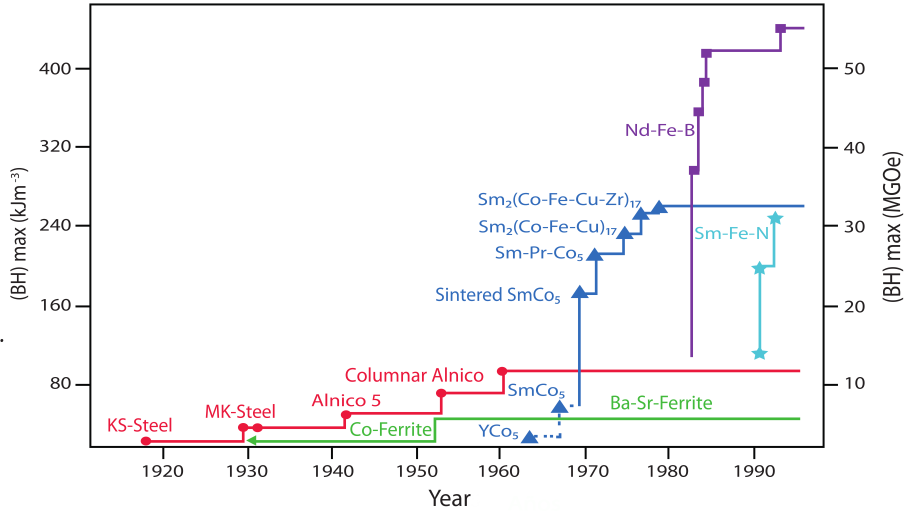


Figure 1.1: Evolution of the energy product value of different families of permanent magnets. Source: Institute of ceramic and glass, CSIC.[1]

- Remanence ( $B_r$ ): is the residual magnetization of a ferromagnetic material that have been magnetized up to its saturation in a closed magnetic circuit, after an external magnetic field is removed.
- Coercivity ( $H_c$ ): is a measure of the capability of a PM to withstand an external magnetic field without becoming fully demagnetized.
- Maximum energy product ( $BH_{max}$ ): Is the amount of energy that a PM can provide to an external magnetic circuit.
- Reversible temperature coefficient of Br ( $\alpha_B$ ): describes the the change in PM remanence with the change of PM temperature.
- Reversible temperature coefficient of Hc ( $\alpha_H$ ): describes the the change in PM coercivity with the change of PM temperature.
- Maximum operating temperature ( $T_{max}$ ): is the maximum temperature a PM withstand without suffering changes on its magnetic properties.
- Curie temperature ( $T_c$ ): is the temperature at which the material losses its magnetism.

In addition, all PMs can be found sintered and bonded. Bonded magnets are obtained blending thermo-elastomer and thermo-plastic resins together

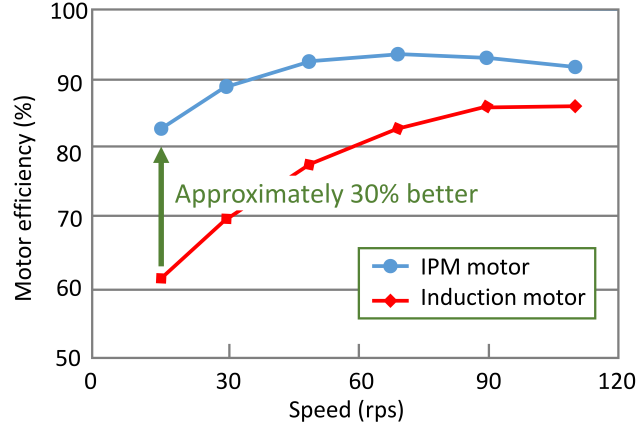


Figure 1.2: Comparison of efficiency of interior permanent magnet synchronous machine and induction motor. Source: Hitachi magnets [2]

with a variety of magnetic powders, can be formed into complex shapes and insert molded directly onto other components. Bonded magnets are not capable of high performance (i.e. provide high energy to a magnetic circuit), since part of its composition is a nonmagnetic material [3, 4]. Sintered magnets, on the other hand, are formed by compression and heat, avoiding the use of bonding materials, resulting therefore in higher performance [5].

For applications with in PMSMs, is desirable a magnet with high energy product, which implies high  $B_r$  and  $H_c$  values, and with high working temperature. Sintered NdFeB PMs are the primary option in high performance PMSMs, as they are the strongest in terms of energy product [6] although they present the poorest thermal performance (i.e. high thermal coefficients). AlNiCo provides the highest operating temperature of all magnetic materials, however, its coercivity is relatively low [7], which entails low energy product, being easily demagnetized. Ferrite magnets can be found in low cost PMSMs, with poor performance in terms of energy product but with good thermal stability, and SmCo magnets are used in applications that require a wide temperature operating range, e.g. aerospace [8], as they keep high energy products at high temperature [9].

When the temperature of the PM increases, its remanence and coercivity reduces, its relationship being given by the temperature coefficients,  $\alpha_B$  and  $\alpha_H$  [10], respectively. Both the remanence and coercivity, return to their initial state when the PM temperature returns to its initial value (i.e. room temperature) and the maximum working temperature of the magnet is not

surpassed. If the magnet is subjected to temperatures closed to its maximum working temperature, local/global demagnetization may occur, and remanence and coercivity wont return to its original value. Even more, the PM will loose its magnetic properties if Curie temperature is reached.

Irreversible temperature effects will change the behavior of the machine [11], e.g. additional harmonics will be reflected in the BEMF, power losses will increase, average torque will be reduced, torque ripple will be increased... Among all magnets, AlNiCo present the maximum working temperature, i.e. 540°C, with the lowest  $\alpha_B$  and  $\alpha_H$ , ferrite and SmCo magnets withstand around 350°C, while pure NdFeB with no extra alloying elements maximum working temperature is below 60°C[12], with the highest  $\alpha_B$  and  $\alpha_H$ .

Although NdFeB magnets provides the maximum energy to a magnetic circuit, its maximum working temperature is the lowest among all machine parts; coils can withstand up to 240°C, and steel sheets and bearings can be found for up to 350°C. Temperature issues of PMs are therefore one of the main issues in PMSMs equipping NdFeB magnets.

Higher temperature range in NdFeB magnets can be achieved by adding extra rare earth materials (i.e Dysprosium (Dy) or Terbium (Tb)) during the PM manufacturing process, see Fig. 1.3 and Table 1.1. During the manufacturing process a certain amount of Neodymium is substituted by Dy or Tb [13], which increase both the PM temperature range and the PM coercivity ( $H_c$ ) at the cost of a reduction of its remanence ( $B_r$ ). NdFeB magnets that are used in PMSMs typically have a Dy content ranging from 0 to 12%, see Fig. 1.3.

The increasing demand of PMSMs for EVs and wind power generator among others, have increased Dy and Nd market price since 2008, reaching its maximum price in 2011, see Fig 1.4, which has boosted interest in finding alternatives to reduce the use of rare earth materials (i.e. Dy, Tb, Nd...). ARPA-E (Advanced Research Projects Agency-Energy) has created a program to develop alternative materials in critical technologies, rare earth substitution being one of them [14, 15]; several research European projects are focusing also in the development of superconducting-based wind turbines, aiming to substitute high power wind turbines based on rare earth permanent magnets[16, 17]. The increasing cost of rare earth materials have also boosted the interest in developing permanent magnet machines that integrate AlNiCo [18, 19, 20] and ferrite magnets [21, 22, 23] Additionally, combination of magnets can also be found [18, 19, 20] to ease demagnetization/remagnetization.

Since every type of magnet or a combination of them, as it can be found in new PMSMs designs, presents a reversible temperature coefficient, the

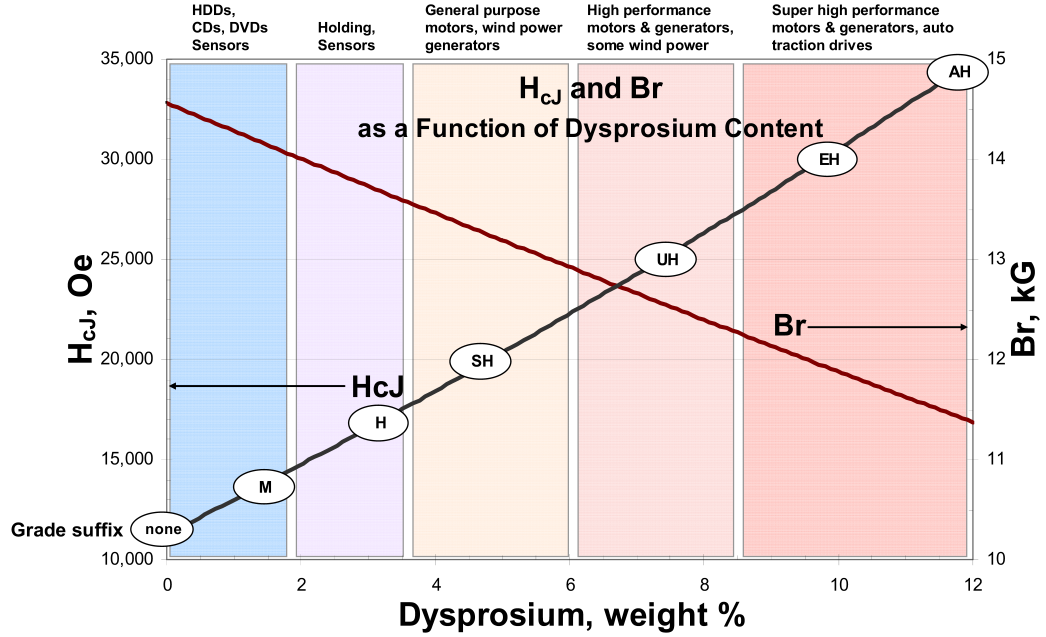


Figure 1.3: Intrinsic Coercivity ( $H_{cJ}$ ) and Residual Induction ( $B_r$ ) as a function of Dysprosium Content. Source: Arnold Magnetics [25]

benefits of knowing the PM temperature are of great importance. This allows to know the maximum energy product for a given temperature in an application. Torque capability of a PMSM, for example, is proportional to the PM flux linkage which depends on the PM temperature. Having a measurement/estimation of the PM temperature while operating the machine will help the control system to compensate temperature effects in the torque reduction. But the knowledge of PM temperature is not only a control issue but also a safety issue since thermal overloading is one of the major causes of motor failure [24]. The availability of PM temperature for the control system will allow the implementation of thermal protection enlarging its life expectancy.

PM temperature can be measured using non-contact (i.e. IR-based) and contact type sensors (i.e. PTC thermistor or thermocouples) [27]. Contact type sensors require the use of slip rings and brushes, or alternatively of a wireless transmission system, which implies high cost of the measurement system (i.e. needs electronics). Non-contact type sensors require the magnet surface to be visible, a modification of the end shield is needed which reduces the machine robustness. This is viable in many SPMSM designs, but is not

Table 1.1: Operating temperatures of NdFeB magnets according to its designator. Elaborated from Bomatec data [26]

Magnet suffix	Rev.Temp.Coeff. of Br, $\alpha$ , %/	Max. Working Temperature
none	-0.11 $\sim$ -0.12	60-80 °C
M	-0.11 $\sim$ -0.12	90-100 °C
H	-0.11 $\sim$ -0.12	120 °C
SH	-0.11 $\sim$ -0.12	150 °C
UH	-0.11 $\sim$ -0.12	180 °C
EH	-0.105 $\sim$ -0.12	200 °C
AH	-0.105 $\sim$ -0.12	220 °C

feasible in most IPMSM designs. Due to this, PM temperature measurement systems are not usually implemented in standard machines, their use being limited for laboratory applications.

An alternative to the PM temperature measurement is the PM temperature estimation. PM temperature estimation methods can be divided into thermal models, BEMF based methods and methods based on the injection of some form of test signal into the stator terminal of the machine. Thermal models require previous knowledge of the machine geometry, materials and cooling system, making the model specific for each machine design and inaccurate due to the lack of thermal parameters of the machine. BEMF based methods estimate the magnet temperature from the rotor PM flux linkage, cannot work at standstill or very low speeds and also require previous knowledge of some machine parameters. Methods based on the injection of a test signal can be further divided into pulse injection based methods and high frequency signal injection based methods. Unlike BEMF-based methods, high frequency signal injection base methods can be used in the whole speed range of the machine and do not require previous knowledge of the machine parameters.

This thesis proposes two temperature estimation methods: the first one for mean magnet temperature estimation (i.e average), the second one for differential magnet temperature estimation. The magnet differential temperature, combined with the average PM temperature can be used to estimate the spatial temperature distribution.

The importance of PM temperature distribution estimation reside in the fact that PM magnet temperature is not uniform in the PM volume. PM



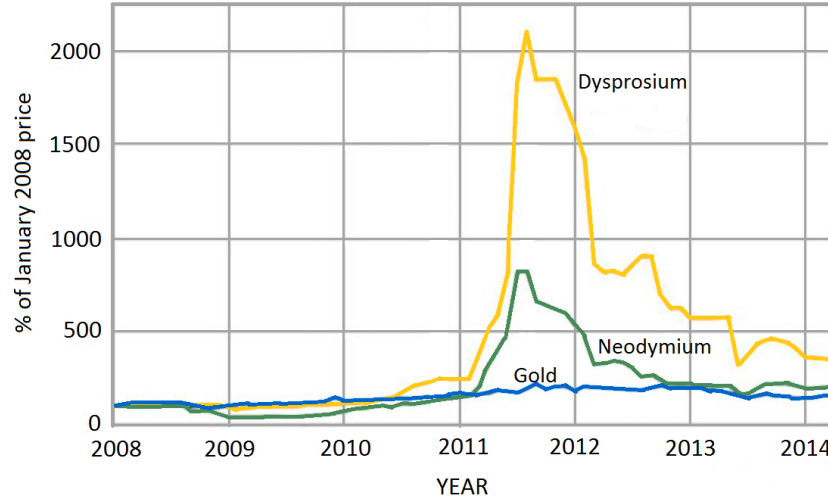


Figure 1.4: Rare earth metal price compared with gold. Source: Bloomberg

temperature distribution estimation methods help detect PM regions with different temperatures, due to non-uniform current densities induced in the PM [28].

Two wireless temperature measurement systems have been developed for the verification of the proposed methods. One of them provides temperature measurement in the axial direction of one PM in real time, the other provides PM temperature and field spatial distribution in real time, for all the magnets with high spatial resolution and sampling rates. Both systems were specifically designed for IPMSMs.

Additionally to PM temperature, knowledge of PMs magnetization state (MS) in a PMSMs is of great interest for control and monitoring purposes. PM magnetization state (MS) estimation methods have been also the focus of growing interest due to the increased use of variable flux permanent magnet synchronous machines (VF-PMSMs) in many traction applications, e.g. EVs and HEVs. These type of machines require accurate MS estimation since its MS can be changed during normal machine operation to allow high speed operation without the need of flux weakening current injection.

MS can be measured or estimated. MS measurement is not easy in practice, once the machine is assembled. Magnet flux linkage can be measured by inserting a magnetometer in the air-gap. However, the end-shield need to be removed or modified as the magnetometer need to be inserted in the air-

gap and the measurement process cannot be carried out during the normal operation of the machine. No on-line (i.e. while the machine is rotating) MS measurement systems have been found up to date.

Existing MS estimation methods are based on the BEMF. Although BEMF based methods are easy to implement, obtaining the PM flux linkage from the stator terminals under load conditions is not possible without previous knowledge of some machine parameters. In addition, this method cannot be implemented at zero or low speed. For this reason, this thesis analyzes the extension of high frequency signal injection based method for MS estimation purposes. A high frequency signal injection MS estimation method based on the magnetoresistive effect of PMs will be proposed. Magnetoresistance is defined as the change of a material electrical resistance when an external magnetic field is applied. Although the magnetoresistance effect on NdFeB magnet materials has already been studied [29], its use for magnetization state estimation in PMSMs has not been proposed yet. The proposed method does not interfere with the normal operation of the drive, can work in the whole speed range of the machine and its sensitivity to machine parameter variation is very low. In order to verify its accurateness, the developed wireless measurement system has been used to obtain field maps in real time, for all the magnets with high spatial resolution and sampling rates.

## 1.2 Motivation

This thesis is focused on PM temperature and magnetization state estimation methods in PMSMs. The motivation for the development of PM temperature and magnetization state estimation techniques for PMSMs comes from the issue that temperature and magnetization are two of the most important concerns regarding these type of machines. Most of previously published methods for PM temperature estimation require of good knowledge of machine parameters, lack of accuracy or are very complicated and specific for each machine design. The method proposed on this thesis overcome these limitations.

The need to find out strengths and weaknesses of the proposed method for PMSMs temperature estimation led to a sensitivity study to different machine designs, stator and rotor configuration and machine assembling tolerances.

The increasing interest in variable flux permanent magnet synchronous machines (VF-PMSMs) proposes a challenge to achieve accurate control

strategies for this specific type. Estimation of magnetization state (MS) is a required control feedback since these machines can reduce PM flux linkage  $\lambda_{PM}$  to lower the requirements for flux weakening current at high speed operation. This thesis proposed a method for MS estimation based on an rarely known intrinsic property of permanent magnets: magnetoreistance. The proposed methods take advantage of this property and treats the magnet as a sensor, describing how the magnet resistance can be estimated and therefore, its MS.

Different permanent magnets were evaluates in terms of magnetoresistance, NdFeB magnet presented the highest variations. As this type of magnets are commonly protected to oxidation with a special coating, it was initially thought that magnet material could be influenced by certain coating materials. This thesis also presents a study of the influence of different coatings to clarify the initial uncertainties.

## 1.3 Reserch contributions

### 1.3.1 Conference papers

- D. Reigosa, D. Fernandez, Z. Q. Zhu and F. Briz, "PMSM magnetization state estimation based on stator-reflected PM resistance using high frequency signal injection," 2014 IEEE Energy Conversion Congress and Exposition (ECCE), Pittsburgh, PA, 2014, pp. 1729-1736.
- D. Reigosa, D. Fernandez, H. Yoshida, T. Kato and F. Briz, "Permanent magnet temperature estimation in PMSMs using pulsating high frequency current injection," 2014 IEEE Energy Conversion Congress and Exposition (ECCE), Pittsburgh, PA, 2014, pp. 5198-5205.
- D. Fernandez, D. Reigosa, T. Tanimoto, T. Kato and F. Briz, "Wireless permanent magnet temperature & field distribution measurement system for IPMSMs," 2015 IEEE Energy Conversion Congress and Exposition (ECCE), Montreal, QC, 2015, pp. 3996-4003.
- D. Reigosa, D. Fernandez, T. Tanimoto, T. Kato and F. Briz, "Sensitivity analysis of high frequency signal injection based temperature estimation methods to machine, assembling tolerances," 2015 IEEE Energy Conversion Congress and Exposition (ECCE), Montreal, QC, 2015, pp.

- D. Reigosa, D. Fernandez, T. Tanimoto, T. Kato and F. Briz, "Permanent magnet temperature distribution estimation in PMSMs using BEMF harmonics," 2015 IEEE Energy Conversion Congress and Exposition (ECCE), Montreal, QC, 2015, pp. 768-775.
- D. Fernandez, D. Reigosa, J. M. Guerrero, Z. Q. Zhu and F. Briz, "Permanent magnet magnetization state estimation using high frequency signal injection," 2015 IEEE Energy Conversion Congress and Exposition (ECCE), Montreal, QC, 2015, pp. 3949-3956.
- D. Fernandez, D. Reigosa, J. M. Guerrero, Z.Q. Zhu and F. Briz, "Influence of PM Coating on PM magnetization State Estimation Methods Based on Magnetoresistive Effect," 2016 IEEE Energy Conversion Congress and Exposition (ECCE), Milwaukee, WI, 2016
- D. Fernandez, D. Reigosa, J. M. Guerrero, Z.Q. Zhu and F. Briz "Influence of Stator Configuration on High Frequency Signal Injection Based Permanent Magnet Temperature Estimation Methods in PMSMs," 2016 IEEE Energy Conversion Congress and Exposition (ECCE), Milwaukee, WI, 2016
- D. Fernandez, Doosoo Hyun, Yonghyun Park, D. Reigosa, Sang Bin Lee, Dong Myung Lee and F. Briz "Permanent Magnet Temperature Estimation in PM Synchronous Motors Using Low Cost Hall Effect Sensors," 2016 IEEE Energy Conversion Congress and Exposition (ECCE), Milwaukee, WI, 2016

### 1.3.2 Journal Papers

- D. Díaz Reigosa, D. Fernandez, Z. Q. Zhu and F. Briz, "PMSM Magnetization State Estimation Based on Stator-Reflected PM Resistance Using High-Frequency Signal Injection," in IEEE Transactions on Industry Applications, vol. 51, no. 5, pp. 3800-3810, Sept.-Oct. 2015.
- D. D. Reigosa, D. Fernandez, H. Yoshida, T. Kato and F. Briz, "Permanent Magnet Temperature Estimation in PMSMs Using Pulsating High-Frequency Current Injection," in IEEE Transactions on Industry Applications, vol. 51, no. 4, pp. 3159-3168, July-Aug. 2015.
- D. Diaz; D. Fernandez; T. Tanimoto; T. Kato; F. Briz, "Sensitivity Analysis of High Frequency Signal Injection Based Temperature Estimation Methods to Machine Assembling Tolerances," in IEEE Transactions on Industry Applications , vol.PP, no.99, pp.1-1

- D. D. Reigosa, D. Fernandez, T. Tanimoto, T. Kato and F. Briz, "Permanent-Magnet Temperature Distribution Estimation in Permanent-Magnet Synchronous Machines Using Back Electromotive Force Harmonics," in IEEE Transactions on Industry Applications, vol. 52, no. 4, pp. 2930-2940, July-Aug. 2016.
- D. Fernandez, D. D. Reigosa, J. M. Guerrero, Z. Q. Zhu and F. Briz, "Permanent-Magnet Magnetization State Estimation Using High-Frequency Signal Injection," in IEEE Transactions on Industry Applications, vol. 52, no. 4, pp. 2930-2940, July-Aug. 2016.
- D. Reigosa; D. Fernandez; T. Tanimoto; T. Kato; F. Briz, "Comparative Analysis of BEMF and Pulsating High Frequency Current Injection Methods for PM Temperature Estimation in PMSMs," in IEEE Transactions on Power Electronics , vol.PP, no.99, pp.1-1

## 1.4 Outline of the document

This thesis is organized in five chapters and two appendix:

- **Chapter 2** analyzes temperature effects in PMSMs, reviews the state of the art of PM magnet temperature estimation methods in PMSMs and proposes two new temperature estimation methods. The first method that is proposed is intended for mean PM temperature estimation in PMSMs, the second one is intended for PM temperature distribution estimation.
- **Chapter 3** evaluates the sensitivity of high frequency signal injection temperature estimation based methods to machine constructive aspects. The objective of this analysis is to provide design guidelines for the development of PMSMs suitable for the implementation of high frequency signal injection based temperature estimation techniques.
- **Chapter 4** introduces and analyzes the magnetoresistive effect in PMs and how this property can be used for PM magnetization state estimation purposes. A system for magnetoresistance measurement in PMs and its equivalence with PMSMs is presented.
- **Chapter 5** summarizes the contributions of this thesis and outlines future research lines.

- **Appendix A** presents a thermocouple based wireless PM temperature measurement system for IPMSMs which provides temperature measurement in the axial direction of one PM of an IPMSM.
- **Appendix B** presents a wireless PM temperature and field measurement system for IPMSMs, temperature measurement being based on I2C digital temperature sensors while field measurement being based on hall-effect analog sensors. The system provides PM temperature and field distribution measurements for all the IPMSM magnets.

# Chapter 2

## Temperature Estimation

### 2.1 Introduction

This chapter discusses how PMs' temperature affects to PMSM performance and presents two temperature estimation methods: the first one for mean magnet temperature estimation, the second one for differential magnet temperature estimation. Two wireless temperature measurement systems have been developed for the verification of the proposed methods, see Appendix A and B.

#### 2.1.1 Temperature dependence of PMSM torque

PMSMs torque-speed characteristics strongly depends on the PM temperature [30, 31, 32, 33, 34]. PM remanent flux,  $B_r$ , typically decreases as the temperature increases, therefore reducing the torque producing capability of the machine. Total torque produced by a PMSMs can be expressed by (2.1). As it can be observed, it is the result of two components: the reluctance torque,  $T_{re}$  (2.2), that depends on the difference between  $d$  and  $q$ -axis inductances, and the electromagnetic torque,  $T_{em}$  (2.3), which is proportional to the PM flux,  $\lambda_{PM}$ . Both the electromagnetic torque and the reluctance torque are influenced by the rotor temperature.

$$T = \frac{3}{2}p(\lambda_{PM}i_q + (L_d - L_q)i_di_q) \quad (2.1)$$

$$T_{re} = \frac{3}{2}p((L_d - L_q)i_d i_q) \quad (2.2)$$

$$T_{em} = \frac{3}{2}p(\lambda_{PM}i_q) \quad (2.3)$$

NdFeB magnets are the most common choice in PMSMs nowadays, though this machines can also be found equipped with other magnet technology such as ferrite [35, 36], SmCo [37, 38] and AlNiCo magnets [18, 19, 20]. Table 2.2, [39], shows typical values of the PM thermal remanent flux coefficient, which is defined as the PM remanent flux rate of variation with temperature,  $\alpha_B$  [32, 31, 40], PM remanent flux,  $B_r$ , and the operating temperature range for commonly used PM materials [39]. The coefficient  $\alpha_B$  is observed to vary significantly depending on the material; SmCo and Alnico magnets present low  $\alpha_B$  values [41], meaning that the variation of their remanent flux (and therefore torque) with temperature is relatively small. Consequently, precise estimation of the magnet temperature is not a major concern in machines equipped with this type of magnets. On the contrary, Ferrite and NdFeB magnets present high  $\alpha_B$  values, the variation of their remanent flux with temperature being therefore relatively large. Thus, realizing a precise control of the torque produced by machines equipping this type of magnets can require precise measurement/estimation of the magnet temperature.

NdFeB magnets can often have up to 12% of the neodymium material substituted by dysprosium (Dy) [25], or terbium (Tb), to preserve their magnetic properties at high temperature. However, this penalizes cost, see Table 2.1. Dysprosium is more than five times more expensive than NdFeB and terbium more than ten, which has raised the interest in development of Dy- and Tb-free magnets [6]. This has also increase the interest in the development of PM temperature measurement/estimation methods.

SmCo, Alnico, ferrite or NdFeB PMs can also suffer irreversible demagnetization under certain PM temperature and loading (i.e.  $i_{dq}$  current) conditions. Demagnetization of PMs in PMSMs has been extensively studied [42, 43, 44], it can occur locally (partial demagnetization) or globally (uniform demagnetization) [42]. The maximum temperature that a PM can reach without irreversible demagnetization defines its maximum working temperature. As it can be observed from Table 2.2, SmCo and Alnico magnets



Table 2.1: China's domestic price of materials contained in a majority of magnets.  
Source: Bomatec Newsletter September 2016

PM Material	Cost (RMB/Kg)	Cost trend (One year)	Details
Terbium metal	3600	↗	min. of 99% purity
Dysprosium metal	1700	→	min. of 99% purity
Neodymium metal	320	↗	min. of 99% purity
Samarium metal	87	→	min. of 99% purity
Cobalt metal	205	→	min. of 99.8% purity

operating temperature range is wider compared to NdFeB and ferrite magnets. In all the cases, demagnetization due to temperature occurs at well defined limit, meaning that a high accuracy estimating the temperature is needed to prevent demagnetization if the machine is expected to operate near PMs temperature limit. It is concluded from the previous discussion that measuring/estimating the magnet temperature is highly desirable for torque control/monitoring purposes and to prevent demagnetization [45, 46, 47].

Table 2.2: Typical values of the PM thermal remanent flux coefficient.

PM material	$\alpha_B$ (%/°C)	$B_r$ (T)	Operating Temperature Range (*)
Alnico 5-7	-0.02	1.35	4 K to 520 °C
Alnico 8	-0.01	0.85	4 K to 520 °C
Ferrite 8	-0.2	0.39	-40 °C to 150 °C
Ferrite 9	-0.18	0.45	-40 °C to 150 °C
SmCo 1:5	-0.045	0.90	4 K to 520 °C
SmCo 2:17	-0.035	1.10	4 K to 520 °C
NdFeB 33EH	-0.11	1.15	150 K to 200 °C
NdFeB 48M	-0.12	1.39	150 K to 100 °C

(\*) °C and K are used as this is the format used by the manufacturer [39].

### 2.1.2 Review of Magnet temperature measurement methods

PM temperature measurement is not easy in practice [48]. It implies modification of the machine, which reduces robustness, and typically needs addi-

tional electronics for conditioning and filtering which increases cost [49, 50]. Due to this, PM temperature measurement systems are not usually available for standard machines, their use being limited for laboratory applications. Temperature measurement methods can be classified depending the used sensors: implementations using non-contact and contact type sensors; both types are briefly discussed following.

#### **a) Non-contact type sensors**

Non-contact type sensors (i.e. IR) [32, 31] require the magnet surface to be visible. This is viable in many SPMSM designs, but is not feasible in most IPMSM designs. Further concerns for this type of sensors include price, accuracy, mounting issues and reduced robustness. The use of an infrared camera was presented in [32]. The measurement system was used in two SPMSMs, in which the magnets surfaces were visible. The system required drilling the machine end frame to have access to the magnet, compromising therefore the machine robustness. The IR camera measures the side face of the magnet, PM temperature distribution measurement in the axial direction not being therefore feasible. The use of an infrared thermometer was presented in [31]. Though it is significantly cheaper than the IR camera [32], it suffers from the same limitations.

#### **b) Contact type sensors**

To overcome some of the limitations of non-contact type sensors, the use of contact type sensors have been proposed [51, 49, 50, 52]. Contact type sensors (e.g. PTC thermistors, thermocouples...) require the use of slip rings and brushes, or alternatively of a wireless transmission system. In all cases the prototypes that have been developed up to date provide either a single measurement or the PM temperature distribution in one dimension. A measurement system of this type is described in [49]. Targeted to induction machines, the rotor was equipped with 6 thermocouples. This method was extended to IPMSMs in [51, 50, 52]. It uses 4 thermocouples to measure the temperature at different locations of the magnet, the remaining two being used to measure the rotor yoke temperature. While this system provides information on the temperature distribution in two points of the magnet, the spatial resolution cannot be provided and does not allow to measure asymmetries among poles.

### 2.1.3 Review of magnet temperature estimation methods

An alternative to the PM temperature measurement is the PM temperature estimation.

PM temperature estimation methods can be divided into thermal models [53, 54, 55, 56, 57], BEMF based methods [58, 59, 60, 61] and methods based on the injection of some form of test signal [32, 31, 62, 51].

#### 2.1.3.1 PM temperature estimation using thermal models

Thermal models consist of thermal nodes which represent uniform temperature regions. The thermal nodes are connected by thermal resistances, which represent the heat transfer. Power sources represent the machine power losses (i.e. magnet, copper and core losses), while heat capacitors represent the heat storage capability for the different parts of the machine. Building a thermal model requires therefore knowledge of the stator and rotor geometry, materials and cooling system. Consequently, thermal models need to be calibrated for each specific machine [63, 56].

Thermal models are normally based on a 2D machine model, a constant temperature in the axial direction is therefore assumed. In addition they do not consider thermal asymmetries between magnets (e.g. due to lamination grain orientation). Thermal 3D can be more accurate but its complexity increases exponentially. The complex machine geometry, heterogeneous materials, and different modes of heat transfer are among others, factors that complicate the thermal modeling [54]. Modeling the heat transfer toward the environment is a common problem for all machine types but it can be estimated using external sensors, as this is usually an accessible part.

#### 2.1.3.2 PM temperature estimation using BEMF based methods

BEMF based methods estimate the magnet temperature from the rotor PM flux linkage, which is estimated from the machine terminal voltages and currents [58, 59, 60, 61]. The physical principles of the magnet temperature estimation using the BEMF can be established from the fundamental model of a PM machine in the synchronous rotor reference frame shown in (2.4), where  $v_{dq}^r$  and  $i_{dq}^r$  are the stator voltage and current complex vectors in the rotor synchronous reference frame,  $R_d$ ,  $R_q$ ,  $L_d$ , and  $L_q$  are the  $d$ - and  $q$ -axis

resistances and inductances respectively,  $\omega_r$  is the machine speed,  $\lambda_{PM}$  is the PM flux and  $p$  is the differential operator.

$$\begin{aligned} \begin{bmatrix} u_d^r \\ u_q^r \end{bmatrix} &= \begin{bmatrix} R_d & 0 \\ 0 & R_q \end{bmatrix} \begin{bmatrix} i_d^r \\ i_q^r \end{bmatrix} + p \begin{bmatrix} L_d & 0 \\ 0 & L_q \end{bmatrix} \begin{bmatrix} i_d^r \\ i_q^r \end{bmatrix} \\ &+ \begin{bmatrix} 0 & -\omega_r L_q \\ \omega_r L_d & 0 \end{bmatrix} \begin{bmatrix} i_d^r \\ i_q^r \end{bmatrix} + \begin{bmatrix} 0 \\ \lambda_{PM} \omega_r \end{bmatrix} \end{aligned} \quad (2.4)$$

The PM flux,  $\lambda_{PM}$ , only affects to the  $q$ -axis. Therefore, only the  $q$ -axis equation is needed for the estimation of the PM flux, and consequently for temperature estimation, (2.5). In (2.5),  $R_q$  is function of the stator temperature,  $T_s$ ,  $\lambda_{PM}$  is function of the magnet temperature,  $T_r$ , while  $L_d$  and  $L_q$  are both function of  $T_r$  and  $i_{dq}^r$  current. Eq. (2.5) can therefore be expressed as (2.6), from which the PM flux can be obtained as (2.7).

$$u_q^r = R_q i_q^r + p L_q i_q^r + \omega_r L_d i_d^r + \lambda_{PM} \omega_r \quad (2.5)$$

$$u_q^r = R_{q(T_s)} i_q^r + p L_{q(T_r, i_q^r, i_d^r)} i_q^r + \omega_r L_{q(T_r, i_q^r, i_d^r)} i_d^r + \lambda_{PM(T_r)} \omega_r \quad (2.6)$$

$$\lambda_{PM(T_r)} = \frac{u_q^r - \left( R_{q(T_s)} i_q^r + p L_{q(T_r, i_q^r, i_d^r)} i_q^r + \omega_r L_{q(T_r, i_q^r, i_d^r)} i_d^r \right)}{\omega_r} \quad (2.7)$$

$$\lambda_{PM(T_r)} = \lambda_{PM(T_0)} \left( 1 + \beta (T_r - T_0) \right) \quad (2.8)$$

The PM flux variation with the magnet temperature can be expressed as (2.8), where  $T_0$  is the room temperature and  $\beta$  is the magnet flux thermal coefficient. The magnet temperature  $T_r$ , is obtained from (2.8).

Obtaining the  $\lambda_{PM(T_r)}$  from (2.8) when the machine is rotating under no-load condition, i.e  $i_{dq}^r = 0$ , is relatively simple, is given by 2.9. On the contrary, obtaining  $\lambda_{PM(T_r)}$  when  $i_{dq}^r \neq 0$  is not trivial; knowledge of the stator temperature is needed to estimate the  $q$ -axis resistance variation using 2.10, where  $\alpha_{cu}$  is the copper thermal resistive coefficient. Also previous knowledge

of  $d$  and  $q$ – axis inductance maps is needed (i.e. variation of the  $d$  and  $q$ –axis inductance with  $i_{dq}^r$  to compensate their effect in (2.6)-(2.7) [58, 59, 60, 61].

$$\lambda_{PM(T_r)} = \frac{v_q^r}{\omega_r} \quad (2.9)$$

$$R_{q(T_s)} = R_{q(T_0)} + (1 + \alpha_{cu}(T_s - T_0)) \quad (2.10)$$

### 2.1.3.3 PM temperature estimation based on a signal injection

#### *a) Magnet temperature estimation using rotating voltage injection*

If the stator of a PMSM is fed with a high-frequency voltage, the magnet-flux-dependent term in (2.4) can be safely neglected, since it does not contain any high-frequency component, and the high-frequency model is obtained.

Subscript  $hf$  in (2.11) stands for the high-frequency component of the corresponding machine variables and parameters. Thus, if the frequency of the injected high-frequency signal is sufficiently higher than the rotor frequency, the rotor-speed-dependent terms in (2.11) can be safely neglected. An orientative threshold for this assumption can be  $\omega_{hf} > \omega_r + 2\pi 500$ . The simplified high-frequency model shown in (2.12) is then obtained.

$$\begin{aligned} \begin{bmatrix} u_{dhf}^r \\ u_{qhf}^r \end{bmatrix} &= \begin{bmatrix} R_{dhf} & 0 \\ 0 & R_{qhf} \end{bmatrix} \begin{bmatrix} i_{dhf}^r \\ i_{qhf}^r \end{bmatrix} + p \begin{bmatrix} L_{dhf} & 0 \\ 0 & L_{qhf} \end{bmatrix} \begin{bmatrix} i_{dhf}^r \\ i_{qhf}^r \end{bmatrix} \\ &\quad + \begin{bmatrix} 0 & -\omega_r L_{qhf} \\ \omega_r L_{dhf} & 0 \end{bmatrix} \begin{bmatrix} i_{dhf}^r \\ i_{qhf}^r \end{bmatrix} \end{aligned} \quad (2.11)$$

$$\begin{bmatrix} u_{dhf}^r \\ u_{qhf}^r \end{bmatrix} = \begin{bmatrix} R_{dhf} & 0 \\ 0 & R_{qhf} \end{bmatrix} \begin{bmatrix} i_{dhf}^r \\ i_{qhf}^r \end{bmatrix} + p \begin{bmatrix} L_{dhf} & 0 \\ 0 & L_{qhf} \end{bmatrix} \begin{bmatrix} i_{dhf}^r \\ i_{qhf}^r \end{bmatrix} \quad (2.12)$$

The  $d$ – and  $q$ –axis components of the high-frequency resistances  $R_{dhf}$  and  $R_{qhf}$  are function of both the stator and rotor high-frequency resistances (2.13), where  $R_{hf}$  ( $d$ – or  $q$ –axis) is the high-frequency resistance seen from the stator terminals,  $R_{shf}$  is the contribution of the stator circuit to the high-frequency resistance and  $R_{rhf}$  ( $d$ – or  $q$ –axis) is the stator-reflected rotor

high-frequency resistance. Both resistances are affected by the corresponding stator and rotor temperatures, as generically shown by (2.14). For the case of the stator  $\alpha = \alpha_{cu}$ , which is the copper thermal resistive coefficient (stator high-frequency resistance), while for the case of the rotor,  $\alpha = \alpha_{mag}$ , which is the magnet thermal resistive coefficient (rotor high-frequency resistance).  $R(T_0)$  is the stator/rotor resistance at the room temperature. The magnet temperature will affect to the PM strength (2.15), where  $B_r(T_0)$  is the remanent PM flux at the room temperature,  $T$  is the temperature, and  $T_0$  is the room temperature.

$$R_{hf} = R_{shf} + R_{rhf} \quad (2.13)$$

$$R_T = R_{T_0} + (1 + \alpha(T - T_0)) \quad (2.14)$$

$$R_T = R_{T_0} + (1 + \alpha_{B(T)}(T - T_0)) \quad (2.15)$$

From (2.13) and (2.14), the high-frequency resistance seen at the stator terminals can be expressed as (2.16), where  $T_s$  and  $T_r$  are the stator and rotor temperatures, respectively.

$$R_{hf}(T_s, T_r) = R_{shf(T_s)} + R_{rhf(T_r)} \quad (2.16)$$

It is seen from (2.16) that the magnet temperature can be estimated from the high-frequency resistance, with prior knowledge of the high-frequency resistance of the machine at the room temperature and of the stator temperature being required. The high frequency resistance of the machine at the room temperature can be measured during a commissioning process, while the stator temperature can be easily measured via a contact-type temperature sensor (e.g., thermocouple, resistance temperature detectors, etc.).

Different forms of high-frequency excitation can be used to estimate the high-frequency resistance. While all of them respond to the same physical principles, differences in their practical implementation and performance exist. The use of the rotating voltage injection has already been proposed [32] and is briefly described here for illustrative purposes. When a rotating high-frequency voltage (2.17) is applied to the stator windings of a PM machine,

its high-frequency model is obtained by replacing the  $p$  operator in (2.11) by  $j\omega_{hf}$ , (2.18) being obtained. By solving (2.18), the stator high-frequency currents in the rotor synchronous reference frame (2.19) and (2.20) are obtained.

$$v_{dqhf}^r = V_{hf} e^{j\omega_{hf} t} \quad (2.17)$$

$$\begin{bmatrix} v_{dhf}^r \\ v_{qhf}^r \end{bmatrix} = \begin{bmatrix} R_{dhf} + j\omega_{hf} L_{dhf} & -\omega_r L_{qhf} \\ \omega_r L_{dhf} & R_{qhf} + j\omega_{hf} L_{qhf} \end{bmatrix} \begin{bmatrix} i_{dhf}^r \\ i_{qhf}^r \end{bmatrix} \quad (2.18)$$

$$i_{qhf}^r = \frac{v_{dhf}^r - \omega_r L_{dhf} i_{qhf}^r}{R_{qhf} + j\omega_{hf} L_{qhf}} \quad (2.19)$$

$$\begin{aligned} i_{qhf}^r &= \left[ v_{dhf}^r + \frac{\omega_r L_{qhf} v_{qhf}^r}{R_{qhf} + j\omega_{hf} L_{qhf}} \right] \\ &\quad \frac{R_{qhf} + j\omega_{hf} L_{qhf}}{(R_{dhf} + j\omega_{hf} L_{dhf})(R_{qhf} + j\omega_{hf} L_{qhf}) + \omega_r^2 L_{dhf} L_{qhf}} \end{aligned} \quad (2.20)$$

Obtaining  $R_{dhf}$  and  $R_{qhf}$  from (2.19) and (2.20) is not trivial. On one hand, there is cross-coupling between the  $d$ -axis and the  $q$ -axis. In addition, the high-frequency impedances  $L_{dhf}$  and  $L_{qhf}$  can change with  $i_d^r$  and  $i_q^r$  currents during the normal operation of the machine. Furthermore, they are multiplied by the rotor speed. Equations (2.19) and (2.20) can be enormously simplified if it can be assumed that  $\omega_{hf} \gg \omega_r$ , i.e., the high frequency signal has a frequency significantly larger than the rotor speed (e.g.,  $\omega_{hf} > \omega_r + 2\pi 500$ ) [30]. In this case, the off-diagonal terms in (2.18) can be neglected and (2.19) and (2.20) can be simplified to 2.21 and 2.22. In this case,  $R_{dhf}$  and  $R_{qhf}$  are obtained from the real part of the  $d$ - and  $q$ -axis currents in (2.21) and (2.22), respectively.

$$i_{dhf}^r = \frac{v_{dhf}^r}{R_{dhf} + j\omega_{hf} L_{dhf}} \quad (2.21)$$

$$i_{qhf}^r = \frac{v_{qhf}^r}{R_{qhf} + j\omega_{hf} L_{qhf}} \quad (2.22)$$

While the assumption that  $\omega_{hf} \gg \omega_r$  can be realistic in SPMSMs, it cannot be applied in general to IPMSMs. In IPMSMs, the magnets are buried in the rotor lamination, which means that a lower frequency can be needed for the highfrequency signal to penetrate into the rotor lamination and excite the PMs. In addition, IPMSMs are often designed to operate at high speeds, which places further restrictions to the assumption that  $\omega_{hf} \gg \omega_r$ . It is concluded that (2.21) and (2.22) cannot be generally applied in IPMSMs and (2.19) and (2.20) should be used instead to obtain  $R_{dhf}$  and  $R_{qhf}$ . This makes the implementation more difficult, also significantly increasing the parameter sensitivity.

***b) Magnet temperature estimation using pulse voltage injection***

In [51, 62] a method to estimate the magnet temperature in PMSMs by exploiting the  $d$ -axis saturation effects in the steel stator core was proposed. A voltage pulse is applied in the  $d$ -axis while measuring the  $d$ -axis current. It is known that the  $d$ -axis inductance  $L_d$  is highly influenced by the  $d$ -axis saturation level of the machine which is dependent on the magnetization level of the PMs. When a  $d$ -axis pulse voltage is injected in the stator terminals, variation of  $L_d$  can be detected by measuring the slope of the induced  $d$ -axis current (2.23). Thus,  $d(i_d)/dt$  will change upon changes when magnetization level of the PMs. This will be used as indicator for the PM temperature when MS is not influenced by other variables.

$$v_d = L_d \frac{di_d}{dt} \quad (2.23)$$

## 2.2 Magnet temperature estimation using d-axis pulsating signal injection

To overcome the aforementioned limitations of temperature estimation using rotating high-frequency voltage injection, the use of pulsating high-frequency signals (i.e. current and voltage injection) is proposed and analyzed following.



### 2.2.1 Magnet temperature estimation using $d$ -axis pulsating current injection

In the proposed strategy, a sinusoidal high-frequency current is injected in the  $d$ -axis of a PMSM (IPMSM or SPMSM), with the high-frequency  $q$ -axis current being therefore forced to be equal to zero (2.24). A resonant controller is used for this purpose, with the resulting commanded high-frequency voltages being of the form shown by (2.25). By taking the  $d$ -axis component of the resulting high-frequency voltage complex vector  $v_{dqhf}^{r*}$  in (2.25), the voltage complex vector  $v_{dqhf}^{r'}$  (2.26) is defined. Both (2.24) and (2.26) can be decomposed into positive sequence ( $i_{dqhfpc}^{r'}$  and  $v_{dqhfpc}^{r'}$  and negative sequence ( $i_{dqhfnec}^{r'}$  and  $v_{dqhfnec}^{r'}$ ) components (2.27) and (2.28), each with a magnitude equal to half of that of the original signal. The  $d$ -axis impedance (2.29) can be obtained from (2.27) and (2.28) using either the positive or the negative sequence components (2.31), where  $\varphi_{Zd}$  (2.30) is the phase of the  $d$ -axis PMSM impedance (2.29).

$$i_{dqhf}^{r*} = \begin{bmatrix} i_{dhf}^{r*} \\ i_{qhfh}^{r*} \end{bmatrix} = \begin{bmatrix} I_{hf}^* \cos(\omega_{hf}t) \\ 0 \end{bmatrix} \quad (2.24)$$

$$v_{dqhf}^{r*} = \begin{bmatrix} v_{dhf}^{r*} \\ v_{qhfh}^{r*} \end{bmatrix} = \begin{bmatrix} (R_{dhf} + j\omega_{hf}L_{dhf})i_{dhf}^r \\ 0 \end{bmatrix} \quad (2.25)$$

$$\begin{aligned} v_{dqhf}^{r'} &= \begin{bmatrix} v_{dhf}^{r*} \\ 0 \end{bmatrix} = \begin{bmatrix} (R_{dhf} + j\omega_{hf}L_{dhf})I_{hf}^* \cos(\omega_{hf}t) \\ 0 \end{bmatrix} \\ &= \begin{bmatrix} V_{dqhf}^{r'} \cos(\omega_{hf}t + \varphi_{Zd}) \\ 0 \end{bmatrix} \end{aligned} \quad (2.26)$$

$$i_{dhf}^{r*} = \frac{I_{hf}}{2} e^{j\omega_{hf}t} + \frac{I_{hf}}{2} e^{-j\omega_{hf}t} = i_{dqhfpc}^{r*} + i_{dqhfnec}^{r*} \quad (2.27)$$

$$v_{dhf}^{r*} = \frac{|v_{dqhf}^{r'}|}{2} e^{j(\omega_{hf}t - \varphi_{Zd})} + \frac{|v_{dqhf}^{r'}|}{2} e^{j(-\omega_{hf}t - \varphi_{Zd})} \quad (2.28)$$

$$Z_d = R_{dhf} + j\omega_{hf}L_{dhf} \quad (2.29)$$

$$\varphi_{Zd} = \tan^{-1} \left( \frac{\omega_{hf} L_{dhf}}{R_{dhf}} \right) \quad (2.30)$$

$$Z_d = R_{dhf} + j\omega_{hf} L_{dhf} = \frac{v_{dqhfpc}^{r'}}{i_{dqhfpc}^{r*}} = \frac{v_{dqhfnc}^{r'}}{i_{dqhfnc}^{r*}} \quad (2.31)$$

The overall  $d$ -axis resistance (2.32) is split into the stator and rotor contributions  $R_{dshf}(T_s)$  and  $R_{drhf}(T_r)$  (2.33), which are function of the stator and rotor temperatures  $T_s$  and  $T_r$ , respectively.

$$R_{dhf} = Z_d \cos(\varphi_{Zd}) \quad (2.32)$$

$$R_{dhf}(T_s, T_r) = R_{dshf}(T_s) + R_{drhf}(T_r) \quad (2.33)$$

$$\begin{aligned} R_{dhf}(T_s, T_r) = & R_{dshf}(T_s)(1 + \alpha_{cu}(T_s - T_0)) \\ & + R_{drhf}(T_r)(1 + \alpha_{mag}(T_r - T_0)) \end{aligned} \quad (2.34)$$

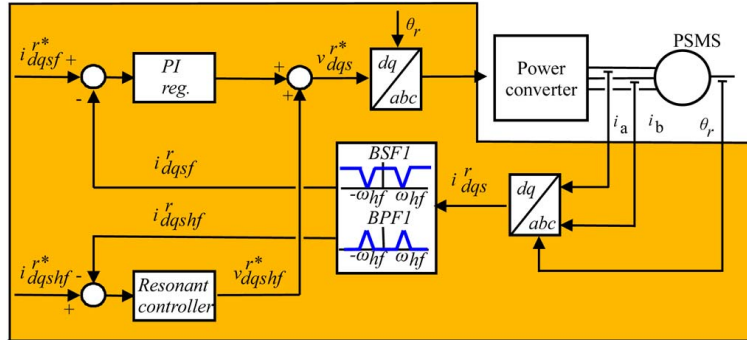
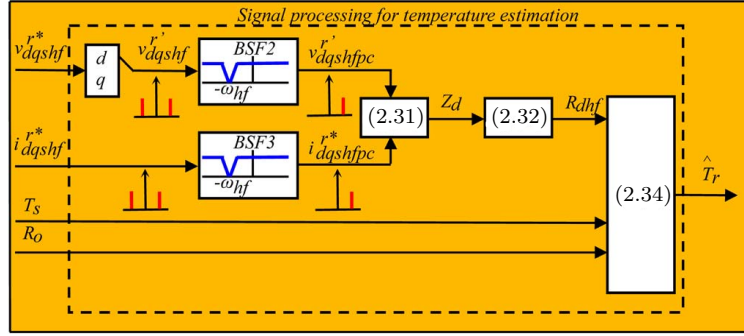


Figure 2.1: Implementation of the  $d$ -axis pulsating current injection

Figure 2.1 shows the inverter control and signal processing block diagrams used for temperature estimation with pulsating high frequency current injection. A band-stop filter ( $BSF1$ ) is used in the current feedback to prevent

Figure 2.2: Signal processing for the  $d$ -axis pulsating current injection

the reaction of the fundamental current regulator against the injected high-frequency current, while a bandpass filter ( $BPF1$ ) is used to isolate the high-frequency component of the overall stator current. A high-frequency resonant current controller is used to follow the commanded high-frequency current (2.35) with no error where  $K_p$  is the proportional gain,  $\omega = \omega_{hf}$  is the resonant frequency, and  $c$  is the location of the zero of the controller.

$$\text{Resonant Controller} = K_p \frac{(s + c)^2 + \omega^2}{s^2 + \omega^2} \quad (2.35)$$

The inputs to the temperature estimation block (see Fig.2.2) are the output voltage of the high-frequency resonant current controller  $v_{dqhf}^{r*}$  (2.25), the commanded high-frequency current  $i_{dqhf}^{r*}$  (2.24), the stator temperature  $T_s$ , and the stator resistance at the room temperature  $R_0$ . The  $d$ -axis impedance  $Z_d$  (2.29) is estimated from the positive sequence component of the commanded high-frequency current  $i_{dqhf}^{r*}$  (2.27) and the  $d$ -axis component of the high-frequency current resonant controller output voltage  $v_{dqhf}^{r'}$  (2.28). Two band-stop filters ( $BSF2$  and  $BSF3$  in Fig.2.2) are used to remove the negative sequence components. The magnet temperature is estimated using (2.32) and (2.34).

### 2.2.2 Magnet temperature estimation using $d$ -axis voltage injection and $q$ -axis current cancellation

In the method described in the previous section, a high-frequency current was injected in the  $d$ -axis, with the  $q$ -axis current being forced to be zero. It

is possible, however, to inject a high-frequency voltage in the  $d$ -axis instead of a high-frequency current. If a high-frequency voltage signal is applied in the  $d$ -axis (2.36) and a current cancellation strategy is applied to the  $q$ -axis (2.37), the resulting high-frequency voltage and current complex vectors, which are expressed in the synchronous rotor reference frame, are (2.38) and (2.39), respectively. The complex vector that results from taking only the real part of (2.38) is (2.40). Both (2.39) and (2.40) can be expressed as two rotating signals, each of half-amplitude of the original signal, rotating in opposite direction, (2.41) and (2.42), respectively, with the  $d$ -axis impedance being obtained from (2.41) and (2.42) using either the positive or the negative sequence components (2.43).

$$v_{drhf}^{r*} = V_{hf} \cos(\omega_{hf}t) \quad (2.36)$$

$$i_{drhf}^{r*} = 0 \quad (2.37)$$

$$v_{dqhf}^r = \begin{bmatrix} v_{dhf}^{r*} \\ v_{qhf}^r \end{bmatrix} = \begin{bmatrix} V_{hf} \cos(\omega_{hf}t) \\ \omega_r L_{dhf} i_{dhf}^{r*} \end{bmatrix} \quad (2.38)$$

$$i_{dqhf}^r = \begin{bmatrix} i_{dhf}^r \\ i_{qhf}^{r'} \end{bmatrix} = \begin{bmatrix} V_{dhf}^r / (R_{dhf} + j\omega_{hf} L_{dhf}) \\ 0 \end{bmatrix} \quad (2.39)$$

$$v_{dqhf}^r = \begin{bmatrix} v_{dhf}^{r*} \\ v_{qhf}^r \end{bmatrix} = \begin{bmatrix} V_{hf} \cos(\omega_{hf}t) \\ 0 \end{bmatrix} \quad (2.40)$$

$$i_{dqhf}^r = \frac{|i_{dhf}^r|}{2} e^{j\omega_{hf}t} + \frac{|i_{dhf}^r|}{2} e^{-j\omega_{hf}t} = i_{dqhfpc}^r + i_{dqhunc}^r \quad (2.41)$$

$$i_{dhf}^{r*} = \frac{V_{hf}}{2} e^{j(\omega_{hf}t - \varphi_{zd})} + \frac{V_{hf}}{2} e^{j(-\omega_{hf}t - \varphi_{zd})} = v_{dqhfpc}^{r'} + v_{dqhunc}^{r'} \quad (2.42)$$

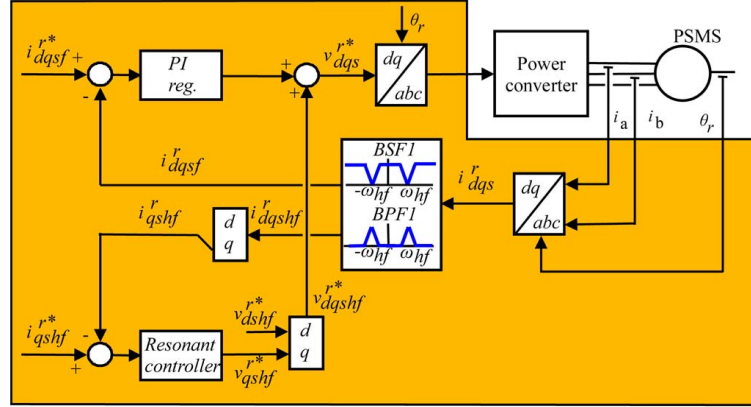


Figure 2.3: Implementation of the  $d$ -axis pulsating voltage injection with  $q$ -axis current cancellation

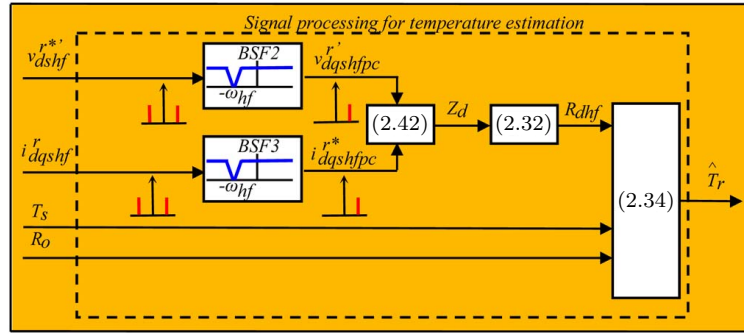


Figure 2.4: Signal processing for the  $d$ -axis pulsating current injection with  $q$ -axis current cancellation

$$Z_d = R_{dhf} + j\omega_{hf}L_{dhf} = \frac{v_{dqhfpc}^{r'}}{i_{dqhfpc}^r} = \frac{v_{dqhfnc}^{r'}}{i_{dqhfnc}^r} \quad (2.43)$$

Fig.(2.3) and Fig.(2.4) show the inverter control and signal processing block diagram for temperature estimation when a  $d$ -axis high-frequency voltage injection and  $q$ -axis current cancellation strategy is used. As for the implementation shown in Fig. (2.1), a band-stop filter ( $BSF1$  in Fig. (2.3)) is used in the fundamental current feedback control loop to prevent the fundamental current regulator reaction against the high-frequency signal. A bandpass filter ( $BPF1$  in Fig. (2.3)) is used to isolate the high-frequency current. A resonant controller, whose reference is (2.37), guarantees that no

high-frequency current circulates through the  $q$ -axis, while the commanded  $d$ -axis high frequency voltage  $v_{dhf}^{r*}$  is (2.36).

The inputs to the temperature estimation block (see Fig. (2.4)) are the commanded high frequency voltage  $v_{dhf}^{r*}$ , (2.36), the resulting high-frequency current  $i_{dqhf}^r$  (2.39), the stator temperature  $T_s$ , and the resistance at the room temperature  $R_0$ . The  $d$ -axis impedance  $Z_d$  (2.43) is estimated from the positive sequence components of the resulting high-frequency current  $i_{dqhfpc}^r$  (2.41) and the commanded  $d$ -axis high-frequency voltage  $v_{dqhfpc}^{r'}$  (2.42), which are obtained after removing the negative sequence components from the overall high-frequency current  $i_{dqhf}^r$  and voltage  $v_{dqhf}^{r'}$ , respectively. The magnet temperature is estimated using (2.32) and (2.34).

### 2.2.3 Comparison among high frequency signal injection methods

Although the methods described in sections 2.1.3.3, 2.2 and 2.2.2, respond to the same physical principles, differences in their performance exist that can be relevant in practice. The relationship between the  $d$ -axis high-frequency voltage and current both for the case of pulsating  $d$ -axis high-frequency current injection (2.24) and for the case of  $d$ -axis high-frequency voltage injection described in sections 2.2 and 2.2.2, respectively, is given by (2.44). On the other hand, the relationship between the  $d$ -axis high-frequency voltage and current, for the case of a rotating high-frequency voltage injection (2.17) described in section 2.1.3.3 is given by (2.20), while for the case of a pulsating  $d$ -axis voltage injection (2.45), is given by (2.46).

$$i_{dhf}^{r*} = \frac{v_{dhf}^{r*}}{R_{dhf} + j\omega_{hf}L_{dhf}} \quad (2.44)$$

$$v_{dqhf}^{r*} = \begin{bmatrix} v_{dhf}^{r*} \\ v_{qh}^{r*} \end{bmatrix} = \begin{bmatrix} V_{hf}^* \cos(\omega_{hf}t) \\ 0 \end{bmatrix} \quad (2.45)$$

$$i_{dhf}^r = \frac{v_{dhf}^{r*}(R_{qh} + j\omega_{hf}L_{qh})}{(R_{dhf} + j\omega_{hf}L_{dhf})(R_{qh} + j\omega_{hf}L_{qh}) + \omega_r^2 L_{dhf}L_{qh}} \quad (2.46)$$

The benefits of injecting a pulsating high-frequency current or voltage in the  $d$ -axis combined with the  $q$ -axis current cancellation strategy versus

injecting either a rotating voltage or a pulsating voltage become clear from the analysis of these equations. It is observed from (2.44) that the resistive component of the high-frequency current (i.e., the component of the current in phase with the high-frequency voltage) exclusively depends on the  $d$ -axis high-frequency resistance, not being affected by the rotor speed or by the  $d$ - and  $q$ -axis inductances. On the contrary, the resistive component of the resulting high-frequency current for the case of high-frequency voltage injection (either rotating (2.20), or pulsating (2.45)) given by (2.20) and (2.46), respectively, depends on the inductances and on the speed, increasing the sensitivity of the method to the machine operating conditions.

### 2.2.4 High frequency signal selection

Criteria for the selection of the magnitude and frequency of the injected high-frequency signal are discussed here.

#### *a) Frequency Selection*

Increasing the frequency will increase the spectral separation with the fundamental excitation frequency, making filtering easier. However, it will increase the weight of the inductive component (undesired component) over the resistive component (desired component) in the overall high-frequency impedance. Therefore, low frequencies would be preferred. A pulsating  $d$ -axis current of 250 Hz was selected for the experimental verification in this chapter, as it was found to provide an adequate balance. Since the pulsating signal is injected in the synchronous rotor reference frame, the spectral separation with the fundamental excitation is maintained constant, independent of the machine speed. It is finally noted that the frequency of the high-frequency signal ( $\omega_{hf}$ ) plus the machine excitation frequency ( $\omega_r$ ) needs to be smaller than half of the switching frequency (Nyquist frequency).

#### *b) Magnitude Selection*

Increasing the magnitude of the injected high-frequency current is advantageous for the accuracy of the method because it improves the signal-to-noise ratio of the measured current signals. However, increasing the magnitude of the high-frequency current magnitude will increase the rotor and stator losses and will also produce acoustic noise and vibration. A high-frequency current magnitude of 0.05  $p.u.$  was found to provide a good compromise, with the induced losses being  $\approx 1.5e - 4 p.u.$  for the SPMSM and  $\approx 2e - 4 p.u.$  for the IPMSM. A stator temperature increase in  $\approx 0.25 ^\circ C$  due to the injection of the high-frequency signal was measured for the IPMSM test machine. The measured magnet temperature increase was  $\approx 0.45 ^\circ C$ . As expected,

the impact of the high-frequency signal injection on the stator and magnet temperature can be considered of slight relevance.

### 2.2.5 Implementation of the proposed methods

The proposed methods have been tested on both an IPMSM and an SPMSM; pictures of both machines are shown in Fig. 2.5, with the corresponding parameters being shown in Table 2.3.



Figure 2.5: SPM and IPM test machines

As already mentioned, the stator temperature and the stator high-frequency resistance at the room temperature are needed to decouple the stator resistance contribution to the overall high-frequency impedance (see Figs. 2.2 and 2.4). The stator resistance at the room temperature can be easily measured and stored during a commissioning process; a wide variety of temperature devices can be used for this purpose. In this experiments, a PT-100 was used to measure the stator temperature in both machines. To evaluate the performance of the proposed method, the magnet temperature was measured during machine operation using an IR camera for the SPMSM (see Fig. 2.5).

Table 2.3: Machine parameters

Machine	$P_{RATED}[kW]$	$V_{RATED}[V]$	$I_{RATED}[A]$	$\omega_r[rpm]$	Poles
SPMSM	8.6	300	18.5	1000	8
IPMSM	7.5	350	14	1800	6

For the case of the IPMSM, the rotor is equipped with 13 thermocouples located along one PM, and this is shown schematically in Fig. A.3. The thermocouple wires are taken out throughout a hollow shaft and connected



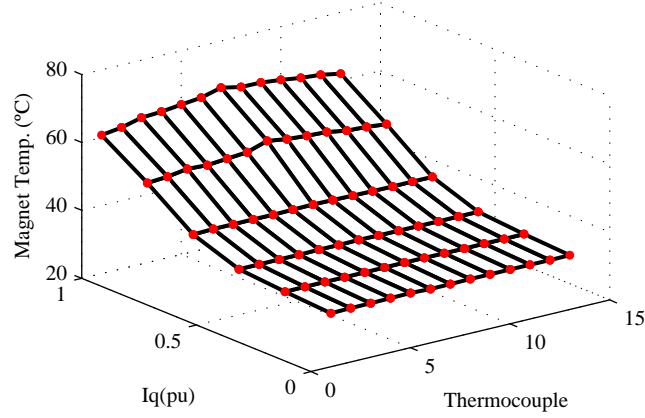


Figure 2.6: Magnet temperature measured by each thermocouple as a function of  $I_q$ .  $\omega_r = 30$  Hz.

to a measurement and wireless transmission device designed for this purpose. This device is explained in the Appendix A and includes the signal conditioning, digital signal processor, battery, and Wi-Fi module. For the experimental results shown in this chapter, a sampling rate of 1 Hz for the temperature measurement was found to be enough.

Fig. 2.6 shows the measured temperature by the 13 thermocouples when the  $I_q$  current changes from 0 to 1 p.u. in steps of 0.2 p.u.

The temperatures are measured 30 min after the  $I_q$  current is changed; the  $I_d$  current is set to 0 (i.e., the maximum torque per ampere (MTPA) strategy is not implemented), when the rotor has reached a steady-state thermal condition. The reason for not using MTPA for the IPMSM is to analyze the effects of changes in  $I_q$ ,  $I_d$ , and  $\omega_r$ , separately. As expected, the magnet temperature increases with  $I_q$ . It is observed that the temperature along the magnet is not constant, being higher at the central region of the magnet.

As expected, the central region of the PM has larger temperatures, therefore being more critical in regard to the potential adverse impact of the temperature on the magnets. It is also observed that temperature  $T_{13}$  is slightly higher than temperature  $T_1$ . This could be due to heat transfer between the IPMSM and the load induction machine through the mechanical coupling. Fig. 2.7 shows the temperature variation along the magnet. Temperature measured by thermocouple  $T_1$  (see Fig. A.3) was taken as the base value, the temperatures of thermocouples  $T_1$  to  $T_x$  represent the temperature difference

of thermocouple  $x$  with respect to  $T_1$ .

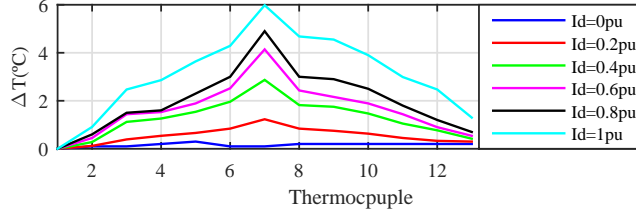


Figure 2.7: Experimentally measured temperature variation along the magnet.

## 2.2.6 Experimental results

The experimental results obtained from the proposed methods with both SPMSM and IPMSM are presented and discussed here. For the experimental verification, a Fuji Electric 1200 V 100 A insulated-gate bipolar transistor power module was used. The internal resistance of the power switches is  $\approx 20e^{-3} \Omega$  at 100 A and  $25^\circ\text{C}$ , which is more than two full orders of magnitude smaller than the overall machine high-frequency resistance ( $\approx 3.8 \Omega$  at  $25^\circ\text{C}$  and 250 Hz for the SPMSM and  $\approx 4.1 \Omega$  at  $25^\circ\text{C}$  and 250 Hz for the IPMSM); therefore, it can be safely neglected. It is noted, however, that the effect of the power switches' internal resistance could be more relevant in power modules using a MOSFET. This issue has not been analyzed in detail yet.

Two different operating regions, i.e.,  $\omega_r < 1$  p.u. ( $I_d = 0$ ) and  $\omega_r > 1$  p.u. ( $I_d \neq 0$ ), respectively, can be distinguished in the figures. For  $\omega_r < 1$  p.u., the effect of  $I_q$  (i.e., torque) and speed can be studied, while for  $\omega_r > 1$  p.u., the effects of changing  $I_d$  can be analyzed.

### 2.2.6.1 Experimental results for a SPMSM

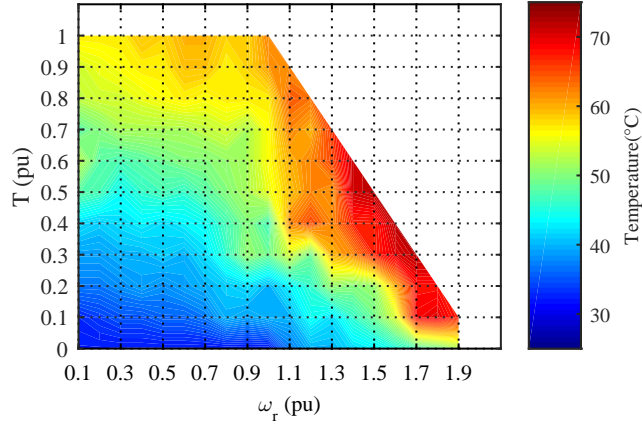
Fig. 2.8 shows the experimental results for the SPMSM, for pulsating  $d$ -axis current injection. Data were collected for different operating conditions, with both torque and speed being varied from zero to their corresponding rated value in steps of 0.1 p.u. Fig. 2.8(a) and 2.8(b) shows the measured stator and magnet temperature maps, respectively. The stator temperature was measured using a contact-type thermometer (PT-100), while the surface magnet temperature was measured using an IR camera. It is observed that the stator and rotor temperatures increase with the load due to the copper,

eddy current, and hysteresis losses, as expected. It is also observed that the machine temperature increases with the speed, due to the increase of eddy currents and hysteresis losses with frequency, with the most critical working conditions (higher temperatures) occurring in the flux-weakening region.

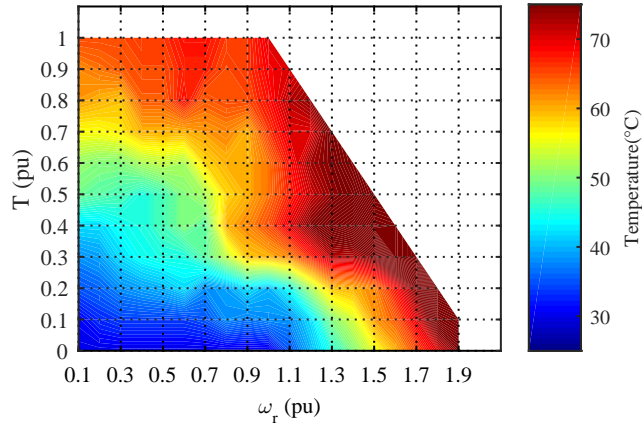
Fig. 2.8(c) shows the estimation error, i.e., the difference between the measured magnet temperature using the IR camera and estimated magnet temperature using the proposed method. It is observed that the speed has a negligible impact on the temperature estimation error, as predicted by (2.31) and (2.32); in addition, the load ( $I_q$ ) has a limited impact on the accuracy of the method (the maximum error is  $\approx 2.5^\circ C$ ). The variation of the error with the load observed in Fig. 2.8(c) is not predicted by (2.31) and (2.32) and is believed to be caused by the magnetization state variation with  $I_q$ , due to the cross-coupling between  $d$ -axis and  $q$ -axis. PM magnetization state variation leads the magnet resistivity to change due to the magnetoresistive effect. When this occurs, both the temperature variation and the magnetoresistive effect affect the resistivity, eventually resulting in an error in the estimated temperature. This effect has not been considered in the high-frequency model of the machine.

The estimated stator high-frequency resistance  $R_{dshf}(T_s)$ , rotor high-frequency resistance  $R_{drhf}(T_r)$ , and overall high frequency resistance  $R_{dhf}(T_s, T_r)$  maps are not shown due to room restrictions. However, these maps can be easily obtained from (2.14), with  $R_{dshf}(T_s)$  changing linearly with the stator temperature,  $R_{drhf}(T_r)$  changing linearly with the estimated rotor temperature, and  $R_{dhf}(T_s, T_r) = R_{dshf}(T_s) + R_{drhf}(T_r)$ .

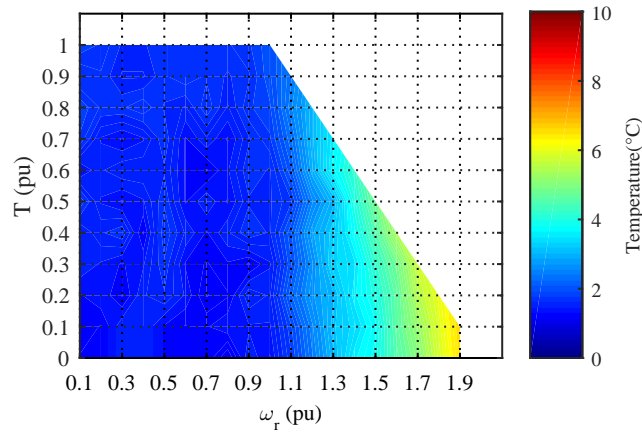
A noticeable dependence of the error in the estimated temperature with the  $d$ -axis current ( $I_d$ ) injected for field weakening, in the high-speed region, is also observed. Although this behavior was not predicted by the high-frequency model of the machine, it was expected due to the magnetoresistive effect, since the  $I_d$  current injection leads the magnetization state of the machine to change.



(a) Measured stator temperature



(b) Measured rotor temperature



(c) Magnet temperature estimation error.

Figure 2.8: SPMSM: Experimentally measured stator and rotor temperatures and magnet temperature estimation error.  $\omega_{hf} = 2\pi 250$  rad/s,  $V_{hf} = 0.1$  p.u., and  $I_{hf} = 0.05$  p.u.

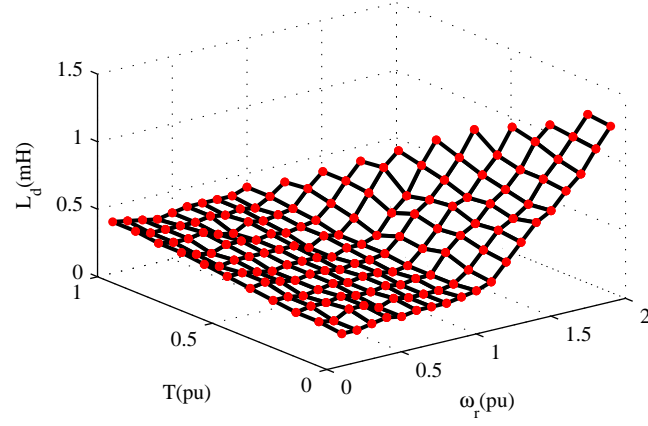


Figure 2.9: SMPSM: Estimated high-frequency inductance  $L_{dhf}$ .  $\omega_{hf} = 2\pi 250$  rad/s and  $I_{hf} = 0.05$  p.u.

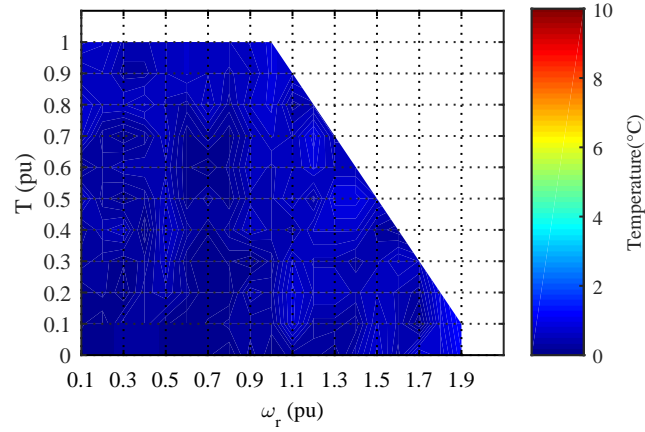


Figure 2.10: SMPSM: Magnet temperature estimation error after decoupling the magneto-resistive effect for different speeds and torque levels.  $\omega_{hf} = 2\pi 250$  rad/s and  $I_{hf} = 0.05$  p.u.

$L_{dhf}$  is a reliable indicator of the magnetization state of the machine and could be used to decouple the magneto-resistance effect. As shown by (2.31),  $L_{dhf}$  can be estimated from the imaginary part of (2.31) for pulsating current injection. Fig. 2.9 shows the estimated  $L_{dhf}$  for all the operating range of the machine, when a pulsating  $d$ -axis high-frequency current is injected. Fig. 2.10 shows the error in the estimated magnet temperature after decoupling the magneto-resistive effect using the estimated  $L_{dhf}$ . It is

observed that, after decoupling the magnetoresistive effect, the error in the estimated magnet temperature is limited to  $\approx 2^\circ\text{C}$ .

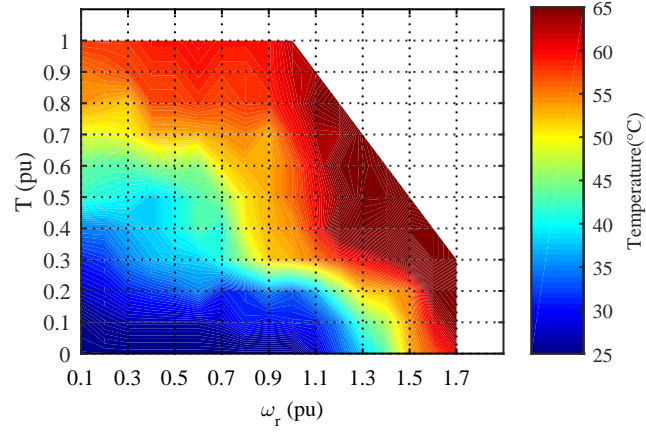
### 2.2.6.2 Experimental results for an IPMSM

Experimental data for the case of the IPMSM were for the same operating conditions described for the SPMSM.

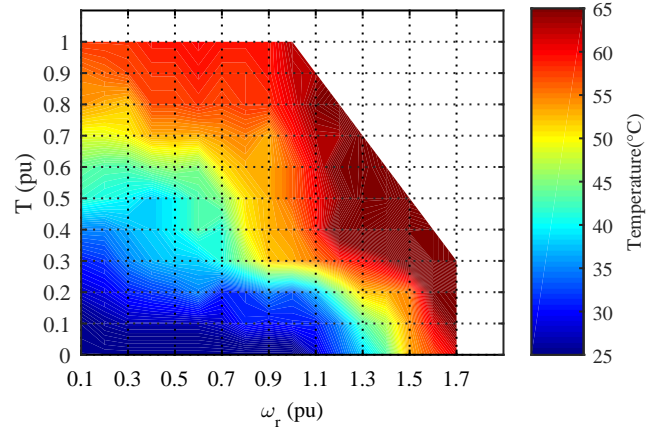
Fig. 2.11 shows the experimental results for the case of rotating and pulsating  $d$ -axis current injection. Fig. 2.11(a) and 2.11(b) shows the measured stator and magnet temperature contours, respectively. The stator temperature was measured using a PT-100. The magnet temperature was obtained as the average of the measurement provided by the 13 sensors in the system described in the Appendix A. A similar behavior as for the SPMSM for the stator and magnet temperature is observed, with the most critical working conditions (higher temperatures) occurring also at high speed, in the flux-weakening region.

Fig. 2.11(c) shows the error in the estimated magnet temperature, which is obtained as the difference between the average value of the measurements (see Fig. 2.7) and the estimated temperature. Note the different color bar scale for Fig. 2.11(c) compared to Figs. 2.8(c), 2.10 and 2.13. As for the SPMSM, for the case of rotating voltage injection, the estimation error increases as the load ( $I_q$ ) and the speed ( $\omega_r$ ) increase. It is also observed in Fig. 2.11(c) that the estimation error increases as load ( $I_q$ ) and flux-weakening current ( $I_d$ ) increase, while the speed has a negligible impact in the temperature estimation error. As for the case of the SPMSM, MTPA is not implemented, (i.e.,  $I_d = 0$  for  $\omega_r < 1$  p.u. and  $I_d = 0$  for  $\omega_r > 1$  p.u.). The variation of the temperature estimation error with  $I_q$  and  $I_d$  currents is due to the magnetoresistance effect (same explanation as for the SPMSM). Both  $I_q$  and  $I_d$  currents lead the magnetization state of the PMs to change, which is reflected in the  $d$ -axis high-frequency inductance  $L_{dhf}$ . As for the SPMSM,  $L_{dhf}$  is a reliable metric of the magnetization state of the PMs and could be used to decouple the magnetoresistance effect. Fig. 2.12 shows the estimated  $L_{dhf}$  from the imaginary part of (2.31) for the different operating conditions. Fig. 2.13 shows the error in the estimated magnet temperature after decoupling the magnetoresistive effect using the estimated  $L_{dhf}$ . After decoupling the magnetoresistive effect, the error in the estimated magnet temperature is reduced to a maximum value of  $\approx 2.5^\circ\text{C}$ .

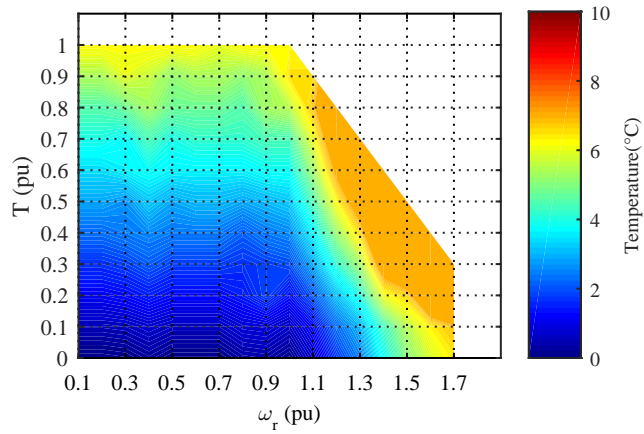
It is finally noted that all the experimental results presented here were obtained with the machine operating in the steady state. A delay of  $\approx 2.5$  ms,



(a) Measured stator temperature



(b) Measured rotor temperature



(c) Magnet temperature estimation error.

Figure 2.11: IPMSM: Experimentally measured stator and rotor temperatures and magnet temperature estimation error.  $\omega_{hf} = 2\pi 250$  rad/s,  $V_{hf} = 0.1$  p.u., and  $I_{hf} = 0.05$  p.u.

due to the signal processing, exists in the temperature estimation. This delay is considered irrelevant, as the machine thermal time constant is significantly larger.

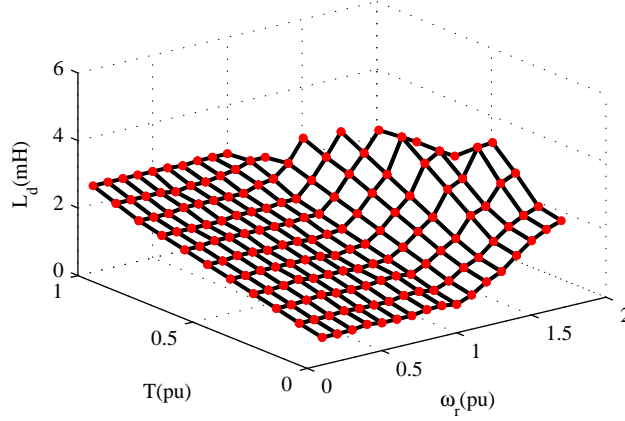


Figure 2.12: IPMSM: Estimated high-frequency inductance  $L_{dhf}$ .  $\omega_{hf} = 2\pi 250$  rad/s and  $I_{hf} = 0.05$  p.u.

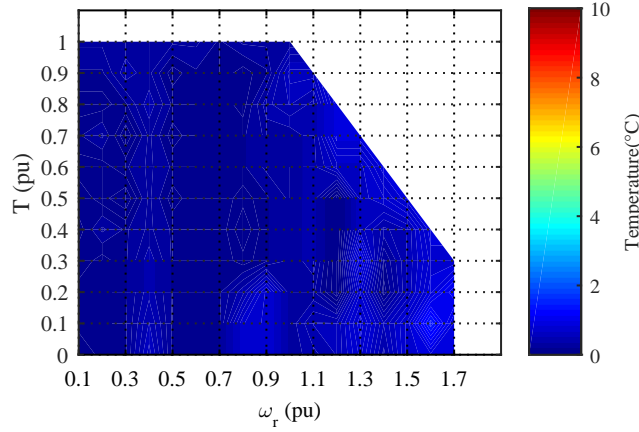


Figure 2.13: IPMSM: Magnet temperature estimation error after decoupling the magnetoresistive effect for different speeds and torque levels.  $\omega_{hf} = 2\pi 250$  rad/s and  $I_{hf} = 0.05$  p.u.



## 2.3 PM temperature distribution estimation

As already mentioned, PMs of PMSMs are subject to irreversible demagnetization if their temperature becomes too high [32, 31]. Demagnetization can be global [42], when the temperature in the PM is uniform, or partial (local) when the spatial temperature distribution is not uniform [42, 64]. Consequently, estimation not only of the average temperature, but also of the maximum PM temperature, can be crucial to prevent partial demagnetization of the PMs. Additionally, estimation of the spatial temperature distribution can be used to compensate its effects on the torque ripple in the machine.

Temperature estimation methods explained in previous sections (i.e., BEMF based methods in section 2.1.3.2, high frequency resistance based methods in sections 2.1.3.3 and 2.2), provide a lumped temperature, i.e. with no information of the PM temperature spatial distribution.

This section analyzes the effects of a non-uniform magnet temperature distribution on the BEMF harmonics, and its use to estimate the magnet differential temperature. The magnet differential temperature, combined with the average PM temperature can be used to estimate the spatial temperature distribution.

### 2.3.1 Temperature Estimation using BEMF

Back-EMF based methods estimate the magnet temperature from the PM flux linkage ( $\lambda_{PM}$ ), which is obtained from the machine terminal voltages and currents. While obtaining the PM flux linkage from the stator terminals when  $I_d = I_q = 0$  is relatively simple, it becomes challenging when either  $I_d$  or  $I_q$  are different from zero. Knowledge of several machine parameters is needed in this case (i.e.  $d$  and  $q$ -axis inductance maps with  $i_{dq}$ ), increasing the parameter sensitivity of the method. On the other hand, no additional signal needs to be injected.

The fundamental model of a PM machine in the synchronous rotor reference frame is described by 2.4. Since the PM flux  $\lambda_{PM}$  is only present in the  $q$ -axis equation of the machine 2.4, only the  $q$ -axis voltage equation (2.5) is needed.

In (2.5),  $R_q$  is function of the stator temperature,  $T_s$ ,  $\lambda_{PM}$  is function of the magnet temperature,  $T_r$ , while  $L_d$  and  $L_q$  are both function of the rotor temperature,  $T_r$ , and of the  $d$  and  $q$ -axis currents  $i_{dq}$ . Consequently (2.5) can be transformed to (2.6),  $\lambda_{PM}$  being obtained as (2.7). If it is assumed

that  $i_{dq} = 0$ , the PM flux can be obtained from (2.9). The PM flux variation with the magnet temperature can be expressed as (2.8), where  $T_0$  is the room temperature and  $\beta$  is the magnet flux thermal coefficient. Finally, the magnet temperature,  $T_r$ , can be obtained using (2.47). As for high frequency signal injection methods, the estimated temperature is a lumped value, not providing therefore information on its spatial distribution.

$$T_r = \frac{1}{\beta} \left[ \frac{\lambda_{PM}(T_r)}{\lambda_{PM}(T_0)} - 1 \right] + T_0 \quad (2.47)$$

### 2.3.2 Estimation of the magnet temperature distribution

Fig. 2.14 shows the IPMSM design that will be used both for simulation and experimental verification. It is a 36 slot 6 pole machine equipped with NdFeB magnets (N-42SH). The uniform and non-uniform temperature profiles considered are shown in Fig. 2.15(a) and Fig. 2.15(b) respectively. For the non-uniform temperature distribution, a quadratic law (2.48) was found to adequately fit with the temperature distribution experimentally measured. The PM dimensions in (2.48) are indicated in Fig. 2.15, where  $T_{min}$ ,  $T_{max}$  and  $T_r$  are the minimum, maximum and mean PM temperature respectively, and  $PM\ length$  is the PM length.

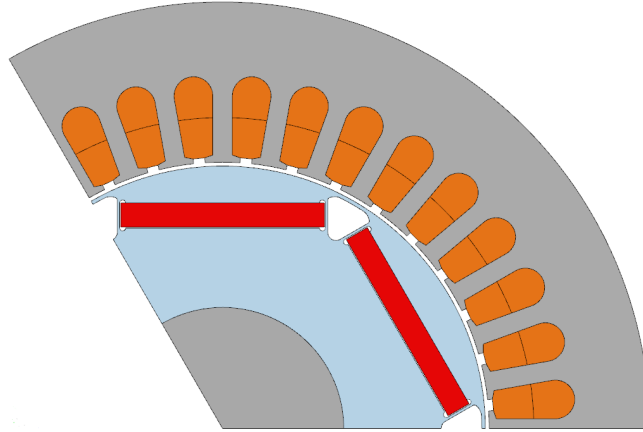


Figure 2.14: One third of the cross Section of the IPMSM used for simulations and experimental results

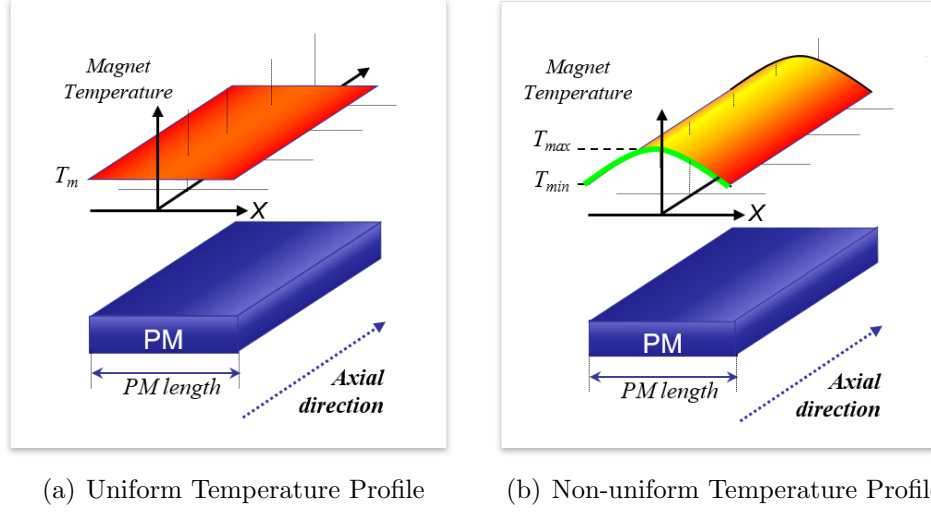


Figure 2.15: Magnet temperature distribution

$$\begin{aligned}
 T_{magnet} &= \frac{T_{min} - T_{max}}{(PM_{length}/2)^2} X^2 + T_{max} = \\
 &\frac{T_{min} - T_{max}}{(PM_{length}/2)^2} X^2 + \left( T_r + \frac{T_{max} - T_{min}}{2} \right)
 \end{aligned} \tag{2.48}$$

To obtain the magnet temperature distribution using (2.48), the mean PM temperature  $T_r$  and the differential PM temperature  $T_{min}-T_{max}$  need to be estimated. Methods to do this are discussed following.

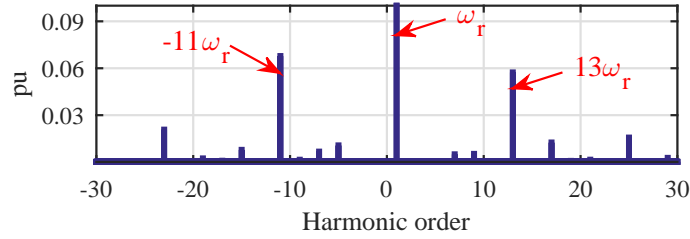
### 2.3.3 Estimation of the mean magnet temperature

This subsection evaluates the mean PM temperature estimation. Use of the BEMF (2.47) and of a pulsating  $d$ -axis high frequency current signal injection are discussed, both for the case of uniform and non-uniform temperature distributions. Finite element analysis (FEA) will be used for this analysis. Table 2.4 shows the temperature profiles used for simulation. Fig. 2.16 shows the FFT of the BEMF for the cases of a uniform and a non-uniform magnet temperature distributions (see Table 2.4). The results are normalized in pu with respect to the 1<sup>st</sup> harmonic of the BEMF. A logarithmic scale is used for the magnitudes. The harmonic content is the same for uniform and non-uniform temperature distributions, harmonic magnitudes

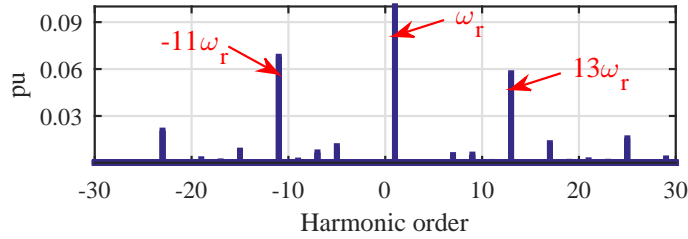
being slightly different. Three components of interest are observed:  $\omega_r$ ,  $13\omega_r$  and  $-11\omega_r$  harmonics.

Table 2.4: Case of study for different temperature distribution conditions

Cases	Uniform Magnet temperature distribution	Non-uniform Magnet temperature distribution		
	$T_r(^{\circ}C)$	$T_{max}(^{\circ}C)$	$T_{min}(^{\circ}C)$	$T_r(^{\circ}C)$
1	100	100	100	100
2	90	100	90	94
3	80	100	80	88
4	70	100	70	82
5	60	100	60	76
6	50	100	50	70
7	—	100	40	64
8	—	100	30	58



(a) Uniform magnet temperature distribution



(b) Non-uniform magnet temperature distribution

Figure 2.16: BEMF frequency spectrum  $\omega_r = 2\pi 50 \text{ rad/s}$

Fig. (2.17) shows the magnitude variation of the 1<sup>st</sup> harmonic of the

BEMF (component at  $\omega_r$ , 50Hz), and which corresponds to  $v_q^r$  in (2.9), as the mean magnet temperature changes,  $T_r$  (see Table (2.4)). As predicted by (2.9)-(2.8), its magnitude decreases as the mean magnet temperature increases. It is observed that the same BEMF magnitude is induced both for the cases of a uniform and a non-uniform magnet temperature distributions. It is therefore concluded that the 1<sup>st</sup> harmonic of the BEMF does not contain information on the magnet temperature distribution. However, it can be used for mean PM temperature estimation.

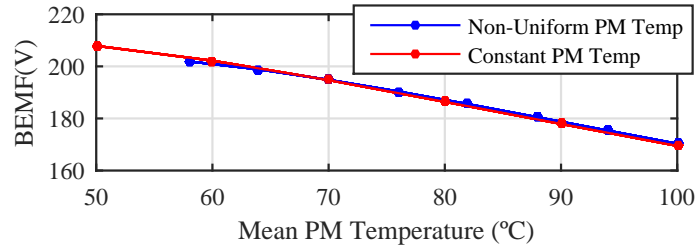


Figure 2.17: Fundamental component of the BEMF vs. mean magnet temperature.  $I_d = I_q = 0$  pu and  $\omega_r = 2\pi 50$  rad/s.

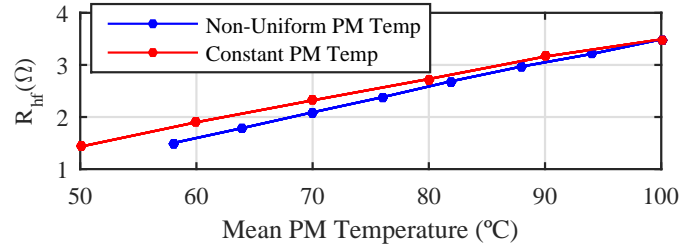


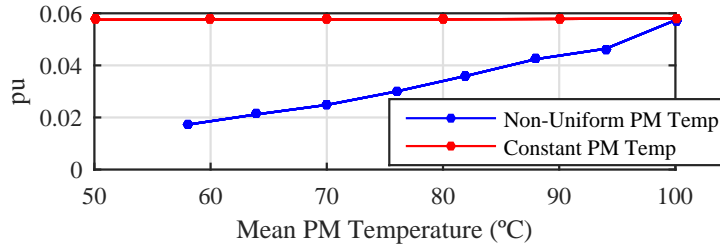
Figure 2.18: Estimated  $d$ -axis high frequency resistance. Pulsating  $d$ -axis high frequency current injection,  $\omega_{hf} = 2\pi 250$  rad/s,  $I_{hf} = 0.05$  pu.  $I_d = I_q = 0$  pu and  $\omega_r = 2\pi 50$  rad/s.

Fig. 2.18 shows the estimated rotor  $d$ -axis high frequency resistance,  $R_{drhf}$   $T_r$  (2.34), when a pulsating  $d$ -axis high frequency current is injected, both for the cases of a uniform and a nonuniform magnet temperature distribution, its magnitude decreasing as the mean magnet temperature decreases, see (2.34). It is also observed that the estimated  $d$ -axis high frequency resistance variation with the mean PM temperature is higher for the non-uniform magnet temperature distribution case compare to the uniform temperature

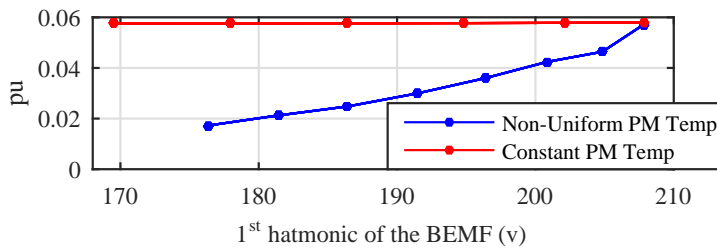
distribution case. This means that different PM temperatures would be estimated for the same PM high frequency resistance, inducing therefore an error in the estimated temperature. This variation could be potentially used to estimate the differential magnet temperature  $T_{min}-T_{max}$ . This is an ongoing research issue.

### 2.3.4 Differential magnet temperature estimation

This subsection analyzes differential PM temperature estimation using the BEMF harmonics. Simulation details are the same as for mean PM temperature estimation. Fig. 2.16 shows the frequency spectrum of the BEMF, three components of interest are observed:  $\omega_r$ ,  $13\omega_r$  and  $-11\omega_r$ . As discussed in previous subsection, the component at  $\omega_r$  does not contain information of the differential PM temperature; however, it can be used to estimate the mean PM temperature. On the contrary,  $13\omega_r$  and  $-11\omega_r$  harmonics can be used for PM differential temperature estimation, this is analyzed following.



(a) BEMF 13<sup>th</sup> harmonic magnitude vs. mean magnet temperature



(b) BEMF 13<sup>th</sup> harmonic magnitude vs. the 1<sup>th</sup> harmonic magnitude of the BEMF.

Figure 2.19: BEMF 13<sup>th</sup> harmonic magnitude vs. mean magnet temperature and vs. the 1<sup>th</sup> harmonic magnitude of the BEMF.  $\omega_r = 2\pi \cdot 50$  rad/s.

Fig. 2.19(a) shows the magnitude of the BEMF 13<sup>th</sup> harmonic (see Fig.

2.16), as a function of the mean magnet temperature, while Fig. 2.19(b) shows the same harmonic as a function of the fundamental component of the BEMF. In both cases the 13<sup>th</sup> harmonic is shown in pu of the fundamental component of the BEMF. This normalization compensates for the effects due to the variation of the average temperature. It is observed from Fig. 2.19 that for the case of a constant magnet temperature distribution, the relative magnitude of the 13<sup>th</sup> harmonic is almost insensitive to the variations of the mean magnet temperature and of the fundamental component of the BEMF. On the contrary, it is observed for the case of the non-uniform magnet temperature distribution, that the 13<sup>th</sup> harmonic magnitude increases with the mean magnet temperature, as well as with the magnitude of the fundamental component of the BEMF. Consequently, the *p.u.* value of the 13<sup>th</sup> harmonic decreases as  $T_{max}-T_{min}$  increases. The different behavior of the 13<sup>th</sup> harmonic for the case of a uniform and a non-uniform temperature distribution can be potentially used to estimate the differential temperature due to a non-uniform magnet temperature distribution.

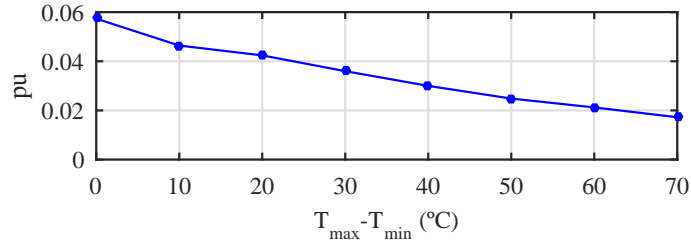


Figure 2.20: Back-EMF 13<sup>th</sup> harmonic magnitude vs. differential magnet temperature, i.e.  $(T_{max}-T_{min})$ .  $\omega_r = 2\pi 50 \text{ rad/s}$ .

Fig. 2.20 shows the 13<sup>th</sup> harmonic component magnitude vs. the differential magnet temperature, i.e.  $T_{max}-T_{min}$ , for the case of non-uniform temperature distribution. It is seen to change almost linearly with the differential temperature. This relationship can be used to estimate  $T_{max}-T_{min}$ , which combined with the mean PM temperature,  $T_r$ , can be used to estimate the magnet temperature distribution from (2.48). It was shown in the previous subsection that  $T_r$  can be estimated either by injecting a high frequency signal (see Fig. 2.18), or from the fundamental component of the BEMF (see Fig. 2.17 and 2.47). It is finally noted that although the 13<sup>th</sup> harmonic of the BEMF has been used in the preceding discussion, the 11<sup>th</sup> harmonic was observed to have a similar behavior. Though higher order harmonics could also potentially be used, the magnitude of the voltage harmonic decreases

with the harmonic order. This results in a reduction of the signal-to-noise ratio, therefore compromising the accuracy of the method.

### 2.3.5 Experimental results

Verification of the proposed concepts will require measurement of the PM temperature distribution. Sensors setup reported in the literature [32, 31, 51, 49, 50, 52] for this purpose has limited spatial resolution. Among these, the highest resolution was provided by the system described in A, in which the rotor was equipped with 13 thermocouples located along one PM. This allows the measurement of the temperature along one PM in the rotor axial direction, but not in the tangential direction, being therefore inadequate for the analysis presented in this chapter. To overcome this limitation, a temperature measurement system that allows measurement of both axial and tangential temperature distributions has been developed, and it is explained in Appendix B. The test machine has the same design as the simulated machine (see Fig. 2.14). The machine parameters are shown in Table 2.3.

Fig. 2.21 shows the PM temperature measured by the 3x5 sensor array, when  $I_q$  current changes from 0 to 1 p.u. in steps of 0.2 p.u. and for  $I_q=2$  p.u. (2 p.u. overload). No  $d$ -axis current was injected ( $I_d=0$ ), MTPA is not implemented therefore. Consequently, observed temperature variations are due exclusively to the  $q$ -axis current.

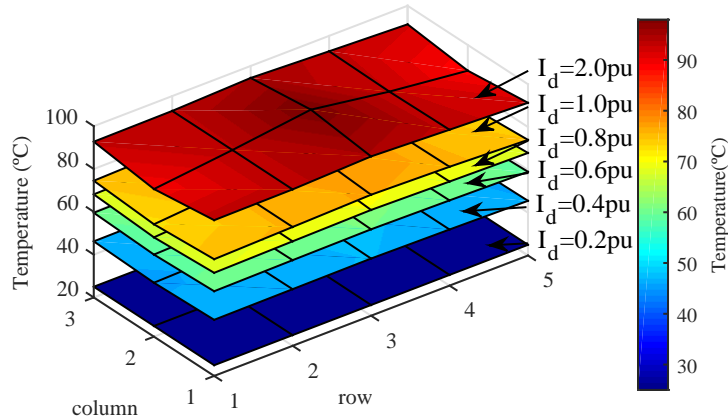


Figure 2.21: Experimentally measured magnet temperatures for  $I_q$  current of: 0.2, 0.4, 0.6, 0.8, 1.0 and 2.0 p.u.  $I_d=0$  p.u.,  $\omega_r = 2\pi 50$  rad/s (1pu).



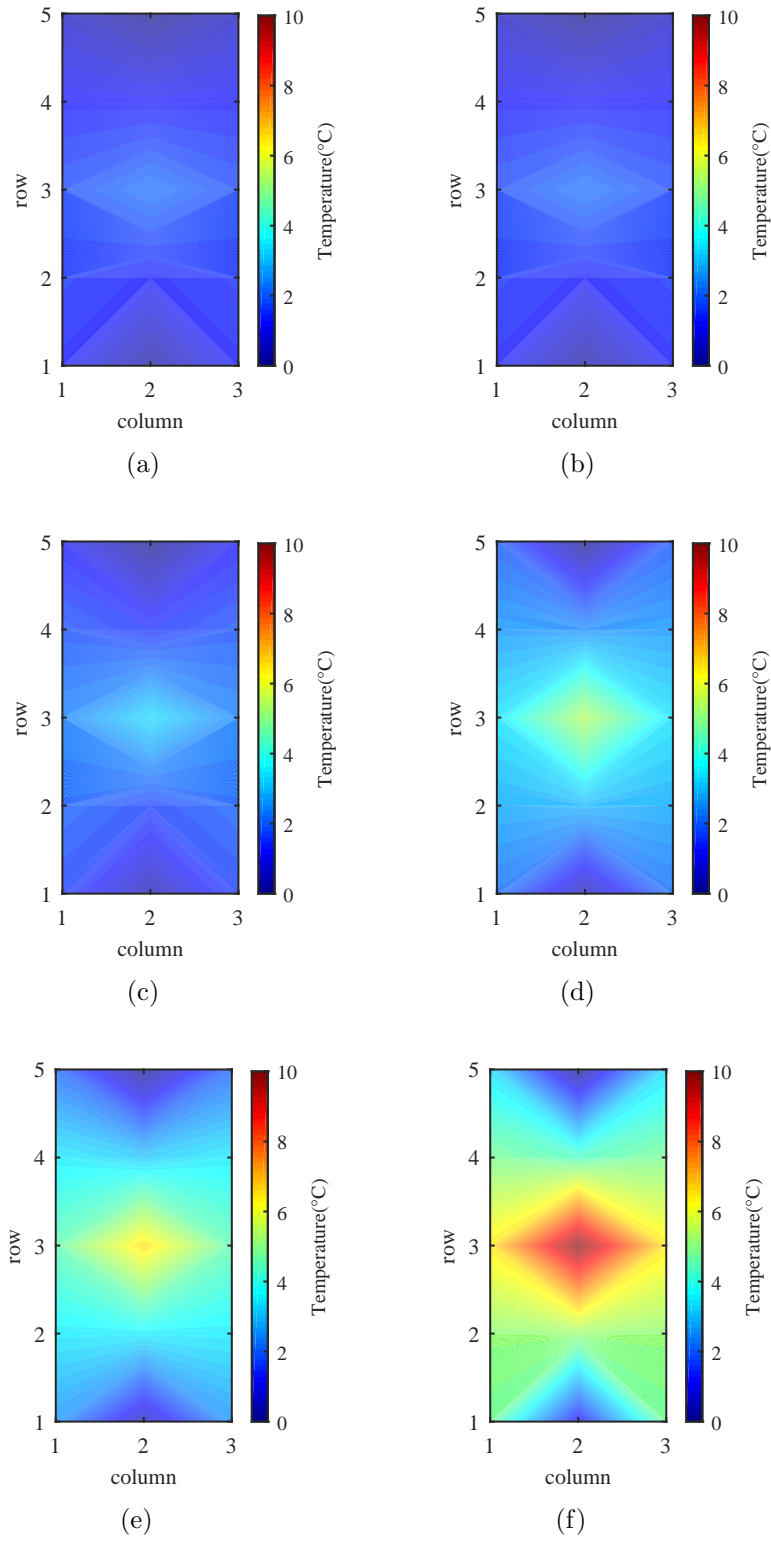


Figure 2.22: Experimentally measured magnet differential temperature, for the experimental results shown in Fig. 2.21.

For each operating condition, the temperature is measured 30 min. after  $I_q$  is established. This time was seen to be enough for the machine to reach its steady state thermal condition. As expected, the magnet temperature increases with  $I_q$ . It is also observed that the magnet temperature is not uniform, being higher at the central area, the risk of demagnetization being therefore higher in this region. It is also observed that temperatures measured by sensors in row 1 are a little bit higher than for sensors in row 5. Row 1 is the closest to the mechanical coupling with the load machine, (see Appendix B). The heat transfer between the IPMSM and the load IM through the mechanical coupling could cause this effect.

Fig. 2.22 shows the differential temperature for the experimental results shown in Fig. 2.21. Temperature measured by sensor T(1,2) (see Appendix B) is used as the base temperature, as it always exhibits the lowest temperature.

It can be observed that the bigger the  $I_q$  current is, the bigger the differential temperatures are. The maximum differential temperature without using  $d$ -axis current is  $\approx 9.92^\circ\text{C}$ . It is noted that the stack length of the test machine is 100 mm; higher temperature variations would be therefore expected in larger machines.

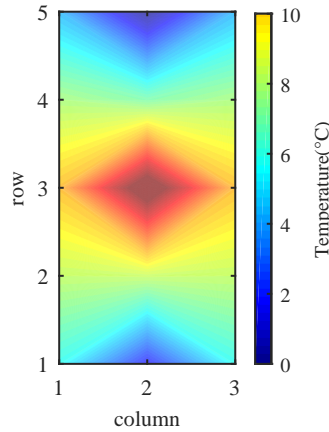


Figure 2.23: Experimentally measured magnet differential temperature.  $I_d=0.9$  p.u.,  $I_{dq}=1$  p.u.,  $\omega_r=2\pi 85$  rad/s (1.7 p.u.).

Finally, Fig. 2.23 shows the magnet differential temperature for a speed of  $\omega_r=1.7$  p.u., which is the maximum operating speed of the test machine, with  $I_{dq}=1$  pu and  $I_d=0.9$  pu, i.e. deep flux-weakening operation. The maximum differential temperature in this working condition is  $\approx 15^\circ\text{C}$ .

### a) Mean Magnet Temperature Estimation ( $T_r$ )

Fig. 2.24 shows the BEMF for the case of  $\omega_r=1$  pu, the BEMF being obtained from the fundamental current controller output. Fig. 2.25(a) and 2.25(b) show the FFT of the BEMF for the case of uniform and non-uniform magnet temperature distributions respectively. Magnitudes are normalized in pu with respect to the fundamental component of the BEMF, a logarithmic scale being used.

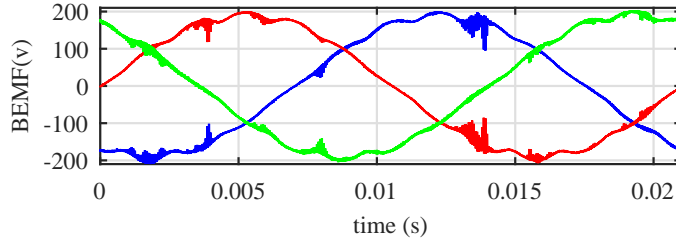
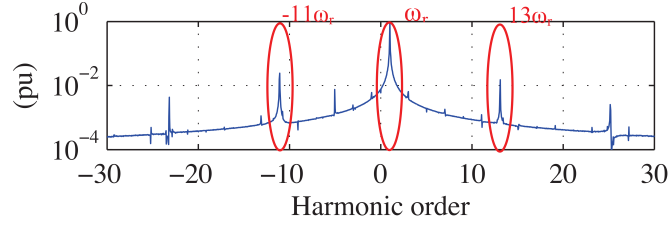


Figure 2.24: BEMF of the IPMSM

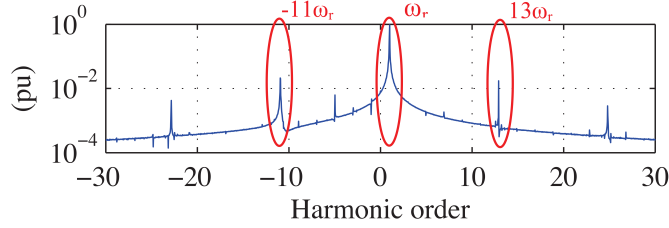
Fig. 2.26 and 2.27 show the magnitude of the fundamental component of the BEMF and the estimated rotor  $d$ -axis high frequency resistance respectively, as a function of the mean magnet temperature (see Table 2.4). Both the fundamental component of the BEMF and the estimated  $d$ -axis high frequency resistance, are seen to change almost proportional to the mean PM temperature. Consequently, both terms can be used to estimate the mean PM temperature, which is consistent with the simulation results shown in Fig. 2.19(a) and 2.19(b). It is also observed that the differences both in the fundamental component of the BEMF (Fig. 2.26) and high frequency resistance (Fig. 2.27) for the case of a uniform and a non-uniform temperature distributions are very small or even negligible. Consequently, the use of these terms for differential PM temperature estimation is not viable.

### b) Differential magnet temperature estimation ( $T_{max} - T_{min}$ )

Fig. 2.28(a) shows the magnitude of the BEMF 13<sup>th</sup> harmonic vs. PM temperature, both for the cases of uniform and nonuniform PM temperature distributions. Similarly, Fig 2.28(b) shows the magnitude of the BEMF 13<sup>th</sup> harmonic vs. the magnitude of the fundamental component of the BEMF. The minimum, maximum, and mean temperatures, i.e.  $T_{min}$ ,  $T_{max}$  and  $T_r$  for these experimental results are shown in Table 2.4, the maximum differential temperature being  $\approx 15^\circ C$ . Experimental results shown in Fig. 2.28 are in good agreement with simulation results shown in Fig. 2.19, confirming the



(a) BEMF frequency spectrum for uniform magnet temperature distribution



(b) BEMF frequency spectrum for non-uniform magnet temperature distribution

Figure 2.25: BEMF frequency spectrum of the IPMSM  $I_d = I_q = 0$   $\omega_r = 2\pi 50$  rad/s.

usefulness of the 13<sup>th</sup> harmonic of the BEMF for differential PM temperature estimation purposes.

Fig. 2.29 shows the magnitude of the BEMF 13<sup>th</sup> harmonic variation vs. the differential magnet temperature for the nonuniform PM temperature distribution case. This relationship being consistent with the simulation results (see Fig 2.20), a remarkable agreement between simulation and experimental results being observed in general.

### *c) Magnet temperature distribution estimation*

Fig. 2.30a-f shows the magnet temperature estimation error for the experimental results shown in Fig. 2.21 - 2.22. The mean PM temperature is estimated either from the fundamental component of the BEMF or the estimated  $d$ -axis high frequency resistance, see Fig. 2.26 and 2.27, the BEMF has been used for the experimental results in Fig. 2.30. The differential temperature,  $T_{max}-T_{min}$ , is estimated from the 13<sup>th</sup> harmonic of the BEMF. The estimation error in Fig. 2.30 is the difference between the measured temperatures and the estimated temperatures using 2.48. It is observed that the maximum temperature estimation error is  $<1.75^\circ C$  (Fig. 2.30) and occurs in an overloaded condition, with i.e.  $I_q=2$  p.u. It is also observed that

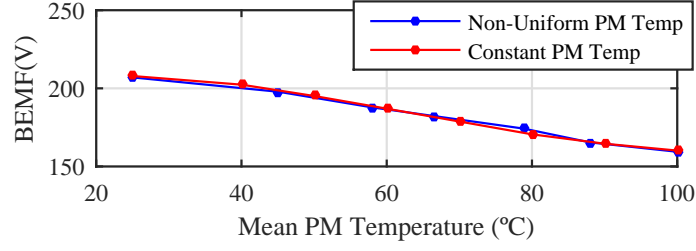


Figure 2.26: Fundamental component of the BEMF vs. mean magnet temperature for the case of uniform and non-uniform temperature distributions.  $\omega_r = 2\pi 50 \text{ rad/s}$ .

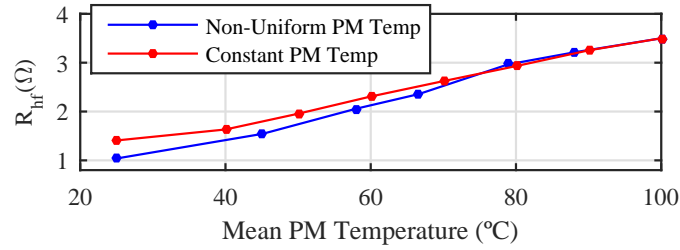
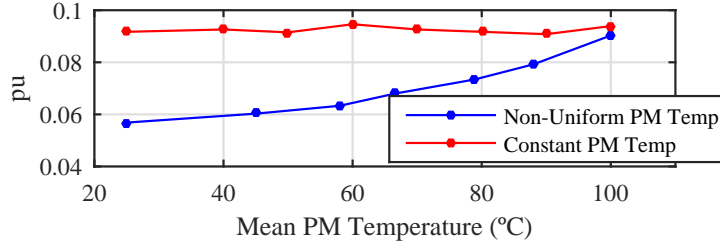


Figure 2.27: Estimated  $d$ -axis high frequency resistance for the case of uniform and non-uniform temperature distributions. Pulsating  $d$ -axis high frequency current injection,  $\omega_{hf} = 2\pi 250 \text{ rad/s}$ ,  $I_{hf}=0.05 \text{ pu}$ .  $I_d = I_q = 0 \text{ pu}$  and  $\omega_r = 2\pi 50 \text{ rad/s}$ .

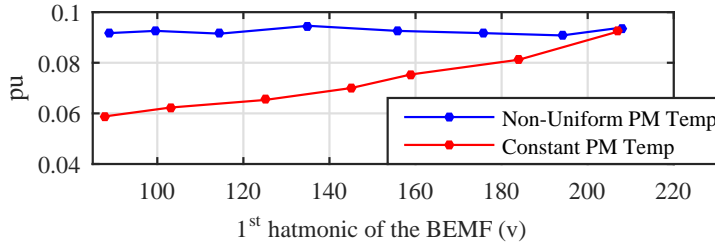
the maximum temperature estimation errors occur at the magnet corners. Although FEA magnet temperature distribution color maps are not shown, this effect was not predicted by FEA. It is also observed that the temperature estimation error is not symmetric in the axial direction with respect to the center of the magnet (row 3). This asymmetry is believed to be due to the heat transfer between the IPMSM and the load IM through the mechanical coupling.

## 2.4 Conclusions

A method for mean magnet temperature estimation and a method for magnet spatial temperature distribution estimation in PMSMs (IPMSMs and SPMSMs) have been proposed in this chapter.



(a) Magnitude of the 13<sup>th</sup> harmonic for case of uniform and nonuniform temperature distributions vs. mean magnet temperature



(b) Magnitude of the 13<sup>th</sup> harmonic for case of uniform and nonuniform temperature distributions vs. fundamental component of the BEMF

Figure 2.28: BEMF 13th harmonic magnitude for the case of uniform and nonuniform temperature distributions  $\omega_r = 2\pi 50 \text{ rad/s}$ .

The proposed method for mean magnet temperature estimation is based on the injection of a pulsating high-frequency current signal. This, overcomes the limitations of rotating high-frequency voltage injection methods, such as the sensitivity to the machine speed and to  $L_q$  and  $L_d$  changes. It has been shown that both  $I_q$  and  $I_d$  currents have an important impact over the temperature estimation error due to the magnetoresistance effect, which can be decoupled by the estimated  $d$ -axis high-frequency inductance ( $L_{dhf}$ ). Extensive experimental results using different forms of high-frequency excitation, and for both the case of SPMSM and IPMSM, have been provided to demonstrate the viability of the proposed method.

The proposed method for differential magnet temperature estimation is based on the modification of the harmonic content of the BEMF, due to the changes produced in PM flux linkage between the rotor and the stator, by a non-uniform temperature profile in the magnet. As any parameter estimation method based on BEMF, it needs the machine to rotate, not being suitable

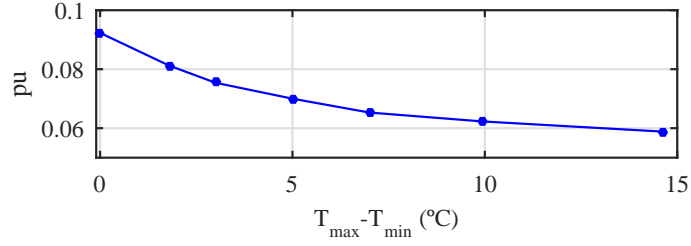


Figure 2.29: Back-EMF 13<sup>th</sup> harmonic magnitude vs. differential magnet temperature  $T_{\max} - T_{\min}$ .  $\omega_r = 2\pi 50 \text{ rad/s}$ .

for low/zero speed. Simulations using FEA and experimental results have been provided to demonstrate the viability of the method.

PM spatial temperature distribution in PMSMs is obtained from mean and differential PM temperature. Mean PM temperature can be estimated using either the fundamental component of the BEMF or injecting a pulsating  $d$ -axis high frequency current signal and measuring the  $d$ -axis high frequency resistance. The differential PM temperature is estimated using higher order harmonics of the BEMF. The method is applicable to IPMSMs; extension of the method to SPMSMs or other machine designs has not been evaluated yet.

The principles of the method as well as simulation and experimental results have been presented to demonstrate its viability.

Finally, in order to validate the PM temperature distribution estimation method, a wireless PM temperature measurement system has been developed, see Appendix B. The system was used in the IPM machine shown in Table 2.3, placing a flexible thin film PCB under each machine pole, including an array of 3 by 5 sensors, i.e. 15 measurement points per magnet. The wireless measurement system is battery powered, which allows the measurement at any rotor speed or load.

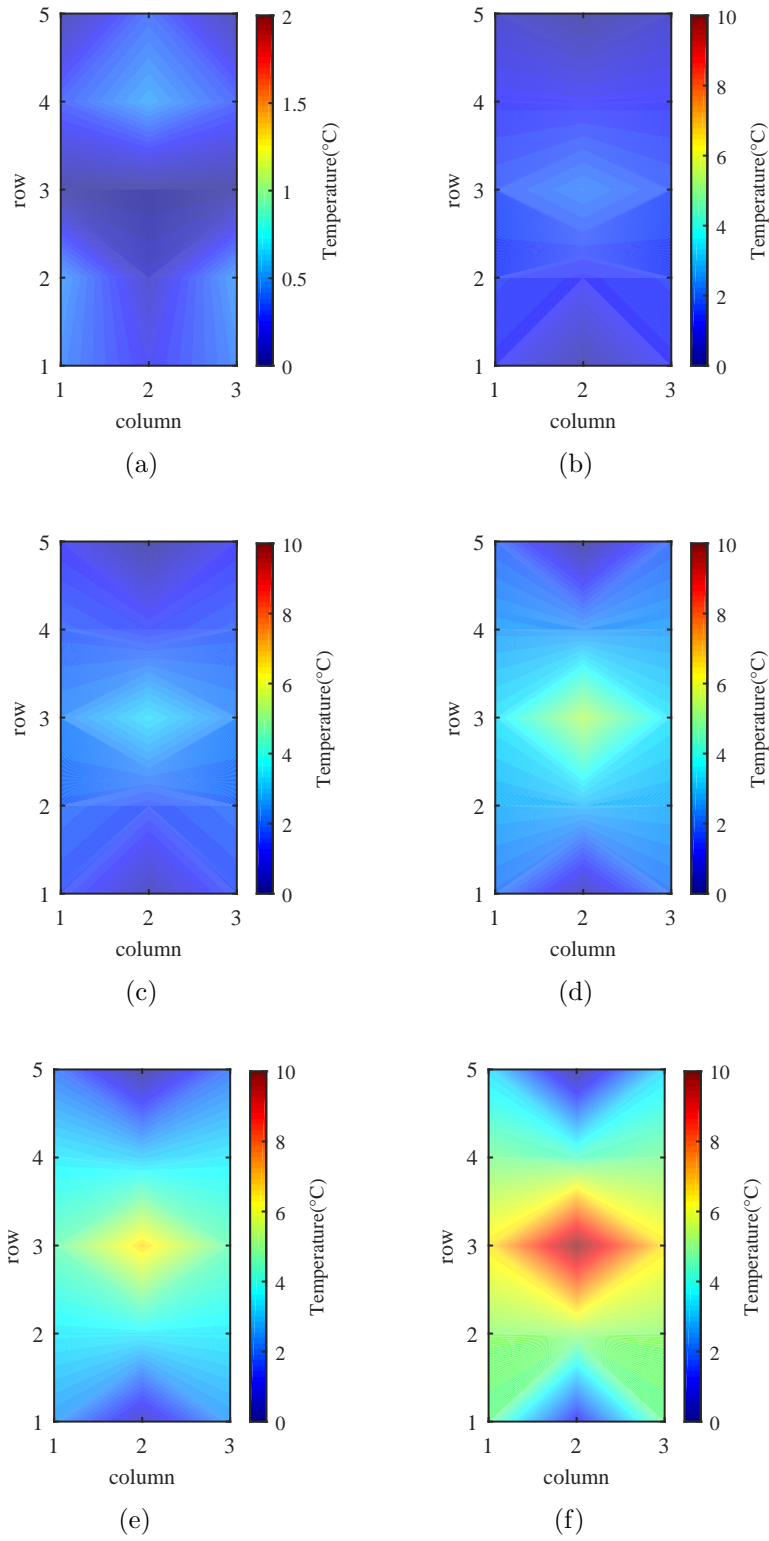


Figure 2.30: Temperature estimation error for the same experimental results that are shown in Fig. 2.22 and 2.23.



## Chapter 3

# Influence of Stator Configuration and Machine Assembling Tolerances On High Frequency Signal Injection Based Permanent Magnet Temperature Estimation Based Methods

### 3.1 Introduction

It has been shown in the previous chapter that the injection of a high frequency signal in the stator via inverter has been proven to be a viable option to estimate the magnet temperature in PMSMs. Among proposed injection signals (rotating voltage, pulsating  $d$ -axis current, pulsating  $d$ -axis voltage combined with  $q$ -axis current cancellation), pulsating  $d$ -axis current is especially appealing, as it is insensitive to the speed,  $L_d$  and  $L_q$  inductance variations. Furthermore, it is suitable both for IPMSMs and SPMSMs.

Regardless of high frequency signal injection temperature estimation based methods promising characteristics, there are a number of issues which can reduce its accuracy, including stator and rotor designs, slots/pole combination,

magnet shape and volume, assembling tolerances (e.g. static, dynamic and mixed eccentricities, magnet assembling tolerances...), stator/rotor lamination grain orientation, sensitivity to rotor eccentricities, PM assembling tolerances and lamination grain orientation.

This section analyzes the sensitivity of temperature estimation methods using pulsating  $d$ -axis high frequency current injection to: rotor eccentricities, PM assembling tolerances, lamination grain orientation, stator configuration and slot/pole (s/p) combination. Preliminary results show that these issues can have a relevant impact on the performance of high frequency signal injection based methods.

## 3.2 Sensitivity of High Frequency Signal Injection Based Temperature Estimation Methods to Machine Assembling Tolerances

The estimated rotor temperature  $T_r$ , obtained with high frequency signal based methods, is a lumped temperature, i.e. it provides an estimation of the average magnets temperature but does not contain information on temperature asymmetries among poles. Such asymmetries could be due to several reasons: stator/rotor lamination grain orientation; asymmetries in the reluctance paths, e.g. due to eccentricities; or magnet assembling tolerances. The following subsections will analyze the effect of all these issues on the accuracy of the method.

### 3.2.1 Effects of the eccentricity in the estimated PM temperature

Eccentricities produce a non-uniform airgap between stator and rotor. Eccentricities can be static, dynamic and mixed. In the static eccentricity case, the rotor turns around its own rotation axis, which is misaligned from the stator axis of symmetry (see Fig. 3.1(b)). Therefore, the location of the minimum airgap is fixed. The static eccentricity is typically caused by stator core ovality or incorrect positioning of the stator and/or rotor during the assembling stage. With the dynamic eccentricity, the stator axis of symmetry coincides with the rotor rotational axis (see Fig. 3.1(c)), but misaligned with the rotor axis of symmetry. The dynamic eccentricity is typically caused by

bent shafts or bearing wear. Both types of eccentricities, static and dynamic, can coexist in practice, being named mixed eccentricity (see Fig. 3.1(d)), [65, 66].

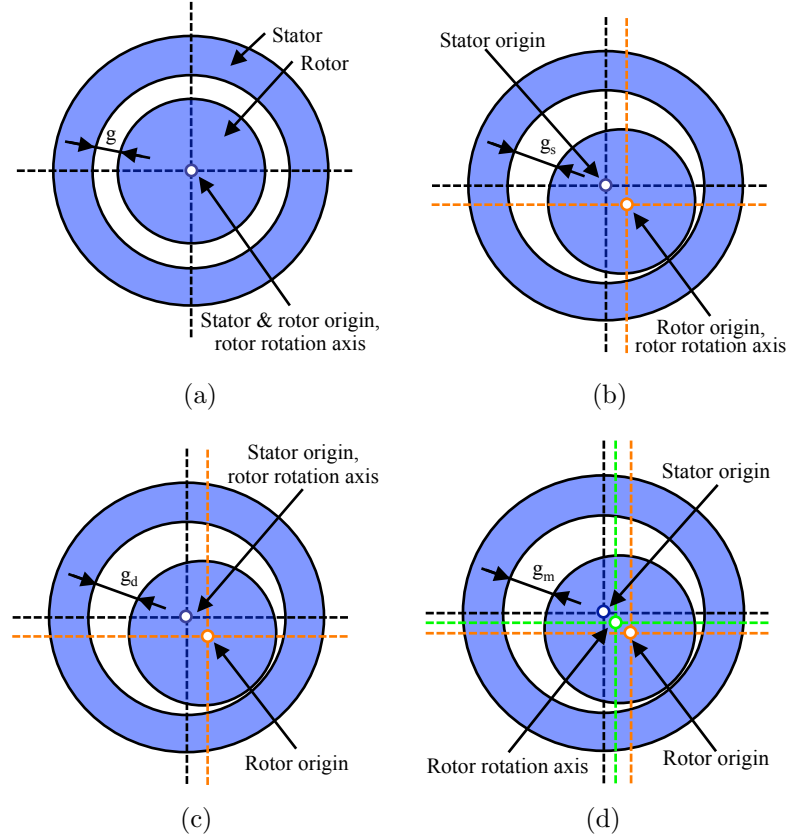


Figure 3.1: Schematic representation of different types of eccentricities.

Fig. 2.14 shows the machine design that will be used to evaluate the eccentricities in this subsection, as well as assembling tolerances and the effects of lamination grain orientation. FEA will be used for this purpose. It has 6 poles, 36 slots, the design parameters can be found in Table 2.3. The rated machine airgap is 0.8mm.

### 3.2.1.1 Static Eccentricity

Four levels of static eccentricities have been simulated: 0, 0.2 mm, 0.4 mm and 0.6 mm, which corresponds to  $\Delta_s=0, 0.25, 0.5$  and  $0.75$ , with  $\Delta_s$  being the static eccentricity in pu of the nominal airgap. Fig. 3.2 shows the

estimated  $d$ -axis high frequency resistance (see 2.34) for different levels of static eccentricity. Fig. 3.3 shows the FFT of the estimated  $d$ -axis high frequency resistance in Fig. 3.2 (note the logarithmic scale for the magnitude). Two components of interest are highlighted in Fig. 3.3: DC component and component at  $\omega_r$ .

- DC component: represents the mean value of the magnet high frequency resistance. This component is used for temperature estimation (see (2.34)). It is observed that the estimated high frequency resistance magnitude decreases as the eccentricity increases (see 3.2). If no compensation is introduced, this would produce therefore an error in the estimated temperature.
- Component at  $\omega_r$ : its magnitude increases as the eccentricity does; its magnitude is zero when there is no eccentricity. This component can potentially be used both to decouple the eccentricity effect from the estimated high frequency resistance (DC component in Fig. 3.2 and 3.3) and to estimate the static eccentricity degree (diagnostic purposes).

Fig. 3.4(a) and Fig. 3.4(b) show the magnitude of the DC component and  $\omega_r$  component of the estimated high frequency resistance respectively, as a function of the static eccentricity. It is observed that the estimated DC component decreases as the eccentricity increases. On the contrary, the component at  $\omega_r$  increases with the eccentricity.

Compensation of the static eccentricity effect was implemented using (3.1), where  $R_{pcDC}$  and  $R_{pcDC(\Delta_s)}$  are the DC component of the estimated high frequency resistance before and after static eccentricity effect compensation respectively,  $R_{pc1\omega_r}$  is the component at  $\omega_r$  of the estimated high frequency resistance and  $k_{\Delta_s}$  is an static eccentricity constant, experimentally adjusted to be  $k_{\Delta_s} = 4.03$ .

Fig. 3.4(a) also shows the estimated magnet resistance after compensating the static eccentricity effect using (3.1). It is observed that the estimated magnet resistance after compensation is practically insensitive to the static eccentricity, thus making the temperature estimation insensitive to it.

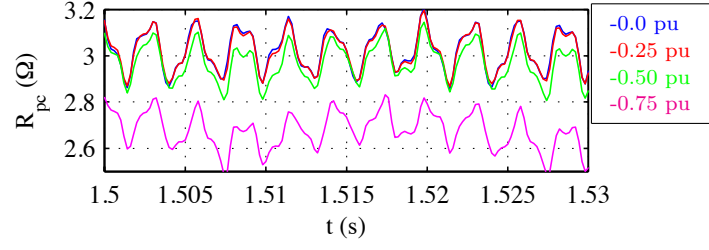


Figure 3.2: Estimated  $d$ -axis high frequency resistance for eccentricities of 0, 0.25, 0.5 and 0.75 pu.  $I_{dq}=0$  A,  $\omega_r=2\pi 90$  Hz,  $\omega_{hf}=2\pi 250$  Hz.

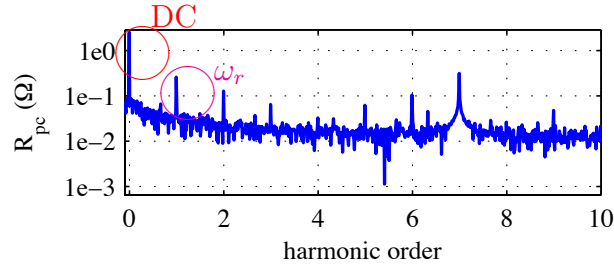
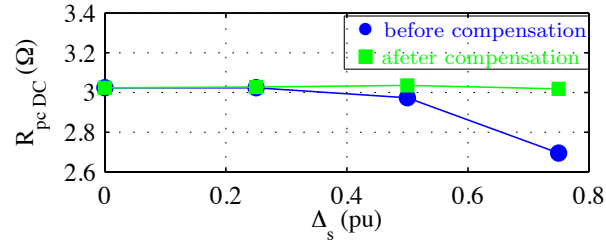
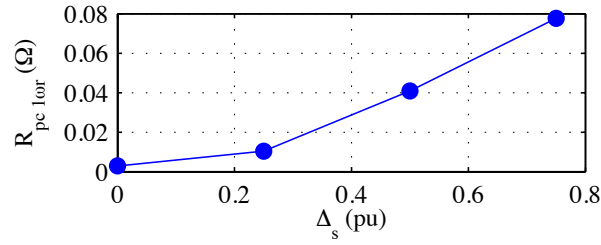


Figure 3.3: FFT of the estimated  $d$ -axis high frequency resistance for eccentricity 0.75pu.  $I_{dq}=0$  A,  $\omega_r=2\pi 90$  Hz,  $\omega_{hf}=2\pi 250$  Hz.



(a)



(b)

Figure 3.4: a) DC component before and after static eccentricity compensation and b) component at  $\omega_r$  of the estimated  $d$ -axis high frequency resistance.  $I_{dq}=0$  A,  $\omega_r=2\pi 90$  Hz,  $\omega_{hf}=2\pi 250$  Hz.

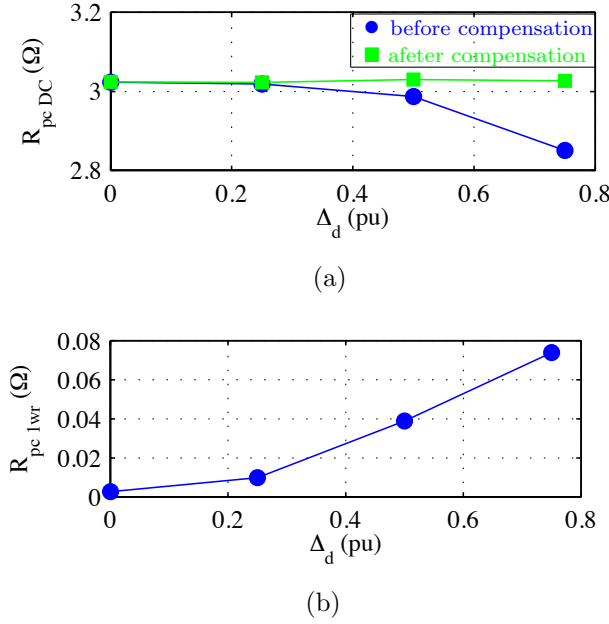


Figure 3.5: a) DC component before and after dynamic eccentricity compensation and b) component at  $\omega_r$  of the estimated  $d$ -axis high frequency resistance.  $I_{dq}=0$  A,  $\omega_r=2\pi 90$  Hz,  $\omega_{hf}=2\pi 250$  Hz.

$$R_{pcDC}(\Delta_s) = R_{pcDC} + R_{pc1\omega_r} * k_{\Delta_s} \quad (3.1)$$

### 3.2.1.2 Dynamic Eccentricity

The same four levels as for the static eccentricity have been used for the dynamic eccentricity.

Fig. 3.5 shows the magnitude of the DC component (see Fig. 3.5(a)) and the magnitude of the component at  $\omega_r$  (see Fig. 3.5(b)) of the high frequency resistance as a function of the dynamic eccentricity. It is observed that the estimated high frequency resistance magnitude decreases as the eccentricity increases, while the magnitude of the component at  $\omega_r$  increases with the dynamic eccentricity. Similar to the static eccentricity case, the dynamic eccentricity effect is compensated using (3.2), where  $R_{pcDC}(\Delta_d)$  is the DC component of the estimated high frequency resistance after dynamic eccentricity

compensation and  $k_{\Delta_d}$  is the dynamic eccentricity constant,  $k_{\Delta_d} = 3.07$ .

$$R_{pcDC(\Delta_d)} = R_{pcDC} + R_{pc1\omega_r} * k_{\Delta_d} \quad (3.2)$$

Fig. 3.5(a) also shows the estimated magnet resistance after compensation of the dynamic eccentricity effect on the magnet high frequency resistance using the measured component at  $\omega_r$ . Similarly to the static eccentricity case, the estimated magnet resistance after compensation is practically insensitive to it.

### 3.2.1.3 Mixed Eccentricity

Finally, as for the static and dynamic eccentricities, four levels of mixed eccentricities have been simulated, mixed eccentricities levels being obtained by a combination of four static and dynamic eccentricities degrees; the eccentricity degrees that have been simulated are shown in Table 3.1. Both static,  $k_{\Delta_s}$ , and dynamic,  $k_{\Delta_d}$ , eccentricities being set to the same value, i.e. 0, 0.125, 0.25 and 0.375 pu, which in pu corresponds to =0, 0.25, 0.5 and 0.75, with  $k_{\Delta_m}$  being the mixed eccentricity in pu. Fig. 3.6 schematically shows how the static and dynamic eccentricities were combined.

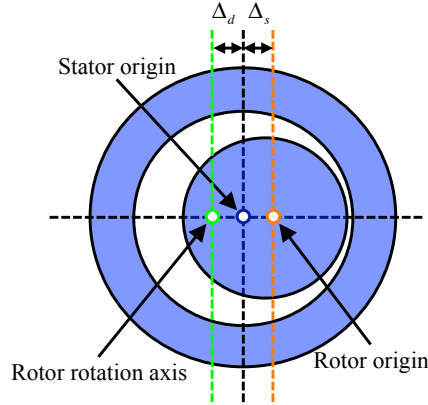


Figure 3.6: Mixed eccentricity simulation.

Fig. 3.7 shows the simulation results for the mixed eccentricity case. As expected, they are a combination of the results of the static and dynamic eccentricities cases shown in Fig. 3.4 and Fig. 3.5 respectively.

Table 3.1: Degree of eccentricity

Static eccentricity ( $\Delta_s$ )	Dynamic eccentricity ( $\Delta_d$ )	Mixed eccentricity ( $\Delta_m$ )
0.0	0.0	0.0
0.125	0.125	0.25
0.250	0.250	0.5
0.375	0.375	0.75

As for the static and dynamic eccentricities cases, the component at  $\omega_r$  can be used to decouple the mixed eccentricity effect on the estimated magnet high frequency resistance making the temperature estimation method insensitivity to the machine mixed eccentricity. The mixed eccentricity effect is decoupled by (3.3), where  $R_{pcDC(\Delta_m)}$  is the DC component of the estimated high frequency resistance after mixed eccentricity effect compensation and  $k_{\Delta_m}$  is the mixed eccentricity constant,  $k_{\Delta_m}=3.79$ .

$$R_{pcDC(\Delta_m)} = R_{pcDC} + R_{pc1\omega_r} * k_{\Delta_m} \quad (3.3)$$

### 3.2.2 Lamination grain orientation effects on the estimated PM temperature

Stator and rotor lamination steel can be non-grain-oriented (i.e. made without special processing to control crystal orientation) or grain-oriented. In non-grain-oriented laminated steel, the magnetic properties are similar in all directions, both for stator and rotor; since it is an isotropic material, losses and consequently temperature, are uniformly distributed.

In grain-oriented steel, the desired magnetic properties are obtained in the rolling direction, usually called *easy-magnetization axis* [67, 68, 69]. The orthogonal axis, usually called *hard-magnetization axis* [68], has a slightly worse magnetic properties than the *easy-axis* (see Fig. 3.8). Differences in the magnetic properties between *hard-* and *easy-axes* result in reduced losses in the *easy-axis* (20-45%) compared to the *hard-axis* [67, 68, 69]. This can produce asymmetries in the rotor lamination temperature along the *hard-* and *easy-axes*. This is graphically illustrated in see Fig. 3.8(b).

A thermal model of the machine using FEA has been used to evaluate the effect of the lamination grain orientation on the temperature distribution. Fig. 3.8 shows the schematic design of the machine. It is the same



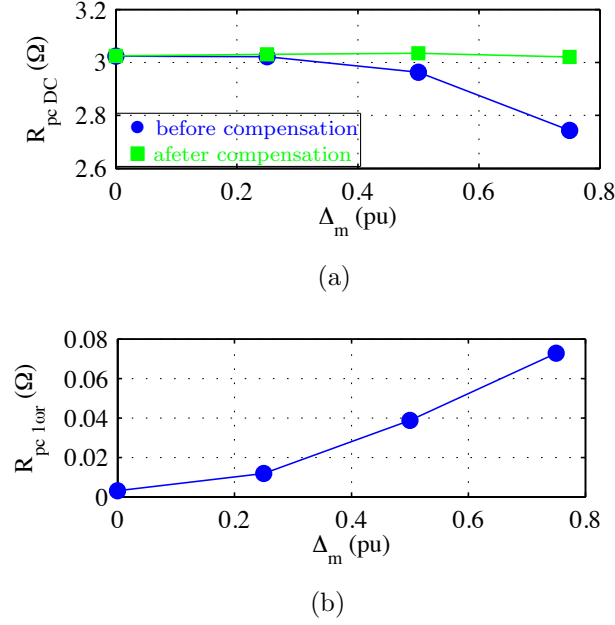


Figure 3.7: a) DC component before and after mixed eccentricity compensation and b) component at  $\omega_r$  of the estimated  $d$ -axis high frequency resistance.  $I_{dq}=0$  A,  $\omega_r=2\pi 90$  Hz,  $\omega_{hf}=2\pi 250$  Hz.

machine design as in Fig. 2.14, three different cases have been considered. Case #1 corresponds to a non-grain-oriented design, while cases #2 and #3 corresponds to a grain oriented design, with a loss reduction in the easy axis of 15% and 25% respectively. Table 3.2 shows, for each case, the resulting PM temperature for magnets 1 to 6, as well as the mean temperature of the six PMs.

Table 3.2: Resulting PM temperature

Case	PM Temperature ( $^{\circ}\text{C}$ )		
	PM 1 & 4	PM 2, 3, 5 & 6	$T_{mean}$ (3.1)
#1	100	100	100
#2	98.7	89.5	92.56
#3	96.3	85.3	88.97

Fig. 3.9 shows the estimated  $d$ -axis high frequency resistance as a function of the mean temperature of the six PMs. It is observed that there is an almost linear relationship between the estimated  $d$ -axis high frequency

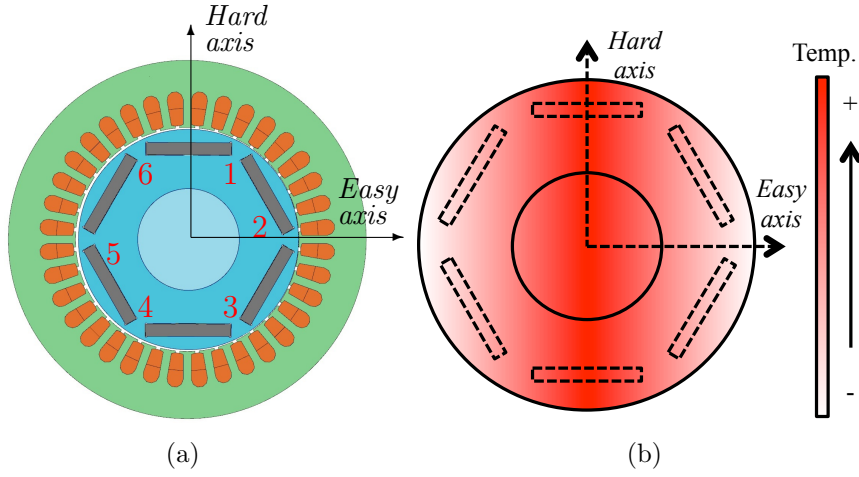


Figure 3.8: a), Schematic machine rotor design, showing the *easy* and *hard-axes* and b), schematic rotor temperature distribution due to lamination grain orientation.

resistance and the mean temperature of the PMs. These simulation results confirm that the pulsating  $d$ -axis high frequency current injection method effectively measures the average temperature, but do not allow to detect temperature asymmetries among the PMs. Consequently, lamination grain orientation will induce errors in the estimated temperature that need to be considered.

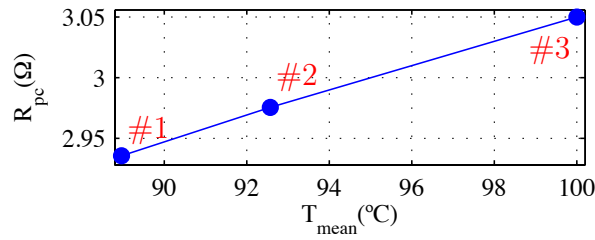


Figure 3.9: Estimated  $d$ -axis high frequency resistance vs. average temperature of the six PMs for the three cases shown in Table 3.2.  $\omega_r=2\pi 90$  Hz,  $I_{hf}=0.01$  pu,  $\omega_{hf}=2\pi 250$  Hz.

### 3.2.3 Effects of the PM assembling tolerances on the estimated PM temperature

The effects due to assembling tolerances in the process for mounting the PMs in the rotor have also been analyzed. Fig. 3.10 shows the ideal PM location, with the PM centered in the rotor cavity, and the location of the magnet when it is shifted by an amount of  $\Delta x$  and  $\Delta y$  from the ideal location. The maximum value of  $\Delta x$  and  $\Delta y$  is 0.2mm, which corresponds to the PM assembling tolerance.

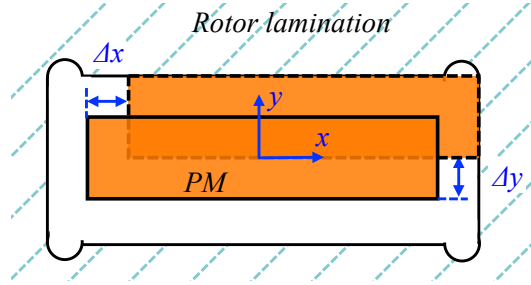


Figure 3.10: Schematic representation of the PM placement.

Fig. 3.11 shows the estimated magnet high frequency resistance estimated using pulsating  $d$ -axis high frequency current injection for the values of  $\Delta x$  and  $\Delta y$  shown in Table 3.3. It is observed that the magnet assembling tolerances produce a very small variation of the high frequency resistance ( $<0.01\Omega$ ), which can be considered negligible compared with the effects of the other effects previously discussed. It is therefore concluded that PM assembling tolerances have an almost negligible impact on the estimated magnet temperature.

Table 3.3: Case of study for different magnet position

	Case								
	#1	#2	#3	#4	#5	#6	#7	#8	#9
$\Delta x$ (mm)	0	0.2	-0.2	0	0	-0.2	0.2	0.2	-0.2
$\Delta y$ (mm)	0	0	0	0.2	-0.2	0.2	0.2	-0.2	-0.2

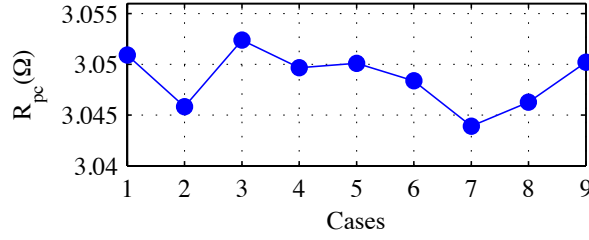


Figure 3.11: Estimated  $d$ -axis high frequency resistance for different magnet position.  $\omega_r=2\pi 90$  Hz,  $I_{hf}=0.01$  pu,  $\omega_{hf}=2\pi 250$  Hz.

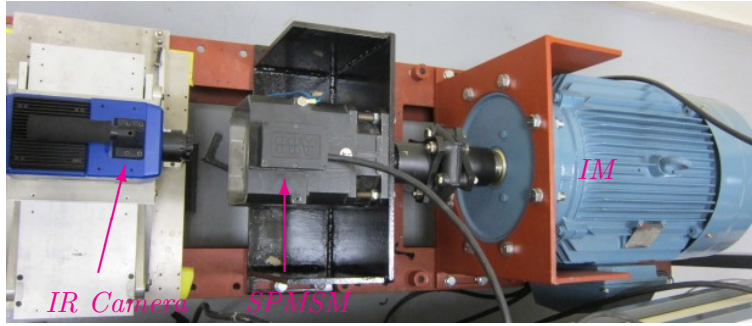


Figure 3.12: Experimental test bench, PMSM and load machine (IM).

### 3.2.4 Experimental results

Fig. 3.12 shows the test bench that will be used for the experimental verification. Parameters of the PMSM are shown in Table 2.3.

#### 3.2.4.1 Dynamic eccentricity

To create the dynamic eccentricity, a mass is attached to the rotor to produce an asymmetry (see Fig. 3.13), the resulting centrifugal forces being (3.4), where  $m$  is the weight and  $r$  is the rotor radius.

$$F_c = m\omega_r^2 r \quad (3.4)$$

Three different weights of 30, 61 and 93 g., have been used. When the machine rotates at  $\omega_r=1$ pu, they produce a dynamic eccentricity of 0.04 mm, 0.2 mm and 0.35 mm, which in pu corresponds to = 0.05, 0.26 and 0.44 respectively.

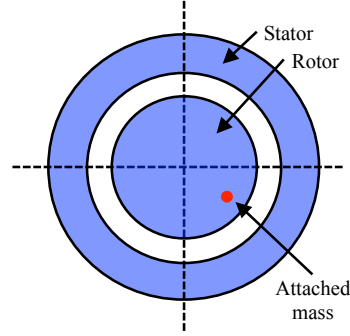


Figure 3.13: Attached mass for dynamic eccentricity.

The dynamic eccentricity has been measured by using an infrared camera (see Fig. 3.12), with an image resolution of 320x256 pixels, 0.056 mm/pixel and 380 frames/s. A circular window of diameter 12 mm was drilled in the end frame, the airgap being visually accessible (Fig. 3.14(a)). Fig. 3.14(b) shows a thermal image obtained with the camera, while Fig. 3.14(c) shows a schematic representation of the image.

Fig. 3.15 shows the FFT of the estimated  $d$ -axis high frequency resistance for  $\Delta=0.44\text{pu}$  (note the logarithmic scale for the magnitude). The same two components of interest as predicted by FEA, see Fig. 3.3, are observed: DC component (i.e. mean value of the magnet high frequency resistance) and component at  $\omega_r$  (i.e. indicates the eccentricity degree).

Fig. 3.16 shows the magnitude of the DC component and  $\omega_r$  component of the estimated high frequency resistance as a function of the dynamic eccentricity respectively; the estimated high frequency resistance magnitude decreases as the eccentricity increases, while the magnitude of the component at  $\omega_r$  increases with the eccentricity, which is consistent with FEA results. As in FEA the dynamic eccentricity effect is decoupled by (3.2), the dynamic eccentricity constant,  $\Delta_d=6.83$ , being slightly different from FEA result; this difference could be induced by modeling inaccuracies. This issue is under ongoing investigation. It is observed from Fig. 3.16(a) that the estimated magnet resistance after compensation is practically insensitive to the dynamic eccentricity, thus making the temperature estimation insensitive to it.

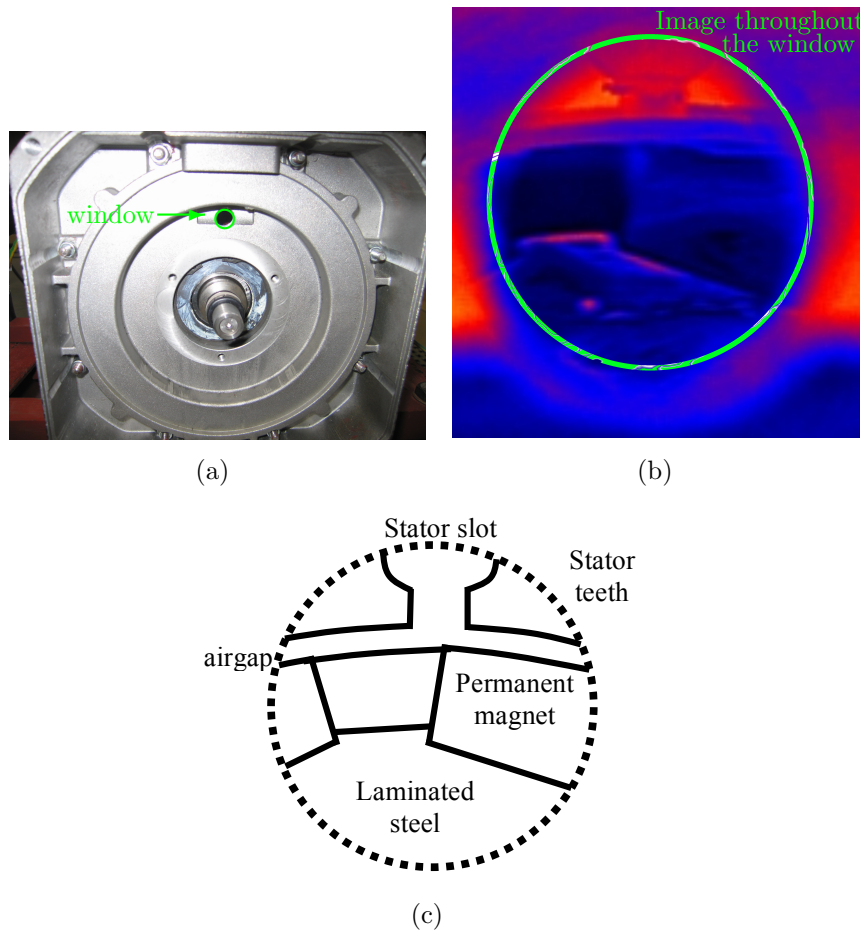


Figure 3.14: a) end shield, b) thermal image of the rotor, c) schematic representation of the thermal image

### 3.3 Influence of Stator Configuration on High Frequency Signal Injection Based Permanent Magnet Temperature Estimation Methods in PMSMs

Another potential concern for high frequency signal injection based methods is their sensitivity to different machine configurations. Stator and rotor designs, slots/pole combination or winding configuration could affect to the sensitivity to PM temperature estimation based methods.

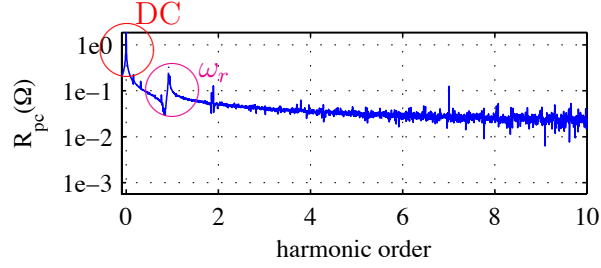


Figure 3.15: Attached mass for dynamic eccentricity.

This section analyzes the influence of the stator design, slot/pole combination and coil pitch factor on the sensitivity of high frequency signal injection based temperature estimation methods.

Most common stator configurations and slots/pole combinations in traction and general purpose applications will be analyzed. For the analysis being presented in this section, all machine designs will have the same dimensions and rated power. The objective of this analysis is to provide guidelines for the design of PMSM suitable for the implementation of high frequency signal based temperature estimation techniques.

Fig. 3.17 shows the four rotor topologies that will be considered, with 6, 8, 10 and 16 pole. For each rotor design, distributed winding with different coil pitch and concentrated winding configurations will be evaluated. Table 3.4 summarizes the designs being considered. Stator and rotor lamination materials and magnet material are the same in all the cases. The distance between the center of the magnet and the gap is also kept constant, meaning that the reluctance paths are similar for all designs. Magnet thickness is also the same for all models, skin effect being therefor similar [70]. Magnet volume also remains invariant.

Table 3.5 shows the main characteristics of all machines designs including  $d$  and  $q$ -axis inductances, average gap flux density, number of turn, voltage constant and torque constant. It is noted that some of the machines included in Table 3.5 with low coil pitch (i.e. 18/6(1), 36/6(1), 36/6(2), 60/10(1), 60/10(2)...) might not be viable in practice due to their low efficiency. Nevertheless, they have been included for the sake of completeness of the analysis.

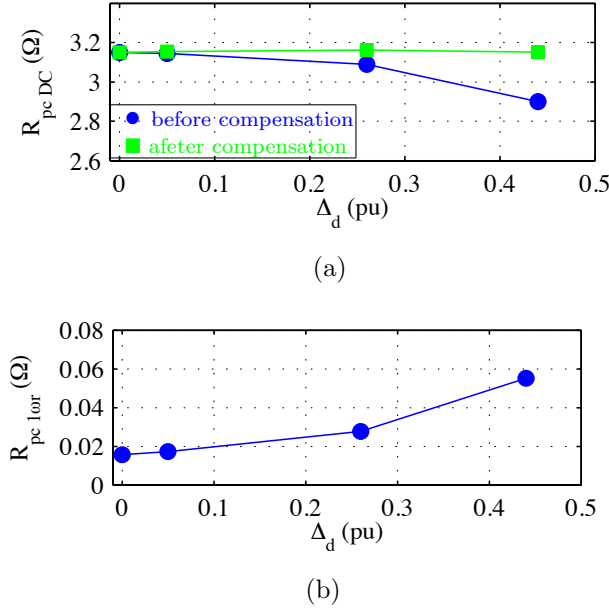


Figure 3.16: a) DC component before and after dynamic eccentricity compensation and b) component at  $\omega_r$  of the estimated  $d$ -axis high frequency resistance.  $Idq=0$  A,  $\omega_r=2\pi 90$  Hz,  $\omega_{hf}=2\pi 250$  Hz.

### 3.3.1 FEA Results

The effects of the stator configuration and stator/slot combination on the sensitivity of high frequency signal injection based temperature estimation methods are analyzed in this section. For the simulation results that are shown in this chapter a magnitude of 1A (0.05 pu) will be used for both rotating and pulsating injections, 20A being the rated current of all machines. FEA will be used for this purpose. Although experimental results are not included in this thesis due to the unaffordable fabrication cost for all configurations being evaluated, FEA has been demonstrated to provide accurate estimation [71].

Fig. 3.18 shows the FEA results for all configurations of the 36/6 machine, see Table 3.4. Fig. 3.18 shows the  $d$ -axis high frequency resistance vs. magnet temperature obtained using rotating and pulsating signal injection. Three different PM temperatures of 20, 60 and 80 °C, and two different frequencies for the injected high frequency signal are considered.

It is observed from Fig. 3.18 that the estimated high frequency resistance increases as both magnet temperature and frequency do. It is also observed



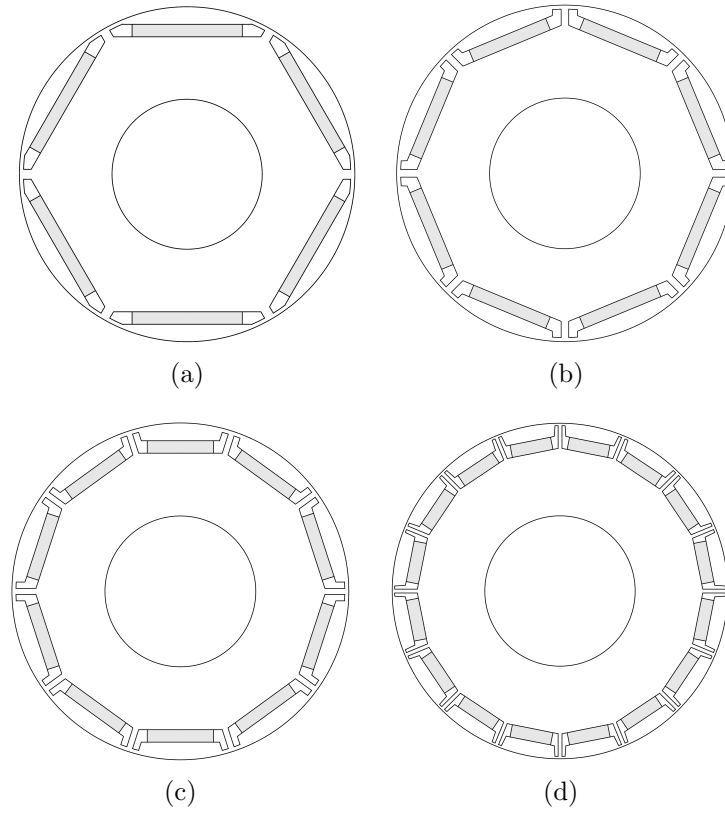


Figure 3.17: Cross section of the studied rotors: a) 6 poles, b) 8 poles, c) 10 poles and d) 16 poles rotor.

Table 3.4: Machine dimensions and possible configurations

Dimensions		Machine	Feasible Coil Pitch (s/p)
Outer Diameter (mm)	112	9/6	1
Rotor Diameter (mm)	67	9/8	1
Airgap (mm)	0.5	12/8	1
Stack length (mm)	40	9/10	1
Magnet Thickness (mm)	2.5	30/10	1, 2, 3
Magnet Volume (mm <sup>2</sup> )	2200	24/16	1
Distance from the center of the magnet to the rotor surface (mm)	27.5	18/6	1, 2, 3
		36/6	1, 2, 3, 4, 5, 6
		48/8	1, 2, 3, 4, 5, 6
		60/10	1, 2, 3, 4, 5, 6

Table 3.5: Rated machien parameters

Slot/pole (coil pitch)	Ld (mH)	Lq (mH)	Bgap (T)	N	Kt (Nm/A)	Kv (Vs/rad)
9/6(1)	28.9	24.5	0.649	149	1.313	1.506
9/8(1)	29.2	24.6	0.700	140	1.307	1.501
12/8	24.4	20.9	0.637	118	1.314	1.502
9/10(1)	33.6	27.8	0.678	150	1.312	1.518
30/10(1)	26.6	25.2	0.905	96	1.308	1.515
24/16(1)	22.4	18.2	0.557	79	1.309	1.509
18/6(1)	30.5	20.3	0.841	132	1.314	1.510
18/6(2)	20.3	20.7	0.650	66	1.307	1.508
18/6(3)	22.2	22.1	0.845	56	1.314	1.505
36/6(1)	32.7	27.3	0.857	128	1.305	1.508
36/6(2)	23.6	24.3	0.801	64	1.309	1.508
36/6(3)	21.0	22.3	0.824	43	1.316	1.522
36/6(4)	20.0	21.9	0.787	34	1.310	1.520
36/6(5)	19.4	21.4	0.848	30	1.315	1.519
36/6(6)	18.3	20.7	0.813	28	1.314	1.514
48/8(1)	28.1	23.2	0.788	109	1.307	1.509
48/8(2)	23.4	21.2	0.749	55	1.313	1.519
48/8(3)	20.7	19.4	0.756	36	1.308	1.495
48/8(4)	19.4	18.5	0.745	28	1.309	1.526
48/8(5)	17.4	17.7	0.783	24	1.316	1.504
48/8(6)	17.0	17.1	0.730	23	1.308	1.555
60/10(1)	27.1	24.6	0.868	94	1.312	1.500
60/10(2)	22.9	22.6	0.853	47	1.316	1.508
60/10(3)	21.0	20.7	0.814	31	1.308	1.496
60/10(4)	19.0	19.7	0.846	24	1.317	1.513
60/10(5)	17.9	18.9	0.845	21	1.309	1.523
60/10(6)	15.6	17.3	0.822	19	1.314	1.482

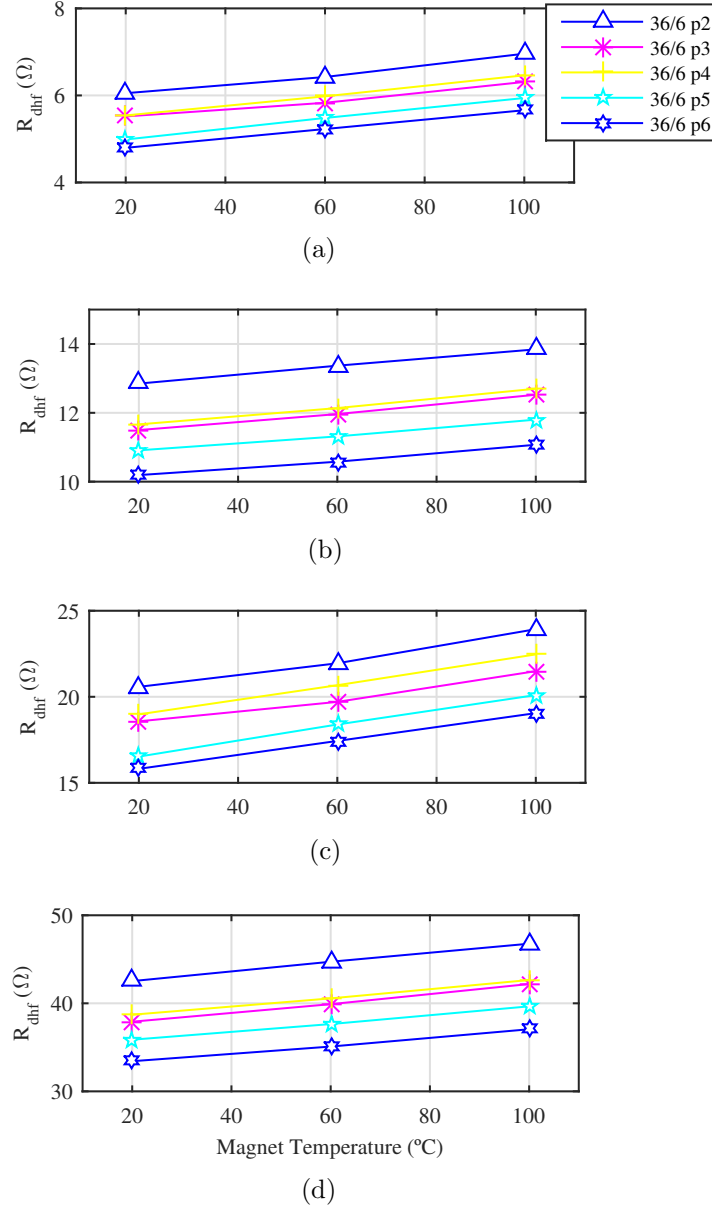


Figure 3.18: Estimated high frequency resistance vs. magnet temperature of a 36/6 machine for different types of high frequency excitation, a),  $d$ -axis pulsating (250Hz), b), Rotating (250Hz) c),  $d$ -axis pulsating (500Hz), d), rotating (500Hz) and for five different coil pitch.  $I_{hf}=1\text{A}$  (0.05pu),  $I_{dq}=0\text{A}$ .

Table 3.6:  $R_{dhf}$  calculated using pulsating  $d$ -axis high frequency current (0.05 pu)

High frequency resistance, $R_{dhf}$ ( $\Omega$ ) for PM temperature 20°C								R <sub>hf</sub> at 20°C
f <sub>hf</sub> (Hz)	s/p	Pitch 6	Pitch 5	Pitch 4	Pitch 3	Pitch 2	Pitch 1	
250	9/6						8.934	
	9/8						10.908	
	9/10						8.544	
	12/10						13.62	
	30/10						19.590	
	24/16						13.077	
	18/6				5.541	5.729	7.335	
	36/6	4.796	4.988	5.546	5.567	6.051	7.595	
	48/8	6.211	6.041	7.076	8.923	14.340	17.250	
	60/10	6.522	7.403	8.349	10.670	17.090	45.250	
500	9/6						32.162	
	9/8						39.765	
	9/10						30.661	
	12/10						50.260	
	30/10						45.81	
	24/16						40.002	
	18/6				18.681	19.361	25.418	
	36/6	15.812	16.538	18.987	18.574	20.578	26.556	
	48/8	18.122	17.474	19.897	23.087	30.987	41.179	
	60/10	19.131	21.32	23.309	27.270	36.200	74.58	

that rotating high frequency excitation typically shows higher high frequency resistances compared to pulsating excitation. This is because pulsating vector rotates synchronously with the rotor, meaning that the induced field interacts always with the same part of the rotor, typically the center of the magnet. For all IPMSMs designs that have been evaluated, this corresponds to the maximum airgap, and therefore to the maximum reluctance path. On the contrary, rotating excitation excites the entire magnet surface, the reluctance being an average of the whole machine circumference.

Instead of representing the high frequency resistance as a function of the magnet temperature, it was found more insightful to represent the  $d$ -axis high frequency resistance at 20°C,  $R_{dhf}$ , and the rate of variation of  $R_{dhf}$  with the magnet temperature, i.e.  $R_{dhf}$  sensitivity the magnet temperature (3.5).

$$\alpha_{mag} = \frac{\partial R_{drhf}(T_r)}{\partial T_r} \quad (3.5)$$

Tables 3.6 to 3.9 summarizes the FEA results for all machine topologies in Table 3.5. A color code is used to represent the goodness of each design. Dark



Table 3.7:  $R_{dhf}$  calculated using rotating high frequency current (0.05 pu)

High frequency resistance, $R_{dhf}$ ( $\Omega$ ) for PM temperature 20°C								$R_{dhf}$ at 20°C
$f_{hf}$ (Hz)	s/p	Pitch 6	Pitch 5	Pitch 4	Pitch 3	Pitch 2	Pitch 1	
250	9/6						10.932	Low
	9/8						11.421	
	9/10						10.692	
	12/10						13.325	
	30/10						23.435	
	24/16						14.070	
	18/6				10.791	11.162	14.727	
	36/6	10.191	10.912	11.665	11.501	12.856	18.102	
	48/8	9.561	8.938	10.259	12.352	18.341	20.879	
	60/10	8.734	9.862	10.951	13.578	20.378	48.508	
500	9/6						40.807	Low
	9/8						42.181	
	9/10						39.655	
	12/10						49.62	
	30/10						61.17	
	24/16						44.31	
	18/6				35.350	36.670	48.951	
	36/6	33.435	35.874	38.751	37.917	42.524	50.226	
	48/8	30.86	29.01	32.632	36.780	47.031	55.921	
	60/10	27.589	31.125	33.71	38.847	49.23	87.65	

Table 3.8:  $\alpha_{mag}$  calculated using pulsating  $d$ -axis high frequency current (0.05 pu)

Stator-reflected high frequency resistance sensitivity $\alpha$ (1/K)								Sensitivity
$f_{hf}$ (Hz)	s/p	Pitch 6	Pitch 5	Pitch 4	Pitch 3	Pitch 2	Pitch 1	
250	9/6						1.441	High
	9/8						0.779	
	9/10						0.9815	
	12/10						0.684	
	30/10						0.037	
	24/16						0.045	
	18/6				1.481	1.437	1.886	
	36/6	1.731	2.388	2.08	1.793	1.873	1.651	
	48/8	1.563	1.532	1.422	1.255	0.864	1.035	
	60/10	1.322	1.332	1.307	1.214	0.821	0.948	
500	9/6						1.501	High
	9/8						1.053	
	9/10						1.241	
	12/10						0.808	
	30/10						0.132	
	24/16						0.112	
	18/6				1.643	1.594	2.049	
	36/6	1.929	2.703	2.223	1.961	2.035	1.656	
	48/8	2.047	2.038	1.942	1.87	1.534	1.665	
	60/10	1.822	1.897	1.789	1.706	1.664	1.575	

Table 3.9:  $\alpha_{mag}$  calculated using rotating high frequency current (0.05 pu)

Stator-reflected high frequency resistance sensitivity $\alpha$ (1/K)								Sensitivity
$f_{hf}$ (Hz)	s/p	Pitch 6	Pitch 5	Pitch 4	Pitch 3	Pitch 2	Pitch 1	
250	9/6						1.451	High  Low
	9/8						0.993	
	9/10						1.219	
	12/10						0.768	
	30/10						0.089	
	24/16						0.298	
	18/6				1.1591	1.304	1.404	
	36/6	1.08	1.021	1.111	1.115	0.967	0.842	
	48/8	1.281	1.369	1.253	1.151	0.867	0.994	
	60/10	1.112	1.186	1.098	1.010	0.989	0.948	
500	9/6						1.548	High  Low
	9/8						0.822	
	9/10						1.054	
	12/10						0.717	
	30/10						0.063	
	24/16						0.057	
	18/6				1.247	1.413	1.526	
	36/6	1.357	1.325	1.273	1.411	1.248	1.112	
	48/8	1.484	1.59	1.479	1.468	1.282	1.424	
	60/10	1.402	1.51	1.387	1.349	1.256	1.297	

green is used to represent the most favorable cases, i.e. highest sensitivity and lowest resistance at 20°C, dark red is used for the least favorable cases, i.e. lowest sensitivity and highest resistance at 20°C.

It observed from Tables 3.8 and 3.9 that  $R_{dhf}$  sensitivity to the magnet temperature is not the same in all configurations. For the use of high frequency signal injection temperature estimation based techniques, the higher is the sensitivity of  $R_{dhf}$  to the magnet temperature, the more adequate is the design. Moreover, low  $R_{dhf}$  magnitude at 20°C would be the preferred cases, as  $R_{dhf}$  is a reliable indicator of the magnet losses, i.e.  $R_{dhf}$  is proportional to the magnet losses (machines with high sensitivity and low magnet losses would be preferred).

Among all analyzed topologies, fractional integer (36/6, 48/8 and 60/10) and integer slot machines (18/6), are the most favorable cases as they show the highest sensitivity. Only for these slot/pole arrangements, every rotor pole matches the stator coil center as shown in Fig 3.19. It can be also observed from Table 3.8 that in all the cases the sensitivity decreases as the number of poles increases. This is because, as the total machine magnet volume is divided in a larger number of pieces, the equivalent electrical resistance seen from the stator is increased [71]. The same trends are observed

for the rotating signal injection, shown in Table 3.9.

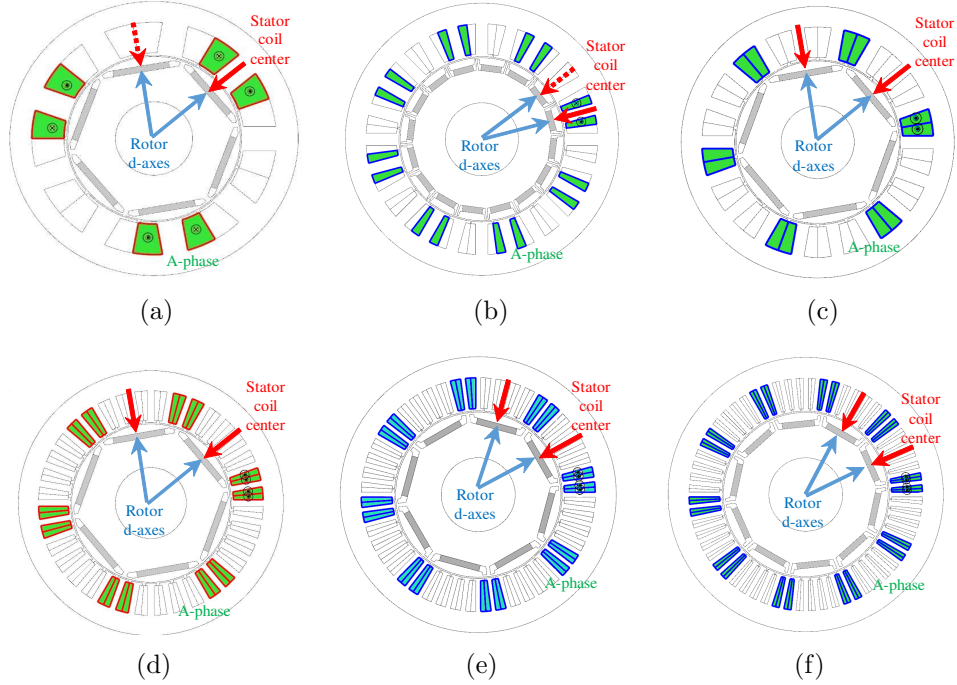


Figure 3.19: Cross section of: a) 9/6 IPM machine, b) 24/16 IPM machine, c) 18/6 IPM machine, d) 36/6 IPM machine, e) 48/8 IPM machine and f) 60/10 IPM machine.

For concentrated winding machines, rotor magnets do not always match the stator coil center, the equivalent reluctance path being therefore higher than for the case of distributed winding machines. In addition, the injected signal does not excite uniformly the PMs in all the poles, which results in a lower sensitivity of the stator reflected magnet high frequency resistance to the magnet temperature variation (see Fig.3.19(a) and Fig. 3.19(b)).

It can be also observed that for fractional slot winding machines, higher coil pitches present, in general, higher sensitivities. Arrangements with coil pitch of 5 and 6 for fractional slot machines uses different number of stator slots to accommodate the coils of every phase. Coil pitch 6 arrangement, encloses 5 teeth (i.e. the induced flux is driven through 5 teeth), see Fig. 3.21(a) while coil pitch 5, encloses only 4, see Fig 3.21(b). When flux is driven through 4 teeth, all of them match the magnet length, On the other hand, when the flux is driven through 5 teeth, two of them actually face the flux barriers, see Figs.3.19(d)-3.19(f), 3.21(a). The result of the stator

teeth perfectly matching the magnet length, see Fig. 3.21(b) is an increased sensitivity, as shown in Table 3.8 for 36/6 and 60/10 machine, coil pitch 5; 48/8 machine showing small differences between coil pitches 5 and 6.

The case of the 18/6 integer slot winding machine can be observed in Fig. 3.20(b). Highest sensitivity is obtained with the lowest coil pitch. The reason for this is that, as for the case of fractional slot machines, the coil pitch 3 arrangement drives the flux generated by the coil through 3 teeth, one of which is facing the magnet center, the other two facing both the magnet and the flux barrier. Coil pitch 1 arrangement, on the contrary, drives all generated flux through the magnet center, increasing therefore the sensitivity of the high frequency resistance to magnet temperature.

The highest sensitivity occurs for the 36/6 configuration (see Fig. 3.20(d)). This is because the stator coil center perfectly matches the rotor  $d$ -axis for all the PMs, maximizing therefore the coupling between the stator high frequency flux and the PM.

Among all 36/6 configurations, pitch 5 provides the best results (see Table 3.8). The reason for this is that it is the fractional slot machine with the lowest number of poles being evaluated. Coil pitch 5 arrangement provides the highest sensitivity for this machines, due to the position between stator teeth enclosed by one phase coil and the rotor magnets, see Fig. 3.21(b).

It is finally noted that the same trends are observed for the two frequencies that have been evaluated, i.e. 250Hz and 500Hz. Although the sensitivity for the 500Hz case is in general higher than for the 250Hz case, use the 250Hz is considered advantageous,  $R_{dhf}$  at 20°C is lower at 250 Hz (see Tables 3.8 and 3.6), meaning that the induced magnet losses are lower too. In addition, as the frequency of the injected signal increases, the weight of the inductive component increases (undesired component) over the resistive component (desired component) in the overall high frequency impedance, see (2.31), what might result in a reduction of the accuracy of the method. It can also be observed from Tables 3.6 and 3.7 that for fractional slot machines the estimated resistance at 20°C increases for both 250 and 500Hz for lower coil pitch. The reason is that lower coil pitches produce higher flux density spots in the magnet (see Fig 3.21(c)) which increases the magnet losses.

It can be also observed from Tables 3.8 and 3.9 that for all machines, the sensitivity decreases as the number of poles increase. This is because as the number of poles decreases, the magnet edges are closer to the airgap, the reluctance path being therefore lower in these cases, which results in an increased sensitivity.

Fig 3.20 shows the magnetic flux density contour of the same machines



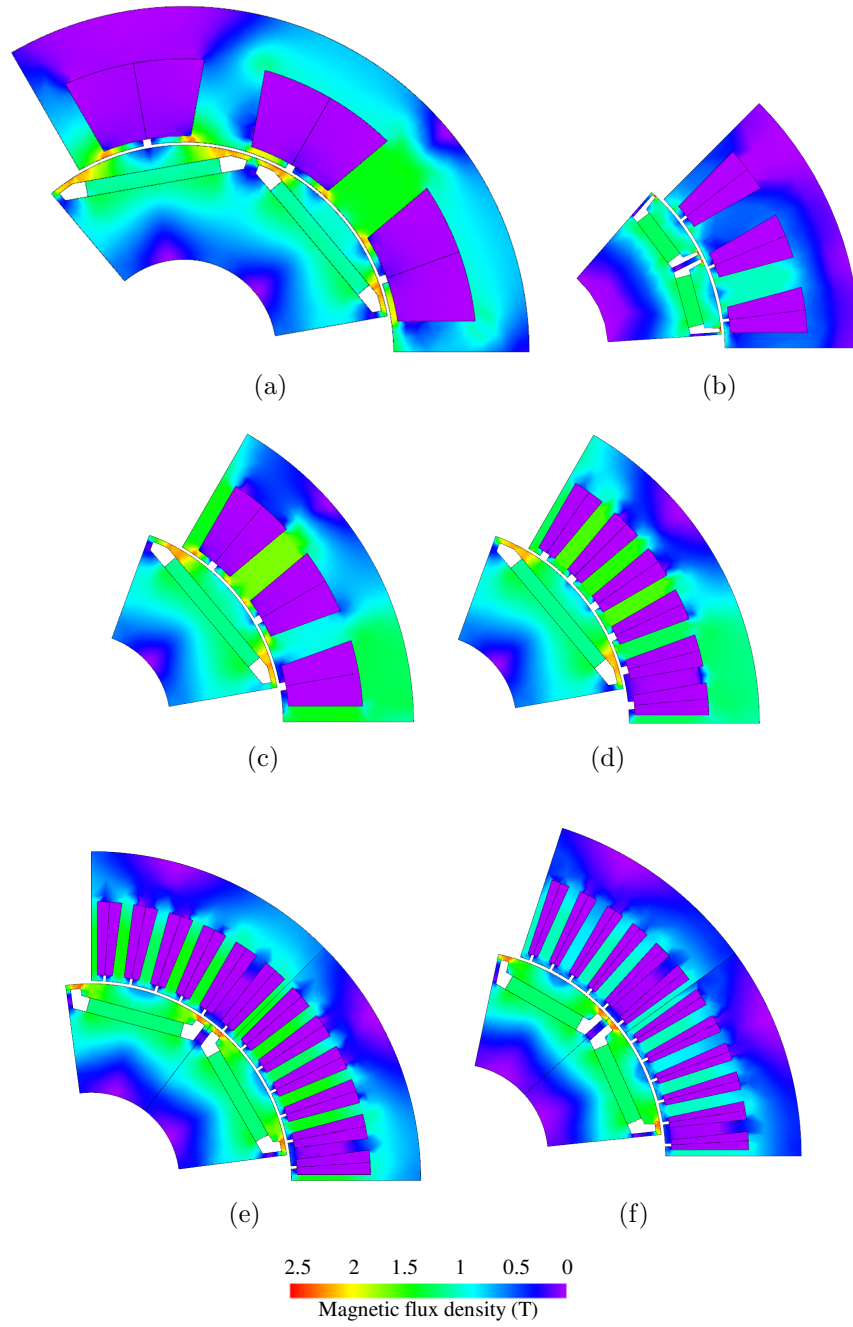


Figure 3.20: Contour plot of the magnetic flux density for a) 9/6 IPM machine, b) 24/16 IPM machine, c) 18/6 IPM machine, d) 36/6 IPM machine, e) 48/8 IPM machine and f) 60/10 IPM machine.  $I_{hf}=1A$  (0.05pu),  $I_{dq}=0A$ .

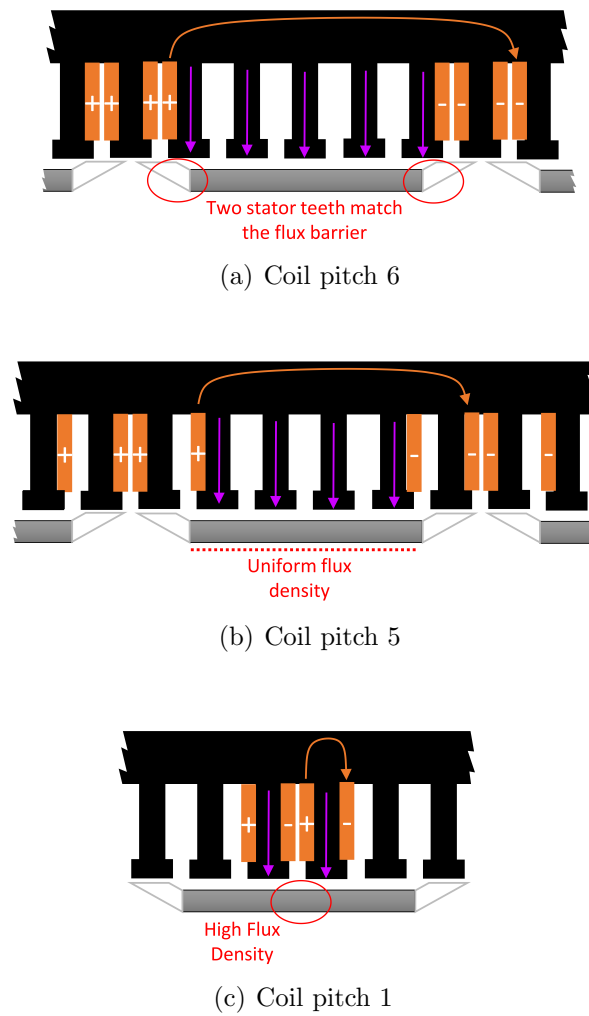


Figure 3.21: Representation of the coil flux and the magnet position for the d-axis injection for different coil pitches of a 36 slot 6 pole machine.

shown in Fig. 3.19, no load being applied. The flux density contour are shown for the instant when the pulsating current is maximum in phase a. Fig. 3.20(a) corresponds to 9/6 machine (most favorable concentrated winding configuration) while Fig. 3.20(b) corresponds to 24/16 configuration (most unfavorable concentrated winding configuration). It is observed that the 9/6 machine shows higher flux density in the stator tooth that matches the magnet width. The same behavior is observed for flux density in the stator teeth for machines with distributed winding, i.e. Fig. 3.20(c)-3.20(f). As previously stated, the 30/10 and the 24/10 machines show the lowest sensitivity of  $R_{dhf}$  to magnet temperature variations.

### 3.4 Conclusions

This chapter analyzes in the first section the sensitivity of pulsating  $d$ -axis high frequency current injection PM temperature estimation method to machine assembling tolerances (e.g. static eccentricities, dynamic eccentricities, mixed eccentricities and magnet assembling tolerances). The second section presents an analysis of the stator configuration, slots/pole combination and coil pitch factor on the sensitivity of high frequency signal injection based magnet temperature estimation methods for PMSM.

It has been shown that the static, dynamic and mixed eccentricities have an important impact on the estimated magnet high frequency resistance; however, their effects can be easily decoupled using the component at  $\omega_r$  that is induced in the estimated high frequency resistance. Furthermore this component can also be used to estimate the eccentricity degree. It has also been shown that the PM assembling tolerances have a negligible impact over the estimated magnet temperature. Consequently, eccentricity and assembling tolerances are not expected to limit the accuracy and therefore the usefulness of the method in a real application. Finally, it has been shown that the lamination grain-orientation can have an important effect on the estimated magnet temperature, which could compromise the accuracy of the method.

For the study of the stator configuration and slots/pole combination effects on the estimated PM temperature using high frequency signal based methods, a set of IPMSMs with the same rated values were analyzed, machines being designed to provide the same torque-speed characteristic and having the same dimensions. Two high frequency injection waveforms and two frequencies have been used, rotating and pulsating. It has been shown

that the pulsating injection shows higher sensitivity than the rotating injection and that the frequency of the injected signal plays an important role on the sensitivity of high frequency signal injection temperature estimation based methods.

It has been also shown that the slot/pole and pitch configuration affects  $R_{dhf}$  sensitivity to the magnet temperature. The highest sensitivity to the magnet temperature is obtained when the coil pitch is selected so that none of the stator teeth faces a rotor flux barriers but a magnet. The most favorable stator configuration is the 36/6 (pitch 5) for pulsating and the 9/6 for rotating signal injection. Distributed winding machines present higher sensitivities to magnet temperature variation. In addition the sensitivity analysis, the magnet resistance obtained at 20°C was also analyzed, since it is an indicator of the PM losses. It was concluded that lower coil pitches increase produce higher magnet losses.

# Chapter 4

## Permanent Magnet Magnetization State Estimation

### 4.1 Introduction

A large variety of PMs can be used in PMSMs, including Alnico, ferrite, SmCo and NdFeB. Although NdFeB PMs are currently the primary option in high performance PMSMs [72, 73, 74, 75, 35] as they can provide the highest energy product  $BH_{max}$  of any material today [76], applications equipping SmCo [37, 38], AlNiCo [18, 19, 20] and ferrite magnets [21, 22, 23] can also be found.

SmCo permanent magnets are widely applied in aerospace [77], aviation and military-related industries [78] due to their advantages under high temperature over NdFeB magnets. However, they are brittle, and prone to cracking and chipping. In addition, the brittleness in manufacturing results in 20-30% of raw materials wasted [78].

Ferrite magnets are commonly used in low cost applications including domestic appliances, and STFMM for general purpose applications, with the goal of reducing cost (see Table 4.1, [39]) and the dependence on rare earth materials [79], at the price of decreasing the machine performance. It is noted however that PM machines using ferrite magnets still provide higher performance than induction and synchronous reluctance motors [80, 81].

The interest in AlNiCo magnets has recently increased as its low coercivity and high remanence makes them a potential option for the development

of VFMs [82] and Switched flux memory motors [83, 84]. However, they are rarely used in conventional PMSMs as the magnet can be easily demagnetized by the stator current during normal operation [82].

Ferrite [35, 36], SmCo [37, 38] or AlNiCo magnets combined with NdFeB magnets [18, 19, 20] are also commonly used in VFMs [37, 38, 84].

Table 4.1: Cost and temperature sensitivity of different magnet materials

Material	Alnico 8	Ferrite 9	SmCo 2:17	NdFeB 33EH	NdFeB 48M
(\$/Kg)	35	15	100	200	150
$\alpha_B$ (%/°C)	-0.01	-0.18	-0.035	-0.11	-0.12

In most PMSMs, the  $d$ -axis current is used to weaken the PM flux [35, 36], allowing constant power operation above base speed in SPMSM, IPMSM and STFMM, as well as to realize MTPA or other optimization strategies in IPMSM [72] and STFMM [18]. In addition,  $d$ -axis current is also used to permanently change the PM flux in VFM [37, 38].

PM magnetization state of ferrite, Alnico, SmCo and NdFeB also changes with temperature [32]. Table 4.1 shows typical values of the PM thermal remanent flux coefficient,  $\alpha_B$  which is defined as the rate of PM remanent flux variation with temperature [32, 31, 40]. The coefficient  $\alpha_B$  is observed to vary significantly for different materials, PM field typically decreasing as the temperature increases [40]. Furthermore, even for the case of machines with identical designs, assembling tolerances and minor differences in the magnet geometries and alloys may affect the machine magnetization state [85].

While in many cases, a rough estimation of the magnetization state is enough (e.g., applications using conventional SPMSMs and IPMSMs and with moderate requirements in the estimated torque accuracy), PM magnetization state estimation in PMSMs can be important for precise torque control and magnet state monitoring purposes of PM machine designs [58, 86, 87], including IPMSM, SPMSM, VFM or STFMM.

Magnetization state of PMs, typically occurs in classical IPMSM and SPMSM, due the heat produced by the stator and rotor losses [72, 73, 30], with potential PM irreversible demagnetization if the temperature becomes too high [72, 73]. However, as shown in Table 4.1, the variation of the magnetization state with temperature is relatively small. Consequently, the torque production capability of the machine will not change dramatically during normal operation, meaning that a highly precise magnetization state estimation will not be required for this type of machines. On the contrary, VFM and

STFMM can be magnetized/demagnetized during normal operation of the machine, magnetization state estimation after this process [37] being critical.

The PM magnetization state variation by the injection of a  $d$ -axis current is frequently used to reduce the magnet flux and allow constant power operation above base speed [88], [89] in conventional IPMSMs and SPMSMs, to achieve maximum torque per ampere or other optimization strategies with IPMSM, as well as to magnetize/demagnetize the PMs in VFM [35, 36], [38, 37, 90].  $Q$ -axis current can also make the magnetization state to change due to the cross-coupling that typically exists between  $d$ -axis and  $q$ -axis [74, 91].

Magnet flux distribution measurement in PM machines is not trivial once the machine is assembled. Magnet remanent flux can be measured by inserting a magnetometer in the air gap. However, the end frame needs to be removed and can only be used with SPMSMs as the magnetometer has to be placed on the magnet surface. On the contrary, for the case of IPMSMs, the flux measured on the rotor surface does not account for the actual PM flux due to the leakage flux. In either case, this method cannot be applied during the normal operation of the machine.

To overcome the aforementioned limitations, estimation methods using measurable stator electrical variables have been proposed [35, 92, 59, 60]. Back electromotive force (back EMF) methods are particularly easy to implement, being therefore very popular [35, 92, 59, 60]. Obtaining the PM flux linkage from the stator terminals when  $I_d = I_q = 0$  is relatively simple. However, obtaining the PM flux linkage when  $I_d = 0$  and  $I_q \neq 0$  or  $I_d \neq 0$  and  $I_q \neq 0$  is not possible without previous knowledge of some machine parameters (e.g.,  $d$ -axis and  $q$ -axis inductance maps, resistance, etc.). Injecting an additional signal [92, 60], measuring or estimating the machine parameters [58], or setting the machine parameters to their nominal values [?] as been proposed to overcome this problem. Using nominal values has low accuracy due to their variation with load and temperature. Measuring/estimating machine parameters is therefore preferred. It is finally noted that back EMF methods require the machine to be rotating.

Magnet flux variation can also be estimated from the variation of the electrical properties of the PM with its magnetization state. This relationship is given by the magnetoresistance, which is the change of a material electrical resistance when an external field is applied [93, 94, 29, 95]. Although the magnetoresistance effect on NdFeB magnets has already been studied for other applications [29, 95], its use for magnetization state estimation in PMSMs has not been proposed yet.

This chapter analyzes the use of the stator-reflected PM high frequency resistance variation to estimate the magnetization state of the rotor PMs. Additionally the effects that the PM coating, which is commonly used in PMs to prevent oxidation, has on the magnetoresistive effect will be also analyzed. The proposed method measures the stator-reflected PM high-frequency resistance, from which a lumped magnetization state estimation is obtained. A small-magnitude high-frequency voltage superimposed on the fundamental excitation is used for this purpose. The resulting stator high frequency current will be shown to be dependent on the magnet high-frequency resistance, the PM magnetization state being estimated from the reflected PM high-frequency resistance variation. Implementation of this method will require compensating the contribution of the stator resistance to the overall high-frequency impedance of the machine. The stator resistance can be measured or estimated using the measured stator windings temperature. Previous knowledge of other machine parameters (e.g.,  $d$ -axis and  $q$ -axis inductance maps) is therefore not needed, which is advantageous compared with the back-EMF-based methods, which require such parameters. In addition, the proposed method can be used in the whole speed range of the machine, even at standstill.

## 4.2 Magnetoresistance effect in Permanent Magnets

Magnetoresistance is defined as the change of the material's electrical resistance/resistivity with the application of a magnetic field [96]. For large electrical resistance variation ( $> 10\%$ ) this effect is called giant magnetoresistance (GMR) [29, 95]. Magnetoresistance was initially discovered in thin-film structures alternating ferromagnetic and nonmagnetic conductive layers. The effect was later also found in granular NdFeB magnets [29, 95]. This effect enables therefore NdFeB magnets to be used as a sensor that converts magnetic field changes into electrical resistance changes. Magnetoresistance  $MR$  is defined by (4.1), where  $R(0)$  is the resistance of the material in the absence of magnetic field,  $R(H)$  (4.2) is the resistance of the material when a given magnetic field strength  $H$  is applied,  $\beta$  is the sensitivity of the material resistance to an external field  $H$ .

Magnetic flux density  $B$  can be used instead of magnetic field strength  $H$  as it is the output of most field sensors; the relationship between both quantities being defined by (4.3), where  $\mu_{CO}$  is the absolute permeability of



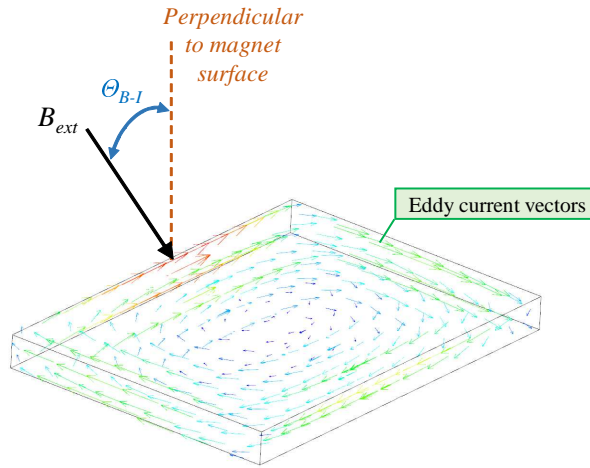


Figure 4.1: External magnetic field,  $B_{ext}$ , and induced eddy current vectors

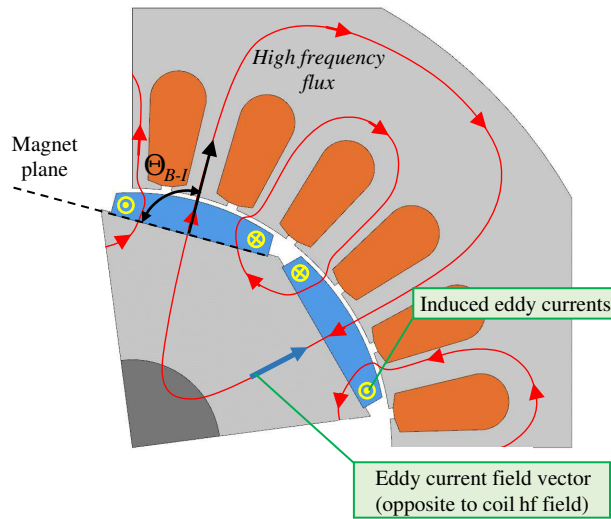


Figure 4.2: Simplified 2D representation of the flux lines in a PMSM (red) and magnet eddy current vectors

the core.

$$MR = \frac{\Delta R}{R(0)} \quad (4.1)$$

$$R(H) = R(0)(1 + \beta(H - H(0))) = R(0)(1 + \beta(\Delta H)) \quad (4.2)$$

$$H = \mu_{CO} B \quad (4.3)$$

Changes of PM electrical resistance can be estimated from the induced magnet eddy currents when an alternating magnetic field is applied to the PM [28]. The angle of the magnet surface,  $\Theta_{B-I}$ , respect to the external magnetic field vector (*Bext*) will determine the relationship between the resistivity variation and the external magnetic field variation [96] (see Fig. 4.1). For the particular case of a PMSM, the eddy current vector can be assumed to be perpendicular to the electromagnetic field produced by the stator windings (see Fig. 4.2), the change of the material electrical resistivity due to the external magnetic field being therefore maximum, even with skewed machines.

In addition to the magnetoresistance effect, the PM electrical resistance also changes with temperature [28]. Both effects can be combined, the PM electrical resistance being expressed as (4.4) [28], where  $R(T_0, B_{r-ini})$  is the resistance at room temperature,  $T_0$ ,  $B_{r-ini}$  is the initial remanent PM flux,  $\beta$  is the coefficient that links the PM field variation and the resistance variation [32, 94, 29] and  $\alpha_{mag}$  is the permanent magnet thermal resistive coefficient.

$$R_{(T,B)} = R_{(T_0, B_{r-ini})}(1 + \alpha_{mag}\Delta T + \beta\Delta B) = R_{(T_0, B_{r-ini})}(1 + \alpha_{mag}(T - T_0) + \beta(B - B_{r-ini})) \quad (4.4)$$

#### 4.2.1 Magnetoresistance Measurement System

Measurement of the magnetoresistive effect in the magnets of a PMSM is not easy due to the large number of design parameters that can affect the results [28], in the stator (e.g. stator teeth shape, number of stator slots, number of poles...) and rotor (rotor geometry, number of PMs layers,

PMs shape and size, flux barriers...). It is noted, however, that variations in the machine design will affect the sensitivity of its terminal properties (i.e. stator currents and voltages) to the magnetoresistance effect, but not to the magnetoresistance effect itself, since this is a property of the material. It is therefore advantageous to evaluate the magnetoresistive effect in the PM before it is mounted in the machine, provided that the conclusions remain valid for the PMSM case.

Three PM technology will be analyzed: Ferrite, SmCo and NdFeB. Two sample shapes will be considered: disk-shaped (see Fig 4.3), and segmented magnets(see Fig 4.4). Disk-shaped magnets were chosen to adapt the shape of the developed system for magnetoresistance measurement and segmented magnets due to their importance for high speed machines [97], including electric vehicles [18, 98] and high power machines [99]. The system shown in Fig. 4.5 has been developed for measurement the magnetoresistance effect of the samples.

It consists of a core made of iron powder blocks (BK8320-26 and CK2020-26,  $\mu_r=26$ ) [95]. Two different coils will be used: a 490 turns coil for magnet disks evaluation and a two series connected coils (335 turns) for segmented magnets evaluation. The dimensions of the magnet and the central column of the core perfectly match with each other (see Fig. 4.6), minimizing therefore the flux leakage.



Figure 4.3: Ferrite, SmCo and NdFeB magnet disks

It is noted that in the platform shown in Fig. 4.5, the applied external field is perpendicular to the eddy current vector and there is no airgap between the core and the magnet (see Fig. 4.6). On the contrary, PMSM present an air-gap between stator and rotor. Consequently, the setup in Fig 4.5 will have a reduced equivalent reluctance, enhancing therefore the magnetoresistive effect.

The high frequency equivalent circuit of the platform shown in Fig. 4.5 is given in Fig. 4.7, where  $v_{hfp}^p$  and  $i_{hfp}^p$  is the coil high frequency voltage

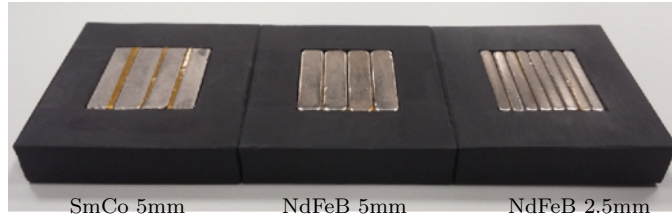


Figure 4.4: Segmented magnet arrangements (SmCo and NdFeB).

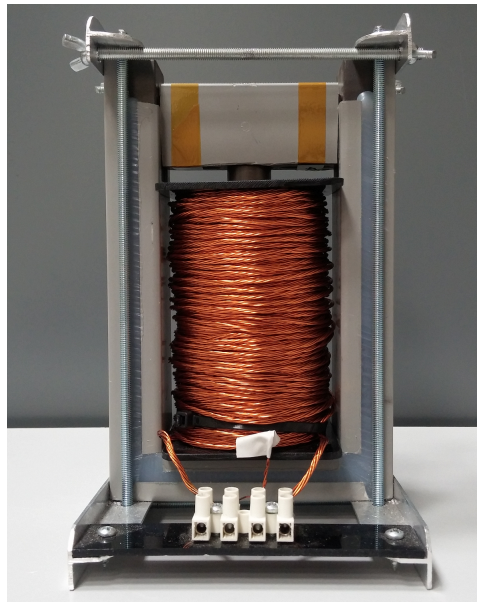


Figure 4.5: Experimental setup for the PM magnetoresistance evaluation

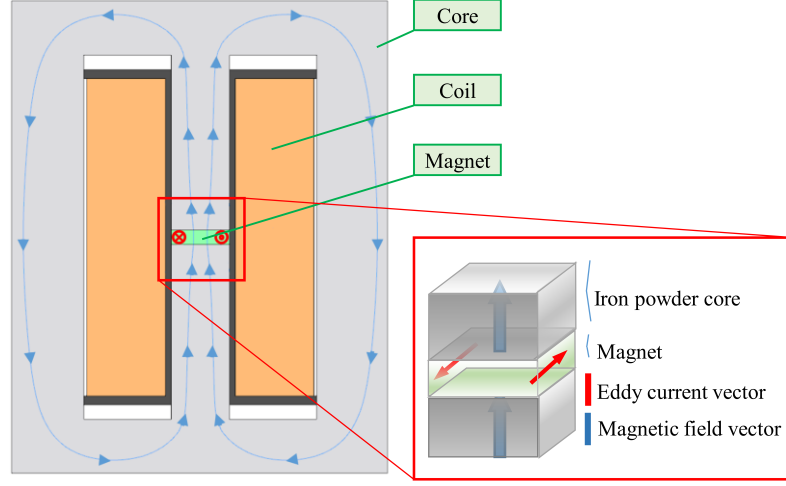


Figure 4.6: Simplified representation of flux lines (blue) and magnet eddy current vectors (red) in the experimental setup

and current,  $R_{hfp}^p$ ,  $R_{hFEp}^p$ , and  $R_{hfs}^s$  are the coil, core and magnet high frequency resistances respectively,  $L_{hfp}$  and  $R_{hfs}^s$  are the coil and magnet high frequency inductances,  $\omega_{hf}$  is the frequency of the high frequency signal,  $i_{hfs}^s$  is the magnet high frequency current (eddy current) and  $M_{ps}$  is the mutual coupling between the primary and the secondary. It will be shown that  $R_{hFEp}^p$  can be safely neglected due to the reduced eddy currents induced in the iron powder core [28].

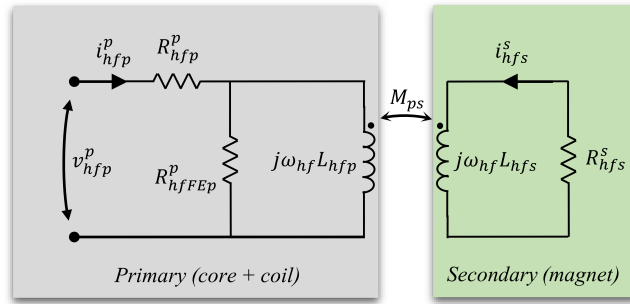


Figure 4.7: Equivalent high frequency model of the simplified geometry

The high frequency model of the experimental setup, see Fig. 4.7, is rep-

resented by (4.5)-(4.6), which corresponds to the transformer based model in Fig. 4.7. The secondary high frequency current (4.7) can be obtained from (4.6). Combining (4.7) and (4.5), (4.8)-(4.9) are obtained, the high frequency impedance being (4.10), its real component being (4.11). Assuming that the eddy currents are typically limited by the material resistance (i.e.  $R_{hfs}^s \gg L_{hfs}^s$ ), (4.12) is finally obtained. The magnet high frequency resistance reflected in the primary terminals (coil terminals),  $R_{hfs}^p$ , is obtained from (4.13). It is noted that the proposed method provides a lumped estimation of the magnet high frequency resistance and therefore of the magnet magnetization state.

$$v_{hfp}^p = \left( R_{hfp}^p + j\omega_{hf} L_{hfp} \right) i_{hfp}^p + j\omega_{hf} M_{ps} i_{hfs}^s \quad (4.5)$$

$$0 = \left( R_{hfs}^s + j\omega_{hf} L_{hfs} \right) i_{hfs}^s + j\omega_{hf} M_{ps} i_{hfp}^p \quad (4.6)$$

$$i_{hfs}^s = \frac{-j\omega_{hf} M_{ps} i_{hfp}^p}{R_{hfs}^s + j\omega_{hf} L_{hfs}} \quad (4.7)$$

$$v_{hfp}^p = \left( R_{hfp}^p + j\omega_{hf} L_{hfp} \right) i_{hfp}^p - j\omega_{hf} M_{ps} \frac{-j\omega_{hf} M_{ps} i_{hfp}^p}{R_{hfs}^s + j\omega_{hf} L_{hfs}} \quad (4.8)$$

$$v_{hfp}^p = \left( R_{hfp}^p + j\omega_{hf} L_{hfp} \right) i_{hfp}^p + \frac{\omega_{hf}^2 M_{ps}^2}{R_{hfs}^s + j\omega_{hf} L_{hfs}} i_{hfp}^p \quad (4.9)$$

$$Z_{hfp} = \frac{v_{hfp}^p}{i_{hfp}^p} = \left( R_{hfp}^p + j\omega_{hf} L_{hfp} \right) + \frac{\omega_{hf}^2 M_{ps}^2}{R_{hfs}^s + j\omega_{hf} L_{hfs}} = \quad (4.10)$$

$$R_{hf} + j\omega_{hf} L_{hf}$$

$$R_{hf} = R_{hfp}^p \frac{\omega_{hf}^2 M_{ps}^2 R_{hfs}^s}{R_{hfs}^s{}^2 + j\omega_{hf}^2 L_{hfs}^2} \quad (4.11)$$

$$R_{hf} = R_{hfp}^p + \frac{\omega_{hf}^2 M_{ps}^2}{R_{hfs}^s} \quad (4.12)$$

$$R_{hfs}^p = \frac{\omega_{hf}^2 M_{ps}^2}{R_{hfs}^s} = R_{hf} - R_{hfp}^p \quad (4.13)$$

### 4.2.2 High frequency signal injection for magnetization state estimation

Injection of a periodic high frequency signal has been shown to be a viable option for magnet high frequency resistance estimation [28]. Choosing the magnitude of the high frequency signal involves a tradeoff between the signal-to-noise ratio and induced magnet losses; larger magnitudes result in larger losses due to eddy current. However, it also increases the signal-to-noise ratio, which is advantageous for the practical implementation of the method. Choosing the frequency of the high frequency signal involves a tradeoff between the induced power losses and skin effect consideration. Induced magnet power losses can be expressed as (4.14), where  $B_m$  is the flux density,  $f_{hf}$  is the frequency of the injected signal,  $\rho$  is the resistivity of the magnet and  $K_e$  is a constant which depends on material size. It is observed from (4.14) that the losses are proportional to the square of the frequency of the injected signal and to the flux density. Skin depth can be calculated using (4.15), where  $\delta$  is the skin depth, and  $\mu_0$  and  $\mu_r$  are the magnetic permeability of the air and the magnet respectively. Generally speaking, the skin depth should be larger than the magnet height, otherwise there will be a loss in magnetoresistance sensitivity, as the eddy currents will only flow over a portion of the magnet height equal to the skin depth. The maximum frequency of the injected signal,  $f_{hf-max}$ , can be calculated using (4.16), and occurs when the skin depth is equal to the magnet height.

$$P = K_e \frac{(B_m f_{hf})^2}{\rho} \quad (4.14)$$

$$\delta = \sqrt{\frac{2\rho}{2 * \pi f_{hf} \mu_0 \mu_r}} \quad (4.15)$$

$$f_{hf-max} = \frac{2\rho}{2\pi\delta^2\mu_0\mu_r} \quad (4.16)$$

Table 4.2 shows the magnet parameters and the maximum frequency of high frequency signal that will be used for the NdFeB, SmCo and ferrite disks to analyze (see Fig. 4.3).

Fig. 4.8 schematically shows the signal processing used for magnet resistance estimation. The inputs are the primary voltage and current,  $v_{Lp}^p$

Table 4.2: Magnet parameters

Magnet Type	Height (mm)	Radius (mm)	$\mu_r$	$\rho$ ( $\Omega m$ )	$f_{hf-max}$ (kHz)
NdFeB	5	10	1.05	$1.44 \times 10^{-6}$	6.6
SmCo	5	10	1.05	$85 \times 10^{-6} V$	$4 \times 10^2$
Ferrite	5	10	1.05-1.10	$1 \times 10^3 - 1 \times 10^4$	$2 \times 10^3$

and  $i_{Lp}^p$ , and the stator primary (coil) high frequency resistance  $R_{hfp}$ . Two band-pass filters (BPF1 and BPF2) are used to separate the high frequency voltage and current from the DC current, which is used to change the PM magnetization state.

## 4.2.3 Experimental results

### 4.2.3.1 Signal injection

Experiments were conducted using the geometry shown in Fig. 4.5. The coil is fed from a power converter as shown in Fig. 4.9. Table 4.3 shows the coil and power converter data. Fig. 4.10 shows the control block diagram for the injection of the DC current used to change the PM magnetization state and the high frequency signal used to estimate the magnet high frequency resistance. A PI regulator is used to control the DC current, the high frequency signal being added on top of the PI controller output voltage. A band-stop filter (BSF1) is used to remove the induced high frequency current in the coil to prevent the current regulator reaction to the injected high frequency signal.

Figs. 4.11(a) and 4.12(a) show an example of the injected voltage and current for the case of a DC current of 12 A and a high frequency voltage of 10 V. Figs. 4.11 and 4.11 show the applied voltage and the resulting current, as well as the corresponding frequency spectra. The DC and high frequency components at 250 Hz are readily observed. Though higher order components also exist, they are negligible (note the logarithmic scale in the frequency spectra).

The methodology for the experiment is as follows: The DC current and the high frequency voltage command are set simultaneously. Both DC and high frequency signals reach steady state in  $\approx 30$  ms. After that, the high frequency resistance is estimated using the signal processing shown in Fig.



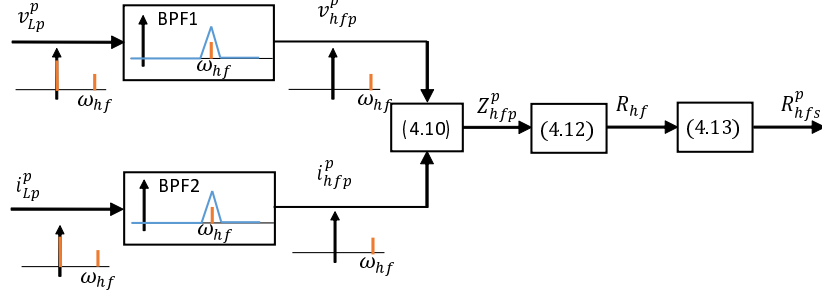


Figure 4.8: Signal processing used for magnet high frequency estimation using high frequency/voltage injection

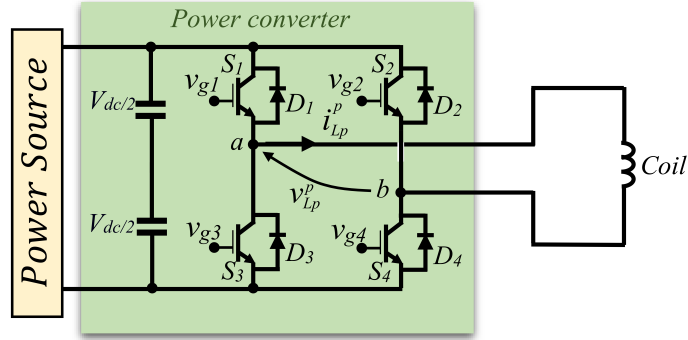


Figure 4.9: H-Bridge power converter

4.8. Estimation of the high frequency resistance takes  $\approx 10$  ms, meaning that that the whole process takes  $\approx 40$ ms.

Both coil and magnet temperatures are measured before and after the test, the change of the magnet temperature during the experiment being negligible.

#### 4.2.3.2 Magnetoresistance of the coil and core

Prior to the analysis of the magnetoresistive effect of the magnets, measurement of the magnetoresistance effect in the experimental coil and core is needed to further decouple these effects from the measurements. The total resistances seen from the coil terminals include coil, core and magnet resistance (see Fig. 4.7).

Table 4.3: Experimental Setup parameters

Coil Parameters			Inverter Rated Parameters	
	Disks	Segmented Magnets		
Number Of Turns	335	490	Switching Frequency	10 kHz
Resistance	0.3236 $\Omega$	0.6995 $\Omega$	Voltage	380 V
Parallel Wires Per Turn	14	7	Current	75 A
Inductance (nH)	5.2	12.5	<i>BSF1</i>	10Hz
$\alpha_{cu}(1/K)$	$3.9 \times 10^3$	$3.9 \times 10^3$	Bandwidth	200Hz
			Current Reg.	

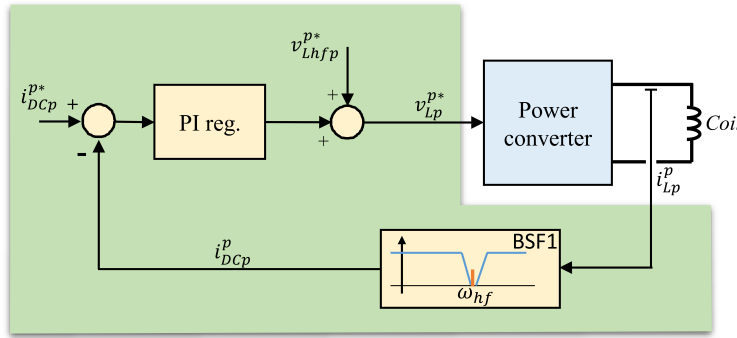


Figure 4.10: Control block diagram of the DC and high frequency signal injection

Figure 4.14 shows the measured high frequency resistances for the coil and the core. The coil high frequency resistance was measured by applying a high frequency voltage to the coil previous to the insertion of the coil in the core (i.e. air core coil). For the estimation of the core high frequency resistance, a high frequency voltage was applied to the coil terminals with the coil being mounted in the core as shown in Fig. 4.5. No magnet was inserted in the airgap in this case (see Fig. 4.13(a)). The H-Bridge is used to apply the coil a DC voltage and a high frequency voltage simultaneously. The DC voltage controls the DC current needed to change the magnetic flux density; the high frequency AC voltage, which is superposed on the DC voltage, is used for coil and core high frequency resistance estimation. The core high frequency resistance shows a peak at  $\approx -0.1T$ . This behavior is due to the fact that the iron powder core shows a small remanent magnetization when a high DC field

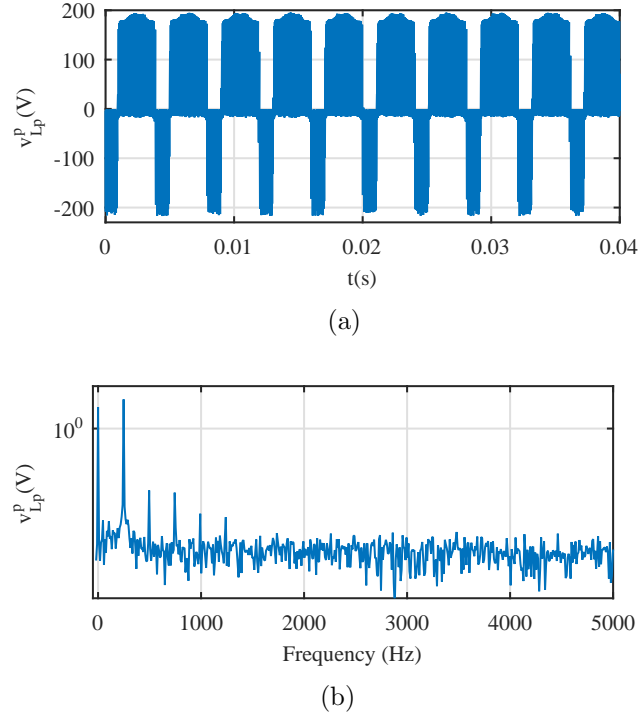


Figure 4.11: a) Injected voltage  $v_{Lp}^p$  and b) corresponding frequency spectrum  $I_{DC} = 12A$ ,  $f_{hf} = 250Hz$  and  $V_{hf} = 10V$ .

is applied. The direction of this remanent magnetization produces the shift observed in Fig. 4.14. It is observed from Fig. 4.14 that the coil with air core presents an almost constant high frequency resistance as the magnetic flux density changes, i.e. magnetoresistive effect being negligible. On the other hand, the high frequency resistance of the core slightly changes with the magnetic field, meaning that core presents relatively small magnetoresistive effect. However, this effect will be shown to be negligible when compared with the magnetoresistive effect in NdFeB magnets. The magnetic flux density created by the injected DC current is measured by a Hall-effect mono-crystal gallium arsenide (GaAs) sensor [100]. Its measuring range is 0-3T. This is larger than the fields produced in the experimental setup and in PMSMs, which typically is in a range of 0-1.8T. Its maximum operating temperature being 125°C. Location of the field sensor is shown in Fig. 4.13.

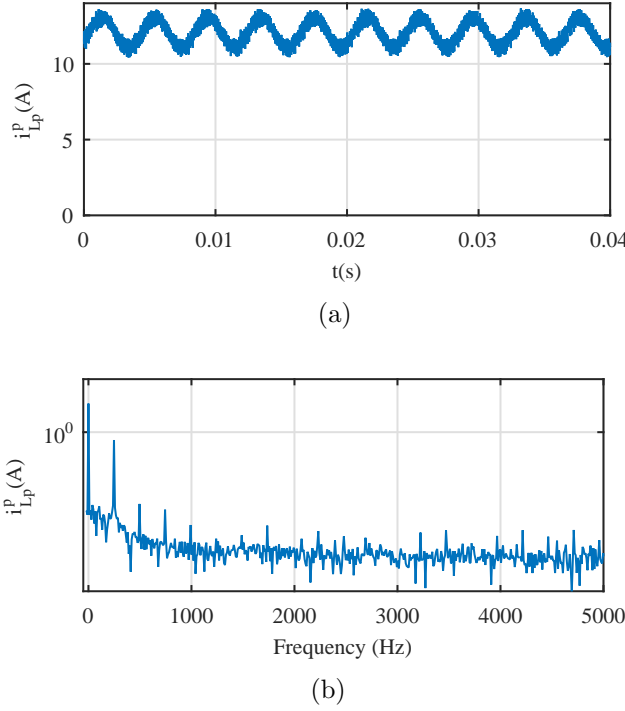


Figure 4.12: a) Injected current  $i_{Lp}^p$  and b) corresponding frequency spectrum  $I_{DC} = 12A$ ,  $f_{hf} = 250Hz$  and  $V_{hf} = 10V$ .

#### 4.2.3.3 Magnetoresistance effect in demagnetized samples

This subsection analyzes the magnetoresistance effect in demagnetized magnet samples. The demagnetized PMs are inserted in the core as shown in Fig. 4.5 and 4.13(b). NdFeB, SmCo and ferrite magnet disks will be evaluated (see Fig. 4.3). The magnets were initially fully demagnetized. Figure 4.16 shows the reflected magnet high frequency resistance of ferrite, NdFeB and SmCo disks. As for the experimental results of the core and coil magnetoresistance effect evaluation, a DC current (needed to create the magnetic field) and a high frequency voltage (needed for high frequency resistance estimation) are injected simultaneously. The magnetic field is measured by the field sensor (see Fig. 4.13(b)), the DC current being adjusted to produce the desired field. The core and coil high frequency resistances are decoupled from the overall estimated high frequency resistance, ((4.11)), using the data shown in Fig. 4.14.

It is observed that, for the three magnet materials, the reflected magnet

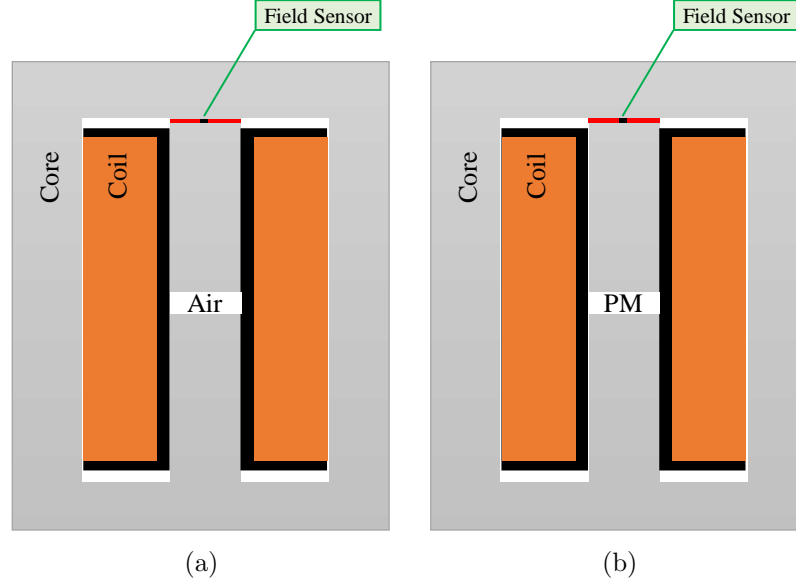


Figure 4.13: Simplified representation of the experimental setup when the magnet is removed, a), and when the magnet is inserted, b). Placement of field sensor is indicated.

high frequency resistance decreases as the magnetic flux density (i.e. magnetization state) increases. NdFeB magnet shows the largest resistance variation, which is due to its iron composition [25, 26]. SmCo and ferrite magnets show a significantly reduced magnetoresistive effect. These results demonstrate that the magnetoresistive effect exists in ferrite, NdFeB and SmCo magnets, and that the variation of the magnet high frequency resistance can be used for magnetization state estimation.

#### 4.2.3.4 Magnetoresistance effect in magnetized samples

This subsection analyzes the magnetoresistance effect in magnetized PMs. Figure 4.17 shows the reflected magnet high frequency resistance of ferrite, NdFeB and SmCo disks. The PMs were initially magnetized to the following magnetization states. NdFeB:  $\approx 0, 0.25, 0.5, 0.75, 0.95$  and  $\approx 1.2\text{T}$  which correspond to  $\approx 0.2, 0.4, 0.6, 0.8$  and  $1\text{pu}$ ; SmCo:  $\approx 0, 0.2, 0.4, 0.8\text{T}$ , which correspond to  $\approx 0, 0.25, 0.5$  and  $1\text{pu}$ ; ferrite:  $0, 0.25$  and  $0.35\text{T}$ , which correspond to  $0, \approx 0.7$  and  $1\text{pu}$ . The magnets are magnetized using the pulse magnetizer, shown in Fig. 4.18 the magnetization circuit parameters are shown in Table 4.4.

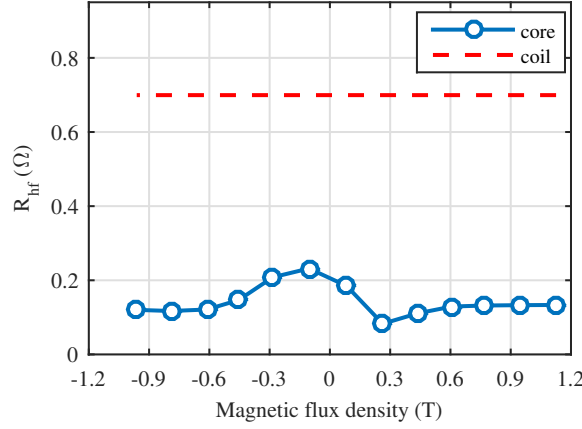


Figure 4.14: Estimated high frequency resistance  $R_{hfs}^p$  of the iron powder core  
 Estimated high frequency resistance  $R_{hfs}^p$  of the iron powder core when the  
 air-gap is equivalent to the height of the magnet,  $\circ$ , and when there is no  
 core,  $-$ ,  $f_{hf} = 250$  Hz,  $V_{hf} = 0.05$  pu.

Table 4.4: Magnetization Circuit Parameters

External Source Max Voltage	750V
Capacitor "C"	11750 $\mu F$
Diode "D"	1000 V, 1250 A
IGBT	1700 V 1400A
Coil "L"	1960 turns

Once the samples are magnetized, they are inserted in the core shown in Fig 4.5 and 4.13(b). No DC current is injected in this case, the magnetic field shown in Fig. 4.17 therefore being due exclusively to the PM field, i.e. remanent flux. A high frequency signal is applied to the coil terminals for magnet high frequency resistance estimation. Comparing Fig. 4.17 and Fig. 4.16, similar tendencies for the demagnetized and magnetized samples are observed, the higher the magnetic flux density is, the lower is the reflected high frequency resistance. While magnetoresistance effect exists in all magnets, i.e. NdFeB, ferrite and SmCo, ferrite and SmCo are less sensitive to this effect than NdFeB, which is consistent with the experimental results obtained for the demagnetized samples shown in Fig. 4.16.

Finally, it is also observed from Fig. 4.16 that the estimated magnet high frequency resistance is asymmetric with respect to the zero magnetic

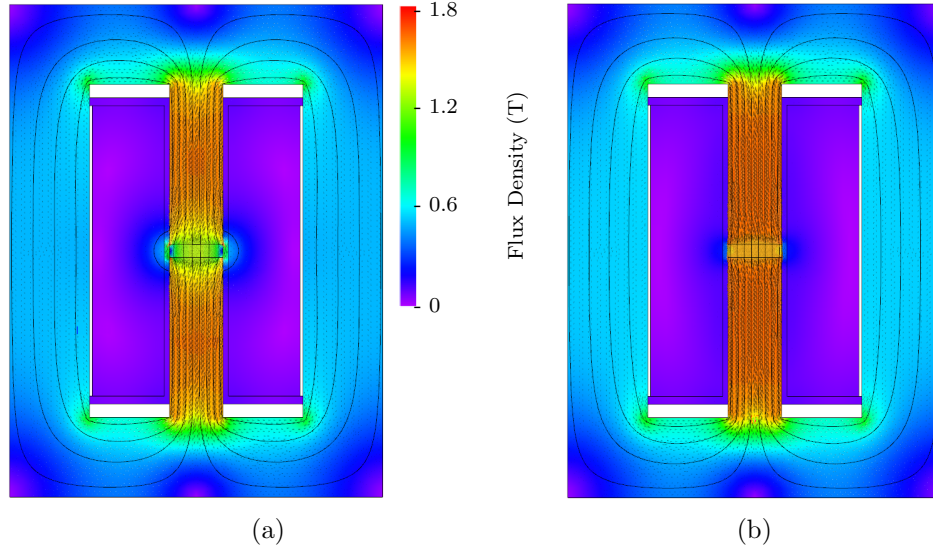


Figure 4.15: FEA results showing the magnetic flux density when the DC current injected in the coil a) intensifies and b) weakens the magnet flux.

flux density point (i.e. 0 T). The experimental setup used for this section uses a single magnetic field sensor (see Fig. 4.13). Consequently, a uniform magnetic flux distribution in the core and PM is assumed. However, both magnetic fluxes in the core and the PM will be in general non-uniform, which can induce the asymmetric behavior in the estimated magnet high frequency resistance as observed in Fig. 4.16. Figs. 4.15(a) and 4.15(b) show the core and PM magnetic flux density contours obtained by FEA when the flux induced by the current injected in coil intensifies (Fig. 4.15(a)) or weakens (Fig. 4.15(b)) the magnet flux. As it can be observed, the field distribution on the magnet surface is not uniform, and cannot be measured therefore using a single field sensor (see Fig. 4.13). This produces an error between the measured and actual average magnet flux. It is also observed from Fig. 4.15(b) that a flux leakage close to magnet edges exists. This flux leakage increases when a DC current is injected to weaken (or demagnetize) the PM and becomes zero when the PM magnetization direction changes.

#### 4.2.3.5 Magnetoresistance effect in magnetized samples combined with flux-weakening and flux intensifying

This subsection analyzes the magnetoresistance effect in magnetized PMs combined with flux-weakening and flux-intensifying current injection. A

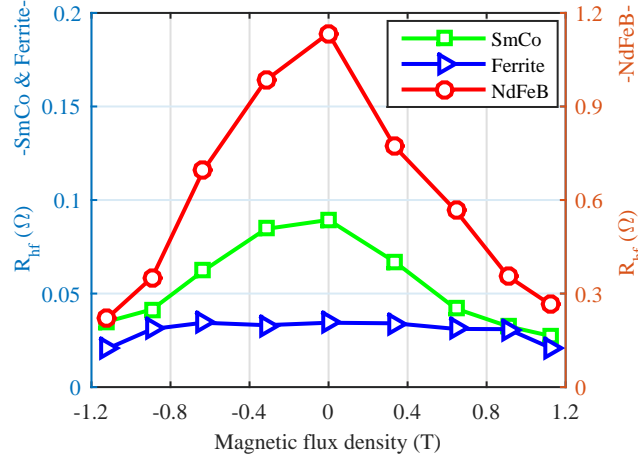


Figure 4.16: Coil reflected magnet high frequency resistance,  $R_{hfs}^p$  of a ferrite,  $\blacktriangleright$ , NdFeB,  $\circ$ , and SmCo disks,  $\square$ .  $f_{hf} = 250$  Hz,  $V_h f = 0.05$  pu.

DC current is being injected to decrease (partially counteract), i.e. flux-weakening current, or increase, flux-intensifying current, the PM field. As in the previous cases a high frequency signal is superposed to the DC current for PM high frequency resistance estimation.

For each initial magnetization state, the PM flux is weakened or intensified by injecting a DC current. It is observed that in all cases, the estimated magnet high frequency resistance decreases as the injected DC current increases, i.e. the magnetic flux density decreases or increases with respect to the magnet remanent flux. The expected behavior was that the magnetized samples would follow a similar behavior as the non-magnetized samples (see Fig. 4.16), the maximum magnitude of the high frequency resistance being obtained at zero magnetic flux density. This result was therefore unexpected and is a subject of ongoing research.

It is also observed that the estimated high frequency resistance when the PM field is counteracted by the DC current (and the resulting overall field is therefore null, i.e. temporary demagnetization) and when magnet is permanently demagnetized and no DC current is injected (see Fig 4.17) is different. This suggests that the estimated high frequency resistance allows to distinguish permanent and temporary demagnetization. This is a very interesting feature from a fault monitoring perspective. This is a subject of ongoing research.

It is concluded from the experimental results shown in Fig. 4.19- 4.21



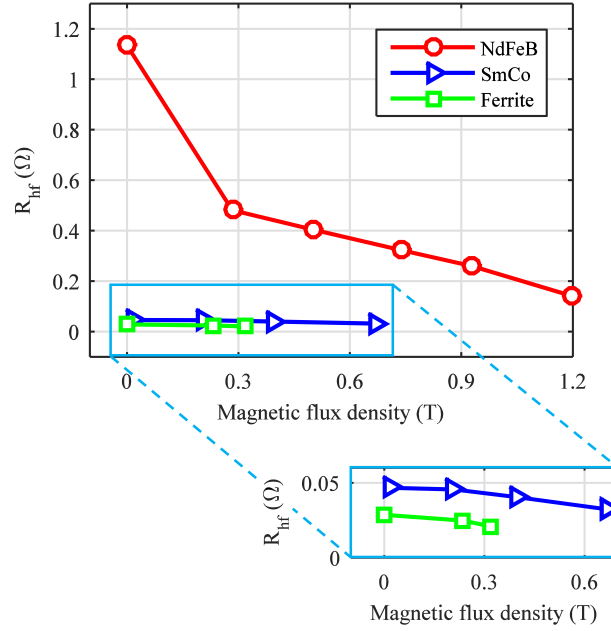


Figure 4.17: Coil reflected magnet high frequency resistance for different values of the remanent field, and no DC current for ferrite,  $\square$ , NdFeB,  $\circ$ , and SmCo disks,  $\triangleright$  disks.  $f_{hf} = 250$  Hz,  $V_{hf} = 0.05$  pu.

that the magnetoresistive effect exists in NdFeB, SmCo and ferrite magnets and that it can be potentially used for magnetization state estimation. It is also observed that the magnetoresistive effect produces larger high frequency resistance variations in NdFeB magnets than in SmCo and ferrite magnets. Consequently, magnetization state estimation in machines equipping SmCo and ferrite magnets might be more sensitive to signal-to-noise issues, AD converters resolution limits, etc.

#### 4.2.3.6 Magnetoresistance effect in segmented magnets

The same experiments as for the disks magnets have been carried out for segmented NdFeB and SmCo magnets, see Fig. 4.4. Both isolated and non-isolated configurations have been used. Kapton tape ( $60 \mu m$ ) was used to isolate the magnets (Fig. 4.4).

Figure 4.22 shows experimental results for NdFeB segmented magnets with and without isolation, for magnet thickness of 5mm and 2.5 mm respectively. The PMs were initially demagnetized, the magnetic field being

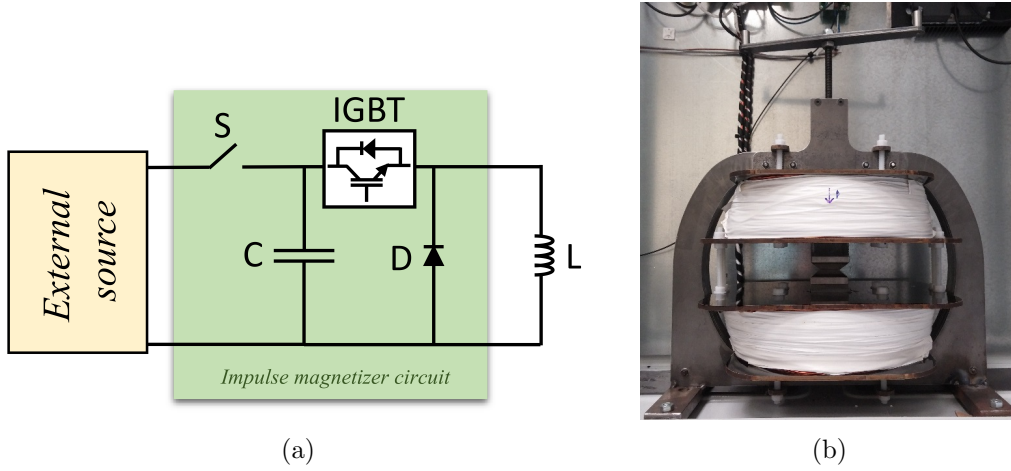


Figure 4.18: Schematic representation of the circuit used for PM magnetization and demagnetization.

then changed by means of a DC current. As in the previous experimental results, a high frequency signal is superposed to the DC current for PM high frequency resistance estimation.

It is observed from Fig. 4.22 that the reflected magnet high frequency resistance is reduced by  $\approx 60-70\%$  when the magnets are isolated. It is also observed that the reflected magnet high frequency resistance decreases with the magnet thickness decrease, what reduces the sensitivity to the magnetoresistance effect. A reduction of the reflected magnet high frequency resistance (4.13), implies an increase of the actual magnet high frequency resistance, and consequently a reduction of the induced eddy currents in the magnets and of the induced losses. It is finally noted that for the segmented magnet case, the reflected magnet high frequency resistance is always smaller than for the magnet disk, even without insulation, see Fig. 4.16 .

Figure 4.24 shows the same experimental results as in Fig. 4.22 for SmCo 5mm segmented magnets. Experimental results using SmCo 2.5mm thickness magnets were not feasible due to magnetization/demagnetization limitations using the experimental setup shown in Fig. 4.18. The same conclusions as for the NdFeB are reached in this case.

Finally, Figs. 4.23 and 4.25 shows the same experimental results as in Figs. 4.19 and 4.21, but for the case of segmented magnets (5mm thickness). The same tendencies as in Figs. 4.19 and 4.21 are observed, the conclusions being consequently the same too. Experiments with 2.5 mm thickness NdFeB

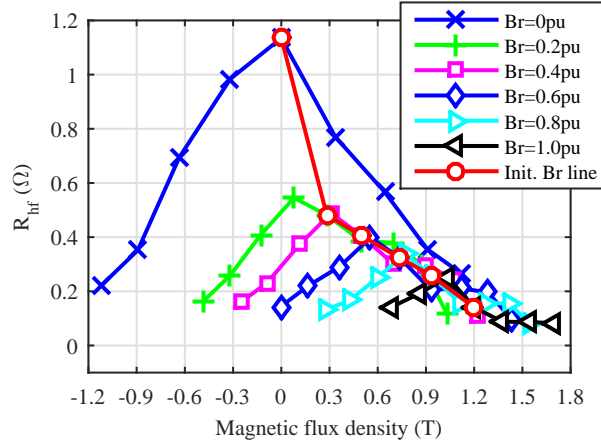


Figure 4.19: Coil reflected magnet high frequency resistance for NdFeB magnets vs. the flux density, for different values of the remanent field.  $f_{hf} = 250$  Hz,  $V_h f = 0.05$  pu.

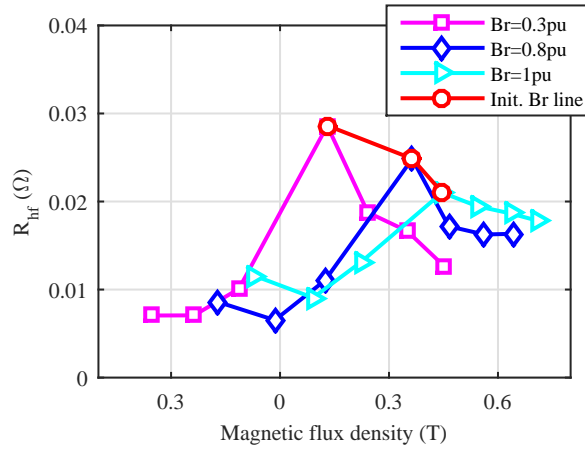


Figure 4.20: Coil reflected magnet high frequency resistance for a ferrite magnets vs. the flux density, for different values of the remanent field.  $f_{hf} = 250$  Hz,  $V_h f = 0.05$  pu.

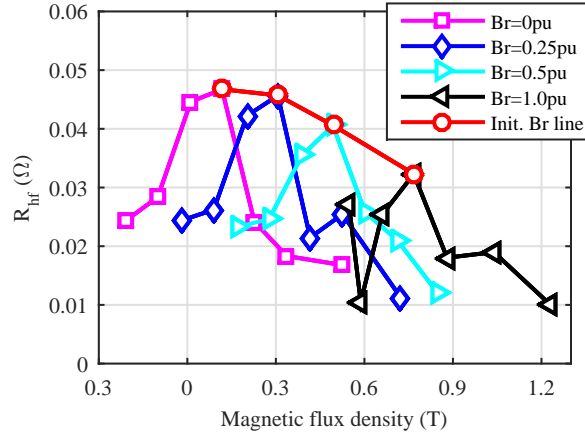


Figure 4.21: Coil reflected magnet high frequency resistance for a SmCo magnets vs. the flux density, for different values of the remanent field.  $f_{hf} = 250$  Hz,  $V_h f = 0.05$  pu.

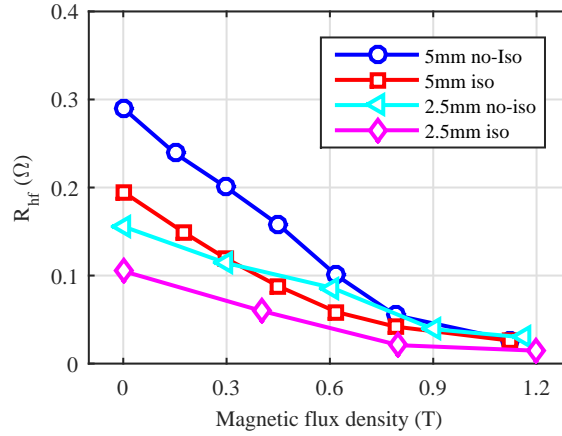


Figure 4.22: Coil reflected magnet high frequency resistance in 5 mm and 2.5 mm NdFeB segmented magnets when magnets are electrically isolated,  $\triangleleft$  and  $\diamond$ , and when there is no electric isolation,  $\circ$  and  $\square$ .  $f_{hf} = 250$  Hz,  $V_h f = 0.05$  pu.

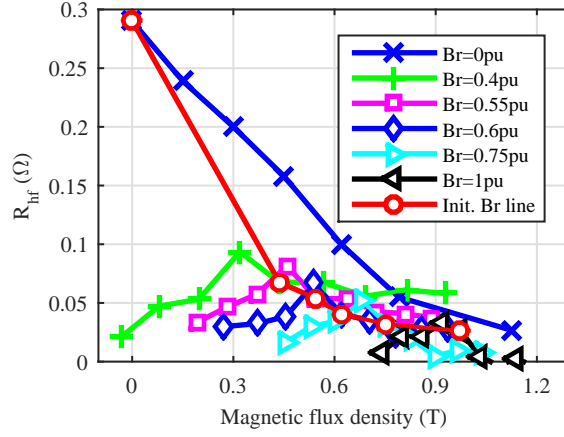


Figure 4.23: Coil reflected magnet high frequency resistance  $R_{hf}^p$  of non-isolated segmented (5 mm) NdFeB magnets.  $f_{hf} = 250$  Hz,  $V_{hf} = 0.05$  pu.

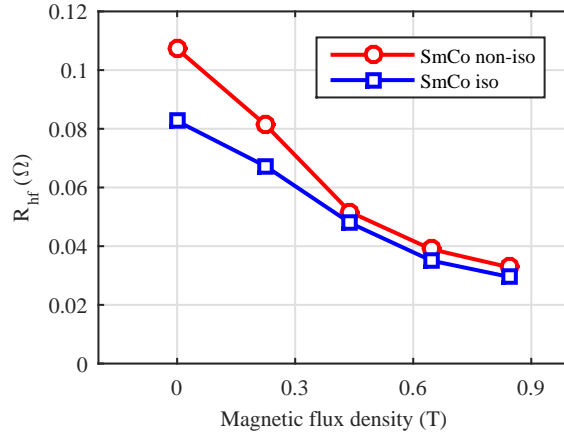


Figure 4.24: Coil reflected magnet high frequency resistance in 5 mm SmCo segmented magnets when magnets are electrically isolated,  $\circ$  and when there is no electric isolation,  $\square$ .  $f_{hf} = 250$  Hz,  $V_{hf} = 0.05$  pu.

magnets showed the same behavior, they are not included. The slope of the curves shown in Figs. 4.16, 4.19 - 4.21, 4.22 - 4.25 corresponds to the  $\beta$  coefficient in 4.4.

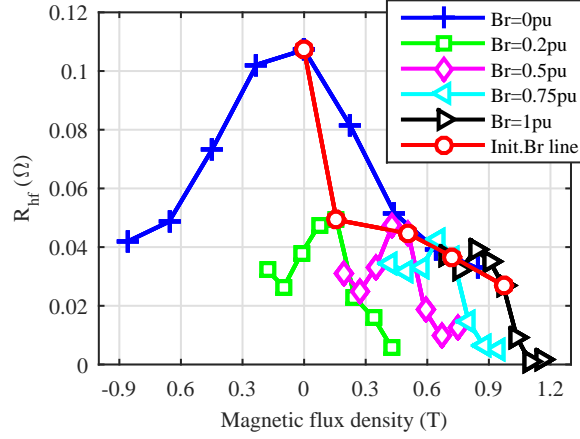


Figure 4.25: Coil reflected magnet high frequency resistance  $R_{hf}^p$  of non-isolated segmented (5 mm) SmCo magnets.  $f_{hf} = 250$  Hz,  $V_{hf} = 0.05$  pu.

### 4.3 Influence of the PM coating in the magnetoresistance effect

PMs in PMSMs often use coating for protection, e.g. NdFeB magnets are usually protected to oxidation with NiCuNi coating. Previous studies have shown that coating can improve the magnetoresistance sensitivity in the machines equipped with Ferrite, AlNiCo or SmCo magnets [101, 97]. However, this effect has not been studied in detail yet. This section analyses the effects of the PM coating on its magnetoresistance sensitivity. An experimental setup especially designed for this purpose will be used.

#### 4.3.1 Magnetoresistance effect in thin film layers

Not all materials have the same sensitivity to the magnetoresistance effect. As already explained in previous subsection, NdFeB magnets have a higher sensitive compared to Ferrite and SmCo magnets. PMs in PMSMs often use coating for protection, e.g. NdFeB magnets are usually protected to oxidation with NiCuNi coating because these type of magnets react to oxygen

and oxidizes quickly if untreated. Previous studies have shown that coating can improve the magnetoresistance sensitivity in the machines equipped with Ferrite, AlNiCo or SmCo magnets [101, 97]. However, this effect has not been studied in detail yet.

Certain layer stack arrangement designs, e.g. the layer stack arrangement shown in Fig. 4.26, can be used to increase the sensitivity to magnetoresistance effect in magnetoresistive sensors, the sensitivity increasing with the number of layers [101]. Giant magnetoresistance (GMR) is defined when the variation of the electrical resistance is higher than 10% [29]. A common arrangement to achieve GMR is a three-layer stack made of two ferromagnetic materials (e.g. Nickel, Iron...) and an electric conductor, non-ferromagnetic material (e.g. copper, gold..., see Fig. 4.26). The resistor model for GMRs is defined by (4.17) where  $R_{\uparrow\downarrow}$  is the resistance with opposite magnetization in layers (i.e. in absence of  $H$ ),  $R_{\uparrow\uparrow}$  is the resistance measured when the same direction of field  $H$  is applied to the layers and  $\delta_H$  is the GMR [101]. Therefore  $\beta$  is function of both  $MR$  and  $\delta_H$  (4.18).

It is interesting to note the similarities between the arrangements shown in Fig. 4.26 to maximize the magnetoresistive effect in the magnetoresistive sensors and the NiCuNi coating used with NdFeB magnets to avoid oxidation (see Fig. 4.28). Nickel is ferromagnetic material, copper is a non ferromagnetic material but electrical conductor, and different magnetization direction can be achieved in the ferromagnetic layers by changing the magnetization direction of the magnet.

$$\delta_H = \frac{\Delta R}{R(0)} = \frac{R_{\uparrow\uparrow} - R_{\uparrow\downarrow}}{R_{\uparrow\downarrow}} \quad (4.17)$$

$$\beta(H, \uparrow\uparrow, \uparrow\downarrow) = \frac{R(H, \uparrow\uparrow) - R(H_0, \uparrow\downarrow)}{\Delta H R(H_0, \uparrow\downarrow)} \quad (4.18)$$

### 4.3.2 Improved magnetoresistance measurement system

An initial design to isolate and measure the magnetoresistance effect found in PMSMs, avoiding the large number of design parameters that can affect to the results in a PMSM, was presented and explained in section 4.2.1. Such system does not allow to insert a field sensor on the magnet surface. To

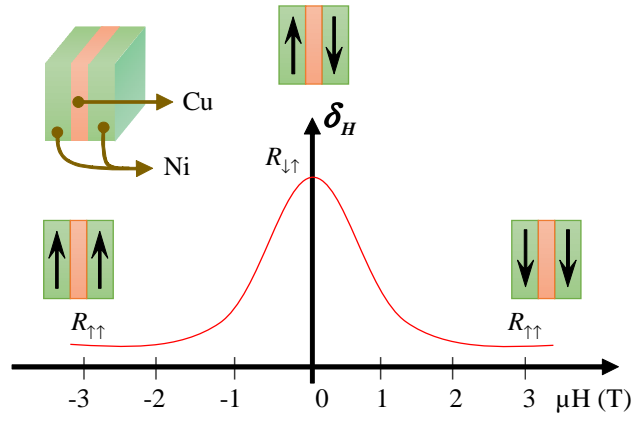


Figure 4.26: Magnetoresistance variations in multilayer structures.

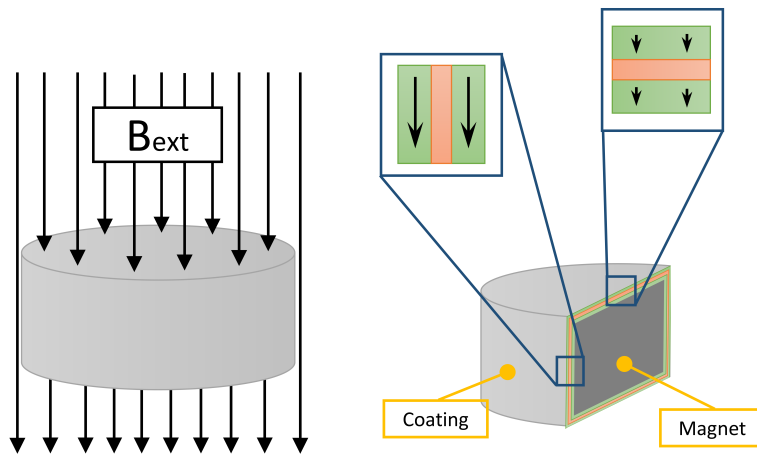


Figure 4.27: Magnetization direction of the coating layers when an external magnetic field is applied on a demagnetized magnet



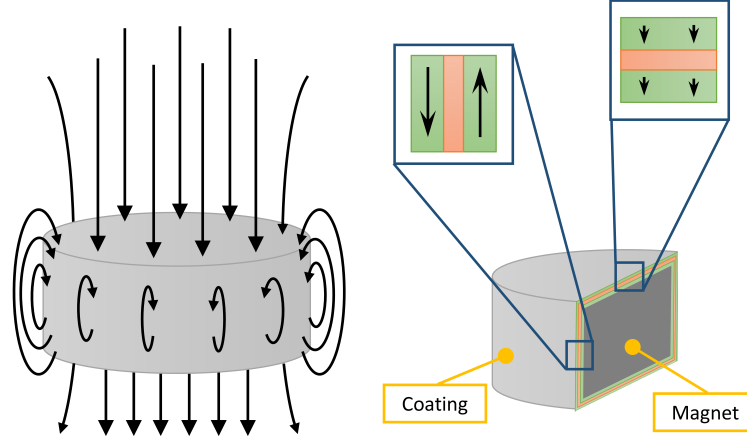


Figure 4.28: Magnetization direction of the coating layers for a magnetized magnet

overcome this issue, an enhanced experimental setup was built, see Fig.4.29 . As the previous experimental setup, see Fig. 4.5, it consist of a magnetic powder core and a coil but it includes a field measurement system.

The coil in Fig.4.29(a) is fed by an H-bridge 4.9, as explained in section 4.2.1. The H-bridge allows simultaneous injection of both DC current used to change the PM sample magnetization state and the high frequency current used to estimate the magnet sample magnetization state. The system parameters are shown in Table 4.5. Fig. 4.30 shows the power converter control block diagram. A PI controller is used to control the injected DC current  $i_{DCp}^*$ , while a resonant controller is used to control the injected the high frequency current  $i_{hfp}^*$ .

As it was explained in section 4.2.1, when the coil is fed with a high frequency current, the overall high frequency impedance is given by 4.10. The real part of the high frequency impedance,  $R_{hfp}$  is a function of the coil  $R_{hfp}^p$ , core  $R_{hfp}^p$  and magnet  $R_{hfs}^p$  high frequency resistance. Fo the magnet high frequency resistance isolation in previous section, 4.2.1, the core high frequency resistance was considered negligible as powder core is a highly resistive material. Core losses are considered now and estimated for a more accurate magnet high frequency resistance measurement.

The reflected magnet high frequency resistance,  $R_{hfs}^p$ , can be estimated from the overall coil high frequency resistance,  $R_{hfp}$ . However, this requires decoupling of the coil ( $R_{hfp}^p$ ) and core ( $R_{hfp}^p$ ) contributions to the overall

Table 4.5: Enhanced experimental setup parameters

Coil Parameters		Core Parameters	
Number Of Turns	335	Central column diameter (mm)	20
Resistance	0.3236 $\Omega$	Saturation $B_{sat}$ (T)	1.6
Parallel Wires Per Turn	7	Relative $\mu_r$ permeability	26
Inductance (nH)	12.5		
$\alpha_{cu}(1/K)$	$3.9 \times 10^3$		

high frequency resistance.

### 4.3.3 Experimental results

This subsection shows the experimental results obtained with the enhanced magnetoresistance measurement system and its characterization, for different magnets with different coatings. The characterization includes the measurement of the coil and core high frequency resistances for different  $H$  fields and frequencies. Results for the effect of coating on the magnetoresistive effect using the experimental setup shown in Fig. 4.29(a) are also presented in this section.

#### 4.3.3.1 Characterization of the experimental setup

The coil high frequency resistance  $R_{hfp}^p$  can be approximated by removing the coil from the core and injecting a high frequency signal. Under these conditions, the equivalent high frequency circuit is shown in Fig. 4.31(a). Figs. 4.31(b) shows  $R_{hfp}^p$  vs. the frequency of the injected signal. Fig. 4.31(c) show  $R_{hfp}^p$  vs. the strength of the magnetic field,  $H$ , which is produced by forcing a DC current into the coil. As expected,  $R_{hfp}^p$  increases as the frequency does due to the skin effect (see Fig. 4.31(c)). Also as expected,  $R_{hfp}^p$  slightly increases with  $H$ , meaning that the magnetoresistive effect in the coil (made of copper) cannot be negligible.

The core high frequency resistance, i.e.  $R_{hFEP}^p$ , can be estimated by injecting a high frequency signal into the coil with the coil and the core assembled, and replacing the magnet in the central column by a non-ferromagnetic

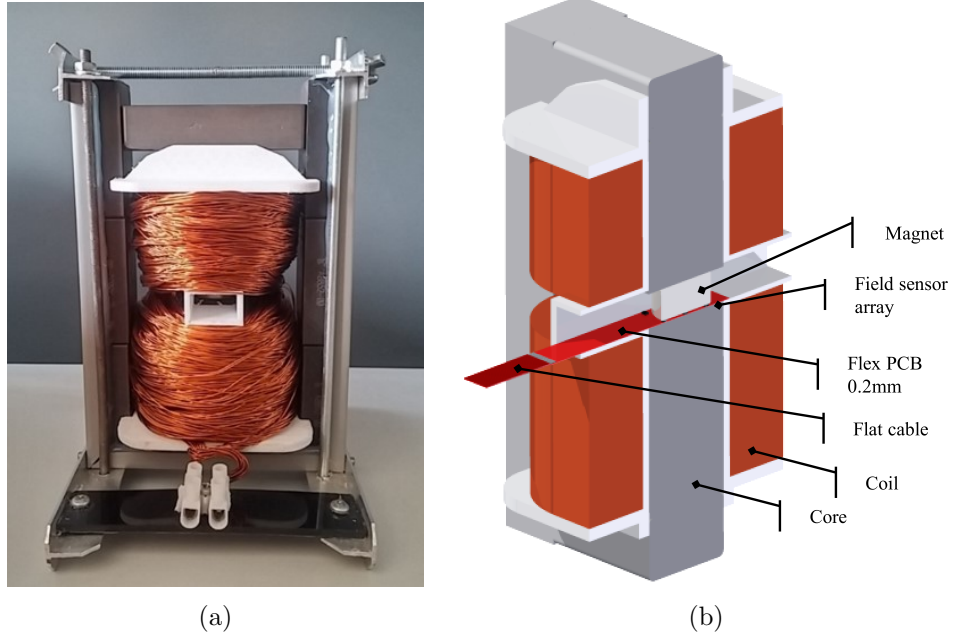


Figure 4.29: Enhanced experimental setup for magnetoresistance evaluation, (a) and section of the experimental setup, (b).

material (see Fig. 4.32(a)). Fig. 4.32(b) shows the equivalent circuit in this case, the core high frequency resistance being obtained after decoupling the coil high frequency resistance,  $R_{hfp}^p$  (4.13). Figs. 4.32(c) and 4.32(d) show  $R_{hFEfp}^p$  vs. the frequency of the injected signal and vs.  $H$ , similar to Figs. 4.31(b) and 4.31(c). As for  $R_{hfp}^p$ ,  $R_{hFEfp}^p$  increases with frequency due to the skin effect (see Fig. 4.32(d)). It is observed from Fig. 4.32(d) that decreases as  $H$  increases, meaning that core is slightly affected by the magnetoresistive effect. This was an expected result [70].

$$R_{hfs}^p = \frac{R_{hfp}^p R_{hFEfp}^s - R_{hfp} R_{hFEfp}^s}{R_{hfp} - R_{hfp}^p - R_{hFEfp}^p} \quad (4.19)$$

Finally, the contribution of the magnet resistance,  $R_{hfs}^p$ , to the overall high frequency resistance can be measured by inserting the magnet in the central column of the core (Fig. 4.33(a)), once the core and coil contribution to the overall high frequency resistances is decoupled (4.19). The equivalent circuit and measured high frequency resistance in this case are shown in Fig.

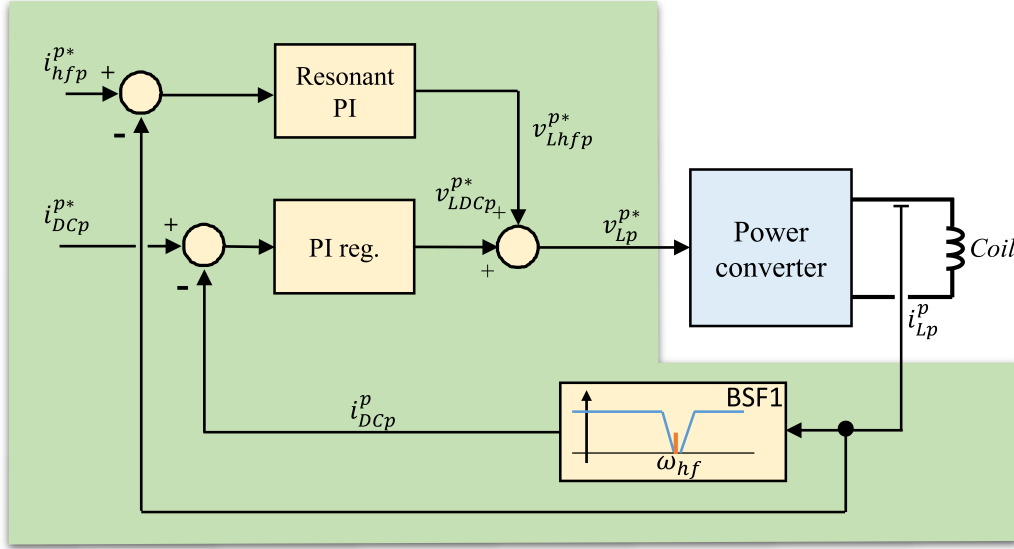


Figure 4.30: Block diagram of the DC and high frequency signal

4.33(b) and Fig. 4.33(c), for a NdFeB magnet. It is observed from this figure that  $R_{hfs}^p$  significantly decreases with  $H$ , Fig. 4.33(d) i.e. the magnet is strongly affected by the magnetoresistive effect.

#### 4.3.3.2 Experimental results for demagnetized samples

Experimental results measuring the effect of coating on the magnetoresistive effect using the experimental setup shown in Fig. 4.29(a) are presented in this section. Demagnetized and magnetized NdFeB, SmCo and AlNiCo disk shaped magnets have been tested. Two types of coatings, NiCuNi and Epoxy were used. Magnet thickness 5 and 10 mm, were selected, all with the same radius (see Fig. 4.34).

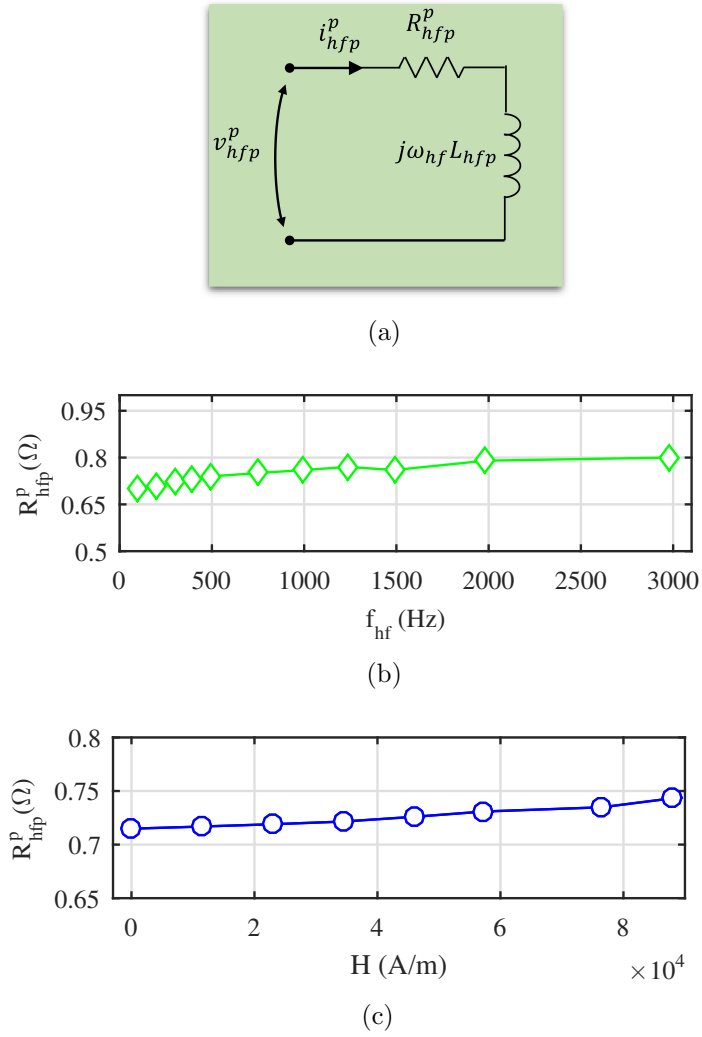


Figure 4.31: a) Equivalent high frequency circuit of the experimental setup without core and magnet, b) coil high frequency resistance,  $R_{hfp}^p$ , for different frequencies, c) coil high frequency resistance,  $R_{hfp}^p$ , for different values of  $H$  values.  $f_{hf}=250\text{Hz}$  and  $i_{hf}=1\text{A}$ .

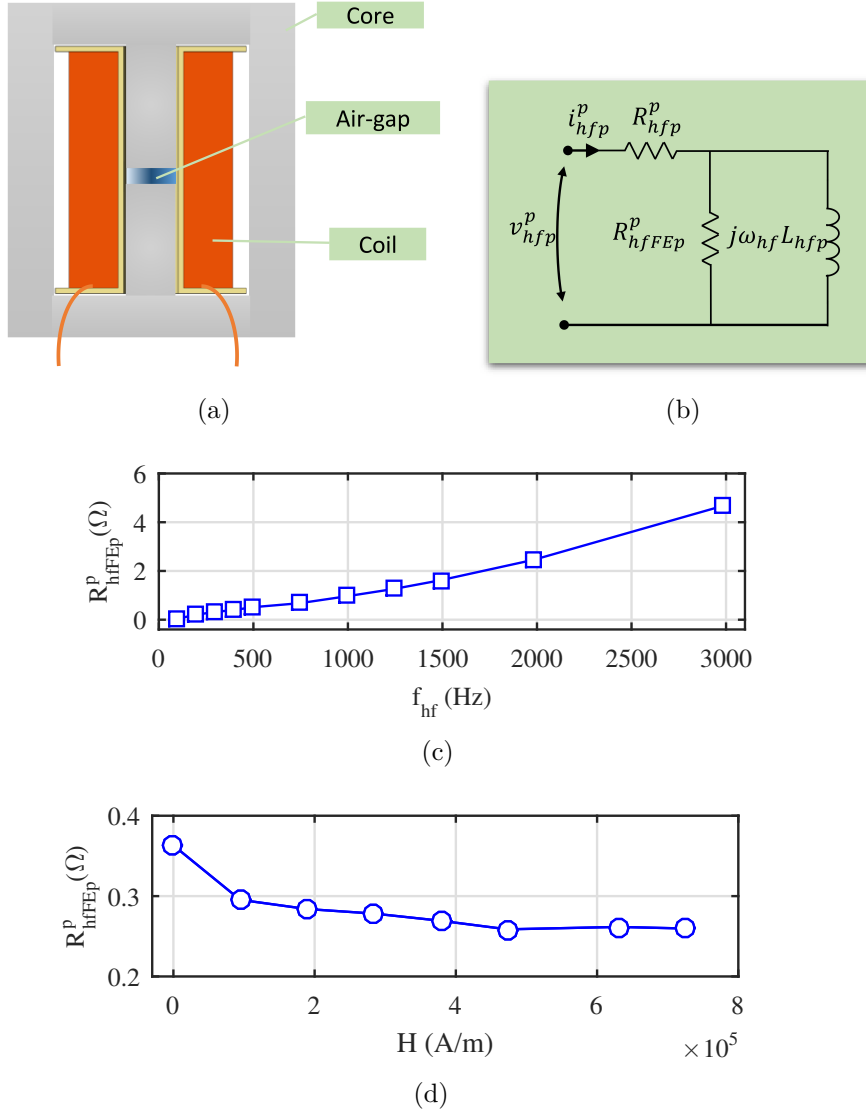


Figure 4.32: a) Experimental setup configured for core high frequency resistance estimation (i.e. without magnet), b) equivalent high frequency circuit and c) core high frequency resistance,  $R_{hfFEp}^p$ , for different frequency values, d)  $R_{hfFEp}^p$ , for different  $H$  values.  $f_{hf}=250\text{Hz}$  and  $i_{hf}=1\text{A}$ .

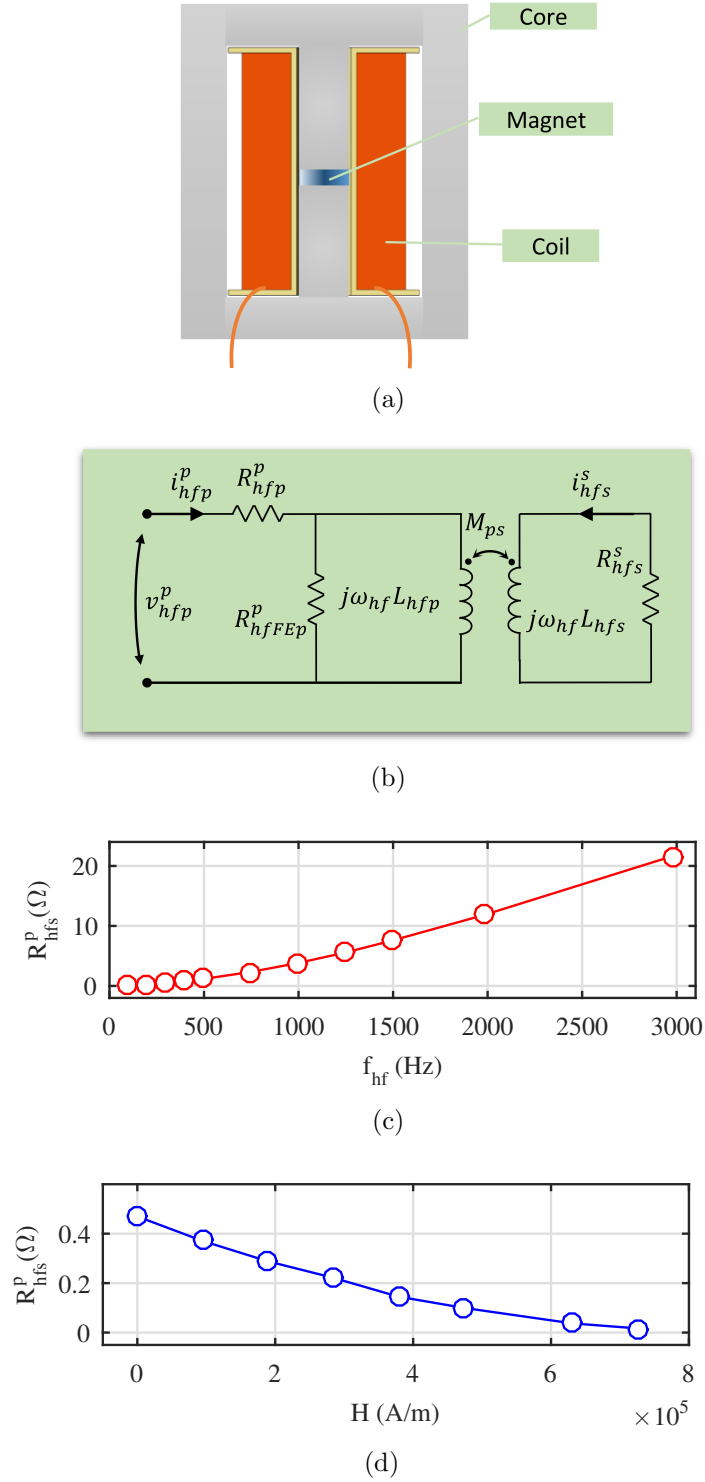


Figure 4.33: a) Experimental setup configured for magnet high frequency resistance estimation, b) equivalent high frequency circuit, c) magnet high frequency resistance for different frequency values, d)  $R_{hfs}^p$ , for different  $H$  values.  $f_{hf}=250\text{Hz}$  and  $i_h=1\text{A}$ .

Table 4.6: Magnetic materials and coating thickness

MAterial	NdFeB (N-42)	SmCo (2:17)	AlNiCo
Ni layer thickness ( $\mu\text{m}$ )	3	3	3
Cu layer thickness ( $\mu\text{m}$ )	4	4	4
NiCuNi total thickness ( $\mu\text{m}$ )	11	11	11
Epoxy thickness ( $\mu\text{m}$ )	6	6	6
Magnet total thickness (mm)	5,10	5,10	5,10

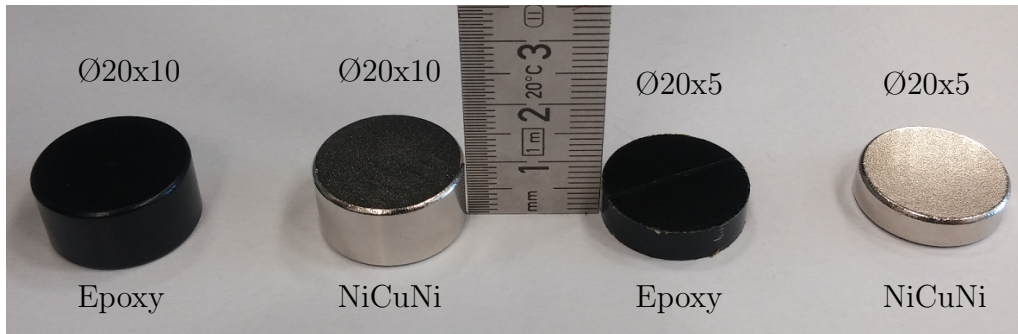


Figure 4.34: Block diagram of the DC and high frequency signal

Epoxy coating presents the same magnetic permeability as air. It was used to keep the same total magnet width, avoiding variations in the equivalent reluctance path of the prototype. In addition, the thickness of the magnet material is also kept constant, avoiding errors due to the differences in volume among samples. Magnets and coating characteristics are summarized in Table 4.6.

If magnetic flux density is measured with only one sensor, errors may occur as the magnetization is not uniform along the magnet surface [70]. To avoid this problem, a thin PCB (0.7mm thickness), see Fig. ??, that is equipped with a matrix of 3x3 hall sensors was designed to measure the magnet flux density distribution on the magnet surface. The measurement provided by all the nine field sensors will be averaged, and used as a metric of the PM magnetic flux density. Fig. 4.35 shows an example of a contour plot of the field measured by the Hall sensor array when the magnet is fully demagnetized and a DC field of  $\approx 0.8$  T is applied by injecting a DC current into the coil terminals, see Fig. 4.33(a).



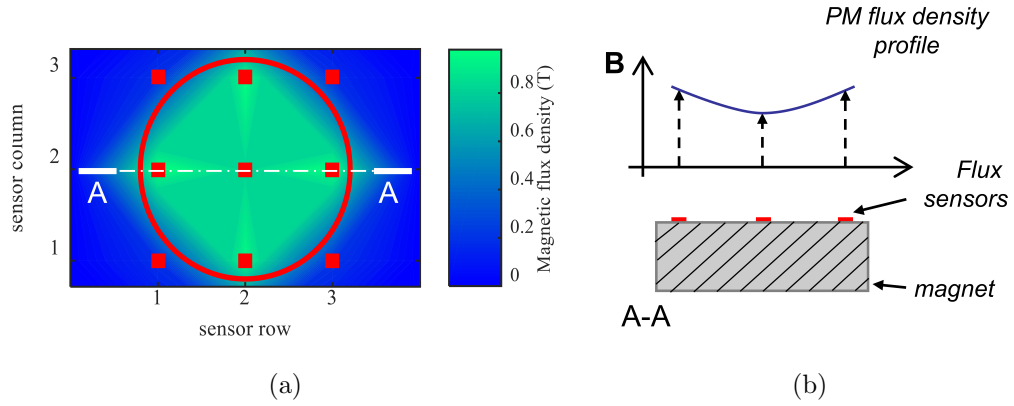


Figure 4.35: a) Magnetic flux density distribution on magnet surface for a demagnetized NdFeB magnet when constant DC field is applied by the coil. Magnet location is indicated by the red circle, sensors location are represented by red squared spots. b) Magnetic flux density trend of a radial cross section of the magnet, A-A.

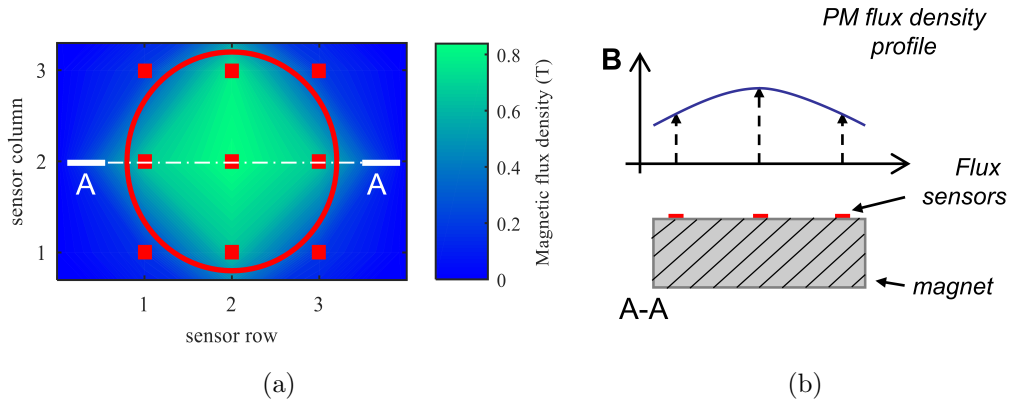


Figure 4.36: a) Magnetic flux density distribution on magnet surface for a fully magnetized NdFeB. Magnet size and position is represented by the red circle, sensors positions represented by red squared spots. b) Magnetic flux density trend of a radial cross section of the magnet, A-A.

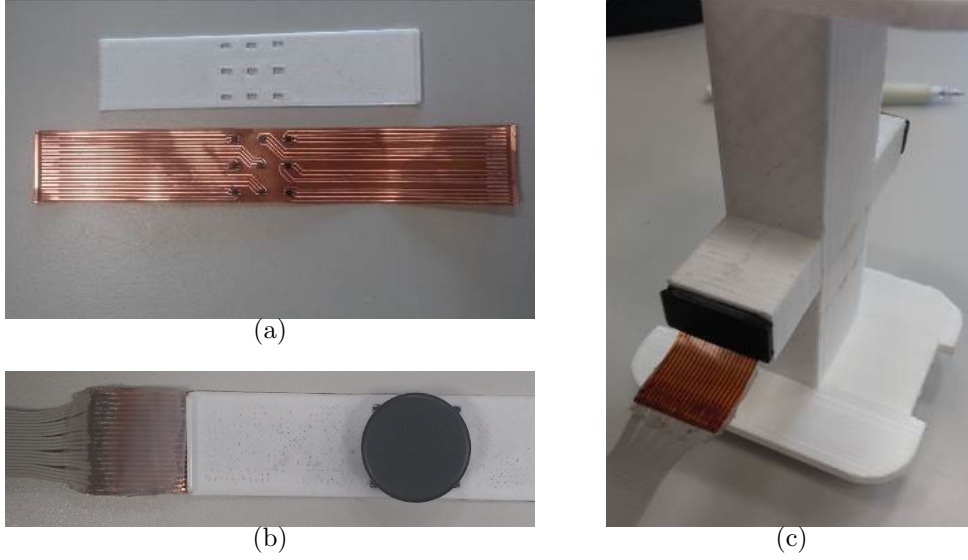


Figure 4.37: a) Flux density sensor, b) position of the magnet on the sensor array, c) flux density sensor inserted in the plastic coil former

#### 4.3.3.3 Experimental results for demagnetized samples

Figs. 4.38-4.40 show the reflected magnet high frequency resistance,  $R_{hf,s}^p$ , for the NdFeB, SmCo and AlNiCo samples. The demagnetized PMs are inserted in the core as shown in Fig. 4.33(a). The magnet, coil and core temperatures are at room temperature. All magnets were initially fully demagnetized,  $B$  being therefore the result of the injected DC current. The high frequency current used for high frequency resistance estimation is superimposed to the DC current. The core and coil high frequency resistances are decoupled from the total estimated high frequency resistance (4.19), using the data shown in Figs. (4.31(c)) and (4.32(d)).

It can be observed from Figs. 4.38-4.40 that the thicker magnets show larger high high frequency resistance when no DC field is applied. Most PMs materials show similar values of the estimated high frequency for large values of the DC field ( $>0.7T$ ), independently of the magnet thickness. The exception is the SmCo magnet, see Fig. 4.40, magnet with epoxy coating, which shows slightly lower resistance at high DC magnetic fields. The highest variation of the high frequency resistance is observed for NdFeB magnets. This was expected as this material presents the largest high frequency resistance variations with the magnetization state.

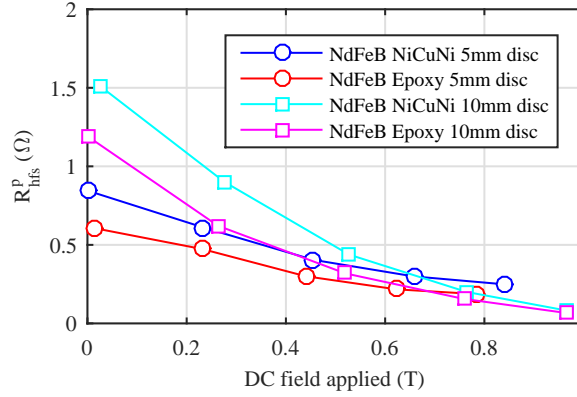


Figure 4.38: Reflected high frequency resistance  $R_{hfs}^p$  of a NdFeB magnet for two different thickness and coating types.  $20^\circ\text{C}$ ,  $f_{hf}=250\text{Hz}$  and  $I_{hf}=1\text{A}$ .

#### 4.3.3.4 Experimental results for magnetized samples

Thicker lines in Figs. 4.41-4.42 show experimental results for NdFeB, Al-NiCo and SmCo magnets, with and without coating, for five different magnetization levels, i.e. remanent fluxes, of 0, 25, 50, 75 and 100 % of its nominal value (1.2 T for NdFeB, 0.8 T for AlNiCo and 0.9 T for SmCo magnets).

The magnet samples were magnetized using a peak magnetizer shown in Fig. 4.18(b). The magnetizer parameters are shown in Table IV. Once the samples are magnetized, they are inserted in the core shown in Fig 8a. No DC current is injected in this case, only the high frequency current signal needed for high frequency resistance estimation is being applied. The magnetic field shown in Figs. 4.41-4.42 is attributed therefore exclusively to the PM remanent flux.

It is observed that in all cases, the higher the magnetization state is, the lower is the reflected high frequency resistance. It is also observed that magnets with NiCuNi coating show larger high frequency resistance variations, meaning that they are more sensitive to the magnetoresistive effect. The estimated high frequency resistance when the magnetic field is produced externally by the coil (see Figs. 4.38-4.40) is different from the estimated high frequency resistance when the flux is produced by the magnet itself. This is mainly due to the differences in the magnetic flux distribution between magnetized magnet and demagnetized magnet within the magnetic circuit (see Figs. 4.35 and 4.36).

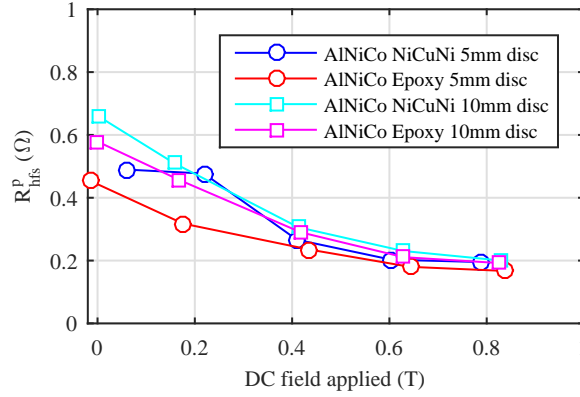


Figure 4.39: Reflected high frequency resistance  $R_{hfs}^p$  of a NdFeB magnet for two different tickness and coating types.  $20^\circ C$ ,  $f_{hf}=250\text{Hz}$  and  $I_{hf}=1\text{A}$ .

#### 4.3.3.5 Experimental results for magnetized samples with flux-weakening and flux intensifying

Figs 4.41-4.42 show experimental results for NdFeB, AlNiCo and SmCo magnets, with and without coating, for different magnetization levels, when flux weakening/ intensifying current is applied. Thicker lines show the high frequency resistance obtained for different DC current levels, for three different values of the initial magnetization level of  $\approx 0$ , 50 and 100%. The maximum injected DC current is limited by the power losses in the coil, as coil and magnet should remain at constant temperature for all the experiments. As in the previous cases, a high frequency signal is superposed to the DC current for high frequency resistance estimation.

For each initial magnetization level, the magnet flux is weakened or intensified by injecting a DC current. It is observed that in all cases the estimated resistance in absence of DC current increases when the permanent magnet flux is weakened and decreases as the magnetic field the magnet surface increases. Different trends are observed by the estimated high frequency resistance for different PM remanences and for magnetized magnets when an external field is used to weaken/intensify its field, no determinant conclusion is reached for this results.

It is concluded from the experimental results that the studied magnet materials coating changes the magnetoresistance effect. The largest high frequency resistance variations are for NdFeB, being slightly smaller for AlNiCo magnets. SmCo magnets show the smallest high frequency resistance variations.

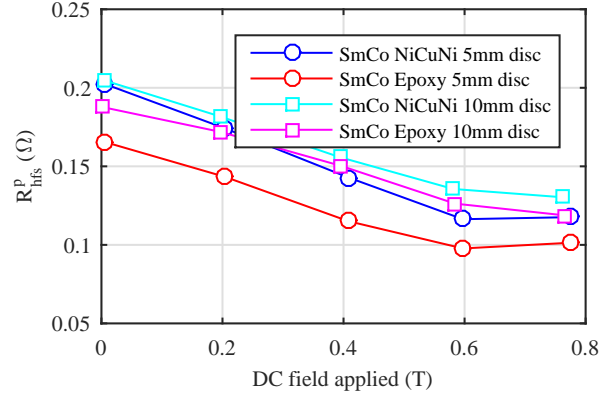


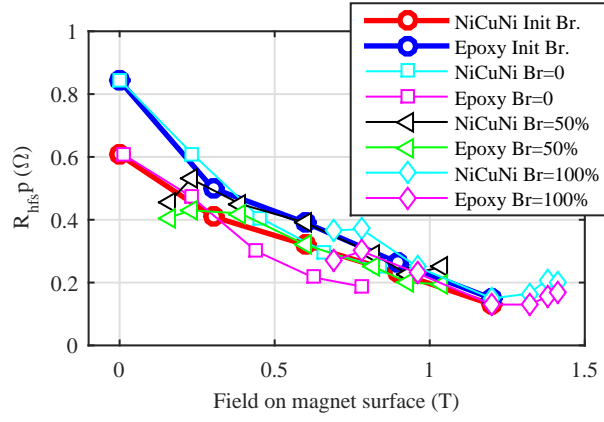
Figure 4.40: Reflected high frequency resistance  $R_{hfs}^p$  of a NdFeB magnet for two different tickness and coating types.  $20^\circ\text{C}$ ,  $f_{hf}=250\text{Hz}$  and  $I_{hf}=1\text{A}$ .

## 4.4 Magnetoresistance effect in PMSMs

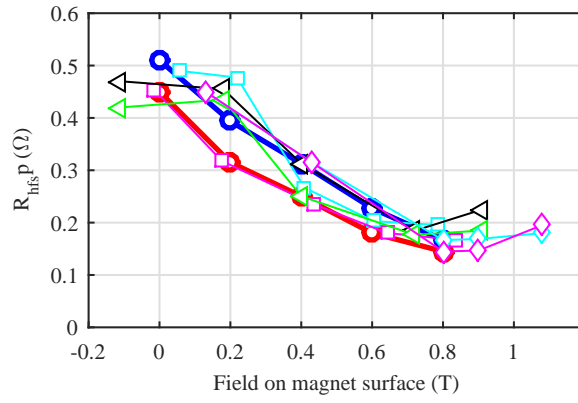
When a high-frequency signal voltage is injected in the stator windings, the PM resistivity variation due to the magnetization state variation (either due to the injection of fundamental current or temperature variations) will affect to the eddy current induced in the magnets, eventually producing effects that are measurable from the stator windings [102]. Finite-element analysis (FEA) will be used to evaluate the eddy-current distribution when the magnetization state of the machine changes. Fig. 4.43 shows the SPMSM design, and the parameters of the machine are shown in Table 2.3. Fig. 4.44(a) shows a pole pitch in more detail, whereas Fig. 4.44(b) shows the XYZ coordinate system to be used to represent the eddy current in the PM.

Fig. 4.45 shows the eddy-current density distribution within a PM obtained using FEA when a pulsating high-frequency voltage is injected, and  $I_q$  and  $I_d$  are equal to zero. The relative position of the rotor with respect to the stator is shown in Fig. 4.44(a), with the location of the stator slots being indicated in Fig. 4.45. The eddy-current direction and density are indicated by the arrows and the color bar, respectively. The coordinate reference system shown in Fig. 4.45 is as for Fig. 4.44(b). It is observed in Fig. 4.45 that the highest value of the eddy-current density due to the injected high-frequency signal is seen to occur in the region of the PM facing the stator slots (stator slotting effect).

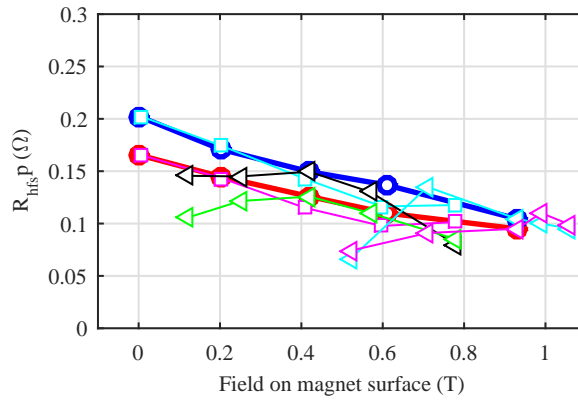
Fig. 4.46 shows the eddy-current density distribution, when  $I_d$  varies from -15 A (-1 pu) to 0 A in steps of 5 A. The flux due to a negative  $I_d$



(a)

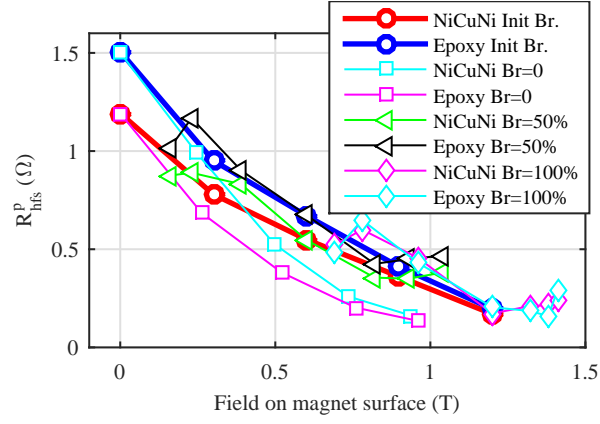


(b)

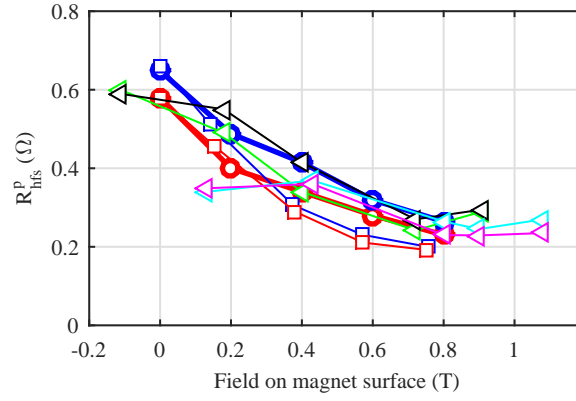


(c)

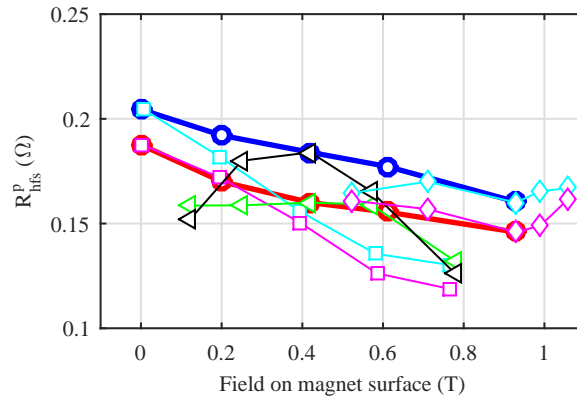
Figure 4.41: Reflected high frequency resistance  $R_{hfs}^p$  of, a), NdFeB magnet, b), AlNiCo magnet, and c) SmCo magnet, for 5mm thickness and for two different coatings.  $20^\circ C$ ,  $f_{hf}=250\text{Hz}$  and  $I_{hf}=1\text{A}$ .



(a)



(b)



(c)

Figure 4.42: Reflected high frequency resistance  $R_{hfs}^p$  of a), NdFeB magnet, b), AlNiCo magnet, and c) SmCo magnet, for 10mm tickness and for two different coatings.  $20^\circ C$ ,  $f_{hf}=250\text{Hz}$  and  $I_{hf}=1\text{A}$ .

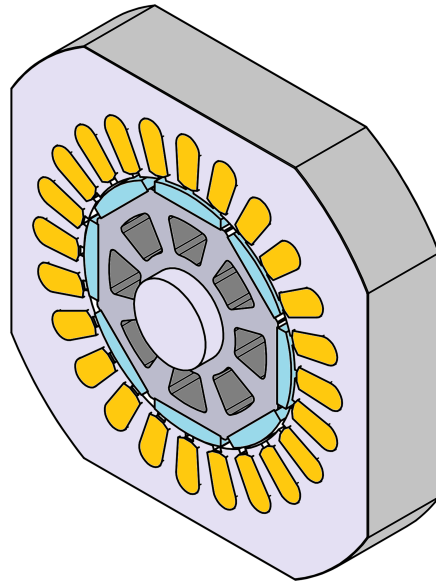


Figure 4.43: SPMSM FEA model.

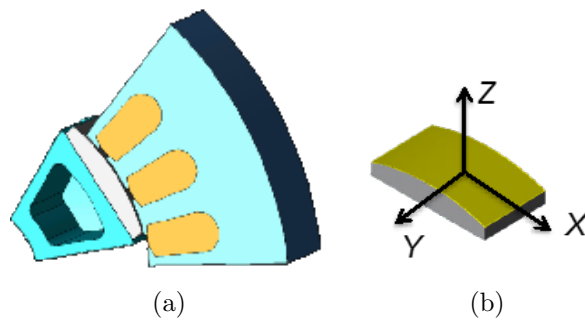


Figure 4.44: Rotor position relative to the stator for all the simulations a), and  $XYZ$  coordinated system, b).



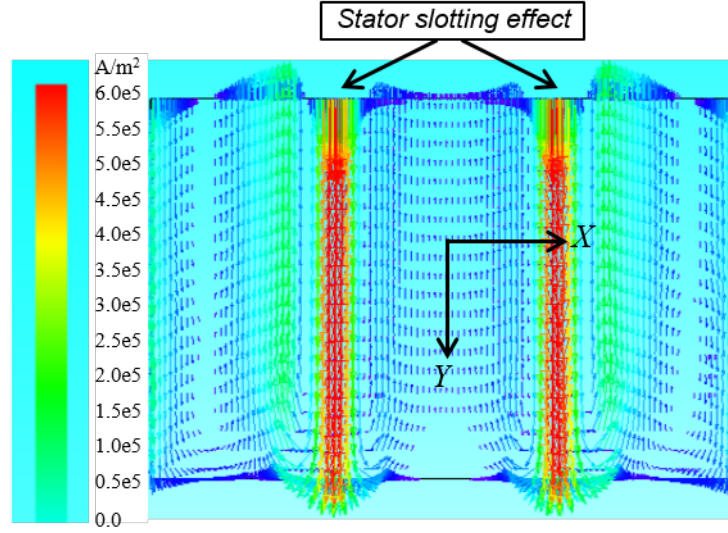


Figure 4.45: Eddy-current distribution in a PM. Pulsating high frequency signal injection,  $V_{hf}=0.05$  pu, 250 Hz.  $I_q=0$ ,  $I_d=0$ ,  $\omega_r=50$  Hz.

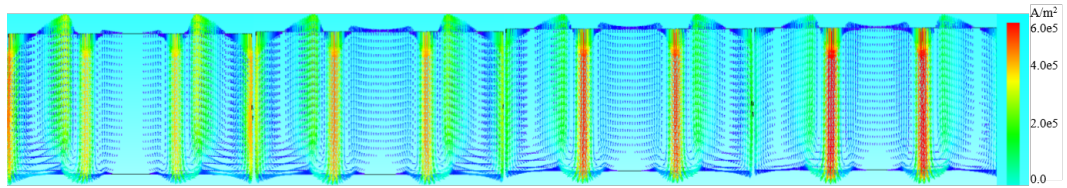


Figure 4.46: Eddy-current density distribution in the PM when  $I_d$  current changes from -15 to 0 A. Pulsating high frequency signal injection,  $V_{hf}=0.05$  pu, 250 Hz.  $I_q=0$ ,  $I_d=0$ ,  $\omega_r=50$  Hz.

current partially counteracts the magnet flux (e.g., flux weakening). It is observed in Fig. 4.46 that the eddy currents induced in the PM due to the injection of the high-frequency voltage decrease as  $I_d$  becomes more negative (higher flux weakening). A decrease in the eddy currents with the injected stator high-frequency voltage kept constant implies an increase in the high-frequency resistance seen from the stator, which can be used to estimate the magnetization state of the PM. The PM stator-reflected high-frequency resistance responds to the model shown in 4.4, which can therefore be used for PM magnetization state estimation.

#### 4.4.1 PM High frequency resistance estimation

The injection of a high-frequency signal in the stator terminals of a PMSM has been shown in chapter 2 to be a viable option to estimate the magnet high-frequency impedance [32, 31]. High-frequency rotating voltage vector (2.17) or a sinusoidal pulsating (2.24) can be used for this purpose [32, 40]. Other forms of high-frequency excitation such as a square wave [30] are also viable.

While all these forms of high-frequency excitation respond to the same physical principles and can potentially provide the same performance, some differences exist in their practical implementation. In SPMSM, the rotor magnets shield the rotor lamination [32, 31], [40]. The injected high-frequency voltage will induce eddy current mainly in the PMs. Consequently, the variations in the measured stator high-frequency resistance will be dominated by the resistivity variation of the PMs, independently of the type of high-frequency signal injection. Rotating (2.17) and pulsating (2.24) high-frequency injection could therefore be used for this machine design [40]. On the contrary, for IPMSMs, both the rotor lamination and the PMs are affected by the high-frequency flux due to the high-frequency signal injection. The assumption that the estimated high-frequency resistance only depends on the PM high-frequency resistance does not hold in this case. The use of pulsating injection in the  $d$ -axis is preferred in this case as it will be more sensitive to effects occurring in the PM. On the contrary, injection of a rotating signal will have the undesirable effect of increasing the sensitivity to effects occurring in the rotor lamination [40]. Pulsating high-frequency signal injection is therefore preferred and will be discussed following.

The estimation of  $d$ -axis high-frequency resistance of a PMSM using pulsating high frequency signal injection was explained in Chapter 2, section 2.2. The  $d$ -axis high-frequency resistance resulting from the combined effect

of stator and rotor high-frequency resistances is obtained from (2.32). The rotor contribution to the stator  $d$ -axis high-frequency resistance is estimated using (4.20), where  $\alpha_{cu}$  is the copper thermal resistive coefficient,  $R_{drhf}$  is the stator-reflected rotor  $d$ -axis high-frequency resistance, and  $R_{dshf}$  is the stator  $d$ -axis high-frequency resistance. It is seen therefore, that knowledge of the stator high-frequency resistance at room temperature is required.

$$R_{drhf} = R_{dhf} - R_{dshf} = R_{dhf} - R_{dshf(T_0)}(1 + \alpha_{cu}(T_s - T_0)) \quad (4.20)$$

It is noted that, although the stator high-frequency resistance mainly depends on the stator winding resistance, it could be also influenced by eddy current and proximity effects occurring in the slot windings. However, the stator winding resistance at the room temperature can be easily estimated and stored in a previous commissioning process, and later accessed during machine operation, with its effects being therefore compensated.

It is finally noted that the stator-reflected PM high-frequency resistance obtained from (4.20) is a lumped parameter, i.e., it does not contain information on the spatial distribution of the magnetization state.

Fig. 6 shows the signal processing used to obtain the stator-reflected rotor  $d$ -axis high-frequency resistance. Two bandpass filters (BPF1 and BPF2) are used to isolate the positive sequence component of the high-frequency voltage and current. The inputs to the estimation block are the commanded high-frequency voltage  $v_{dqhf}^*$ , the measured high-frequency current  $i_{dqhf}^r$ , the stator temperature  $T_s$ , and the stator resistance at the room temperature  $R_{hs(T_0)}$ . The stator temperature can be measured using contact-type sensors [32, 31, 40]: thermocouples (e.g., PT-100) being commonly used for this purpose. PT-100 temperature sensors will be used for the experimental results presented in this subsection.

The proposed method has practically no effect on the motor performance. The high-frequency signal is injected on top of the fundamental excitation, with the torque production capability of the machine not being affected. A relatively simple filtering process effectively separates the high frequency and the fundamental signals, avoiding any interference with the current control or any other outer control loop [32, 31, 40, 103, 104].

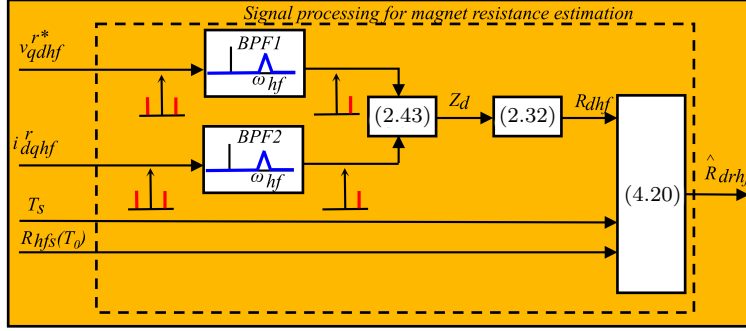


Figure 4.47: Signal processing for rotor high-frequency-resistance estimation using pulsating voltage injection.

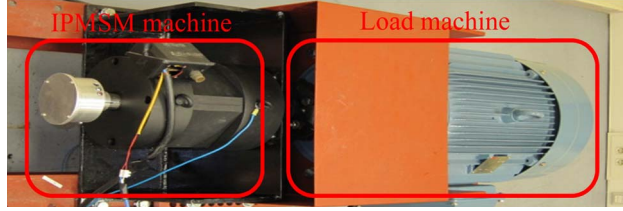


Figure 4.48: Experimental test bench (IPMSM).

#### 4.4.2 Experimental verification of the magneto-resistive effect in PMSMs

#### 4.4.3 Simulation and experimental results

Simulation results using FEA and experimental results using a SPMSM and an IPMSM are presented in this subsection. The machines' parameters are shown in Table 2.3. Fig. 2.5 shows the test machines, whereas Fig. 4.48 shows the experimental setup. An induction machine (IM) was used to load the test machines.

Injection of  $I_d$  current is the most commonly used method to change the PM magnetization state [35, 36, 88, 89]. However, PM magnetization state also can be influenced by the injection of  $I_q$  current due to the cross-coupling that typically exists between  $d$ -axis and  $q$ -axis. However, cross-coupling between  $d$ -axis and  $q$ -axis in the test machines is almost negligible; hence, magnetization state is only proportional to the  $I_d$  current magnitude.

Fig. 4.49 shows the estimated  $d$ -axis stator-reflected magnet high-frequency resistance as a function of the magnetization state due to  $I_d$  current injection.

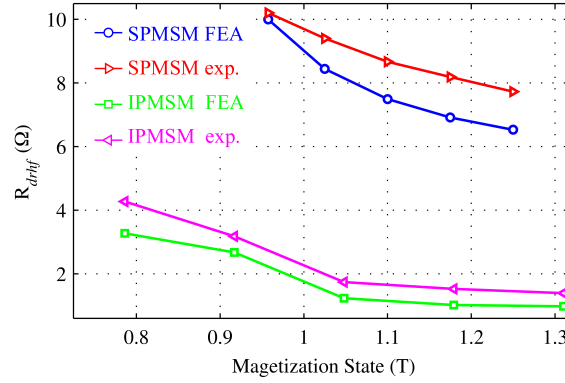


Figure 4.49: Estimated  $d$ -axis stator-reflected magnet high-frequency resistance obtained both by FEA and experimental. Pulsating  $d$ -axis high-frequency voltage injection,  $\omega_{hf} = 250$  Hz,  $V_{hf} = 0.05$  p.u.  $I_q = 0$  p.u. and  $\omega_r = 0$  p.u..

tion, obtained both by FEA and experiment. Machines designs and injected high-frequency signals are the same in both cases. Both simulation and experimental results are obtained using the same variables (stator voltages and currents) and signal processing (see subsection 2.2 and Fig. 4.47). The minimum magnetization state that can be achieved by  $I_d$  current injection is  $\approx 0.957$  T for the SPMSM and  $\approx 0.804$  T for the IPMSM; the magnetization state is changed in steps of  $\approx 0.072$  T for the SPMSM and  $\approx 0.129$  T for the IPMSM. The variation of the estimated  $d$ -axis stator-reflected high-frequency resistance with the magnetization state is readily observed in both machines. This confirms the connection between the PM magnetization state and the  $d$ -axis stator-reflected magnet high frequency resistance and therefore supports the use of the high-frequency resistance for PM magnetization state estimation. It is observed that the higher the magnetization state of the machine is, the lower the rotor magnet resistance due to the magnetoresistive effect. In obtaining the results shown in Fig. 4.49, the rotor is locked. A good agreement between simulation and experimental results is observed. This confirms that the variation of the  $d$ -axis stator-reflected PM high-frequency resistance can be used for magnetization state estimation.

It is also noted that the tendencies observed in the measurement system described in section 4.2.3 (see Fig. 4.19), are confirmed by the simulation and experimental results with an SPMSM and an IPMSM in Fig. 4.49, for the same type of magnets. It is observed that the rate of variation of the estimated high-frequency resistance with the PM magnetization state decreases as the magnet and core become more saturated (higher magnetization state),

which is consistent with the results shown in Fig. 4.19. Consequently, a careful design of the signal acquisition and signal processing will then be required in this case due to the reduction in the sensitivity.

Fig. 4.50 shows experimental results of estimated  $d$ -axis stator reflected magnet high-frequency resistance and magnetization state estimation error versus the magnetization state and speed for two test machines (SPMSM and IPMSM). Magnetization state was varied from the minimum value that can be achieved for each machine (i.e.,  $\approx 0.957$  and  $\approx 0.804$  T for the SPMSM and IPMSM, respectively). The speed varies in steps of 0.1 p.u. from zero to the maximum speed that can be achieved for each magnetization state condition. It is observed that the estimated  $d$ -axis stator-reflected magnet high-frequency resistance decreases as the magnetization state increases, which is consistent with results shown in Figs. 4.19. It is also observed that the speed has a negligible impact on the estimated  $d$ -axis stator-reflected magnet high-frequency resistance [see Fig. 4.50(a) and 4.50(b)] and consequently on the magnetization state estimation error [see Fig. 4.50(c) and 4.50(c)]. This confirms that the proposed method can be used in the whole speed range of the machine, including standstill. It is also observed that the magnetization state estimation error slightly increases as the magnetization state does due to the reduction of the sensitivity of the estimated high-frequency resistance variation with the PM magnetization at high magnetization states. This is also consistent with the results shown in Fig. 4.19. It is noted that, even in the high magnetization state region, the accuracy of the method is acceptable, with the maximum magnetization state estimation error being  $\approx 0.031$  T for the SPMSM and  $\approx 0.052$  T for the IPMSM. The larger error in the magnetization state estimation for the IPMSM compared to the SPMSM is explained by the reduced sensitivity of the IPMSM at high magnetization states observed in Fig. 4.49.

#### 4.4.4 Equivalence between the experimental setup and a PMSM

Equivalences between the experimental setup presented in the previous section and the PMSM model, as well as potential application of the results to the PMSM case, are presented in this section.

Figure 4.51 shows the equivalent high frequency model of a PMSM [29] when a pulsating  $d$ -axis high frequency current is injected;  $v_{dshf}^r$  and  $i_{dshf}^r$  are the  $d$ -axis high frequency voltage and current,  $R_{dshf}$  is the stator winding  $d$ -axis high frequency resistance,  $L_{dshf}$  and  $L_{drhf}$  are the stator and rotor

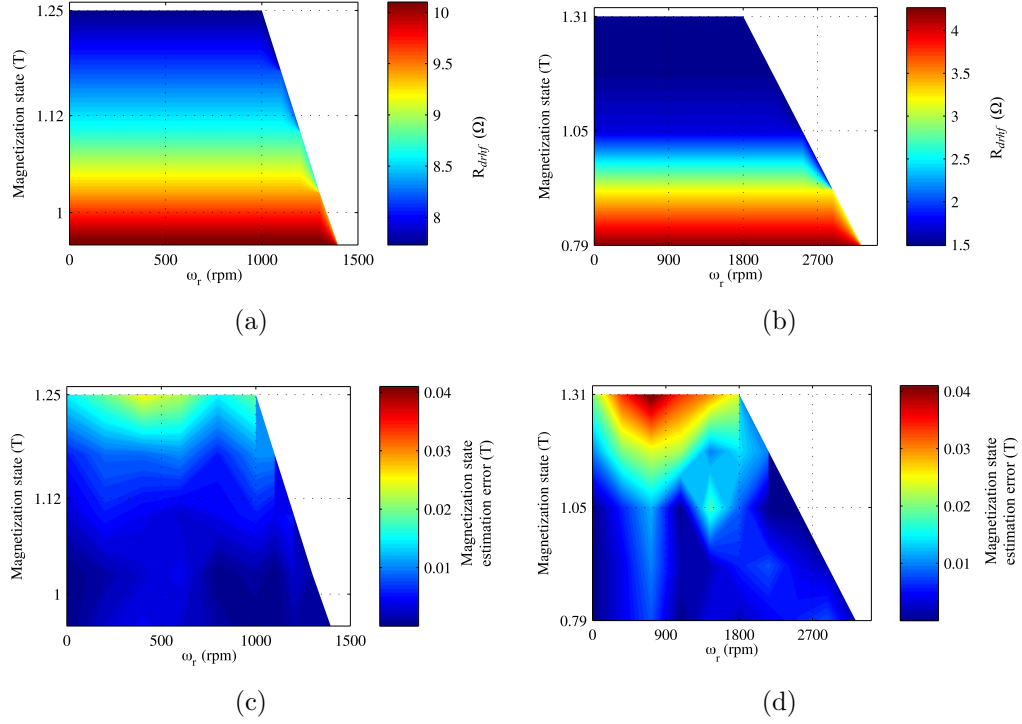


Figure 4.50: Estimated  $d$ -axis stator-reflected magnet resistance vs. magnetization state & speed, for the case of a) SPMSM and b) IPMSM; magnetization state estimation error versus magnetization state & speed for the case of c) SPMSM and d) IPMSM. Pulsating current injection  $\omega_{hf} = 250$  Hz,  $V_{hf} = 0.05$  p.u.

high frequency inductances,  $i_{drhf}^r$  is the rotor high frequency current (rotor lamination and magnet),  $M_{Dd}$  is the mutual coupling between stator and rotor  $d$ -axes,  $R_{drhf}$  is the rotor magnet high frequency resistance and  $R_{dshfFE}$  and  $R_{dshfFE}$  are the stator and rotor core high frequency resistances.

Comparing the equivalent circuits of the experimental setup in Fig. 4.7 and the PMSM in Fig. 4.51, the equivalence between both systems becomes evident. The only difference occurs in  $R_{dshfFE}$ ,  $R_{drhfFE}$  and in for the two magnets (per pole pair) connected in series (i.e. two per pole-pair in the design shown in Fig. 4.2) in the rotor side of the PMSM. Table (4.7) summarizes the equivalences between the experimental setup and the PMSM. Consequently, it is realistic to assume that the results and conclusions obtained from the experimental platform can be extended to PMSMs. This assumption is also supported by the results presented in [28] which verified the method with IPMSM and SPMSM equipped with NdFeB magnets, since

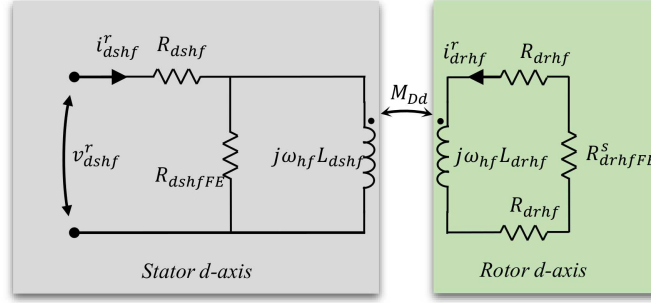


Figure 4.51: Equivalent d-axis high frequency model of a PMSM.

the magnetoresistive effect in NdFeB, SmCo and Ferrite magnets responds to the same principles.

Implementation of the method in an assembled machine would use the same scheme shown in sections IV and V. The high frequency signal voltage would be added in this case to the output voltage of the fundamental current regulator [73, 105, 31, 30, 106], the signal processing being the same as in Fig. 4.8.

It is finally noted that this method is especially interesting in applications using machines in which magnetization state can be changed during normal operation, i.e. VFMs or STFMMs, magnetization state estimation being therefore critical in these machine types.

## 4.5 Conclusions

This chapter analyzed the use of a high frequency signal for PM magnetization state estimation purpose. The method is based on the relationship between the PM electrical high frequency resistance and the PM magnetization state, commonly known as magnetoresistive effect. It has been evaluated using NdFeB, SmCo, ferrite and AlNiCO magnets, which are the most commonly used PMs in PMSMs. Experimental verification of the method has been conducted in an experimental setup using a simple geometry. This is advantageous for the analysis of the phenomena occurring in the magnet and the validation of the method. The physical results obtained using the setup confirms the theoretical predictions and the feasibility of the proposed method.

Additionally, the contribution of the PM coating to magnetoresistance



Table 4.7: Equivalences Between Experimental Setup and a PMSM

Variables in the experimental setup high frequency model	Variables in the PMSM high frequency model
$v_{hfp}^p$ :primary high frequency voltage	$v_{dhf}^r$ : stator $d$ –axis high frequency voltage
$i_{hfp}^p$ :primary high frequency current	$i_{dhf}^r$ : stator $d$ –axis high frequency current
$L_{hfp}$ :primary high frequency self-inductance	$L_{dshf}$ : $d$ –axis high frequency inductance
$R_{hfp}^p$ :primary high frequency resistance	$R_{dshf}$ : $d$ –axis high frequency resistance
$R_{hfFE}^p$ :core high frequency resistance	$R_{dshfFE}$ : stator core $d$ –axis high frequency resistance
$i_{hfs}^s$ :magnet high frequency current	$i_{drhf}^r$ : rotor core and magnet $d$ –axis high frequency current
$M_{ps}$ :Mutual coupling between the primary and the secondary	$M_{Dd}$ : Mutual coupling between stator $d$ –axis and rotor $d$ –axis
$L_{hfs}$ :secondary high frequency self-inductance	$L_{drhf}$ : magnet high frequency self-inductance
$R_{hfs}^s$ :secondary high frequency resistance	$R_{drhf}$ : magnet high frequency resistance
Does not exist in the experimental setup	$R_{drhfFE}$ : rotor core $d$ –axis high frequency resistance

sensitivity was also analyzed, as these protection is essential to avoid oxidation and corrosion in NdFeB magnets. Experimental results using NdFeB, SmCo and AlNiCo magnets with NiCuNi and epoxy coatings have been presented. It has been demonstrated the coating improves the magnetoresistive effect sensitivity to magnetoresistance effect in all cases, NdFeB showing the highest increments in sensitivity among magnets.

The equivalence between the experimental setup and a PMSM has been demonstrated, meaning the obtained results from the experimental setup can be extrapolated to PMSMs, the applicability of the method to PMSMs has been experimentally verified. The proposed method can operate in real

time and without interfering with the normal operation of the machine and can be used in the whole speed range of the machine, even at standstill. Compensation of the contribution of the stator high-frequency resistance to the overall high-frequency impedance of the machine is required for the implementation of the method.

# Chapter 5

## Conclusions and future work

### 5.1 Conclusions

This thesis is focused on PM temperature and magnetization state estimation methods in PMSMs. Chapter 2 is focused on high frequency signal injection PM temperature estimation methods. Two PM temperature estimation methods have been proposed:

- The first method is based on the injection of a pulsating d-axis high frequency current signal. This method provides a lumped estimation of the PM temperature, i.e. it provides an estimation of the mean PM temperature. The method was tested in two test machines, a SPMSM and an IPMSM, in the whole torque-speed range of the machine. It was shown that the speed has a negligible impact on the estimation error as well as the load current, whereas the error produced by the magnetizing current can easily be decoupled. The method can be applied in any type of PMSM and easily implemented in a common field oriented control (FOC). The amplitude and frequency of the injected signal can be selected according to the machine and inverter rated values. In addition, as the thermal time constant of a PMSMs is relatively high (i.e. compared to the machine thermal time constant), the test signal can be injected intermittently to minimize the impact of the induced losses due to the high frequency signal injection.
- The second method is intended for PM temperature distribution estimation, which is obtained from mean and differential PM temperature.

The method was tested with an IPMSM machine and a temperature distribution measurement system was developed to evaluate its accuracy. Although the use of BEMF has limitations related to the minimum speed at which the method can be applied, it provides accurate results in the mid-to-high speed.

The proposed methods have been validated using two PM temperature measurement systems that are introduced in Appendix A and B.

Chapter 3 analyzes the influence of the machine design and constructive aspects in the sensitivity of high frequency signal injection PM temperature estimation methods. The effects of machine assembling tolerances, stator configuration and slot/pole combinations on the estimated PM temperature have been studied.

- For the study of the constructive aspects, it was concluded that all types of eccentricities have an important impact on the estimated parameters, although they can be compensated. Besides, rotor lamination grain orientation can have an impact on the estimated temperature and the impact of magnet assembling was proved negligible on the estimated PM temperature.
- From the analysis of the machine design effects over high frequency signal injection based methods it can be concluded that the slot/pole configuration affects to the method sensitivity. Distributed winding machines with wider coil pitches presented, in general better results in terms of sensitivity but a reductions should be consider when the magnet length is low, and part of the high frequency flux is driven through the flux barriers. Concentrated winding machines show better behavior when the temperature was estimated using rotating voltage injection.

Chapter 4 is focused on the use of a high frequency signal for PM magnetization state estimation. The proposed method is based on the magnetoresistance effect in PMs. Experimental verification for different magnets types and for the most commonly used PM coatings have been presented. PMs coated using NiCuNi show an improvement of magnetoresistance effect sensitivity. NdFeB magnets showed the highest magnetoresistance effect, followed by AlNiCo, the lowest sensitivity was obtained for SmCo and ferrite magnets. Experimental results were carried out using a simplified setup, due to the large number of parameters involve in a PMSM. The results obtained with the experimental setup confirmed the theoretical predictions and the

feasibility of the proposed method. In addition, the equivalences between the simplified geometry and a PMSM were described, so the results can be extrapolated to PMSMs.

The equivalence between the experimental setup and a PMSM was finally demonstrated, meaning the obtaining results from the experimental setup can be extrapolated to PMSMs. The limitation of this method appears when it is applied to magnets at different temperatures. Magnet high frequency resistance also changes with temperature what is not modeled in the MS estimation method.

## 5.2 Conclusions (Spanish)

La presente tesis se centra en métodos de estimación de temperatura y estado de magnetización en máquinas síncronas de imanes permanentes (PMSMs).

El capítulo 2 se centra en métodos de estimación de temperatura de imanes permanentes, donde se proponen dos nuevos métodos:

- El primero de ellos, se basa en la inyección de una señal de corriente pulsante de alta frecuencia. Este método proporciona una estimación de la temperatura media de todos los imanes y se evalúa sobre máquinas de imanes permanentes superficiales y enterrados para diferentes velocidades y cargas. Se demostró que velocidad tiene un impacto despreciable en el error de estimación y que el error producido por la corriente de par puede ser fácilmente desacoplado. El método propuesto se puede aplicar a cualquier máquina síncrona de imanes permanentes y puede ser implementado fácilmente en un sistema de control de campo orientado (FOC). Aunque la selección de la frecuencia y amplitud de la señal puede variar dependiendo de los parámetros nominales del inversor o de la máquina, el capítulo 2 también proporciona unas directrices para lograr la máxima sensibilidad a los cambios de temperatura en el imán. Además, como la constante de tiempo de la temperatura de una PMSM es relativamente alta, la señal de test puede ser inyectada de forma intermitente para minimizar su impacto sobre el imán.
- El segundo método propuesto está destinado a detectar la una distribución no uniforme de la temperatura de los imanes en PMSM. Analizando el contenido armónico de la BEMF, el método propuesto proporciona una estimación de la temperatura media y diferencial de

los imanes para así, poder obtener la distribución espacial de la temperatura de los imanes. Aunque el uso del método se limita a aquellas situaciones en la que el motor se encuentre girando, los resultados que proporciona en media y alta velocidad son precisos.

En este capítulo se proporcionan resultados experimentales donde la precisión en la estimación de ambos métodos es comprobada con la ayuda de dos sistemas de medida de temperatura desarrollados para este fin, descritos en los apéndices A y B

El capítulo 3 analiza la influencia que tienen distintos diseños de máquinas y sus aspectos constructivos en la sensibilidad de los métodos de estimación de temperatura de los imanes. Se analizan aspectos como tolerancias de ensamblaje, configuración de rotor y estator en términos de combinaciones de ranuras/polos, los distintos tipos de excentricidad, anisotropía en la chapa... Ha sido comprobado cómo las excentricidades afectan a la sensibilidad, aunque pueden ser desacopladas. También el efecto que tiene en la sensibilidad el uso de chapa de grano orientado ha sido analizado y se ha descubierto que el efecto que tienen las tolerancias de ensamblaje puede ser despreciable.

De los análisis del efecto que tiene el diseño de máquinas en sobre los métodos de estimación basados en la inyección de señales de alta frecuencia, se puede concluir que la configuración de ranuras/polos afecta a la sensibilidad de este método siendo los bobinados distribuidos con amplios pasos de bobina los que mejores resultados proporcionan. Se comprobó que el incremento de sensibilidad con pasos de bobina mas anchos, se debe a que el flujo del bobinado es mas uniforme sobre la superficie del imán. Aquellas configuraciones con pasos de bobina pequeños, resultaban en una reducción de la sensibilidad, ya que interaccionaban con menos material magnético y producían mas pérdidas, debido a los incrementos de densidad de flujo en algunos puntos del imán. Las máquinas de bobinados concentrados presentaron un mejor comportamiento en términos de sensibilidad, cuando la temperatura de los imanes se estimaba usando un vector de tensión giratorio.

El capítulo 4 se centra en el uso de la inyección de señales de alta frecuencia para la estimación del estado de magnetización de los imanes. El método propuesto se basa en el efecto magnetorresistivo de los materiales. En este capítulo se proporcionan resultados experimentales para distintos tipos de imanes y para los recubrimientos mas usados en estos. Los materiales magnéticos a los que se les había añadido el recubrimiento mostraron una mejora en la sensibilidad al efecto magnetorresistivo. Entre los tipos de imanes analizados, los de neodimio mostraron la mayor magnetorresistencia,

seguidos de los AlNiCo, los de ferrita y SmCo presentaron un peor comportamiento. Los resultados experimentales fueron llevados a cabo usando una geometría simplificada permitiendo aislar el efecto objeto del estudio, algo que no es posible realizar de forma simple en un PMSM debido al gran número de parametros que intervienen en una PMSM. Dichos resultados confirmaron las predicciones teóricas y la viabilidad del método. La equivalencia entre la geometría experimental y una PMSM quedó demostrada en este capítulo, confirmando que los resultados obtenidos con el modelo simplificado pueden ser extrapolados a la PMSM. Las limitaciones del método vienen dadas por su uso a diferentes temperaturas. Esto es debido a los cambios producidos en la resistencia del imán no sólo por variaciones de campos sino también por las variaciones de temperatura.

### 5.3 Future work

In alignment with the PM magnetization and temperature estimation methods that have been analyzed in this thesis, there are several lines which are considered suitable for future work:

- The stator-reflected PM high frequency resistance depends on both MS and PM temperature, up to date it was not found the methodology to separate both effects. The temperature and field measurement device presented in this thesis can be used to find the methodology to evaluate separately the MS and PM temperature effects on the stator-reflected PM high frequency resistance.
- Development of new MS estimation techniques combining, BEMF harmonics and high frequency signal injection techniques. This will allow the estimation of MS under different PM temperatures.
- It has been shown that the stator-reflected PM high frequency resistance changes with  $d$ -axis current. It would be interesting to investigate how magnet losses change depending on the amount of negative  $I_d$  used e.g. for MTPA, high speed under flux weakening...
- Analyze the effects of PM aging on the studied PM temperature and MS estimation methods.
- The influence of changes in environmental variables such as temperature, humidity or pressure, could be studied to increase the reliability of the proposed methods.

- The reduction of Dy content in NdFeB magnets is an actual tendency. It is proposed to evaluate the effect of Dy content on the proposed PM temperature and MS estimation methods
- This thesis proposes a method for the estimation of PM spatial temperature distribution. Changes in the PM spatial temperature distribution will induce changes in the airgap flux density distribution which will have a direct impact on the machine torque. It is proposed to analyze the effect of the PM spatial temperature distribution on the machine torque, noise and vibration.
- The proposed method for temperature distribution estimation has been developed on an empirical basis; a mathematical model can be developed to study its applicability upon other PM machine types.



# Bibliography

- [1] Adrian Quesada. The permanent magnets challenge, 2016. Available at [http://www.icv.csic.es/images/Difusion/DISSEMINATION@ICV\\_The\\_permanent\\_magnets\\_challenge.pdf](http://www.icv.csic.es/images/Difusion/DISSEMINATION@ICV_The_permanent_magnets_challenge.pdf), accessed 12-October-2016.
- [2] Hitachi magnets. Neodymium rare earth permanent magnets, 2016. Available at <http://www.hitachi.com/environment/showcase/solution/materials/neomax.html>, accessed 12-October-2016.
- [3] S. Horita, T. Yanai, M. Nakano, and H. Fukunaga. Prediction of flux loss in a nd;fe ;b-bonded magnet under an external magnetic field. *IEEE Transactions on Magnetism*, 52(7):1–4, July 2016.
- [4] L. Ferraris, E. Pošković, and D. L. Cascia. Design optimization for the adoption of bonded magnets in pm bldc motors. In *IECON 2014 - 40th Annual Conference of the IEEE Industrial Electronics Society*, pages 476–482, Oct 2014.
- [5] K. Hirota, H. Nakamura, T. Minowa, and M. Honshima. Coercivity enhancement by the grain boundary diffusion process to nd;fe;b sintered magnets. *IEEE Transactions on Magnetism*, 42(10):2909–2911, Oct 2006.
- [6] J. D. McFarland, T. M. Jahns, A. M. EL-Refaie, and P. B. Reddy. Effect of magnet properties on power density and flux-weakening performance of high-speed interior permanent magnet synchronous machines. In *2014 IEEE Energy Conversion Congress and Exposition (ECCE)*, pages 4218–4225, Sept 2014.
- [7] J. E. Gould. Permanent magnets. *Electrical Engineers, Proceedings of the Institution of*, 125(11):1137–1151, November 1978.

- [8] T. D. Kefalas and A. G. Kladas. Finite element transient thermal analysis of pmsm for aerospace applications. In *2012 XXth International Conference on Electrical Machines*, pages 2566–2572, Sept 2012.
- [9] J. F. Liu and M. H. Walmer. Thermal stability and performance data for smco 2:17 high-temperature magnets on ppm focusing structures. *IEEE Transactions on Electron Devices*, 52(5):899–902, May 2005.
- [10] Jacek F. Gieras and Mitchell Wing. *Permanent Magnet Motor Technology: Design and Applications*, volume 1 of 1. MARcel Dekker, The address, 2 edition, 1 2002. English Version.
- [11] C. Kral, R. Sprangers, J. Waarma, A. Haumer, O. Winter, and E. Lomonova. Modeling demagnetization effects in permanent magnet synchronous machines. In *The XIX International Conference on Electrical Machines - ICEM 2010*, pages 1–6, Sept 2010.
- [12] J. Pyrhönen, J. Nerg, P. Kurrnen, J. Puranen, and M. Haavisto. Permanent magnet technology in wind power generators. In *Electrical Machines (ICEM), 2010 XIX International Conference on*, pages 1–6, Sept 2010.
- [13] Peter Campbell. *Permanent Magnet Materials and Their Application*, volume 1 of 1. Cambridge University Press, The address, 1 edition, 1 1994. English Version.
- [14] ARPA-E. Rare-earth-free nanostructure magnets, 2016. Available at <https://arpa-e.energy.gov/?q=slick-sheet-project/rare-earth-free-nanostructure-magnets>, accessed 12-October-2016.
- [15] Yanfeng Jiang, Md Al Mehedi, Engang Fu, Yongqiang Wang, Lawrence F. Allard, and Jian-Ping Wang. Synthesis of fe16n2 compound free-standing foils with 20 mgoe magnetic energy product by nitrogen ion-implantation. *NATURE*, 6:25436, May 2016.
- [16] ECOSWING. Energy cost optimization using superconducting wind generators, 2016. Available at <http://www.ecoswing.eu/index.php>, accessed 12-October-2016.
- [17] SUPRAPOWER. Superconducting, reliable, lightweight, and more powerful offshore wind turbine, 2016. Available at <http://www.suprapower-fp7.eu/>, accessed 12-October-2016.

- [18] A. Toba, A. Daikoku, N. Nishiyama, Y. Yoshikawa, and Y. Kawazoe. Recent technical trends in variable flux motors. In *2014 International Power Electronics Conference (IPEC-Hiroshima 2014 - ECCE ASIA)*, pages 2011–2018, May 2014.
- [19] Hengchuan Liu, Heyun Lin, Shuhua Fang, and Xueliang Huang. Investigation of influence of permanent magnet shape on field-control parameters of variable flux memory motor with fem. In *2008 World Automation Congress*, pages 1–4, Sept 2008.
- [20] R. Owen, Z. Q. Zhu, J. B. Wang, D. A. Stone, and I. Urquhart. Review of variable-flux permanent magnet machines. In *Electrical Machines and Systems (ICEMS), 2011 International Conference on*, pages 1–6, Aug 2011.
- [21] M. F. Hsieh, D. G. Dorrell, C. K. Lin, P. T. Chen, and P. Y. P. Wung. Modeling and effects of in situ magnetization of isotropic ferrite magnet motors. *IEEE Transactions on Industry Applications*, 50(1):364–374, Jan 2014.
- [22] W. Zhao, T. A. Lipo, and B. I. Kwon. Comparative study on novel dual stator radial flux and axial flux permanent magnet motors with ferrite magnets for traction application. *IEEE Transactions on Magnetics*, 50(11):1–4, Nov 2014.
- [23] S. I. Kim, J. Cho, S. Park, T. Park, and S. Lim. Characteristics comparison of a conventional and modified spoke-type ferrite magnet motor for traction drives of low-speed electric vehicles. *IEEE Transactions on Industry Applications*, 49(6):2516–2523, Nov 2013.
- [24] F. Briz, M. W. Degner, J. M. Guerrero, and A. B. Diez. Temperature estimation in inverter-fed machines using high-frequency carrier signal injection. *IEEE Transactions on Industry Applications*, 44(3):799–808, May 2008.
- [25] Arnold Magnetics. The important role of dysprosium in modern permanent magnets, 2016. Available at <http://www.arnoldmagnetics.com/en-us/Tech-Library/Technical-Publications>, accessed 12-October-2016.
- [26] Bomatec. Magnet technology of ndfeb magnets, 2016. Available at <http://www.bomatec.ch/en/magnet-technology/ndfeb-magnets.html>, accessed 12-October-2016.

- [27] Miguel A. Perez. *Instrumentación electrónica*, volume 1 of 1. Paraninfo, The address, 1 edition, 1 2014. Spanish.
- [28] D. Díaz Reigosa, D. Fernandez, Z. Q. Zhu, and F. Briz. Pmsm magnetization state estimation based on stator-reflected pm resistance using high-frequency signal injection. *IEEE Transactions on Industry Applications*, 51(5):3800–3810, Sept 2015.
- [29] B. Idzikowski, M. Wolf, A. Handstein, K. Nenkov, F. Stobiecki, and K. H. Muller. Inverse giant magnetoresistance in granular  $\text{Nd}/\text{Fe}/\text{B}$ . In *Magnetics Conference, 1997. Digests of INTERMAG '97., 1997 IEEE International*, pages BQ–BQ, April 1997.
- [30] D. D. Reigosa, F. Briz, M. W. Degner, P. Garcia, and J. M. Guerrero. Temperature issues in saliency-tracking-based sensorless methods for pm synchronous machines. *IEEE Transactions on Industry Applications*, 47(3):1352–1360, May 2011.
- [31] D. D. Reigosa, F. Briz, M. W. Degner, P. Garcia, and J. M. Guerrero. Magnet temperature estimation in surface pm machines during six-step operation. *IEEE Transactions on Industry Applications*, 48(6):2353–2361, Nov 2012.
- [32] D. D. Reigosa, F. Briz, P. Garcia, J. M. Guerrero, and M. W. Degner. Magnet temperature estimation in surface pm machines using high-frequency signal injection. *IEEE Transactions on Industry Applications*, 46(4):1468–1475, July 2010.
- [33] T. Sebastian. Temperature effects on torque production and efficiency of pm motors using  $\text{NdFeB}$  magnets. *IEEE Transactions on Industry Applications*, 31(2):353–357, Mar 1995.
- [34] G. Feng, C. Lai, K. L. V. Iyer, and N. C. Kar. Torque ripple modeling and minimization for pmsm drives with consideration of magnet temperature variation. In *2016 XXII International Conference on Electrical Machines (ICEM)*, pages 612–618, Sept 2016.
- [35] H. Liu, H. Lin, Z. Q. Zhu, M. Huang, and P. Jin. Permanent magnet remagnetizing physics of a variable flux memory motor. *IEEE Transactions on Magnetics*, 46(6):1679–1682, June 2010.
- [36] K. Sakai, K. Yuki, Y. Hashiba, N. Takahashi, and K. Yasui. Principle of the variable-magnetic-force memory motor. In *Electrical Machines*

- and Systems, 2009. ICEMS 2009. International Conference on*, pages 1–6, Nov 2009.
- [37] B. Gagas, T. Fukushige, T. Kato, and R. D. Lorenz. Operating within dynamic voltage limits during magnetization state increases in variable flux pm synchronous machines. In *2014 IEEE Energy Conversion Congress and Exposition (ECCE)*, pages 5206–5213, Sept 2014.
- [38] C. Y. Yu, T. Fukushige, A. Athavale, B. Gagas, K. Akatsu, D. Reigosa, and R. D. Lorenz. Zero/low speed magnet magnetization state estimation using high frequency injection for a fractional slot variable flux-intensifying interior permanent magnet synchronous machine. In *2014 IEEE Energy Conversion Congress and Exposition (ECCE)*, pages 2495–2502, Sept 2014.
- [39] Arnold Magnetics. Catalogs and literature, 2016. Available at <http://www.arnoldmagnetics.com/en-us/Products>, accessed 12-October-2016.
- [40] D. D. Reigosa, D. Fernandez, H. Yoshida, T. Kato, and F. Briz. Permanent-magnet temperature estimation in pmsms using pulsating high-frequency current injection. *IEEE Transactions on Industry Applications*, 51(4):3159–3168, July 2015.
- [41] B. M. Ma, Y. L. Liang, J. Patel, D. Scott, and C. O. Bounds. The effect of fe on the temperature dependent magnetic properties of sm(co,fe,cu,zr)z and smco5 sintered magnets at 450 deg;c. *IEEE Transactions on Magnetics*, 32(5):4377–4379, Sep 1996.
- [42] S. Ruoho, J. Kolehmainen, J. Ikaheimo, and A. Arkkio. Interdependence of demagnetization, loading, and temperature rise in a permanent-magnet synchronous motor. *IEEE Transactions on Magnetics*, 46(3):949–953, March 2010.
- [43] K. C. Kim, S. B. Lim, D. H. Koo, and J. Lee. The shape design of permanent magnet for permanent magnet synchronous motor considering partial demagnetization. *IEEE Transactions on Magnetics*, 42(10):3485–3487, Oct 2006.
- [44] D. Torregrossa, A. Khoobroo, and B. Fahimi. Prediction of acoustic noise and torque pulsation in pm synchronous machines with static eccentricity and partial demagnetization using field reconstruction method. *IEEE Transactions on Industrial Electronics*, 59(2):934–944, Feb 2012.

- [45] S. Moon, J. Lee, H. Jeong, and S. W. Kim. Demagnetization fault diagnosis of a pmsm based on structure analysis of motor inductance. *IEEE Transactions on Industrial Electronics*, 63(6):3795–3803, June 2016.
- [46] X. Xiao and C. Chen. Reduction of torque ripple due to demagnetization in pmsm using current compensation. *IEEE Transactions on Applied Superconductivity*, 20(3):1068–1071, June 2010.
- [47] G. Choi and T. M. Jahns. Post-demagnetization characteristics of permanent magnet synchronous machines. In *2015 IEEE Energy Conversion Congress and Exposition (ECCE)*, pages 1781–1788, Sept 2015.
- [48] P. Milanfar and J. H. Lang. Monitoring the thermal condition of permanent-magnet synchronous motors. *IEEE Transactions on Aerospace and Electronic Systems*, 32(4):1421–1429, Oct 1996.
- [49] M. Ganchev, B. Kubicek, and H. Kappeler. Rotor temperature monitoring system. In *Electrical Machines (ICEM), 2010 XIX International Conference on*, pages 1–5, Sept 2010.
- [50] M. Ganchev, H. Umschaden, and H. Kappeler. Rotor temperature distribution measuring system. In *IECON 2011 - 37th Annual Conference on IEEE Industrial Electronics Society*, pages 2006–2011, Nov 2011.
- [51] M. Ganchev, C. Kral, H. Oberguggenberger, and T. Wolbank. Sensorless rotor temperature estimation of permanent magnet synchronous motor. In *IECON 2011 - 37th Annual Conference on IEEE Industrial Electronics Society*, pages 2018–2023, Nov 2011.
- [52] C. Kral, A. Haumer, and S. B. Lee. Innovative thermal model for the estimation of permanent magnet and stator winding temperatures. In *2012 IEEE Energy Conversion Congress and Exposition (ECCE)*, pages 2704–2711, Sept 2012.
- [53] A. M. EL-Refaie, N. C. Harris, T. M. Jahns, and K. M. Rahman. Thermal analysis of multibarrier interior pm synchronous machine using lumped parameter model. *IEEE Transactions on Energy Conversion*, 19(2):303–309, June 2004.
- [54] C. Kral, A. Haumer, and S. B. Lee. A practical thermal model for the estimation of permanent magnet and stator winding temperatures. *IEEE Transactions on Power Electronics*, 29(1):455–464, Jan 2014.

- [55] B. H. Lee, K. S. Kim, J. W. Jung, J. P. Hong, and Y. K. Kim. Temperature estimation of ipmsm using thermal equivalent circuit. *IEEE Transactions on Magnetics*, 48(11):2949–2952, Nov 2012.
- [56] A. J. Grobler, S. R. Holm, and G. van Schoor. Thermal modelling of a high speed permanent magnet synchronous machine. In *Electric Machines Drives Conference (IEMDC), 2013 IEEE International*, pages 319–324, May 2013.
- [57] T. Huber, W. Peters, and J. Böcker. A low-order thermal model for monitoring critical temperatures in permanent magnet synchronous motors. In *Power Electronics, Machines and Drives (PEMD 2014), 7th IET International Conference on*, pages 1–6, April 2014.
- [58] K. Liu and Z. Q. Zhu. Online estimation of the rotor flux linkage and voltage-source inverter nonlinearity in permanent magnet synchronous machine drives. *IEEE Transactions on Power Electronics*, 29(1):418–427, Jan 2014.
- [59] K. Liu and Z. Q. Zhu. Mechanical parameter estimation of permanent-magnet synchronous machines with aiding from estimation of rotor pm flux linkage. *IEEE Transactions on Industry Applications*, 51(4):3115–3125, July 2015.
- [60] S. J. Underwood and I. Husain. Online parameter estimation and adaptive control of permanent-magnet synchronous machines. *IEEE Transactions on Industrial Electronics*, 57(7):2435–2443, July 2010.
- [61] S. Ichikawa, M. Tomita, S. Doki, and S. Okuma. Sensorless control of permanent-magnet synchronous motors using online parameter identification based on system identification theory. *IEEE Transactions on Industrial Electronics*, 53(2):363–372, April 2006.
- [62] M. Ganchev, C. Kral, and T. Wolbank. Compensation of speed dependency in sensorless rotor temperature estimation for permanent magnet synchronous motor. In *Electrical Machines (ICEM), 2012 XXth International Conference on*, pages 1612–1618, Sept 2012.
- [63] T. Huber, W. Peters, and J. Böcker. Monitoring critical temperatures in permanent magnet synchronous motors using low-order thermal models. In *2014 International Power Electronics Conference (IPEC-Hiroshima 2014 - ECCE ASIA)*, pages 1508–1515, May 2014.

- [64] J. Faiz and H. Nejadi-Koti. Demagnetization fault indexes in permanent magnet synchronous motors; an overview. *IEEE Transactions on Magnetism*, 52(4):1–11, April 2016.
- [65] B. M. Ebrahimi, J. Faiz, and M. J. Roshtkhari. Static-, dynamic-, and mixed-eccentricity fault diagnoses in permanent-magnet synchronous motors. *IEEE Transactions on Industrial Electronics*, 56(11):4727–4739, Nov 2009.
- [66] W. le Roux, R. G. Harley, and T. G. Habetler. Detecting rotor faults in low power permanent magnet synchronous machines. *IEEE Transactions on Power Electronics*, 22(1):322–328, Jan 2007.
- [67] T. Nakata, N. Takahashi, Y. Kawase, and M. Nakano. Influence of lamination orientation and stacking on magnetic characteristics of grain-oriented silicon steel laminations. *IEEE Transactions on Magnetism*, 20(5):1774–1776, Sep 1984.
- [68] K. Tone, H. Shimoji, S. Urata, M. Enokizono, and T. Todaka. Magnetic characteristic analysis considering the crystal grain of grain-oriented electrical steel sheet. *IEEE Transactions on Magnetism*, 41(5):1704–1707, May 2005.
- [69] Z. Cheng, N. Takahashi, B. Forghani, G. Gilbert, J. Zhang, L. Liu, Y. Fan, X. Zhang, Y. Du, J. Wang, and C. Jiao. Analysis and measurements of iron loss and flux inside silicon steel laminations. *IEEE Transactions on Magnetism*, 45(3):1222–1225, March 2009.
- [70] D. Fernandez, D. D. Reigosa, J. M. Guerrero, Z. Q. Zhu, and F. Briz. Permanent-magnet magnetization state estimation using high-frequency signal injection. *IEEE Transactions on Industry Applications*, 52(4):2930–2940, July 2016.
- [71] D. D. Reigosa, D. Fernandez, T. Tanimoto, T. Kato, and F. Briz. Permanent-magnet temperature distribution estimation in permanent-magnet synchronous machines using back electromotive force harmonics. *IEEE Transactions on Industry Applications*, 52(4):3093–3103, July 2016.
- [72] N. Limsuwan, Y. Shibukawa, D. D. Reigosa, and R. D. Lorenz. Novel design of flux-intensifying interior permanent magnet synchronous machine suitable for self-sensing control at very low speed and power conversion. *IEEE Transactions on Industry Applications*, 47(5):2004–2012, Sept 2011.



- [73] S. Wu, D. D. Reigosa, Y. Shibukawa, M. A. Leetmaa, R. D. Lorenz, and Y. Li. Interior permanent-magnet synchronous motor design for improving self-sensing performance at very low speed. *IEEE Transactions on Industry Applications*, 45(6):1939–1946, Nov 2009.
- [74] N. Limsuwan, T. Kato, K. Akatsu, and R. D. Lorenz. Design and evaluation of a variable-flux flux-intensifying interior permanent-magnet machine. *IEEE Transactions on Industry Applications*, 50(2):1015–1024, March 2014.
- [75] T. Fukushige, N. Limsuwan, T. Kato, K. Akatsu, and R. D. Lorenz. Efficiency contours and loss minimization over a driving cycle of a variable flux-intensifying machine. *IEEE Transactions on Industry Applications*, 51(4):2984–2989, July 2015.
- [76] Arnold Magnetics. Products: Neodymium iron boron, 2016. Available at <http://www.arnoldmagnetics.com/en-us/Products/Neodymium-Magnets>, accessed 12-October-2016.
- [77] S. Kumar, T. A. Lipo, and B. I. Kwon. A 32 000 r/min axial flux permanent magnet machine for energy storage with mechanical stress analysis. *IEEE Transactions on Magnetics*, 52(7):1–4, July 2016.
- [78] Z. Xue, Z. Liu, L. Liu, M. Li, S. He, D. Lee, Y. Guo, and A. Yan. Anisotropy of mechanical properties of sm-co permanent magnets doped with dysprosium. In *2015 IEEE Magnetics Conference (INTERMAG)*, pages 1–1, May 2015.
- [79] T. Miura, S. Chino, M. Takemoto, S. Ogasawara, Akira Chiba, and Nobukazu Hoshi. A ferrite permanent magnet axial gap motor with segmented rotor structure for the next generation hybrid vehicle. In *The XIX International Conference on Electrical Machines - ICEM 2010*, pages 1–6, Sept 2010.
- [80] James D. Widmer, Richard Martin, and Mohammed Kimiabeigi. Electric vehicle traction motors without rare earth magnets. *Sustainable Materials and Technologies*, 3(6):7–13, Apr 2015.
- [81] E. Richter, T. J. E. Miller, T. W. Neumann, and T. L. Hudson. The ferrite permanent magnet ac motor—a technical and economical assessment. *IEEE Transactions on Industry Applications*, IA-21(3):644–650, May 1985.

- [82] M. Ibrahim, L. Masisi, and P. Pillay. Design of variable-flux permanent-magnet machines using alnico magnets. *IEEE Transactions on Industry Applications*, 51(6):4482–4491, Nov 2015.
- [83] H. Yang, H. Lin, J. Dong, J. Yan, Y. Huang, and S. Fang. Analysis of a novel switched-flux memory motor employing a time-divisional magnetization strategy. *IEEE Transactions on Magnetics*, 50(2):849–852, Feb 2014.
- [84] H. Yang, Z. Q. Zhu, H. Lin, Y. Zhang, S. Fang, Y. Huang, and N. Feng. Performance improvement of partitioned stator switched flux memory machines with triple-magnet configuration. *IEEE Transactions on Magnetics*, 52(7):1–4, July 2016.
- [85] M. A. Khan, I. Husain, M. R. Islam, and J. T. Klass. Design of experiments to address manufacturing tolerances and process variations influencing cogging torque and back emf in the mass production of the permanent-magnet synchronous motors. *IEEE Transactions on Industry Applications*, 50(1):346–355, Jan 2014.
- [86] A. Khoobroo and B. Fahimi. Magnetic flux estimation in a permanent magnet synchronous machine using field reconstruction method. *IEEE Transactions on Energy Conversion*, 26(3):757–765, Sept 2011.
- [87] X. Xiao, C. Chen, and M. Zhang. Dynamic permanent magnet flux estimation of permanent magnet synchronous machines. *IEEE Transactions on Applied Superconductivity*, 20(3):1085–1088, June 2010.
- [88] N. Bianchi, S. Bolognani, and B. J. Chalmers. Salient-rotor pm synchronous motors for an extended flux-weakening operation range. *IEEE Transactions on Industry Applications*, 36(4):1118–1125, Jul 2000.
- [89] T. M. Jahns. Flux-weakening regime operation of an interior permanent-magnet synchronous motor drive. *IEEE Transactions on Industry Applications*, IA-23(4):681–689, July 1987.
- [90] C. Y. Yu, T. Fukushige, N. Limsuwan, T. Kato, D. D. Reigosa, and R. D. Lorenz. Variable-flux machine torque estimation and pulsating torque mitigation during magnetization state manipulation. *IEEE Transactions on Industry Applications*, 50(5):3414–3422, Sept 2014.
- [91] D. Diaz Reigosa, P. Garcia, D. Raca, F. Briz, and R. D. Lorenz. Measurement and adaptive decoupling of cross-saturation effects and secondary saliencies in sensorless controlled ipm synchronous machines.

- IEEE Transactions on Industry Applications*, 44(6):1758–1767, Nov 2008.
- [92] K. Liu, Q. Zhang, J. Chen, Z. Q. Zhu, and J. Zhang. Online multiparameter estimation of nonsalient-pole pm synchronous machines with temperature variation tracking. *IEEE Transactions on Industrial Electronics*, 58(5):1776–1788, May 2011.
- [93] W. Thomson. On the electro-dynamic qualities of metals: Effects of magnetization on the electric conductivity of nickel and iron. *Proceedings of the Royal Society of London*, 8:546–550, Jan 1857.
- [94] T. McGuire and R. Potter. Anisotropic magnetoresistance in ferromagnetic 3d alloys. *IEEE Transactions on Magnetism*, 11(4):1018–1038, Jul 1975.
- [95] B. Idzikowski, M. Wolf, A. Handstein, K. Nenkov, H. J. Engelmann, F. Stobiecki, and K. H. Muller. Inverse giant magnetoresistance in granular  $\text{Nd}_2\text{Fe}_{14}\text{B}/\alpha\text{-Fe}$ . *IEEE Transactions on Magnetism*, 33(5):3559–3561, Sep 1997.
- [96] S. O. Kasap. *Principles of Electronic Materials and Devices*, volume 1 of 10. McGraw-Hill Education, The address, 3 edition, 7 2005. English Version.
- [97] S. Duan, L. Zhou, and J. Wang. Flux weakening mechanism of interior permanent magnet synchronous machines with segmented permanent magnets. *IEEE Transactions on Applied Superconductivity*, 24(3):1–5, June 2014.
- [98] X. Zhu, S. Yang, Y. Du, Z. Xiang, and L. Xu. Electromagnetic performance analysis and verification of a new flux-intensifying permanent magnet brushless motor with two-layer segmented permanent magnets. *IEEE Transactions on Magnetism*, 52(7):1–4, July 2016.
- [99] M. Ashabani and Y. A. R. I. Mohamed. Multiobjective shape optimization of segmented pole permanent-magnet synchronous machines with improved torque characteristics. *IEEE Transactions on Magnetism*, 47(4):795–804, April 2011.
- [100] Chen Yang Technologies. Hall sensors and measurements, 2016. Available at <http://www.hallsensors.de/CYSJ106C.pdf>, accessed 12-October-2016.

- [101] U. Hartmann. *Magnetic Multilayers and Giant Magnetoresistance*, volume 37 of 1. Springer, The address, 1 edition, 1 2000. English Version.
- [102] A. C. Malloy, R. F. Martinez-Botas, and M. Lampérth. Measurement of magnet losses in a surface mounted permanent magnet synchronous machine. *IEEE Transactions on Energy Conversion*, 30(1):323–330, March 2015.
- [103] D. D. Reigosa, F. Briz, C. Blanco Charro, A. Di Gioia, P. García, and J. M. Guerrero. Sensorless control of doubly fed induction generators based on rotor high-frequency signal injection. *IEEE Transactions on Industry Applications*, 49(6):2593–2601, Nov 2013.
- [104] D. D. Reigosa, F. Briz, C. Blanco, and J. M. Guerrero. Sensorless control of doubly fed induction generators based on stator high-frequency signal injection. *IEEE Transactions on Industry Applications*, 50(5):3382–3391, Sept 2014.
- [105] James D. Widmer, Richard Martin, and Mohammed Kimiabeigi. Electric vehicle traction motors without rare earth magnets. *Elsevier, Sustainable Materials and Technologies*, 3:7–13, Nov 2015.
- [106] L. Alberti, N. Bianchi, and S. Bolognani. High-frequency dq model of synchronous machines for sensorless control. *IEEE Transactions on Industry Applications*, 51(5):3923–3931, Sept 2015.
- [107] Florence Meier. *Permanent-Magnet Synchronous Machines with Non-Overlapping Concentrated Windings for Low-Speed Direct-Drive Applications*. PhD thesis, Royal Institute of Technology, School of Electrical Engineering Electrical Machines and Power Electronics, Stockholm, 2008.
- [108] Duane C. Hanselman. *Brushless Permanent-Magnet Motor Design*, volume 1 of 1. McGraw-Hill Education, The address, 1 edition, 1 1994. English Version.
- [109] N. Bianchi and Thomas M. Jahns. *Design, Analysis, and Control of Interior PM Synchronous Machines*, volume 1 of 1. CLEUP, The address, 1 edition, 1 2004. English Version.
- [110] Texas Instruments. Temperature sensor: Tmp100, 2016. Available at <http://www.ti.com/lit/ds/symlink/tmp100.pdf>, accessed 12-October-2016.

- [111] Microchip. Microcontroller: Pic24fj64ga004, 2016. Available at <http://www.microchip.com/wwwproducts/en/PIC24FJ64GA004>, accessed 12-October-2016.
- [112] Microchip. Dsc: dspic30f6010a, 2016. Available at <http://www.microchip.com/wwwproducts/en/dsPIC30F6010A>, accessed 12-October-2016.
- [113] Microchip. Wireless lan module, 2016. Available at <http://www.microchip.com/wwwproducts/en/RN171>, accessed 12-October-2016.
- [114] Clean Technica. Electric motors use 45 Available at <https://cleantechnica.com>, accessed 12-October-2016.
- [115] P. L. Jansen and R. D. Lorenz. Transducerless position and velocity estimation in induction and salient ac machines. *IEEE Transactions on Industry Applications*, 31(2):240–247, Mar 1995.
- [116] D. Raca, P. Garcia, D. Reigosa, F. Briz, and R. Lorenz. A comparative analysis of pulsating vs. rotating vector carrier signal injection-based sensorless control. In *Applied Power Electronics Conference and Exposition, 2008. APEC 2008. Twenty-Third Annual IEEE*, pages 879–885, Feb 2008.
- [117] Yu seok Jeong, R. D. Lorenz, T. M. Jahns, and Seung-Ki Sul. Initial rotor position estimation of an interior permanent-magnet synchronous machine using carrier-frequency injection methods. *IEEE Transactions on Industry Applications*, 41(1):38–45, Jan 2005.
- [118] D. Reigosa, P. Garcia, F. Briz, D. Raca, and R. D. Lorenz. Modeling and adaptive decoupling of transient resistance and temperature effects in carrier-based sensorless control of pm synchronous machines. In *Industry Applications Society Annual Meeting, 2008. IAS '08. IEEE*, pages 1–8, Oct 2008.
- [119] D. Diaz, D. Fernandez, T. Tanimoto, T. Kato, and F. Briz. Sensitivity analysis of high frequency signal injection based temperature estimation methods to machine assembling tolerances. *IEEE Transactions on Industry Applications*, PP(99):1–1, 2016.
- [120] M. Farshadnia, R. Dutta, J. E. Fletcher, K. Ahsanullah, M. F. Rahman, and H. C. Lovatt. Analysis of mmf and back-emf waveforms for fractional-slot concentrated-wound permanent magnet machines. In

*Electrical Machines (ICEM), 2014 International Conference on*, pages 1976–1982, Sept 2014.

- [121] H. Kubota, M. Sato, and T. Miyazaki. Anomalous temperature dependence of the giant magnetoresistance in ni/cu, ni<sub>95</sub>co<sub>5</sub>/cu and ni<sub>95</sub>fe<sub>5</sub>/cu multilayer films. *Journal of Magnetism and Magnetic Materials*, 167(1-2):12–20, March 1997.

# Appendix A

## Wireless thermocouple based PM temperature measurement system

### A.1 Introduction

A wireless thermocouple base PM temperature measurement system for IPMSMs is presented in this appendix. The proposed system provides temperature measurement in the axial direction of one PM in real time. Potential uses of the system include:

- Obtaining temperature variations in the axial direction
- Evaluation of risks of local and/or global demagnetization
- Development and testing of temperature estimation methods
- Analysis of the internal PM temperature distribution in the axial direction

### A.2 PM temperature measurement system

In the proposed system, one PM of an IPMSM, is equipped with 13 thermocouples in the axial direction, see Fig. A.1. The thermocouple wires are taken out throughout a hollow shaft and connected to a measurement and

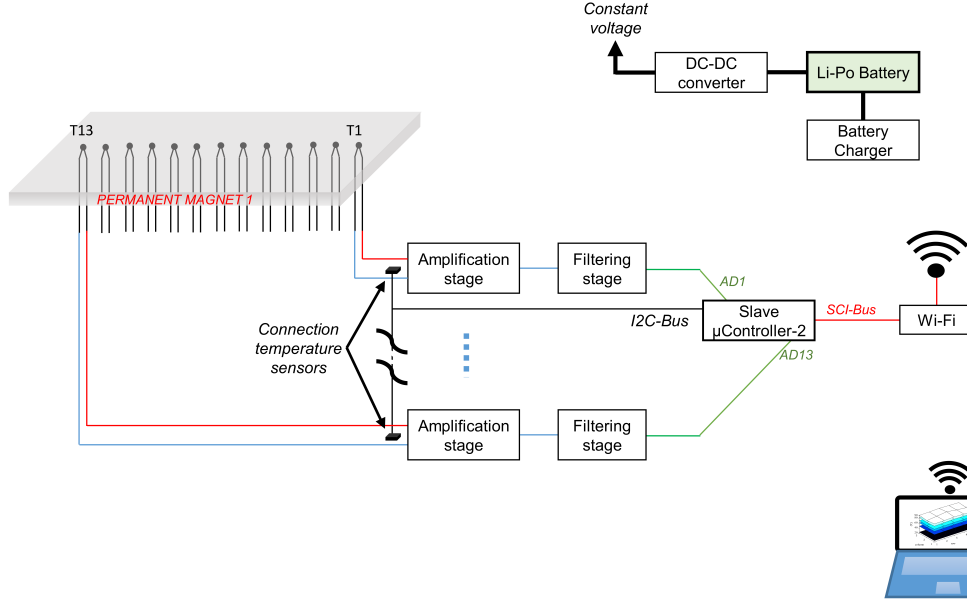


Figure A.1: Schematic representation of the temperature and field measurement system.

wireless transmission device see Fig A.3. The wireless transmission device, see Fig. A.2, includes the signal conditioning, acquisition system, battery, and Wi-Fi module.

Signal conditioning was designed using instrumentation operational amplifiers to guarantee low power consumption, low offset and low noise. In addition, the use of operational amplifiers significantly reduce the use of passive components.

The output voltage of a thermocouple,  $V_{th}$ , is proportional to the difference between the temperature at the sensing point,  $T_{sense}$  and the temperature at the connection point  $T_{conn}$  (A.1),  $k_{th}$  depending on the type of thermocouple,  $41\mu V/$  for the type used in this system ( K type). Temperature measurement using thermocouples implies the use of an additional temperature sensor to know the temperature at the connection point, the temperature at the connection points being measured using I2C temperature sensors [110].

$$V_{th} = k_{th}(T_{sense} - T_{conn}) \quad (A.1)$$

A digital signal processor (DSP) is being used to acquire the 13 analog signals from each thermocouple, communicate through I2C bus with the em-



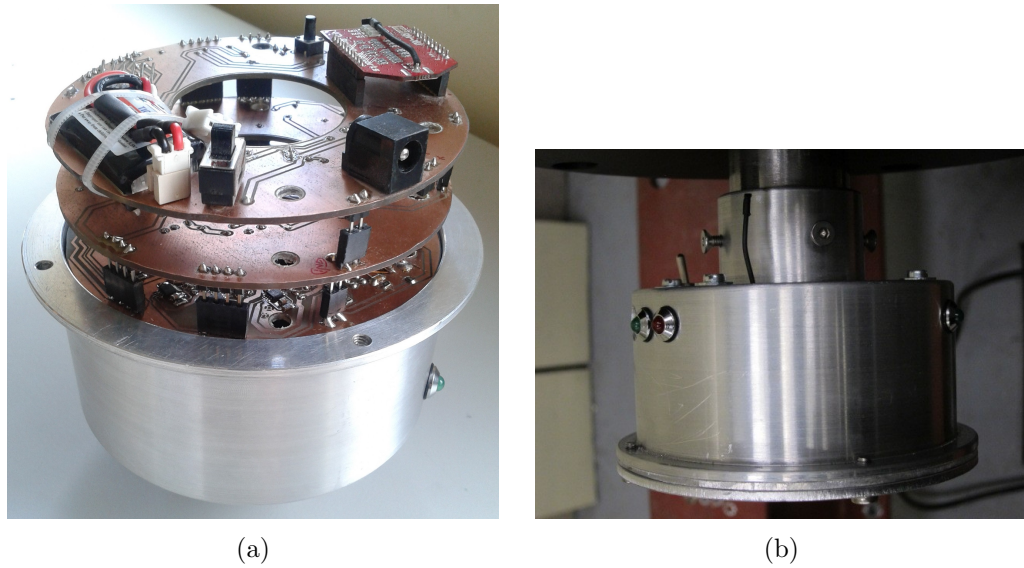


Figure A.2: Temperature measurement and transmission device, a) PCB organization in the aluminum box, b) aluminum box attached to the shaft.

bedded temperature sensors, process the acquired data and send it through SCI-bus to the Wi-Fi device. A dsPIC30F6010A has been used [112].

The wireless transmission link is achieved using an Embedded 2.4 GHz IEEE 802.11 b/g Wireless LAN Module [113]. The module is suitable for portable battery operated devices and implements auto-sleep mode to drop power consumption during standby.

The two cells Li-Po battery has been used to power the system, a battery charger IC being used to manage charging and individual cell balancing. A DC-DC converter was used at the battery output to ensure constant power voltage independently of the state of charge of the battery (see Fig. A.1).

### A.3 Desktop application for temperature and field measurement

A simple desktop application was designed to communicate through a wi-fi link with the  $\mu$ Controller, the application being able to receive, save and plot the temperature data (see Fig. A.4). The "connect" button sends a command to start sampling, creates a text file and automatically saves

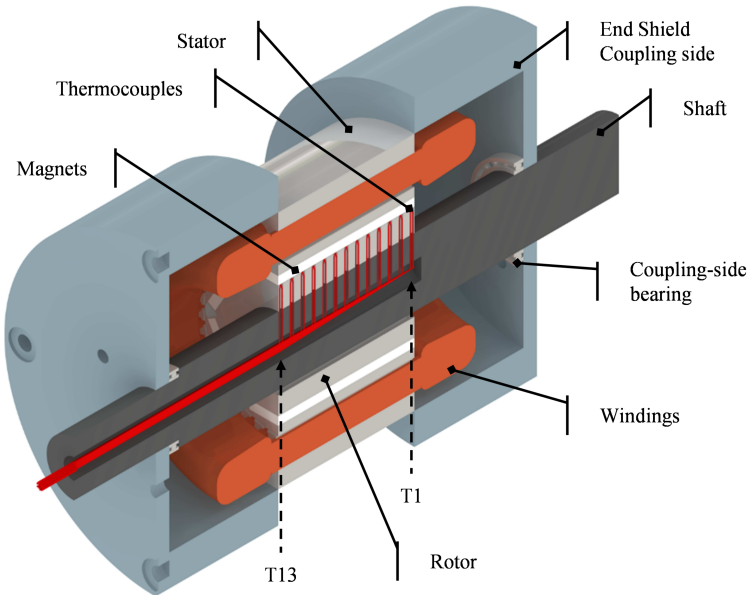


Figure A.3: Thermocouples' location in the IPMSM

the data, including sampling time. A histogram plot is used to see magnet temperature variations and latest data being received. The sampling stops acting over "disconnect" button.

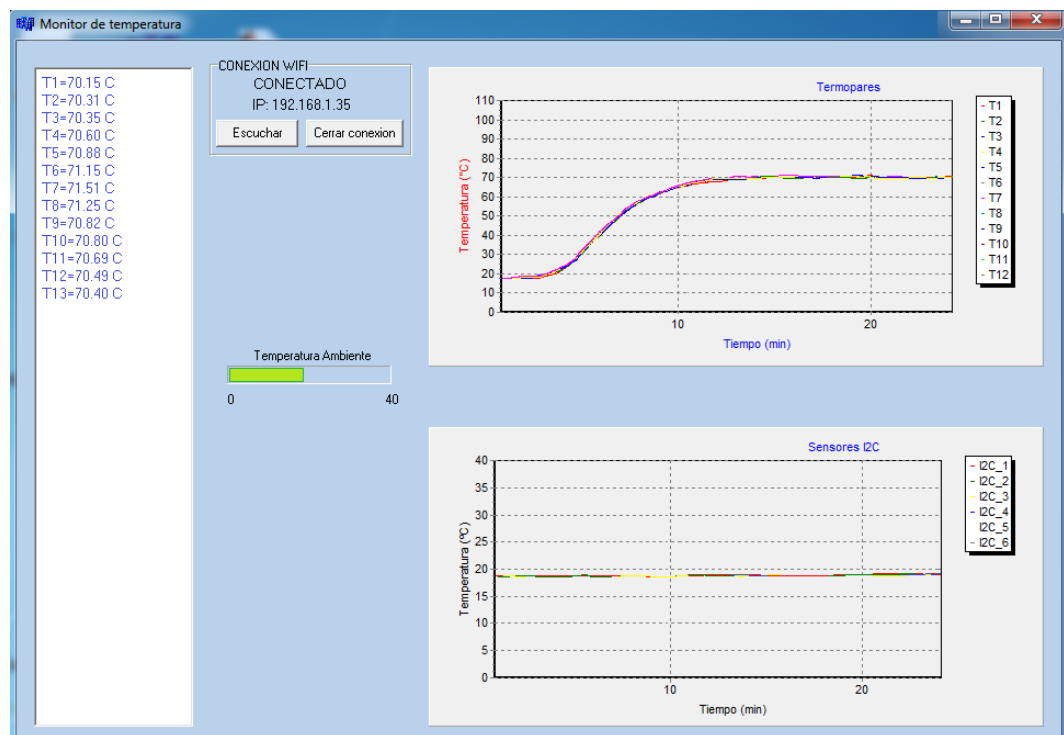


Figure A.4: Desktop application for temperature measurement system.



# Appendix B

## Wireless PM temperature and field measurement array

### B.1 Introduction

A wireless PM temperature and field distribution measurement system for IPMSMs is presented in this appendix. The objective this system is the development of advanced PM temperature and field estimation methods. The proposed system provides PM temperature and field maps in real time for all the magnets with high spatial resolution and sampling rates. Potential uses include:

- Study of the relationship between temperature and flux density
- Evaluation of risks of local and/or global demagnetization
- Development of new temperature/field estimation methods
- Analysis of the internal PM temperature distribution

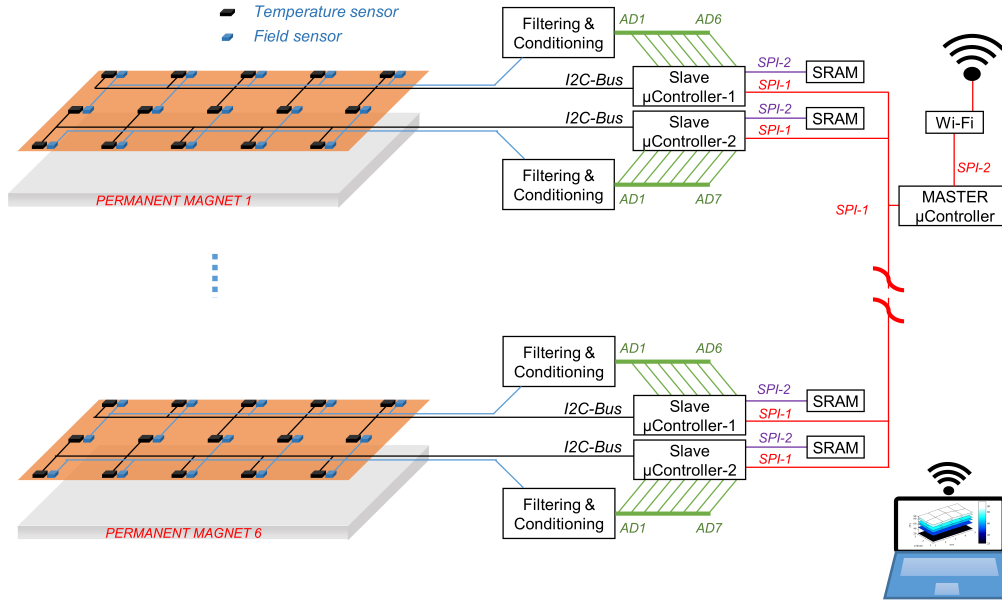


Figure B.1: Schematic representation of the temperature and field measurement system.

## B.2 High resolution PM temperature and field measurement system

Table B.1: System characteristics

	Temperature measurement	Field measurement
Sensor Temperature limit	125 °C	125 °C
Resolution	0.00625	1 mT
Measuring range	-55 to 125 °C	0±3T
Bandwidth	14kHz	50kHz
Sensors per pole	15	15

The system consist of an array of temperature and field sensors, which are attached to each PM of the machine. Fig. B.1 schematically shows the developed temperature and field measurement system. Black and blue cubic spots on the orange film represent the temperature and field sensors respectively. Each sensors array consists of 15 temperature and field sensors

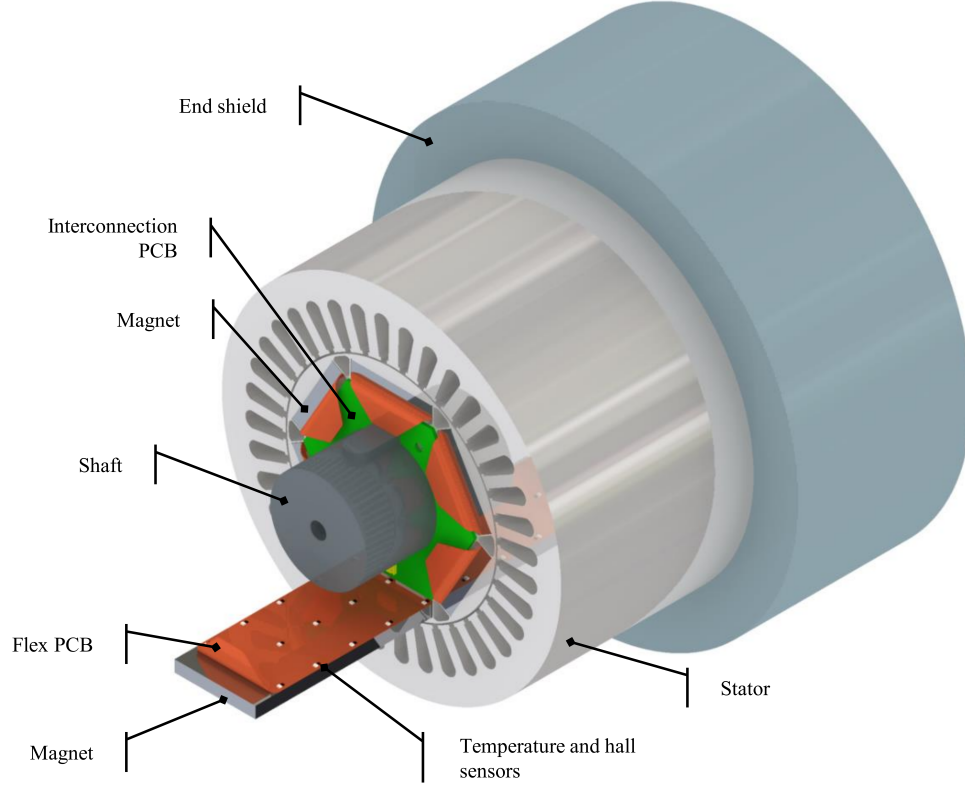


Figure B.2: Field and temperature IC sensors location in the IPMSM

in a 3x5 arrangement that will be placed under the magnet, attached to it.

TMP100 digital temperature sensors with *I2C* interface (serial 2-wire) have been used [110]. They provide a resolution of  $0.0625^{\circ}\text{C}$ , with a maximum operating temperature of  $125^{\circ}\text{C}$ . The *I2C* bus can operate at frequencies above 3.4Mbits/s, i.e. the 15 temperature sensors can be read at a maximum frequency of  $\approx 14\text{kHz}$ , which is fast enough, considering the machine thermal time constant [32, 31]. Each *I2C* bus is connected to the corresponding *I2C* port of a PIC24FJ64GA004 microcontroller (Slave  $\mu$ Controller-1 to 12 in Fig. B.1) [111]. *I2C* allows connection of up to eight sensors to each *I2C*, significantly reducing the number of wires throughout the hollow shaft compared to other implementations, like the one shown in Appendix A [40].

Hall-effect mono-crystal gallium arsenide (GaAs) sensors have been used to measure the field [100]. Their measuring range is 0-3T, which is adequate to measure the PM field in PMSMs, typically in a range of 0-1.8T. Their

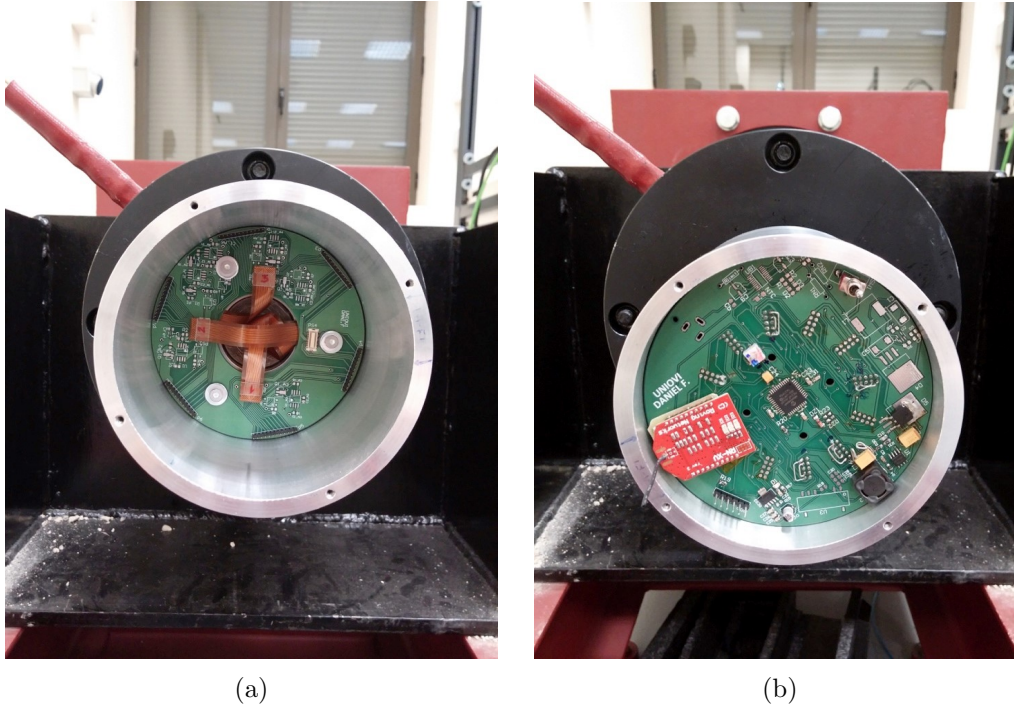


Figure B.3: a) assembling of the connection PCB; b), aluminum box containing master  $\mu$ Controller PCB, Slave  $\mu$ Controllers PCBs, filtering and conditioning PCBs and WiFi module.

maximum operating temperature is  $125^{\circ}\text{C}$ , which is the same as for the temperature sensors. The output of the field sensors is an analog voltage, which is adapted and filtered (see “filtering & conditioning” in Fig. B.1), and further connected to the A/D converter of the slave  $\mu$ Controller-1 to 12 in Fig. B.1. Two microcontrollers, each with 8 A/D channels, are used (see Fig. B.1).

Slave  $\mu$ Controllers, 1 to 12, are connected via SPI to a master  $\mu$ Controller (see Fig. B.1). The master  $\mu$ Controller periodically collects temperature and field measurements from all slave  $\mu$ Controllers, which are transmitted to a central computer using a WiFi link. The baud rate limit due to the WiFi link is 230 kbits/s, i.e. the 15 temperature sensors and the 15 field sensors can be read at a maximum frequency of 550Hz. While this is fast enough for PM temperature transmission, it can be insufficient for field measurement, as this can change significantly faster. To fully exploit the bandwidth of the field sensors, a SPI SRAM memory (1024 kbits) has been connected to the



SPI-1 port of each slave  $\mu$ Controller. The SPI SRAM memory baud rate is 16 Mbits/s, i.e. the 15 field sensors can be read at a maximum frequency of  $\approx 172$  kHz, which is fast enough to store the field variations with an adequate bandwidth. The data stored in the SRAM memory is later accessed and transmitted to the computer via the Wi-Fi Link.

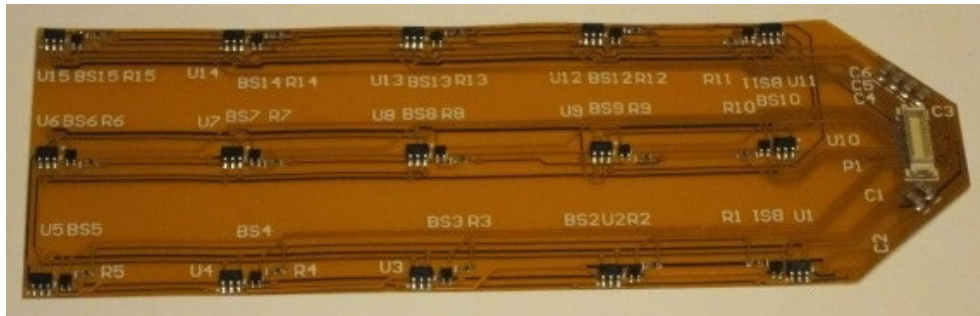
Fig. B.2 shows the field and temperature 3x5 sensors array distribution and its position in the machine. Fig. B.4(a) shows the array of sensors mounted on a flexible PCB. Fig. B.4(b) shows the six flexible PCBs during rotor assembling, one per magnet. All the PCBs are connected to the connection PCB shown in Fig. B.4(c), which is mounted on the shaft. Fig. 2e shows the flexible PCBs and the connection PCB after assembling the rotor. All the I2C buses are connected to the slave  $\mu$ Controllers through-out a hollow shaft using the flexible PCBs shown in Fig. B.4(d), (see Fig. B.4(e)). The filtering and conditioning stages, slave  $\mu$ Controllers, master  $\mu$ Controller, SRAM memories and Wi-Fi module are assembled into an aluminum box that it is coupled to the machine shaft (Fig. B.3(a) and B.3(b)). Table B.1 summarizes the main characteristics.

## B.3 Desktop application for temperature and field measurement

A simple desktop application was designed to communicate through a wi-fi link with the master  $\mu$ Controller, to receive, save and plot the temperature data (see Fig. B.5). The "connect" button sends a command to start sampling, creates a text file for every pole and automatically saves the data, including sampling time. A 3D plot is used to see current magnet temperature distribution and a log box for every pole shows the latest data set received. The sampling stops acting over "disconnect" button. Data can be processed off-line using MatLab.

## B.4 Temperature and field measurements

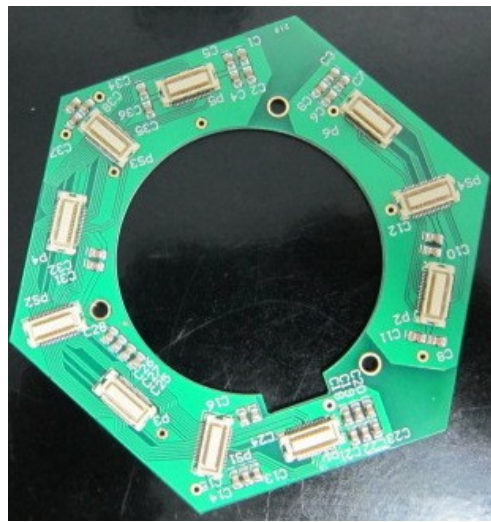
The proposed system has been tested on an IPMSM (see Figs. B.4 and B.3). The machine parameters are shown in Table 2.3. Experimental results of both temperature and field measurement systems are shown in this section.



(a)



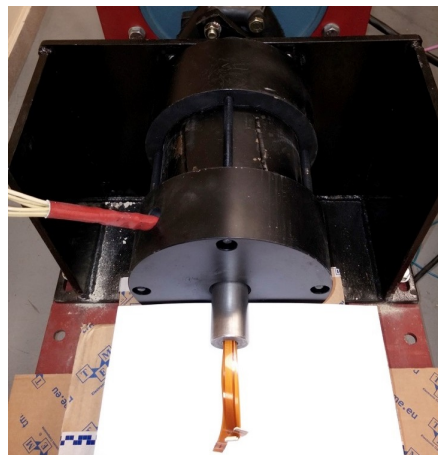
(b)



(c)



(d)



(e)

Figure B.4: a) sensors array mounted on a flexible PCB; b) rotor assembling; c) connection PCB; d) assembled rotor and connection PCBs; e) hollow shaft and connection PCBs;

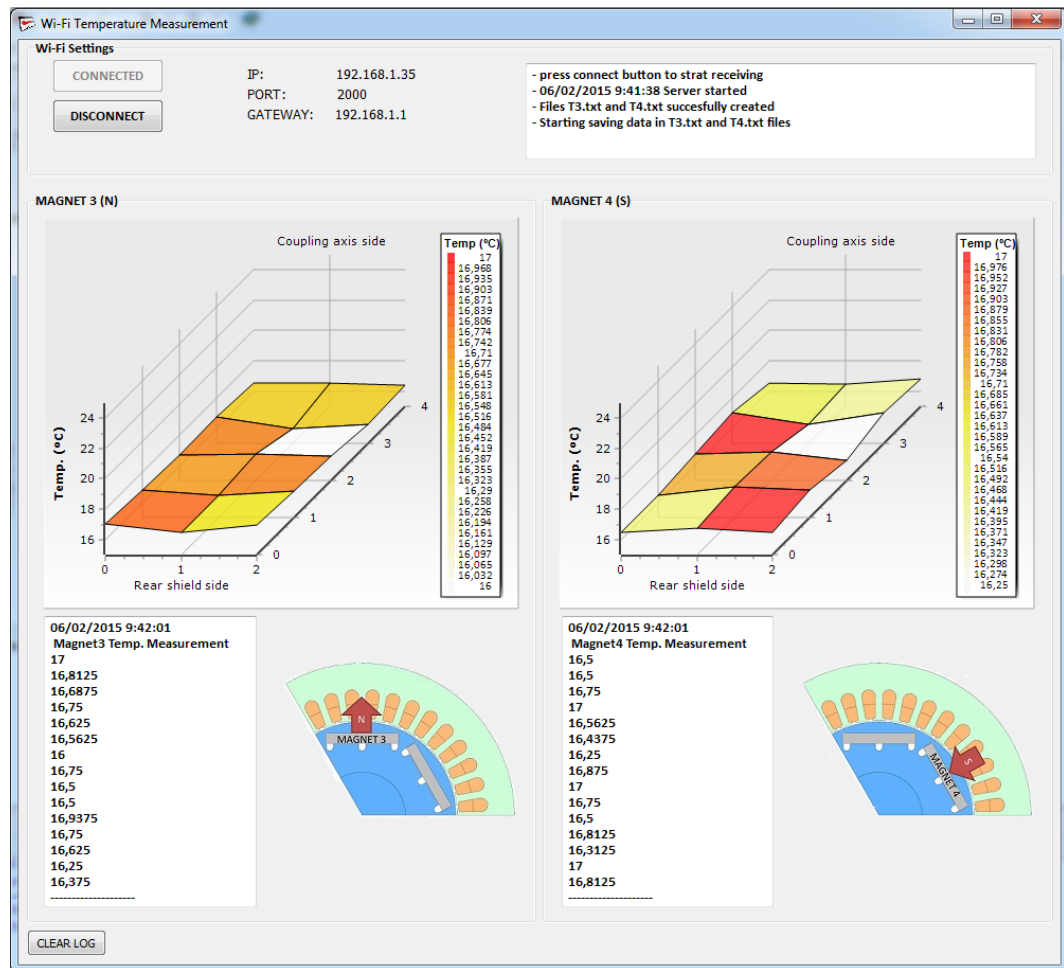


Figure B.5: Desktop application for temperature measurement system.

### B.4.1 Temperature measurements

Fig. B.6 shows the PM temperature measured by the sensors array, when  $I_q$  current changes from 0 to 1pu in steps of 0.2 pu. No  $d$ -axis current was injected ( $I_d = 0$ ), MTPA not being implemented therefore. Consequently, the observed temperature variations are due exclusively to the  $q$ -axis current. Fig. B.7 shows the same experimental results as in Fig. B.6 but for the case of  $I_d$  current changing from 0 to -1pu in steps of 0.2pu, with no  $q$ -axis current being injected. The results shown in Fig. B.6 and Fig. B.7 were taken 30 min. after the corresponding change in the current.

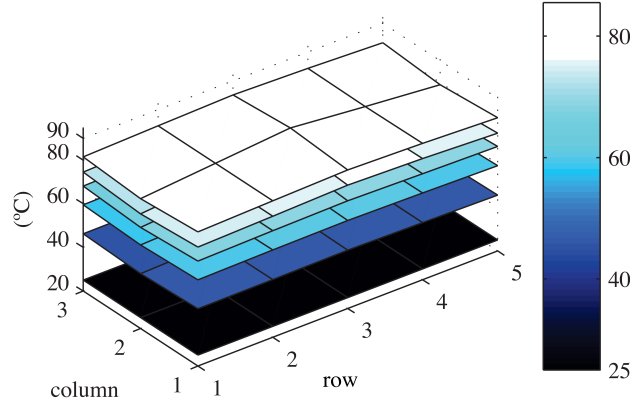


Figure B.6: Experimentally measured magnet temperatures for  $I_q$  current of: 0, 0.2, 0.4, 0.6, 0.8 and 1.0.  $I_d = 0$  pu,  $\omega_r = 2\pi \cdot 50$  rad/s.

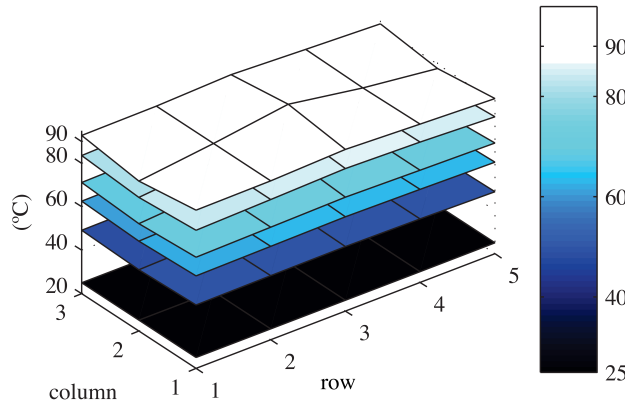


Figure B.7: Experimentally measured magnet temperatures for  $I_d$  current of: 0, 0.2, 0.4, 0.6, 0.8 and 1.  $I_q = 0$  pu,  $\omega_r = 2\pi \cdot 50$  rad/s.

## B.4.2 Field measurements

The field sensors are sampled at 50kHz, the measurements being stored in the SPI SRAM memory (see Fig. B.1), being later transmitted to the computer via WiFi link.

### B.4.2.1 Single sensor test

Fig. B.8 shows the experimentally measured transient response of the magnetic field sensor F8 (see Fig. B.4(a)) after positive and negative step-like changes of the d-axis current.

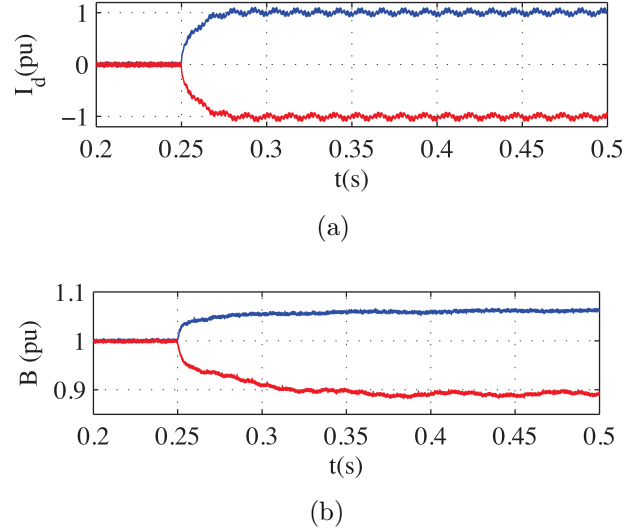


Figure B.8: Experimentally measured  $d$ -axis current a) measured transient response of the magnet field b).  $\omega_r = 2\pi \cdot 50$  rad/s.

### B.4.2.2 Full array measurements

Fig. B.9 shows the mean PM field, measured by the field sensors array, when  $I_d$  changes from -1, i.e. flux weakening current, to 1 pu, i.e. flux intensifying current, in steps of 0.25 pu, no  $q$ -axis current was injected ( $I_q = 0$ ). Fig. B.10 shows the PM field distribution for  $I_d = 1$  pu and  $I_d = -1$  pu.

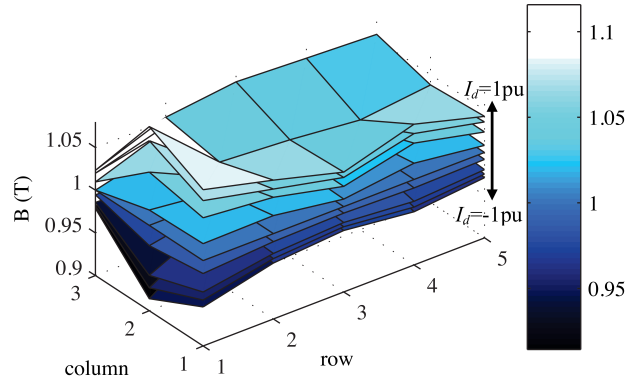


Figure B.9: Experimentally measured magnet field for  $I_q$  current of: 0, 0.2, 0.4, 0.6, 0.8 and 1.0.  $I_d = 0 \text{ pu}$ ,  $\omega_r = 2\pi \cdot 50 \text{ rad/s}$ .

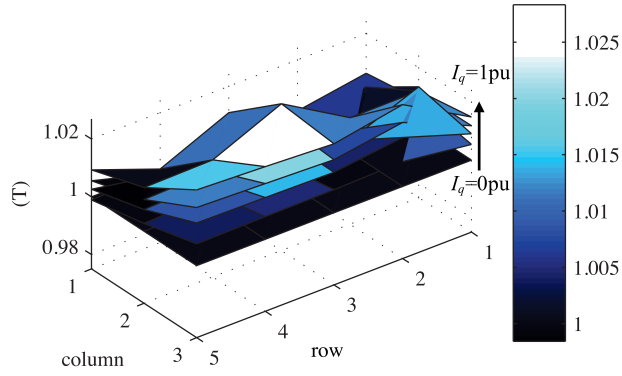


Figure B.10: Experimentally measured magnet field for  $I_d$  current of: 0, 0.2, 0.4, 0.6, 0.8 and 1.  $I_q = 0 \text{ pu}$ ,  $\omega_r = 2\pi \cdot 50 \text{ rad/s}$ .